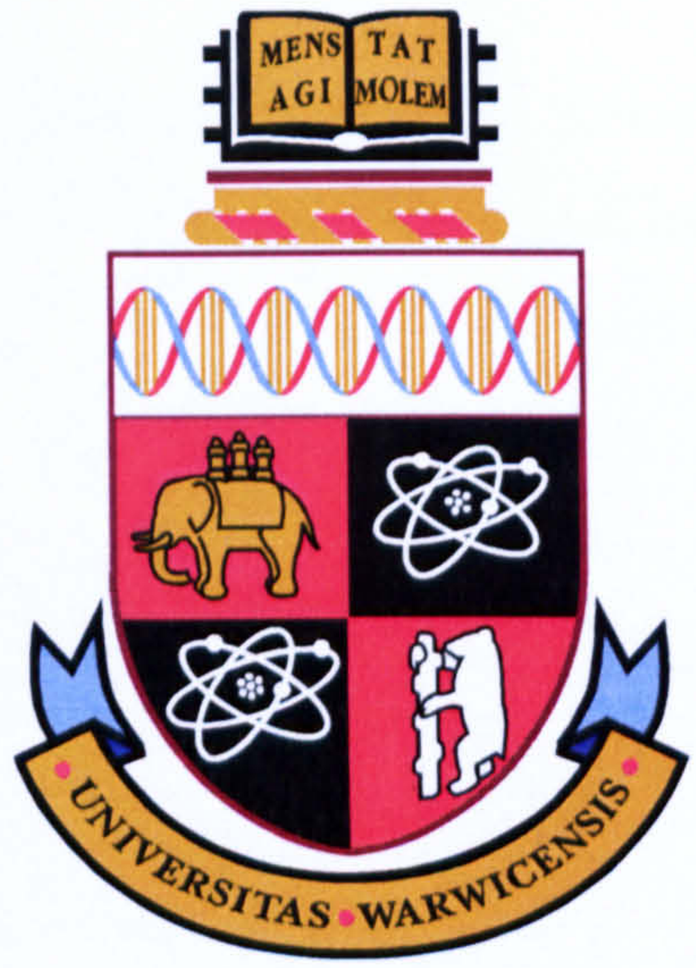

Magnetic resonance studies of point defects in single crystal diamond

by

Andrew Mark Edmonds

Thesis

Submitted to the University of Warwick

for the degree of

Doctor of Philosophy

Department of Physics

July 2008

THE UNIVERSITY OF
WARWICK

ALL MISSING PAGES ARE BLANK

IN

ORIGINAL

Contents

List of Tables

List of Figures

Acknowledgments

First and foremost, I am indebted to Dr. Mark Newton who has been an excellent supervisor for the duration of my PhD. I also thank Mark for helping me to obtain a new position as a Research Assistant in his group. I hope I can pass on some of the guidance and expertise that he has bestowed onto me.

I am grateful to Dr. Philip Martineau and Dr. Daniel Twitchen for their encouragement ("have you submitted yet?") and interest in my work. They also provided most of the samples which were used for the research presented in this thesis. Dr. David Fisher, Ms. Samantha Quinn and Mr. Chris Kelly at DTC have provided invaluable help with sample preparation and initial characterisation. Dr. Chris Welbourn, Prof. Michael Baker and Prof. Jim Butler are also acknowledged for their insightful contributions to my research.

I would also like to thank both the EPSRC and DTC for the financial support they have provided throughout my PhD.

The Warwick diamond group has grown considerably since I began my PhD and I appreciate the contributions and support of past and present members: Brad (for having the knack of asking questions that I *thought* I knew the answer to), Solveig (for assistance with my experiments), Robin (for being there at the beginning and showing me the ropes), Bianca, Radek, Stephanie and Ulrika.

On a personal level I would like to thank my friends at Warwick who have been around during my undergraduate degree and/or subsequent post-graduate research; in no particular order Mike, John, Emma, Dan, Nic, Robin and Ben. A particular mention goes to Emma, for being a good friend during the last 8 years (the time flew by) and Ben, for his moral support during (many) tense Liverpool games. You all made the last few years a genuinely enjoyable and rewarding experience.

Finally I acknowledge the constant help, support and encouragement of my family. This thesis is dedicated to them.

Declaration and published work

I declare that the work presented in this thesis is my own except where stated otherwise, and was carried out entirely at the University of Warwick, during the period of September 2004 to April 2008, under the supervision of Dr. M. E. Newton. The research reported here has not been submitted, either wholly or in part, in this or any other academic institution for admission to a higher degree.

Some parts of the work reported and other work not reported in this thesis have been published, as listed below:

Published papers

[1] A. M. Edmonds, M. E. Newton, P. M. Martineau, D. J. Twitchen, and S. D. Williams, Phys. Rev. B **77**, 245205 (2008).

[2] S. Felton, A. M. Edmonds, M. E. Newton, P. M. Martineau, D. Fisher, and D. J. Twitchen, Phys. Rev. B **77**, 081201 (2008).

[3] A. Tallaire, A. T. Collins, D. Charles, J. Achard, R. Sussmann, A. Gicquel, M. E. Newton, A. M. Edmonds, and R. J. Cruddace, Diam. Relat. Mater. **15**, 1700 (2006).

Conference presentations

[1] A. M. Edmonds, M. E. Newton, P. M. Martineau, and D. J. Twitchen, *EPR studies of silicon related defects in diamond*, SBDD XII, Hasselt (Belgium), poster presentation (2007).

[2] A. M. Edmonds, M. E. Newton, P. M. Martineau, and D. J. Twitchen, *EPR studies of silicon related defects in diamond*, The 58$^{\text{th}}$ Diamond Conference, Warwick, oral presentation (2007).

[3] S. Felton, A. M. Edmonds, M. E. Newton, P. M. Martineau, D. Fisher, and D. J. Twitchen, *The neutral nitrogen vacancy in diamond*, 40$^{\text{th}}$ meeting of the ESR group of RSC, Oxford, poster presentation by S. Felton (2007).

[4] S. Felton, A. M. Edmonds, B. L. Cann, M. E. Newton, P. M. Martineau, D. Fisher, and D. J. Twitchen, *The neutral nitrogen vacancy in diamond*, The 58th Diamond Conference, Warwick, poster presentation by S. Felton (2007).

[5] B. L. Cann, A. M. Edmonds, S. Felton, M. E. Newton, J. M. Baker, K. Haenen, J. Achard, F. Silva, A. Gicquel, P. M. Martineau, et al., *Investigating the structure of a preferentially oriented hydrogen related defect in CVD diamond*, SBDD XIII, Hasselt (Belgium), poster presentation by B. L. Cann (2008).

[6] B. Cann, A. M. Edmonds, S. Felton, M. E. Newton, P. M. Martineau, J. M. Baker, and D. J. Twitchen, *EPR studies of a point defect grown into* {100} *single crystal CVD diamond with a preferred orientation*, The 58th Diamond Conference, Warwick, oral presentation by B. L. Cann (2007).

[7] A. M. Edmonds, M. E. Newton, P. M. Martineau, and D. J. Twitchen, *EPR studies of silicon related defects in diamond*, The 57th Diamond Conference, Cambridge, oral presentation (2006).

[8] A. M. Edmonds, M. E. Newton, P. M. Martineau, and D. J. Twitchen, *EPR studies of silicon doped diamond*, 39th meeting of the ESR group of RSC, Edinburgh, poster presentation (2006).

[9] R. J. Cruddace, A. M. Edmonds, M. E. Newton, P. M. Martineau, and D. J. Twitchen, *Quantitative investigations of defects in single crystal CVD diamond*, The 57th Diamond Conference, Cambridge, oral presentation by R. J. Cruddace (2006).

[10] A. M. Edmonds, R. J. Cruddace, M. E. Newton, P. M. Martineau, S. J. Quinn, and D. J. Twitchen, *Further electron paramagnetic resonance studies of hydrogen defects in diamond*, The 56th Diamond Conference, Oxford, poster presentation (2005).

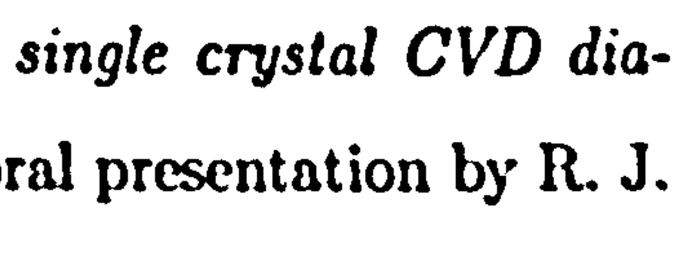

A. M. Edmonds

April 2008

Abstract

Electron paramagnetic resonance (EPR) has been used to study point defects present in synthetic single-crystal diamond grown by chemical vapour deposition (CVD) or high-pressure high-temperature (HPHT) methods.

An EPR fitting method is introduced which employs a generalised lineshape function derived from the Tsallis distribution and pseudomodulation. This method enhances the quality of fits obtained and permits overlapping EPR spectra to be deconvolved. With this system now incorporated into a fitting program, quantitative EPR measurements with a reproducibility of 5% are possible.

The results from EPR studies of CVD diamond which was intentionally silicon doped with isotopes in natural abundance or isotopically enriched are reported. The observation of hyperfine satellites arising due to the presence of ^{29}Si has provided definitive evidence for the involvement of silicon in two EPR centres in diamond which were previously suspected to involve silicon: KUL1 and KUL3. KUL1 is unambiguously identified as the neutral silicon split vacancy defect (V-Si-V)^0, whilst KUL3 is shown to be (V-Si-V)^0 decorated with a hydrogen atom. Data have also revealed that (V-Si-V)^0 is preferentially oriented in samples grown on {110} substrates.

The negative nitrogen-vacancy centre (NV^-) has been investigated. Published parameters for the nitrogen hyperfine interaction produce an unsatisfactory fit to the experimental spectra and hence these parameters are redetermined. Optically-excited EPR has been used to estimate the degree of spin polarisation of the NV^- ground state and the increase in signal intensity with illumination has permitted the interaction between the unpaired electron and neighbouring ^{13}C atoms to be studied. Two sets of ^{13}C hyperfine satellites have been identified, which account for ~ 100% of the unpaired electron probability density.

Despite the predictions that the neutral charge state of NV should have an $S = \frac{1}{2}$ ground state, this charge state has not previously been detected by EPR. Optically excited EPR measurements reveal a trigonal nitrogen containing defect in diamond with an $S = \frac{3}{2}$ excited state populated via optical excitation. Analysis of the spin-Hamiltonian parameters and the wavelength dependence of the optical excitation leads to assignment of this $S = \frac{3}{2}$ state to the $^4A_2$ excited state of NV^0.

Further investigations of the negative nitrogen-vacancy-hydrogen defect are reported. EPR measurements have been obtained at temperatures between 8 and 750 K from samples containing ^{15}N and ^{2}H in natural abundance as well as samples where the source gases have been enriched with these isotopes. The previously published experimentally determined spin-Hamiltonian parameters for this centre have been refined and the effect of isotopic substitution is investigated. The first experimental evidence for dynamics of the hydrogen atom in this defect is presented.

Glossary and abbreviations

A	Hyperfine interaction term
A_s	Isotropic component of the hyperfine interaction
A_p	Anisotropic component of the hyperfine interaction
AFC	Automatic frequency control
ASCII	American standard code for information interchange
B	Applied magnetic field
B_m	Magnetic field modulation amplitude
B_0	Position (in magnetic field) of a resonance line
B_1	Magnetic field component of microwave radiation
CVD	Chemical vapour deposition
D	Zero-field interaction term
E	Energy
EM	Electro-magnetic
EPR	Electron paramagnetic resonance
FTIR	Fourier transform infra-red spectroscopy
g_e	g value for the free-electron
g_N	Nuclear g value
GPIB	General purpose interface bus
$\mathscr{H}$	Spin Hamiltonian term(s)
HF-CVD	Hot-filament chemical vapour deposition
HPHT	High-pressure high-temperature
I	Nuclear spin
IR	Infra-red
k_B	Boltzmann constant
L	Orbital angular momentum
M	Magnetisation
M_S	Projection of electron spin (S) on z-axis

m_I	Projection of nuclear spin (I) on z-axis
m_e	Mass of electron
MP-CVD	Microwave-plasma chemical vapour deposition
N_A	Concentration of acceptors
N_D	Concentration of donors
N_s	Substitutional nitrogen defect
NIR	Near infra-red
NMR	Nuclear magnetic resonance
NV	Nitrogen-vacancy defect
NVH	Nitrogen-vacancy-hydrogen defect
p	Probability of energy level occupation
P	Quadrupole interaction term
$P_{\mu w}$	Microwave power
PAS	Positron annihilation spectroscopy
PL	Photoluminescence
ppm	Parts per million carbon atoms
ppb	Parts per billion carbon atoms
PSD	Phase sensitive detection
q	Tsallis lineshape parameter
Q	Quality factor
S	Electronic spin
$\mathbf{R}$	A proper rotation matrix
SC-CVD	Single crystal diamond grown by chemical vapour deposition
SHQ	Super high Q
SIMS	Secondary ion mass spectroscopy
(V-Si-V)	Silicon split-vacancy defect
(V-Si-V:H)	Silicon split-vacancy defect decorated with hydrogen
T	Temperature
T_1	Spin-lattice relaxation time
T_2	Spin-spin relaxation time
UV	Ultra-violet

VH	Vacancy-hydrogen defect
$\underline{\underline{Y}}$	Spin hamiltonian parameter matrix
ZPL	Zero phonon line
Δ^2	Sum of the squares difference
ΔB_{pp}	Peak-peak EPR linewidth
Γ	Half-width at half-maximum linewidth
γ_e	Gyromagnetic ratio
θ/ϕ	Angle
λ_{h}	Hybridisation ratio
λ_{so}	Russel-Saunders spin-orbit coupling term
μ	Magnetic dipole
μ_B	Bohr magneton
μ_N	Nuclear magneton
μ_s	Absorption coefficient
ν	Microwave frequency
ν_m	Magnetic field modulation frequency
τ	Lifetime
ω_0	Lamour frequency
$\langle hkl \rangle$	A general hkl direction
$[hkl]$	A specific hkl direction
$\{hkl\}$	A general hkl plane
(hkl)	A specific hkl plane

Chapter 1

Introduction

"Better a diamond with a flaw than a pebble without."

— Confucius

1.1 The history of natural diamond

Man's knowledge of diamond dates back to at least 800 BC, when it is believed that the first diamonds were mined from alluvial (river bed) deposits in India. In the early history only unpolished stones were available, which did not display the "fire" observed in diamonds which have been polished and faceted. Despite this the material quickly became regarded as precious due to its rarity, hardness and resilience; the word diamond itself derives from the Greek *adamas* which means unvanquished.

Although possible accounts of diamond exist in Biblical sources (see Tolansky for a discussion [1]), the earliest detailed pseudo-scientific accounts of the material are provided by the Roman philosopher Pliny the elder (A.D. 23–79). His writings clearly reflected the notion of the indestructibility of diamond, with statements such as:

> "They resist blows to such an extent that the hammer rebounds and the very anvil splits asunder"

Whilst not scientifically accurate, their unconquerable status led to the belief that possessing a diamond would bestow the owner with strength in battle and protection from evil forces. Even by the early middle ages diamond was still not worn as an object of beauty, instead holding the status as a magical amulet.

As knowledge of the cutting and polishing of diamond increased it became increasingly regarded as a decorative item. Despite the evidence of table-cut

diamonds existing in the 14th century [1], the art of diamond polishing is usually attributed to the work of Bergham of Bruges in 1476. Bergham is regarded as the first person to fully recognise the importance of the geometrical faceting of diamond for exploiting its optical properties, an understanding which ultimately resulted in the invention of the brilliant cut in the 17th century by Peruzzi in Venice.

Earlier, in 1477, Archduke Maxillian of Austria is believed to have given a diamond ring to Mary of Burgundy as an engagement present, providing the foundation for the modern romantic view of diamonds. De Beers' famous advertising line "A Diamond is Forever", written by Frances Gerety of the N. W. Ayer advertising agency in 1947, has no doubt helped to maintain this image in the mind of the public.

Until the beginning of the 18th century India still provided the world supply of diamonds. In 1725 India lost its status as the world's greatest diamond-producing nation when alluvial deposits were discovered in Brazil. However, both of these sources were quickly eclipsed. In 1866 Eramus Jacobs discovered a 21 carat[1] diamond on the bank of the Orange River in South Africa, which led to the formation of the famous diamond mining town Kimberley.

The mines at Kimberley proved important in the history of diamond mining. Until then all the precious stones had been collected from shallow gravel deposits. Initially this was also the apparent source of diamonds in the Kimberley region, with stones located in loose gravel found on top of an easily crumbled yellow rock. However, diamonds were later found within this yellow ground and further excavation revealed that approximately 15 m beneath this layer existed a much harder blue ground (a mineral known today by the name Kimberlite) which provided an even more plentiful supply of diamonds. Supplies appeared to be inexhaustible and stimulated real development of deep mining fields. By 1889, Cecil Rhodes had formed De Beers Consolidated Mines and the modern age of diamond production began, with the De Beers Company leading the way.

Today the major sources of diamond production also include Botswana, Russia and Australia. Recently, in the period 2001-2005, a yearly average of approxi-

[1] 1 metric carat = 200 mg

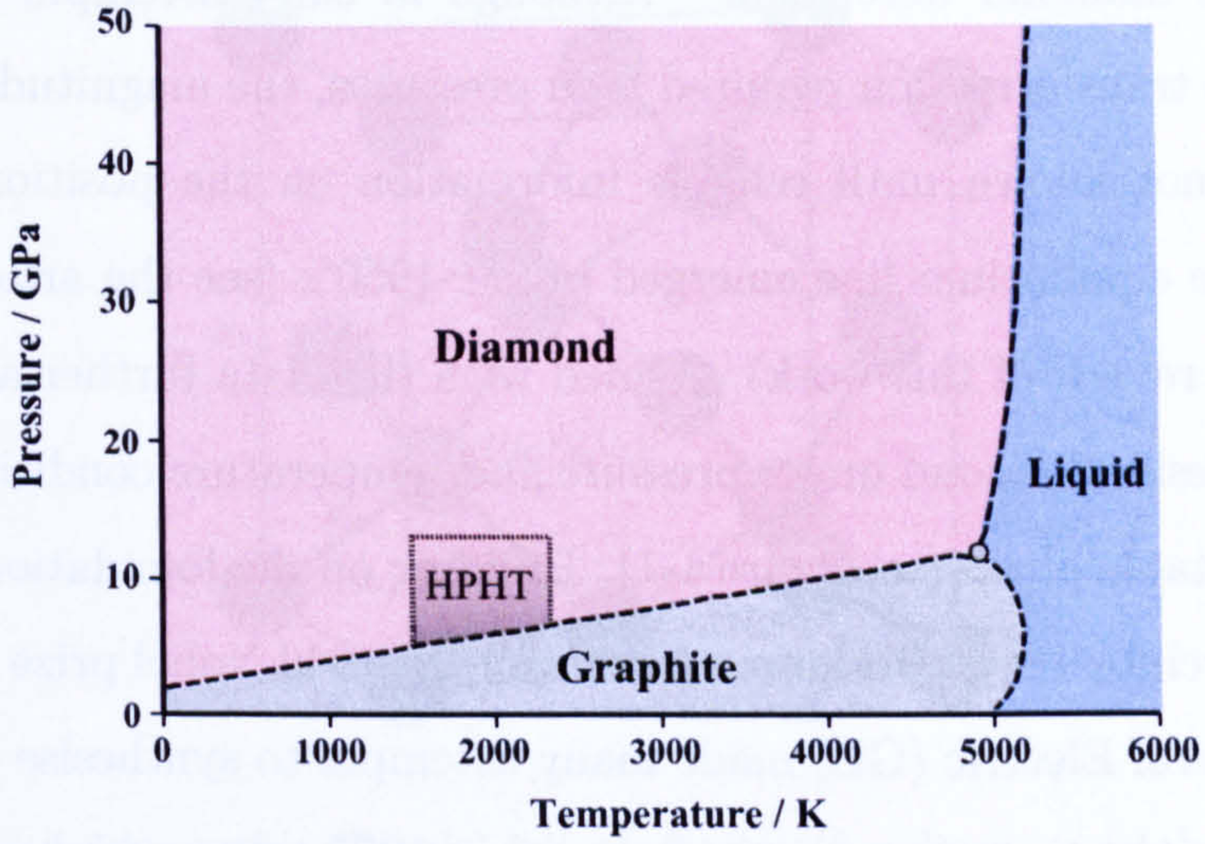

Figure 1-1: The phase diagram of carbon, illustrating the region in which HPHT synthesis occurs. The plot is based on experimental results through to 1994, collated by Bundy *et al.* [4].

mately 170 million carats have been extracted. For this period, Russia ranks first in weight and second in value, but Botswana is first in value and third in weight, just behind Australia [2]. The rough stone market is worth an estimated $13 billion, leading to a $62 billion industry in diamond jewelery [3].

1.2 Synthetic diamond

With diamond being a valuable commodity it is not surprising that the production of diamond in the laboratory ranked with the synthesis of gold as the alchemist's ultimate dream. However, until the 18^{th} century the composition of diamond was not known.

In 1772 Antoine Lavoisier conducted an experiment in which he successfully burnt a diamond contained within a sealed container, using sunlight focused through a lens. The gas produced was identified as carbon dioxide, which led Lavoisier to conclude that diamond must, in some way, be related to charcoal [5]. Later combustion experiments by Smithson-Tennant [6] demonstrated that diamond is comprised solely of carbon.

After this discovery many attempts to transform readily available sources

of carbon into diamond were made. Although in early attempts [7] it was realised that the transformation required high pressures, the magnitude of pressures required was not known until reliable information on the position of the diamond/graphite equilibrium line emerged in the 1950's (see the article by Bundy *et al.* [4] for a review of this work). Armed with this data further attempts were made to synthesise diamond under pressure and temperature conditions where diamond is the stable phase (see figure 1-1). Building on the foundations of the high pressure research by Percy Bridgman (who won the 1946 Nobel prize in physics for his work) General Electric (GE) made many attempts to synthesise diamond and reported the production of synthetic diamond in 1955 using a high-pressure high-temperature (HPHT) method. Unfortunately the sample which was the subject of the paper in Nature announcing their success [8] was later shown to be a natural diamond seed which accidently found its way into the run [9]. Despite this the method was sound and other runs around that time produced synthetic diamond. Subsequently a team working for the Swedish electricity company ASEA reported that they had synthesised diamond using such a technique. Their first success was achieved in 1953 but was not reported until the 1980's. Hence the accolade of the first production of synthetic diamond generally rests with GE.

The earliest proposals for growing diamond at low pressures (where graphite is the thermodynamically stable phase) from a vapour source also came to light in the 1950's, with the first claim of successful synthesis by Eversole in 1958 [10, 11]. In the chemical vapour deposition (CVD) method, instead of trying to mimic the thermodynamic conditions under which stones are formed naturally, diamond is grown from a mixture of hydrogen and hydrocarbons in the vapour phase. The growth of diamond using CVD has evolved significantly since this early work and, with careful control of the growth conditions, it has recently become possible to grow large (gem sized) single-crystal diamonds by microwave plasma CVD (see for example the work of the groups in Carnegie [12, 13] or Paris [14]). The synthesis of diamond by CVD and the incorporation of impurities/dopants is of particular importance to this thesis and will be covered in §2.1.2.

Synthesis techniques have the potential to produce diamond at lower costs than natural sources, but, more importantly they also provide the capability to produce

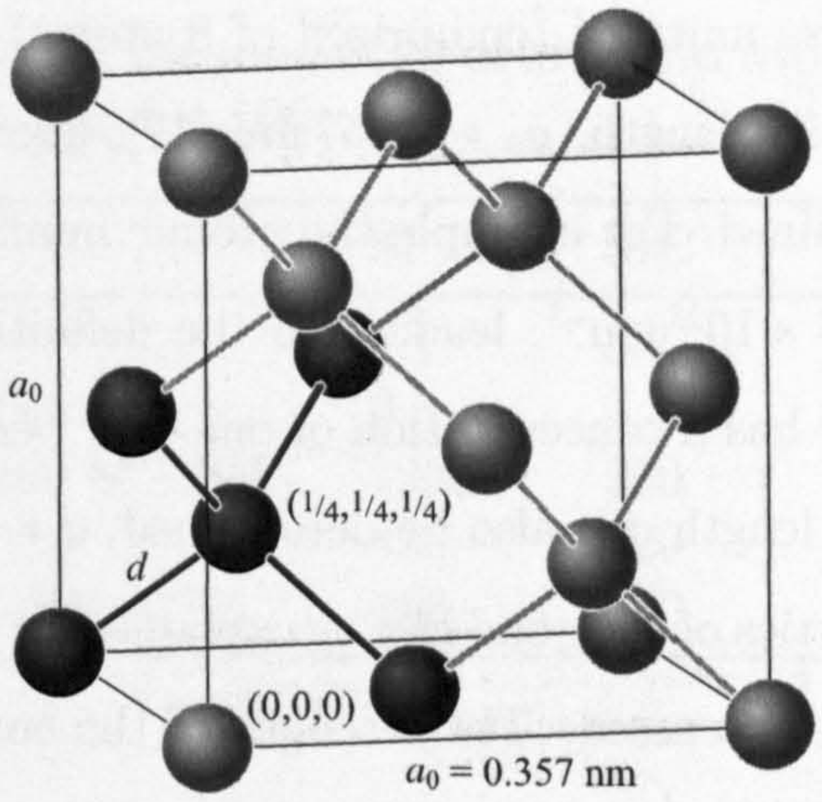

Figure 1-2: The conventional unit cell of diamond, where a_0 is the cubic lattice parameter and d is the C-C bond length. The five darker spheres highlight the tetrahedral structure of diamond.

diamond with tailored properties. For example, when producing synthetics for gemstones, the addition of boron during growth allows stones with an attractive blue colour to be produced (the articles by Shigley *et al.* [15] and Martineau *et al.* [16] provide a review). The production of gem quality CVD diamond has led to research in spectroscopic techniques to distinguish naturals from synthetics [16].

1.3 The properties and applications of diamond

Diamond is an allotrope of carbon, which in its ground state adopts the electronic configuration $1s^2 2s^2 2p^2$, meaning that the isolated atom has two core electrons occupying a 1s orbital and four valance electrons shared equally between 2s and 2p orbitals. In diamond a 2s electron is promoted such that the configuration is $1s^2 2s^1 2p^3$, hence the s orbital mixes with the three p orbitals to form four sp^3 hybridised orbitals. Whilst the promotion of this electron is energetically expensive, diamond is energetically stable as electron sharing (through covalent bonding) results in complete electron shells. The geometry of the hybridised orbital is tetrahedral, hence each carbon atom within diamond has four nearest neighbours.

The resulting crystal structure can be conveniently envisaged as two interpenetrating face-centred cubic (fcc) cells, with one sublattice displaced from the other

by $a/4$ along [111]. The unit cell (comprised of 8 atoms) is illustrated in figure 1-2. Considering the side length, $a_0 = 0.357\,\text{nm}$ [17], allows a number of useful quantities to be determined. For example the atomic number density can be calculated as $8/{a_0}^3 = 1.76 \times 10^{23}\,\text{cm}^{-3}$, leading to the definition that a defect with density $1.76 \times 10^{17}\,\text{cm}^{-3}$ has a concentration of one part per million carbon atoms (ppm). The C–C bond length can also be determined, $d = \sqrt{3}a_0/4 = 0.154\,\text{nm}$.

Several of the properties of diamond can be explained by considering the atomic and electronic structure discussed. The strength of the covalent C–C bonds and the three-dimensional stability of the tetrahedral bonding arrangement are responsible for diamond's intrinsic rigidity and renowned hardness, with natural diamond being used as the maximum (10) for the calibration of the Mohs (scratch) hardness scale. The strong bonding also means that diamond has high chemical stability and is radiation hard. Furthermore, the covalent bonds can transfer atomic vibrations efficiently throughout the crystal, giving rise to a high thermal conductivity; diamond has the highest thermal conductivity of any material at $2500\,\text{W}\,\text{m}^{-1}\,\text{K}^{-1}$ (at 300 K) [18].

The proximity of the carbon atoms causes a large forbidden energy gap between the valance and conduction band states in diamond. The resulting band gap of $\sim 5.47\,\text{eV}$ at 300 K [19] means diamond is typically regarded as a wide band-gap semiconductor (if not an insulator). The wide band gap means diamond is optically transparent to wavelengths down to 227 nm. This transparency extends into the near-infrared ($2.5\,\mu\text{m}$) [20].

The combination of the hardness and high thermal conductivity explains the traditional use of diamond in tools for grinding, sawing and drilling. HPHT synthesised diamonds have been widely used in such applications, accounting for over 90% of the diamond abrasive market [21].

The CVD method provides additional capabilities over the HPHT method, with added flexibility in the size/shape of the deposited material. This has widened the range of potential applications for diamond, which include:

- Thermal management: Modern high-power electronic and opto-electronic devices may suffer cooling problems due to the production of large amounts of heat. By spreading the narrow heat flux between the device and cooling

Table 1-1: A comparison of the properties of diamond with other semiconductors. Table adapted from Hadlington [28].

Property	**Si**	**SiC**	**GaN**	**Diamond**
Bandgap (eV)	1.1	3.2	3.44	5.5
Breakdown field ($MV\,cm^{-1}$)	0.3	3	5	20
Electronic mobility ($cm^2\,V^{-1}\,s^{-1}$)	1450	900	440	4500
Hole mobility ($cm^2\,V^{-1}\,s^{-1}$)	480	120	200	3800
Thermal conductivity ($W\,m^{-1}\,K^{-1}$)	150	500	130	2400

system using a layer of high thermal conductivity, such devices can be cooled. The CVD method permits large area plates to be produced and the nitrogen impurity content and isotopic ratios can be controlled, allowing the thermal conductivity to be maximised [22, 23].

- Optical windows: Due to its optical properties diamond is finding uses in optical components. Combining the optical and thermal properties with its resistance to mechanical and chemical attack means it is attractive for use as an infrared (IR) window in harsh environments. Particular attention has been paid recently regarding its use as a material for high power laser windows [24].
- Protective coatings: The hardness and chemical inertness of diamond mean it is ideal for protective coatings. The CVD method provides the capability to deposit diamond on a range of substrates with almost any shape [25].
- Microelectromechanical devices: The stiffness and wear resistance of diamond mean it is a suitable material for hard-wearing microelectromechanical (MEMS) structures. Such applications exploit the ability to produce thin patterned films by the CVD method [26].

Recently, the finding that high purity single-crystal CVD diamond can have electron and hole mobilities many times higher than those of other semiconductors (4500 and $3800\,cm^2\,V^{-1}\,s^{-1}$ respectively [27]) has led to interest in the use of diamond in certain electronic applications. A comparison of some of the electronic properties of diamond and other semiconductors is shown in table 1-1.

One potential application for diamond is in power electronics for systems that control/modify high electrical powers. In such devices the ability to operate at

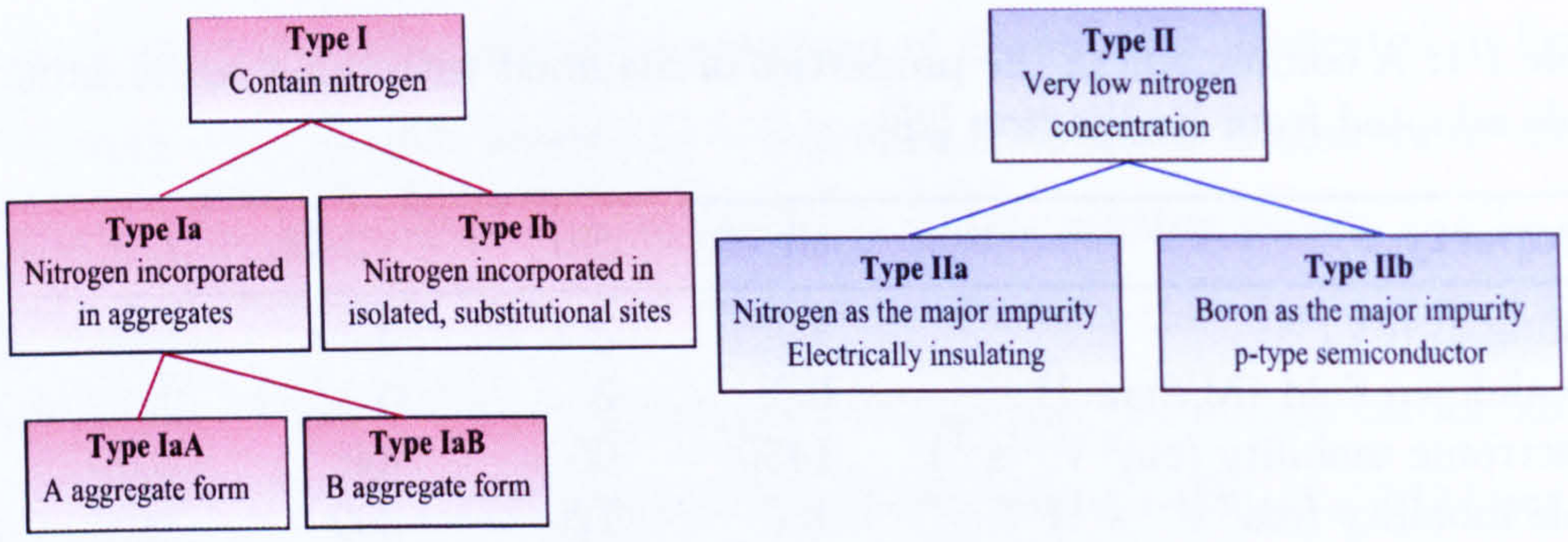

Figure 1-3: The classification scheme for diamond. Adapted from Collins [30].

high temperatures is of paramount importance and it is also desirable to reduce the size of the devices. The wide band gap of diamond compared to silicon means that higher temperatures can be reached before thermally generated charge carriers exceed the background levels due to donor or acceptor dopants. This, coupled to its high thermal conductivity (an order of magnitude higher than many of the alternatives), means that diamond based devices can operate at higher temperatures whilst allowing heat to be dissipated. The higher breakdown voltage also means that fewer devices need to be connected in series, allowing the size of switching systems to be reduced [29]. It is apparent that, in such niche applications, diamond offers clear benefits over silicon.

1.4 Classification of diamond

Examination of the optical absorption spectra of natural diamonds in the early 20^{th} century revealed that a rare subset of natural diamonds exists, which do not contain spectral features that are present in most samples. A proposal to classify diamonds into two "types" (I or II) was therefore suggested by Robertson *et al.* [20]; type I are the samples containing the regular absorption lines, whilst type II are the rarer samples where such features are absent. It is now known that variations in the nitrogen content are responsible for the observed differences in absorption spectra between the two types.

Diamonds which reveal absorption lines in infrared (IR) spectroscopy associated with nitrogen incorporation are assigned to the type I group. Natural diamonds generally fall under this classification, but further spectroscopic mea-

surements have permitted further subdivisions of this category, dependent on the form in which nitrogen is incorporated. In most samples nitrogen is present in the form of aggregates, either as A-centres (a pair of subtitutional N atoms) or B-centres (four N atoms around a vacancy), leading to the assignment to group IaA and IaB, respectively. C-centre defects consist of single substitutional nitrogen atoms in the diamond lattice that are spatially isolated. Diamonds containing C-centres are classified as type Ib.

When neither A, B nor C centres are visible by IR (< 1–2 ppm for each form [31]) the diamond is classified as type II. If semi-conducting (due to presence of boron) diamonds are assigned to type IIb; otherwise they are called type IIa.

This classification scheme is regularly used for natural and synthetic diamond grown by the HPHT method as the nitrogen content in such material is sufficiently high and variable for the divisions to be useful. In modern CVD material, however, nitrogen concentrations can be below the detection limits of IR, hence samples (unless doped with boron) are almost uniformly classed as type IIa.

1.5 Motivation for study: defects in diamond

A *defect* is said to exist in a region where the microscopic arrangement of atoms differs from that of the perfect crystal. An understanding of the structure and constituents of defects in diamond is important since their presence can greatly affect the properties of the material. For example, when discussing the classification of natural diamond in §1.4 it was apparent that the presence of nitrogen in diamond gives rise to additional absorption features in IR spectroscopy. Hence it is clear that nitrogen influences the optical properties of the material. It has also been mentioned that doping with boron gives rise to a blue colouration. Observations such as these have led others to investigate the ways in which nitrogen and boron are incorporated in diamond, to understand *why* such properties arise. It is a similar interest in the fundamental structure of defects in diamond that drives the investigations which are contained within this thesis.

Describing such breaks in the perfect crystal structure using the term "defects" gives the impression that their presence is detrimental. Whilst this is true in some

cases applications exist where the incorporation of impurity atoms is essential. For example, producing diamond based electronic devices as discussed in §1.3 necessitates the doping of diamond to produce p or n-type material. It is established that doping with boron can give rise to p-type conductivity (discussed further in §2.1.2.3), but finding a suitable n-type dopant remains a problem [32].

Some defects have desirable properties in themselves; for example the nitrogen-vacancy centre (§2.2.1.2) has attracted attention recently for its possible use in quantum information processing by acting as a single photon-source or a quantum bit ("qubit") in a quantum computer [33].

The realisation of such novel applications necessitates an understanding of the nature of the defect itself and spectroscopic results play a critical role in this quest. It is the goal of this thesis to contribute to this knowledge base.

1.6 Why use EPR?

In this study the principal tool used is electron paramagnetic resonance (EPR). EPR is a powerful probe of paramagnetic defects (i.e. those containing unpaired electrons) as it can provide structural information, details of electron density distributions and, via the interaction of electrons with nuclei, it acts as an element specific probe which yields information concerning the atomic-scale environment of the electron.

With careful experimental work and analysis EPR can also provide quantitative information regarding spin concentrations and, because of the high sensitivity, it allows quantitative measurements to be obtained when concentrations drop below the sensitivity limits of other spectroscopic methods. For example, it was stated in §1.4 that below ~ 1–2 ppm C-centres (N_s defects) are no longer detected by IR spectroscopy. Using EPR allows N_s^0 concentrations below this level to be readily detected [34], but, since the technique is only able to provide information on paramagnetic defects, it should always be regarded as complementary to other spectroscopic probes.

Illumination during an EPR experiment can be used to stimulate changes in defect concentrations via ionisation; such studies can be used to elucidate the

position of a defect's localised electron energy level within the band gap. In combination with optical excitation, EPR can also, in some cases, probe excited states of a defect and yield information regarding optical transitions, thus providing a bridge between optical and magnetic resonance spectroscopy.

1.7 Nomenclature

Defects identified by EPR are often initially labelled by the first letter(s) of the place or institution where the defect was first observed. This is frequently followed by a number which is incremented each time a new defect is discovered. For instance P1 was the first defect observed by the International Business Machines research group based in Poughkeepsie [35]. A list of defects in diamond observed using EPR prior to 2001 is provided by Ammerlaan [36].

Defects identified by optical spectroscopy are either labelled according to the energy or wavelength at which the zero-phonon line (ZPL) is found, or alternatively, according to the production method. For example a ZPL at 1.673 eV (741 nm) has been observed in diamond, but since this is produced by irradiation it is also referred to as the first general irradiation defect (GR1) [37]. Zaitsev has produced a comprehensive list of optical absorption lines and their labels (through to 1998) [38].

The defects discussed in this thesis are *point* defects. There is not strict limit for how small a point defect should be, but typically the term is used to mean defects which involve at most a few extra or missing atoms without an ordered structure of the defective positions throughout the crystal.

- In cases where an atom is removed from the crystalline lattice and is not replaced the defect is called a vacancy (V).
- Interstitial atoms are those which occupy a site in the crystal structure where there is not usually an atom. In such cases the subscript i is added to the chemical symbol for the atom sitting in the interstitial site, e.g. Ni_i for a nickel interstitial defect.
- If an impurity atom is incorporated at a site normally occupied it is referred to as a substitutional defect. The subscript s is used in such cases, e.g. N_s

for a substitutional nitrogen defect.

In cases where defects have been assigned to specific models a more descriptive name may be assigned using the notations listed above. GR1 and P1 have been conclusively identified as the neutral vacancy [37] and the neutral single substitutional nitrogen [35] defects (discussed in more detail in §2.2.1.1) and are therefore often referred to as V^0 and N_s^0, respectively.

1.8 Thesis outline

This thesis consists of four background and five results chapters:

- The introduction provides a brief overview of diamond and the motivation for the studies presented in the results chapters. Necessary nomenclature is presented and EPR is introduced.
- The literature review in chapter 2 provides a critical overview of previous work which is relevant to the research presented in this thesis. The synthesis of synthetic diamond is discussed with the emphasis on doping studies and the presence of defects in diamond.
- The theory of EPR is covered in chapter 3, where the terms in the spin Hamiltonian, need for this work, are explained. A discussion of symmetry, relating to the simulation of EPR spectra, is also included.
- Chapter 4 is the last background chapter. Here the experimental aspects of EPR are introduced and details regarding the spectrometers and the various experimental setups used are presented. Improvements made regarding the spectrometers themselves and analysis software are also discussed.
- In chapter 5 new EPR spectrum fitting software which has been produced, permitting multiple overlapping EPR spectra to be de-convolved, is presented. The methods used will be shown to have improved the reproducibility and accuracy of quantitative EPR measurements.
- The results obtained during investigations of silicon-doped CVD diamond are shown in chapter 6. Two silicon-related defects have been conclusively identified and the defect models are compared to the predictions from theoretical modelling.

- The investigations presented in chapter 7 reveal that a silicon-related defect is preferentially oriented with respect to the direction of growth. The importance of this is discussed with respect to the formation of the defect as well as the incorporation efficiency of silicon on differently oriented diamond surfaces.
- Chapter 8 concerns the results obtained from nitrogen-doped HPHT and CVD diamond. These samples have permitted investigations of the negative nitrogen-vacancy centre. A new nitrogen-related defect has also been detected and this is shown to be an excited state of the neutral nitrogen-vacancy centre.
- The final section (chapter 9) presents further investigations of the negative nitrogen-vacancy-hydrogen defect in CVD diamond. The use of multi-frequency EPR has enabled improved spin-Hamiltonian parameters to be found and the studies also provide the first experimental indication that the hydrogen atom in this centre exhibits dynamic behaviour.

References

[1] S. Tolansky, *The history and use of diamond* (Methuen & Co. Ltd., London, 1962).

[2] A. J. A. Janse, Gems. Gemmol. **43**, 98 (2007).

[3] *Changing facets*, The Economist. London: Feb 24, 2007. Vol. 382, Iss. 8517; pg. 68.

[4] F. P. Bundy, W. A. Bassett, M. S. Weathers, R. J. Hemley, H. U. Mao, and A. F. Goncharov, Carbon **34**, 141 (1996).

[5] A. L. Lavoisier, Memoire Academie des Sciences pp. 567,591 (1772).

[6] S. Tennant, Philos. Tr. R. Soc. **87**, 123 (1797).

[7] C. H. Desch, Nature **121**, 799 (1928).

[8] F. P. Bundy, H. T. Hall, H. M. Strong, and R. H. Wentorf, Nature **176**, 51 (1955).

[9] H. P. Bovenkerk, F. P. Bundy, R. M. Chrenko, P. J. Codella, H. M. Strong, and R. H. Wentorf, Nature **365**, 19 (1993).

[10] W. G. Eversole and N. Y. Kenmore (1958), US Patent 3030187.

[11] W. G. Eversole and N. Y. Kenmore (1958), US Patent 3030188.

[12] C. S. Yan, H. K. Mao, W. Li, J. Qian, Y. Zhao, and R. J. Hemley, Phys. Status Solidi A **201**, R25 (2004).

[13] C. S. Yan, Y. K. Vohra, H.-k. Mao, and R. J. Hemley, Proc. Natl. Acad. Sci. **99**, 12523 (2002).

[14] A. Tallaire, J. Achard, F. Silva, R. S. Sussmann, and A. Gicquel, Diam. Relat. Mater. **14**, 249 (2005).

[15] J. E. Shigley, S. F. McClure, C. M. Breeding, A. Hsi-tein Shen, and M. Muhlmeister, Gems. Gemmol. **40**, 128 (2004).

[16] P. M. Martineau, S. C. Lawson, A. J. Taylor, S. J. Quinn, D. J. F. Evans, and M. J. Crowder, Gems. Gemmol. **40**, 2 (2004).

[17] J. E. Field, *The properties of natural and synthetic diamond* (Academic Press, London, 1992).

[18] J. W. Vandersande, in *Properties and Growth of Diamond*, edited by G. Davies (INSPEC, London, 1994), chap. 1.7, pp. 33–35.

[19] C. D. Clark, P. J. Dean, and P. V. Harris, Proc. Roy. Soc. Lond. A Mat. **277**, 312 (1964).

[20] R. Robertson, J. J. Fox, and A. E. Martin, Philos. Tr. R. Soc. S-A **232**, 463 (1934).

[21] P. N. Tomlinson, in *The Properties of Natural and Synthetic Diamond*, edited by J. E. Field (Academic Press, London, 1992), chap. 17, pp. 637–665.

[22] R. Berman, in *The Properties of Natural and Synthetic Diamond*, edited by J. E. Field (Academic Press, London, 1992), chap. 7, pp. 291–300.

[23] J. Hartmann and M. Reichling, in *Properties, growth and applications of diamond*, edited by M. H. Nazare and A. J. Neves (INSPEC, 2001), chap. A1.5, pp. 32–39.

[24] C. S. J. Pickles, T. D. Madgwick, R. S. Sussman, and C. E. Hall, Ind. Diamond Rev. **60**, 293 (2000).

[25] P. Ball, New Scientist **2067**, 22 (1997).

[26] M. A. Huff, D. A. Aidala, and J. E. Butler, Solid State Technol. **49**, 45 (2006).

[27] J. Isberg, J. Hammersberg, E. Johansson, T. Wikstrom, D. J. Twitchen, A. J. Whitehead, S. E. Coe, and G. A. Scarsbrook, Science **297**, 1670 (2002).

[28] S. Hadlington, IEE Review **51**, 30 (2005).

[29] P. D. Taylor, D. J. Chamund, and A. Garraway, Ind. Diamond Rev. pp. 19–22 (2006).

[30] A. T. Collins, Physica B **185**, 284 (1993).

[31] G. S. Woods, in *Properties and Growth of Diamond*, edited by G. Davies (INSPEC,

London, 1994), chap. 3.1, p. 83.
[32] M. Nesladek, Semicond. Sci. Tech. **20**, R19 (2005).
[33] F. Jelezko and J. Wrachtrup, Phys. Status Solidi A **203**, 3207 (2006).
[34] R. J. Cruddace, Ph.D. thesis, University of Warwick (2007).
[35] W. V. Smith, P. P. Sorokin, I. L. Gelles, and G. J. Lasher, Phys. Rev. **115**, 1546 (1959).
[36] C. A. J. Ammerlaan, *Paramagnetic centers in diamond* (Springer, 2001).
[37] G. Davies, S. C. Lawson, A. T. Collins, A. Mainwood, and S. J. Sharp, Phys. Rev. B **46**, 13157 (1992).
[38] A. M. Zaitsev, *Optical data on superhard semiconductors, Part 1, Diamond* (ISTOK, 1998).

Chapter 2

Literature review

Rather than attempting to review the entire field of diamond physics this chapter aims to review the literature of direct relevance to the results presented in later chapters. Since the focus of this thesis is on the detection and identification of defects in synthetic diamond this review will start by discussing the literature related to synthesis methods. The results of doping studies in the literature are used to elucidate the solubility of a number of dopants/impurities in synthetic diamond and the influence that they have on growth is discussed. In the final section literature relating to the way in which dopants are incorporated in the form of defects and the effect that these have on the properties of diamond is reviewed.

2.1 Growth of synthetic diamond

2.1.1 High Pressure High Temperature

2.1.1.1 The HPHT method

In the work of Bridgman published in 1947 [1] graphite was compressed to pressures well within the diamond stable region. However, diamond was not produced, revealing that it is not sufficient to simply apply pressures and temperatures within the diamond stable region to convert graphite to diamond (hence Bridgman's quote "graphite is nature's best spring"). A method was needed to overcome the large kinetic barriers between sp^2 hybridised graphite and sp^3 hybridised diamond. The crucial advance that General Electric made was the discovery that a transition metal solvent/catalyst could be used to solve this problem; a finding which led to the first successful synthesis of diamond from graphite using the HPHT process [2]. The techniques used today remain largely unchanged and metals such as Ni,

Co and Fe are the most popular catalysts. Non-metalic catalysts have also been employed [3], although not for commercial synthesis.

The technological aspects of producing and sustaining pressures in excess of 6 GPa and temperatures around 1500 K, required for HPHT synthesis, are the subject of many reviews (e.g. Wedlake *et al.* [4]) and hence will not be discussed here. Of greater relevance to the results presented in this thesis is the research in the literature concerning the solubility of dopants/impurities in HPHT material and the methods involved with doping.

Synthetic diamond is usually grown in a high pressure cell containing air, therefore there is the potential for nitrogen (and other highly abundance gases) to be incorporated. Nitrogen is often found to be present in the grown diamond in an isolated substitutional position [5] and sometimes, dependent on the growth temperature and time, also in aggregated form (A-centres) [6]. Typical concentrations of nitrogen in HPHT material, where no attempt has been made to restrict the incorporation, are of the order of a few hundred atomic parts per million (ppm) [7].

2.1.1.2 Doping studies of HPHT diamond

To limit and control the incorporation of nitrogen in HPHT diamond a chemical partitioning system is most frequently used. In this method, no or only a limited attempt is made to remove the nitrogen from the starting materials, instead a "getter" is added to the solvent/catalyst. This is a metal (commonly Zr, Al or Ti) which has a strong affinity to nitrogen, resulting in most of the nitrogen remaining in the metallic melt [8–10]. However, if any of these additives are considered to be undesirable contaminants in the final grown crystal then the direct physical elimination of the nitrogen by high-temperature degassing is an alternative (but rarely used) method. Strömann *et al.* [11] describe a method whereby the growth capsule is pre-treated to remove the vast majority of the atmospheric gases. At reduced temperatures the removed gases can then be replaced by a selected process gas before the capsule is resealed and subjected to HPHT conditions in the diamond stable region [11].

Doping studies of nitrogen in HPHT diamond can be conducted by the addition

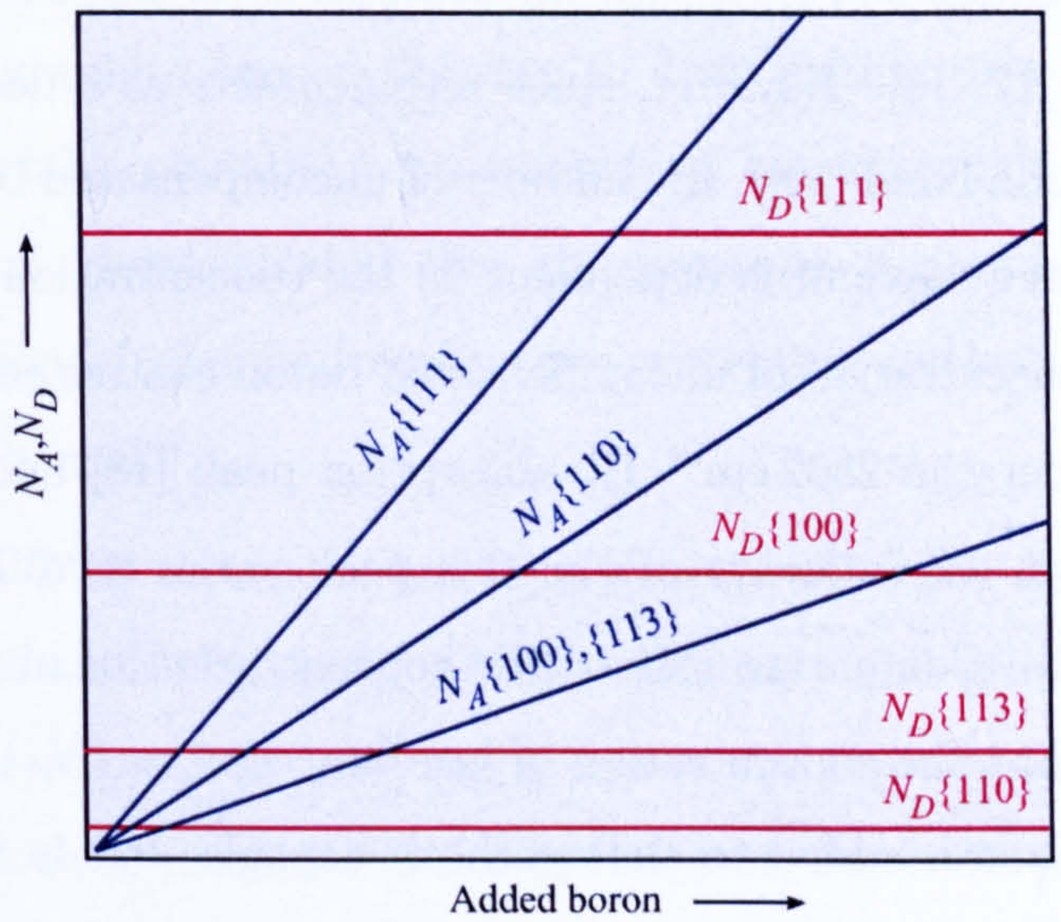

Figure 2-1: Concentration of boron acceptors (N_A) and nitrogen donors (N_D) in different growth sectors of HPHT diamond with increasing boron doping. Adapted from Kanda and Sekine [14].

of nitrogen-containing compounds to the growth system. Using iron nitride (Fe_3N) nitrogen concentrations as high as 3300 ppm have been reported [12].

The concentration of nitrogen in the form of the single substitutional impurity can be inferred from the height of the 1130 cm^{-1} IR absorption peak [5] (see §2.2.1.1). Studies of the intensity of this absorption peak in different growth sectors of HPHT samples have demonstrated that the uptake of nitrogen is growth sector dependent [13]. At regular growth temperatures ($\gtrsim$1350°C) the {111} sectors are found to contain the highest nitrogen concentration followed by, in order of decreasing uptake, {100}, {113} and {110} [13]. As the temperature decreases the incorporation efficiency in both {100} and {111} sectors increases, but the concentration in {100} sectors rises more quickly [14]. Hence at lower temperatures the uptake in {100} sectors can exceed that in {111}. The literature also suggests that the solubility of nitrogen is strongly dependent on the solvent/catalyst used in the growth process [12, 15].

Boron atoms are readily incorporated in the growing diamond if materials containing boron are present in the growth cell [8, 13, 16]. The results of investigations of boron-doped HPHT material and selected natural stones allowed boron to be identified as the impurity responsible for the p-type conductivity observed

in type IIb natural diamond [17], with the acceptor level 0.37 eV above the top of the valance band [17, 18]. However, since nitrogen acts as a deep donor (1.7 eV below the conduction band [19]), the number of uncompensated boron centres and hence the electrical behaviour is dependent on the concentration of nitrogen centres (N_D). The concentration of uncompensated boron centres can be determined from the area under the 2802 cm^{-1} IR absorption peak [18] and doping studies have indicated that the intensity of the this peak varies in differently oriented growth sectors [13]. Comparing this to the concentration of nitrogen led Burns *et al.* to suggest that the concentration of boron acceptors (N_A), is proportional to the amount of boron added to the synthesis capsule, but is highest in {111} sectors, followed by {110} and {100}/{113} sectors [13]. Figure 2-1 indicates the determined correlation between boron and nitrogen concentrations with added boron.

To facilitate investigations of silicon-related centres (see §2.2.3) HPHT diamond has also been doped with silicon. Sittas *et al.* conducted doping studies using various silicon-containing alloys, with silicon added to Ni, Co and Fe [20]. Defects associated with the incorporation of silicon were only observed in specimens grown with nitrogen getters (Ti and Zr) and the uptake of silicon was found to be very inhomogeneous (although no clear sector dependence was apparent). Diamonds grown with a Fe catalyst with silicon added were found to contain a larger number of metallic inclusions, compared to those grown with mainly Ni or Co, suggesting that silicon affects the uptake of other impurities in diamond [20].

2.1.2 Chemical Vapour Deposition

2.1.2.1 The CVD method

Chemical vapour deposition (CVD), as the name implies, involves a chemical reaction in the gas phase occurring above a substrate, which causes deposition onto that surface. In the first demonstrations of the growth of diamond by the CVD method by Eversole in 1958 [21, 22] thermal decomposition of carbon-containing gases at low pressures was used to grow diamond on the surface of natural diamond heated to 900–1100°C. In such early demonstrations of epitaxial diamond synthesis

the growth rates were prohibitively low (no faster than 0.1 μm per hour) and co-deposition of graphite caused the rate to drop further over time, making the method commercially unviable. An important breakthrough occurred in 1968 when Angus *et al.* demonstrated that the presence of atomic hydrogen led to selective deposition of diamond carbon by preventing nucleation and growth of graphitic sp^2 carbon [23].

Although the CVD technique has been greatly advanced since 1968 the basic principles have remained unchanged. The chemistry and growth mechanism for CVD will not be covered in here, since this is the topic of many good reviews on the CVD growth of diamond [24, 25]. However, the basic processes occurring during CVD growth are illustrated in figure 2-2. A gas mixture of H_2 and CH_4 is most frequently used and on dissociation this provides carbon-containing radicals that act as the source of carbon for the growing diamond and atomic hydrogen which, as Angus *et al.* demonstrated [23], is critical for sustaining the growth.

Various vapour-phase activation methods can be employed to accelerate the dissociation of H_2 and to form hydrocarbon free radicals, with the simplest of these involving a hot filament heated to ~ 2000°C placed near the substrate. Although hot-filament CVD (HF-CVD) offers a simple experimental setup [26], film contamination is an issue, as the filament material cannot easily be prevented from being incorporated into the growing diamond. Argoitia *et al.* [27] provide a good review of the method, where typical growth conditions are discussed.

Activation and growth of diamond using a 2.45 GHz microwave plasma was first reported by Kamo *et al.* in 1983 [28]. In contrast to HF-CVD, microwave plasma CVD (MP-CVD) is "sterile", in the sense that there is no electrode sputtering. In a conventional MP-CVD system the 2.45 GHz microwaves emitted from a generator propagate through a set of waveguides to a reaction chamber. The exact setup of the chamber varies, but an example of a commercial (ASTeX) CVD chamber is shown in figure 2-2. A review of past and present reactors can be found in Bachman [29].

Due to the availability of standard 2.45 GHz components and the wide experience accumulated to-date concerning microwave plasma surface processing MP-CVD has found widespread use for diamond synthesis [29]. It has been demon-

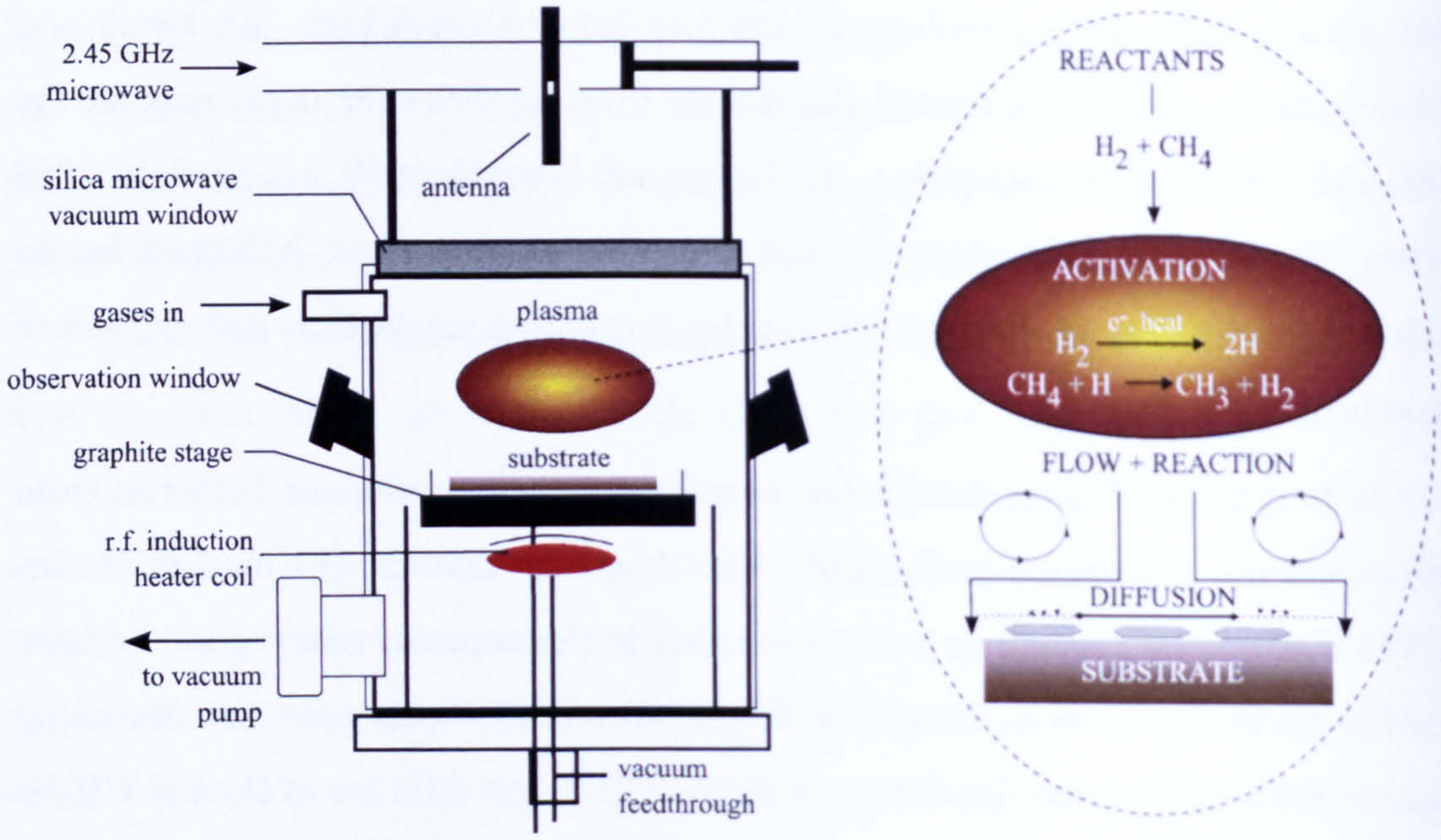

Figure 2-2: An example of a commercial (ASTeX) 2.45 GHz MP-CVD reactor used for deposition of diamond and the processes occurring during growth. Figures adapted from [24, 25, 29].

strated that the MP-CVD method can produce electronic and optical device-grade (and also gem quality) *single-crystal* CVD diamond (SC-CVD) when grown on diamond substrates [30–32]. As a result, much of the focus in the recent literature has concerned the synthesis of such material and the optimisation of the growth parameters used. From an economical point of view it is important to be able to synthesise diamond at relatively high growth rates, while preserving the low concentration of defects and controlling the crystallinity.

2.1.2.2 CVD growth considerations

For homoepitaxial diamond growth using MP-CVD the orientation and preparation of the substrate have both been shown to affect the surface morphology of the sample grown. Several studies have indicated that high quality layers can be more easily obtained on {100} substrates than {111} and {110}, etc [33, 34]. Substrate preparation, for example by chemical etching [35, 36], has been suggested to be important to optimise the conditions for step-flow growth [37] as it reduces the number of lattice defects such as dislocations or polishing lines in the substrate surface which may act as secondary nucleation sites during growth.

Substrate preparation is also an important consideration as dislocations in CVD films can affect the electrical properties of the material. In CVD diamond bundles of dislocations originating from individual point sources at or near the interface with the substrate can be observed in X-ray topography, demonstrating that these structural defects originate from the interface [32]. In high purity material (nitrogen and boron < 1 ppb) the electronic properties are still found to vary between samples of apparently similar quality (characterised by PL and EPR) [38, 39]. Hence it has been suggested that the electronic properties in CVD diamond with < 1 ppb of nitrogen is dominated by dislocations [38]. The highest electron and hole mobilities in diamond were obtained from CVD diamond with dislocation densities < $10^6\,cm^{-2}$ [31], although subsequently densities as low as $400\,cm^{-2}$ (over an area > $0.014\,cm^{-2}$) have been reported [40].

When considering the chemistry at work in the CVD process [24, 25] it is clear that the deposition conditions, including the ratio of CH_4/H_2 in the growth gases, the microwave plasma power density and the substrate temperature, as well as the presence of impurities, can all affect the reactions and transport mechanisms to the substrate. Hence, in order to successfully grow single-crystal diamond with low defect densities careful control of all the growth conditions and dopant levels present in the reactor is needed, as well as an understanding of how they affect the growth.

The ratio of CH_4/H_2 (controlled via flow rates of the respective gas sources) has been shown to be an important variable, as it has a strong influence on the growth rate [41, 42]. However, in some studies very low CH_4/H_2 ratios (< 0.15%) had to be used to maintain good surface morphology [43–46], hence restricting the growth rate to < 1μm/h.

Other studies have shown that the growth rate of single crystals can be increased by the use of higher plasma densities [42, 47, 48]. The use of plasma densities in the range 65–125 $W\,cm^{-3}$ lead to much higher growth rates (up to 19μm/h per hour) [48]. However, the substrate had to be cooled to maintain its temperature at an optimum value (850–900°C), leading to a pulsed-mode technique being employed to grow high quality material at increased growth rates [41, 48, 49]. A higher concentration of methane is required as plasma density is

increased, as diamond etching can become significant and compete with growth, as apparent by the emergence of square etch pits if the plasma density is increased whilst CH_4/H_2 is left unchanged [41].

An increase in the substrate temperature will enhance both the reaction rates occurring at the surface as well as the mobility of the adsorbed species, so that an increase in growth rate would be expected. Not only must a suitable substrate temperature be chosen for growth, but the temperature of the surface must be *maintained* during the deposition; growing thick samples presents the technological difficulty of keeping the surface temperature constant whilst its distance from the substrate holder and plasma changes. The synthesis of multiple samples in a single run also presents the problem of the substrates experiencing different growth temperatures (and hence different growth rates) due to the non-uniformity of the plasma [49].

When growing CVD diamond gases other than H_2 and CH_4 may be present. Nitrogen in the reactor (from the source gas or reactor leaks) in high concentrations (> 100 ppm) has been shown to have a detrimental affect on the quality of the deposited diamond, as it leads to the formation of graphite and/or amorphous carbon [50]. The formation of nitrogen-related defects (see §2.2.1) can also affect the optical and electronic properties of diamond. Recent transient photoconductivity measurements of high quality CVD diamond have demonstrated that concentrations of isolated nitrogen as low as 1 ppb can still influence the electronic properties [38, 39] (reduced external quantum efficiency as nitrogen content increases[1]). It is therefore apparent that, if diamond is to be used in optical and electronic applications, unintentional sources need to be controlled, necessitating purification of the source gases used during growth. Concentrations of isolated nitrogen as low as 0.2 ppb have been reported [51] in CVD diamond.

CVD diamond is synthesised in an environment which contains a number of potential sources of silicon, including the walls/windows [52, 53] of the reactor or, in the case of heteroepitaxial growth of diamond on silicon, the substrate itself [54]. Therefore it is not surprising that silicon is a frequent contaminant in diamond grown by this method (see §2.2.3).

[1]defined as the ratio of the number of collected electrons to the number of incoming photons

The careful removal of the impurities present in the gas phase during CVD growth has enabled systematic studies of the effect that controlled additives to the gas phase have on the growth, as well as providing information on the solubility of various impurities in CVD diamond. Such studies, which will be discussed in the following section, have also led to methods enabling the morphology, growth rate and electronic properties of diamond to be modified.

2.1.2.3 Doping studies of CVD diamond

The first detailed study of the incorporation efficiency of nitrogen in diamond was conducted by Samlenski *et al.* [55, 56]. In this investigation 50 ppm of $^{15}N_2$ was added to the gas phase (the use of ^{15}N gas allowed the film to be checked for unintentional ^{14}N contamination). Nuclear reaction analysis, which has a sensitivity of < 0.5 ppb, was then used to determine the concentration of incorporated ^{15}N in diamond films grown on {100} and {111} substrates. The results of this study indicated that the probability of incorporating a nitrogen atom is growth sector/surface dependent. For a {100} sector the incorporation efficiency (defined as the fraction of the N atoms, relative to carbon atoms, present in the gas phase which become incorporated in the diamond) was found to be 2×10^{-4}, whilst for a {111} sector a value of 6×10^{-4} was determined.

From early work on polycrystalline CVD diamond it was evident that the introduction of modest (< 100 ppm) quantities of N_2 could lead to an improvement of both the growth rates and the surface morphology of diamond films, as well as stabilisation of the {100} texture [55, 57–59]. Such results have prompted similar studies in single-crystal material. The work of the research group at LIMHP/CNRS in Paris has shown that the addition of small concentrations (2–10 ppm) of nitrogen can lead to a factor of 2.5 increase in the growth rate [51]. With the nitrogen addition kept within this range the nitrogen defect concentration (determined from EPR) was kept below 100 ppb. Relating the N_2 content in the gas phase to the incorporation of nitrogen-related defects also permitted the incorporation efficiency to be determined in this study for {100} sectors. An efficiency of 7.5×10^{-5}–1×10^{-4} was determined. Although comparable, the result is lower than that determined by Samlenski *et al.* [55]. Variation of this value

in CVD diamond is not surprising, given the wide range of growth parameters used. One should also note that EPR can only detect charge states of nitrogen-related defects which are paramagnetic, hence the incorporation efficiency may be underestimated.

Samlenski *et al.* have also determined the incorporation efficiency of boron in diamond grown by MP-CVD [56], achieved by the addition of trimethyleborate to the source gases. As for nitrogen, the uptake was found to be growth sector dependent, with an order of magnitude increase in incorporation probability in {111} sectors compared to {100} sectors. The incorporation efficiency was determined to be in the range 10^{-1}–10^{-2}, suggesting that boron is much more soluble in diamond than nitrogen. Hall mobilities as high as $1840\,cm^2\,V^{-1}\,s^{-1}$ at room temperature have been reported for CVD diamond doped with boron [44], leading to considerable interest in such doping to exploit the favourable electronic and thermal properties of the material [30, 60]. Different methods exist for the doping of CVD material with boron [61], but currently the most frequently used technique involves the addition of diborane (B_2H_6) (e.g. [62]). Boron concentrations below 1 ppb are detectable in diamond by cathodoluminescence, for which the emission intensity intensity due to the bound exciton is proportional to the boron content [63].

During the search for a viable n-type dopant in diamond the doping of diamond with phosphorus (P) using the CVD method has been investigated. Using phosphine (PH_3) as a dopant source and a low CH_4 concentration whilst growing on {111} substrates allowed the group at NIRIM, Japan to dope CVD diamond with phosphorus [64]. A high (0.15) incorporation efficiency (determined from SIMS measurements) was suggested for material containing $2.5\times10^{19}cm^{-3}$ P atoms, grown on a {111} oriented diamond substrate. Hall-effect measurements confirmed the n-type conductivity, however, the mobility in such highly doped material was poor ($23\,cm^2\,V^{-1}\,s^{-1}$ at 500 K) [64]. More lightly doped material (also grown on {111} substrates) with $7\times10^{16}cm^{-3}$ P atoms grown by the group has yielded the highest mobility in P-doped material to-date: $660\,cm^2\,V^{-1}\,s^{-1}$ at room temperature [65]. In this higher quality material the incorporation efficiency of P atoms is much lower, equalling approximately 0.04 (based on 10 ppm of PH_3 in CH_4),

illustrating that this is dependent on growth conditions. Temperature-dependent Hall effect measurements have shown that the activation energy in such films is 0.6 eV [65, 66]. Cathodoluminescence [67], photoconductivity [68] and infra-red absorption [69] measurements have all supported the existence of a phosphorous donor level 0.6 eV below the bottom of the conduction band.

Improved control in CVD synthesis has enabled the growth of diamond without observable silicon contamination. With the elimination of silicon incorporation from foreign sources within the reactor controlled doping studies of diamond with silicon become possible. Recently such studies have been undertaken for CVD diamond, achieved by the addition of silane (or other silicon-containing gas) to the growth gases [70].

The results from CVD samples doped with silicon via silane addition to the growth gases indicate that, although the probability of silicon incorporation into bulk diamond via a major {100} growth surface from the gas phase is less that that of boron, it is more efficiently incorporated than nitrogen [70]. Such results explain why the 1.68 eV band (see §2.2.3) is frequently a characteristic of diamond grown by the CVD method. These studies have also shown that the presence of silicon in the source gases can have a dramatic effect on the optical properties of the diamond deposited, especially when nitrogen is present in the growth environment, although the mechanisms and reasons for such changes are not currently understood.

2.2 Defects in synthetic diamond

This section will provide a brief overview of the detection and properties of defects in synthetic diamond. Since this thesis is concerned with the characterisation of isolated defects this review will mainly concentrate on point defects; related to the presence of nitrogen, hydrogen and silicon. However, the evidence for vacancy clusters in diamond is also reviewed, since their presence has been attributed to the brown colouration observed in diamond and their existence has implications for the emergence of other vacancy-related defects when annealing diamond.

2.2.1 Nitrogen-related defects

2.2.1.1 Single substitutional nitrogen

The neutral single substitutional nitrogen defect, N_s^0 (also referred to as P1), was the first defect in diamond to be correctly identified. From EPR measurements performed by Smith *et al.* on a natural diamond in 1959 [71] this defect was found to consist of a nitrogen atom bonded with the four nearest-neighbour carbon atoms, with the extra electron localised in an anti-bonding orbital between the nitrogen atom and one of the four carbon neighbours. In this particular bond the unpaired electron is predominantly localised on the carbon atom and the nitrogen-carbon separation is increased, with theory [72] suggesting an extension of ~ 30%, in reasonable agreement with analysis of the experimentally determined hyperfine parameters [73]. The relaxation also accounts for the depth of the donor level for nitrogen in diamond [72]. This extended bond forms the principle ⟨111⟩ axis of the defect, giving rise to the observed axial symmetry. Cox *et al.* employed ENDOR to determine accurate hyperfine and quadrupole parameters for ^{14}N as well as hyperfine parameters for ^{15}N and ^{13}C [74].

N_s^0 is also observable in infrared absorption spectroscopy. The spectrum has a maximum at $1130\,cm^{-1}$ [5] and a sharp peak at $1344\,cm^{-1}$ associated with a local vibrational mode [75]. The strength of the absorption peak at $1130\,cm^{-1}$ can be used as a quantitative measurement of the concentration of N_s^0; the absorption coefficient (μ_s) at this wavenumber, in units of cm^{-1} can be related to the concentration of N_s^0 in ppm by the following expression [5, 76]:

$$[N_s^0] = 25(5) \times \mu_s(1130cm^{-1}) \tag{2-1}$$

N_s^0 gives rise to the deep-lying donor state mentioned in §2.1.1.2, which means nitrogen can donate an electron to nearby defects, leaving N_s^+. It is evident that N_s^+ is diamagnetic and hence cannot be detected by EPR. However, an absorption line at $1332\,cm^{-1}$, associated with two further peaks at $950\,cm^{-1}$ and $1046\,cm^{-1}$ in IR spectroscopy has been assigned to this charge state of N_s [77]. As for N_s^0 (equation 2-1) the absorption coefficient at this wavenumber can be used as a quantitative estimate of the concentration [77]:

$$[N_s^0] = 5.5(5) \times \mu_s(1332cm^{-1}) \tag{2-2}$$

Newton [78] provides a thorough review of further experimental results and their relation to theory for both charge states of the substitutional nitrogen centre in diamond.

2.2.1.2 The nitrogen-vacancy centre

In diamonds containing N_s irradiation and subsequent annealing at temperatures in excess of 900 K gives rise to an absorption band around 637 nm (1.945 eV), first observed by du Preez in 1965 [79]. The first detailed study of this centre was conducted by Davies and Hamer in 1976, who performed uniaxial stress measurements [80]. This work showed that the zero-phonon line (ZPL) originates from a transition between an A ground state and an E excited state of a centre possessing trigonal symmetry. Since 900 K is the temperature at which the vacancy in diamond is mobile [81] it was suggested that the centre consists of a vacancy next to, or in the vicinity of, a substitutional nitrogen atom (NV) [80].

Loubser and van Wyk [82] conducted EPR experiments on samples that had been irradiated and annealed in similar conditions to those examined by Davies and Hamer [80]. After annealing at temperature around 900 K, a new EPR centre was observed. This $S = 1$ defect had trigonal symmetry with a zero-field splitting of 2.88 GHz and the hyperfine structure revealed the presence of a single $I = 1$ nucleus with ~ 100% abundance, suggesting the involvement of nitrogen. The observation of three equivalent carbon atom positions (from the ^{13}C hyperfine satellites) permitted the symmetry of the defect to determined as C_{3v}. These findings led to the assignment of this EPR spectrum to an NV centre. In this study the EPR spectrum could only be observed when the sample was optically excited, hence it was concluded that the signals originated from a long-lived excited state.

Two-laser hole burning experiments on the 637 nm ZPL by Reddy *et al.* provided a clear link between the optical and EPR centres, as prominent anti-holes were observed at ±2.88 GHz [83]. From these experiments it was suggested that the NV centre has a $^3A_2$ ground state, thus the EPR spectrum should be observable without optical illumination. Subsequent work by Redman *et al.* on samples containing relatively high concentrations of NV, confirmed that the EPR spectrum

could be detected in the dark, allowing the ZPL at 637 nm to be assigned to a $^3A_2 \rightarrow {}^3E$ transition [84].

Studies of the optical centre observed around 575 nm (2.156 eV) revealed that it was also present in type Ib samples that had been irradiated and annealed under similar conditions to those used to produce the 637 nm line [85–87]. Additionally, uniaxial stress measurements suggested that the ZPL originates from an E ground states to an A excited state [86] at a trigonal defect. The similarities between this defect and the 637 nm centre led Collins and Lawson to tentatively assign this to a nitrogen-containing defect involving one or more vacancies [85].

Studies of the absorption spectra of type Ib diamonds subjected to neutron irradiation Mita showed that the intensity of the 637 nm peak is reduced at high irradiation dose, while absorption at 575 nm appears abruptly at a certain dose and continues to increase as the dose is raised further [88]. This effect was interpreted as being due to a change in the charge state of the NV defect and the 637 nm and 575 nm centres were assigned to NV^- and NV^0, respectively, using the following argument: At sufficiently low irradiation doses there is an excess of N_s^0, thus when a new vacancy is produced and trapped by a nitrogen atom a remaining N_s^0 centre can donate an electron to produce NV^-. Eventually a critical point will be reached when there is no remaining N_s^0 to be involved in charge transfer, resulting in a lowering of the Fermi level and the subsequent production of the neutral charge state.

Both NV^- and NV^0 are routinely detected by photoluminescence in as grown CVD diamond [89], suggesting it is grown into the diamond lattice as a unit, or is formed via a vacancy diffusing to N_s^0. The formation of both charge states during CVD growth, following the arguments above, can be explained by the following process:

$$N_s^0 + V^0 \rightarrow NV^0 \tag{2-3}$$

$$NV^0 + N_s^0 \rightarrow NV^- + N_s^+ \tag{2-4}$$

NV^- is studied by optically-excited EPR in chapter 8 and an additional, previously unobserved, defect is identified as an excited state of NV^0.

2.2.2 Hydrogen-related defects

Atomic hydrogen is the most abundant atom in the gas phase during CVD growth (see §2.1.2.1) and the literature demonstrates that hydrogen can be incorporated in CVD diamond when hydrogen atoms are not removed and replaced with a carbon atom during growth.

The earliest studies of hydrogen incorporation in diamond in 1967 concerned natural type Ia diamond, where sharp IR absorption lines at 3107 and 1405 cm^{-1} were observed [90] and attributed to a carbon-hydrogen (C-H) stretch and bend mode at the same defect [90, 91]. It has subsequently been demonstrated that these absorptions can be introduced in natural as well as some synthetic HPHT and CVD diamond by HPHT annealing [92–94] and a correlation between the concentration of nitrogen and the intensity of 3107 cm^{-1} has been observed [94].

Theoretical modelling by Goss *et al.* has suggested that 3107 cm^{-1} could arise from a C-H stretch at a nitrogen-hydrogen (N:H) defect [95], although a number of other models have been suggested (see Cruddace [96] for a review). The recent work of Cruddace [96] has assigned 3107 cm^{-1} and 1405 cm^{-1} to A-E and A-A transitions respectively of a trigonal centre, consistent with the C_{3v} symmetry expected for a N:H defect [96].

Numerous hydrogen-related defects have been identified using EPR. A number of these will be discussed in the following sections.

2.2.2.1 H1 and H2

Two defects, H1 and H2, were examined in polycrystalline CVD diamond by Zhou *et al.* in 1996 [97]. H1 has $S = \frac{1}{2}$ and results in a broad (> 4 G peak-peak) line at $g = 2.0028$ and a weak pair of partially resolved satellites. From the observation of a variation in satellite intensities and positions at Q-band (35 GHz), it was suggested [97] that these satellites arise from forbidden transitions (simultaneous electron-nuclear spin flips) [98]. The determination of the hyperfine parameters for H1 has led Zhou *et al.* to propose that a single hydrogen atom is located ~ 1.9 Å from an unpaired electron; a model which is supported by subsequent ENDOR measurements [99]. H2 was suggested to be a similar defect, but with the hydrogen atom further away (~ 2.3 Å).

For both H1 and H2 it was proposed that a hydrogen atom has entered a stretched bond at a grain boundary or other extended misfit region in CVD material, hence the defect is not incorporated in the bulk diamond lattice of CVD diamonds. This suggestion is reinforced by later work by Talbot-Ponsonby, where EPR imaging revealed a correlation between the intensity of the $g = 2.0028$ EPR line and the distribution of black specks, originating from non-diamond material [100].

2.2.2.2 NVH^-

The first hydrogen-related point defect in the bulk of diamond to be conclusively identified was the negative nitrogen-vacancy-hydrogen (NVH^-) centre, from the work in 2003 of Glover *et al.* [101]. The experimental EPR data indicated a $S = \frac{1}{2}$ defect with C_{3v} symmetry and a model in which the hydrogen, known to be present from electron-nuclear double-spin flip transitions, bonds to the nitrogen atom (separated by 1.04 Å along ⟨111⟩) was suggested [101]. However, *ab initio* calculations have suggested that the lowest energy for the nitrogen-hydrogen bond occurs when the two atoms are approximately 4 Å apart, hence different hyperfine parameters were predicted in this theoretical modelling [102]. Instead a model has been suggested where the hydrogen is bonded to one of the three carbon atoms nearest the vacancy [102–104]. In a static configuration this would result in C_{1h} symmetry, but if the hydrogen atom is permitted to tunnel between the three equivalent C_{1h} configurations on a timescale which is short compared to the EPR experiment C_{3v} symmetry would be observed. Using such a dynamic model has led to reasonable agreement with the experimentally determined hyperfine parameters [102] and it is predicted that the tunneling rate would be sufficiently fast to explain the observed symmetry [104].

Further EPR studies of the NVH^- centre in diamond and the effect of isotopical substitution of hydrogen with deuterium (^2H) in this defect are covered in chapter 9. The results in this chapter provide the first experimental evidence supporting the dynamic NVH model.

2.2.3 Silicon-related defects

As discussed in §2.1.2.2, silicon is a frequent accidental contaminant in CVD diamond. The focus of much of the literature related to silicon in diamond has concerned the 1.68 eV optical centre, which has provided the clearest evidence for the presence of silicon-related defects in diamond grown by the CVD method.

2.2.3.1 The 1.68 eV optical centre

A line at 1.68 eV was first observed by Vavilov *et al.* during cathodoluminescence (CL) investigations of homoepitaxial diamond layers and polycrystalline diamond films grown on silicon substrates [105]. Subsequent ion-implantation experiments determined that this line was also present in natural diamond that had been implanted with silicon ions [106].

The unambiguous association of this centre with silicon was achieved when single-crystal HPHT grown diamonds were doped with silicon (§2.1.1.2). The relatively stress-free nature of such samples allowed low-temperature photoluminescence (PL) and absorption experiments to resolve the fine structure of the 1.68 eV centre. It was found to be comprised of three groups of four lines, with the relative intensity of the groups scaling with the natural abundances of the isotopes of silicon [107]. Recent work has also indicated that the fine-structure lines assigned to ^{29}Si dominate in samples enriched with this isotope [108]. The four component lines associated with each isotope represent a transition from an almost orbitally degenerate ground state, split by 0.2 meV, to a doublet excited state split by 1.07 meV [107].

In studies of the 1.68 eV centre it has also been shown that electron irradiation and subsequent annealing above 700°C leads to an increase in emission and absorption intensity, with the defect surviving annealing temperatures in excess of 2000°C [52, 109]. GR1 (V^0) was seen to anneal out (vacancy is mobile around 700°C [81]) at the same time as the 1.68 eV emission intensity was seen to increase [109], hence implying that the optical centre involves a vacancy trapped in the vicinity of a silicon atom.

To reconcile the involvement of silicon and vacancies in the 1.68 eV defect and to account for the twelve lines in the spectra, theoretical work has been undertaken

on substitutional silicon adjacent to a vacancy, (Si_s-V). Goss *et al.* have suggested that the silicon atom is unstable at a substitutional site and that the system relaxes to a split-vacancy structure [110], (V-Si-V). For $(V\text{-}Si\text{-}V)^0$ it is predicted that the ground state is $^3A_{2g}$ but, since this is orbitally non-degenerate, this cannot account for the observed 1.68 eV band. However, calculations have shown that (V-Si-V) has an acceptor level at around $E_v + 1.5$ eV [111, 112]. $(V\text{-}Si\text{-}V)^-$ is predicted to have a ^2E_g ground state and a $^2E_g \rightarrow {}^2E_u$ optical transition at ~1.9 eV, in tolerable agreement with the 1.68 eV observed. Both the positive and negative charge states of (V-Si-V) are subject to a Jahn-Teller distortion, which could explain the C_2 symmetry suggested for the 1.68 eV centre from incomplete (i.e. insufficient data to parameterise the system) uniaxial stress measurements [113, 114].

2.2.3.2 Substitutional and interstitial silicon

The apparent formation of the 1.68 eV centre post irradiation and annealing, discussed in the previous section, implies that there is a reservoir of silicon present in the samples in other forms, with the suggestion that mobile vacancies are being trapped at Si_s. Despite this there is currently no published experimental identification of Si_s in diamond.

Theory suggests that each Si_s displaces the volume of 1.6 host atoms, with the relaxed Si-C bonds being 12% longer than a C-C bond [112, 115]. Segev *et al.* have suggested that there is a strain-related level just above the valance band maximum [116]. However, Goss *et al.* find that the strain has little impact in the vicinity of the band gap and that Si_s is electrically inert [117].

With Si_s predicted to be invisible to electronic-optical spectroscopy, magnetic resonance and electrical characterisation, vibrational spectroscopy is thought to hold the key to identifying the defect [117]. Several modes of interest in the vicinity of the one-phonon maximum have been highlighted by the literature, including a mode around 1333 cm^{-1} [117]. The main component of this is localised on the four carbon neighbours, hence the shift observed upon isotopic substitution with other silicon isotopes is predicted to be small. The recent experimental observation of a mode around 1338 cm^{-1} in CVD diamond intentionally doped with silicon may be associated with Si_s [118].

Theoretical modelling of silicon at an interstitial site has also been conducted, where the stability of Si_i was assessed by calculating the activation energy for the exchange of silicon with a host atom [117]. The rate-limited step was determined to only be around 2 eV, hence the results from theory suggest that Si_i is not expected be present in significant concentrations in as-grown or implanted and annealed material.

2.2.3.3 EPR centres correlated with silicon incorporation

A trigonal defect with $S = 1$, referred to as KUL1, has been detected in both SC-CVD diamond films [119] and polycrystalline diamond grown on silicon substrates [120]. Polishing the substrate side of the samples deposited on silicon led to a reduction in the intensity of the observed resonance lines, leading to the suggestion that the defect is silicon-related. The $^3A_{2g}$ ground state of $(V\text{-}Si\text{-}V)^0$ is predicted [110] to be paramagnetic with $S = 1$, hence this model has been proposed for KUL1 [119].

The reported experimental data on the hyperfine structure of KUL1 [119, 120] does not match with the predictions of the $(V\text{-}Si\text{-}V)^0$ model, which has D_{3d} symmetry. Tentative assignment of one pair of satellites has been made to ^{29}Si, but the remaining two pairs do not suggest six equivalent carbon atoms (required for D_{3d} symmetry); instead a single site and a pair was observed.

$(V\text{-}Si\text{-}V)^-$ would also be expected to be paramagnetic, with the theoretical models suggesting that $S = \frac{1}{2}$ [110, 117]. Another defect, labelled KUL8, has $S = \frac{1}{2}$ and has been detected in polycrystalline CVD material deposited on silicon substrates [121, 122]. As for KUL1 this was found to be predominately located in proximity to the substrate, but since no hyperfine structure has been resolved it could not be conclusively labelled as being silicon-related and its symmetry could not be probed. Illumination at 457.9 nm of samples containing both KUL1 and KUL8 has suggested that the EPR intensity is transferred from one defect to the other, a result which has been used to speculate that the two features are different charge states of the same defect, with the assignment of KUL8 to $(V\text{-}Si\text{-}V)^-$.

Finally there is the assignment of KUL3 to a $S = \frac{1}{2}$ defect of monoclinic-I (C_{1h}) symmetry [119, 120]. The involvement of hydrogen was inferred due to the

presence of weak satellites around the principal lines, which could be assigned to the forbidden hydrogen electron-nuclear double-spin flip transitions [120]. A correlation between the silicon content and the concentration of KUL3 has been determined; in a single-crystal film which showed variation of the intensity of the 1.68 eV band across the surface the intensity of KUL3 was found to be highest in the silicon-rich regions. A proposed model is that the centre is associated with a neutral divacancy, where one of the six basal carbon atoms is replaced by silicon and one dangling bond (remote to the silicon atom) is passivated by a hydrogen atom [119]. This model is not supported by recent theoretical results from Goss *et al.* who have assigned KUL3 to $(V\text{-}Si\text{-}V)^0$ decorated with a nearby hydrogen atom [117].

Both KUL1 and KUL3 are revisited in chapter 6. New experimental EPR data are presented for both defects and discussed in the light of the models proposed. In chapter 7 the preferential orientation of silicon-related defects is investigated.

2.3 Vacancy clusters

The interest in the presence of extended defects in diamond has recently been reinvigorated due to the suggestion that extended vacancy defects may be responsible for the brown colouration observed in some type IIa diamonds (both natural and synthetic) [123] and the discovery that such colouration can be removed by HPHT processing [32, 124–126].

Brown single-crystal type IIa diamond shows a continuum absorption throughout the bandgap, with no specific detectable onset at low energies nor distinct defect-related bands [125]. An extended defect of vacancies is thought to be more likely to cause the colour rather than point defects, since the latter typically display a sharp absorption edge (as seen in defects such as GR1). Density functional calculations of vacancy clusters suggest that the most stable cluster form is a disk lying on {111} planes, which may contain ~ 200 vacancies [127, 128].

The main evidence for the existence of vacancy clusters in diamond has been provided by positron annihilation spectroscopy (PAS). As the name implies this technique involves the injection of positrons into a material. After injection the

majority interact with electrons and give rise to a dominant bulk lifetime τ_b, which is found to be in the range 97–108 ps in type IIa diamond [129]. Any vacancy-related defects will have a lower electron density than the bulk and hence the lifetime will be increased. Two distinct PAS lifetimes have been observed in natural brown diamond which appear to be specific to this type of diamond; $\tau_2 \sim 132(4)$ ps and $\tau_3 \sim 434(10)$ ps [130]. Similar components have been observed in type IIa CVD diamond [131], with an additional, longer lifetime $\tau_3 \sim 1$ ns. The relatively long lifetimes of τ_2 and τ_3 imply the presence of clusters of vacancies. The presence of such clusters of has important implications regarding the presence of other vacancy-related defects; annealing of diamond has the potential to release vacancies, which may be trapped by other impurities, leading to an increase the concentration of vacancy-related centres.

HPHT annealing studies have revealed that the temperatures required to remove brown colouration are different between natural and CVD diamond; the brown colour begins to disappear at 1400–1600°C in as-grown CVD diamond [126], but temperatures of around 1900°C are required for natural samples [124]. This suggests that either the stabilities of the defect(s) responsible for the absorption continuum and hence brown colouration are significantly different between natural and synthetic diamond or that the mechanisms for their loss are different. Recent work by Hounsome *et al.* have suggested the latter and a possible link with hydrogen [128].

In §2.1.2.1 and §2.2.2 the prevalence and role of hydrogen in CVD growth has been covered. By comparison natural type IIa diamond contains relatively little hydrogen. After HPHT annealing a broad C-H band around 2900 cm^{-1} has been observed [92] and, since such a band is close to the C-H stretch mode on a {111} surface, Hounsome *et al.* have suggested that mobile hydrogen could move to a vacancy disk upon annealing and give rise to this absorption feature [128]. It is this process that could lead to the loss of the brown colouration, as hydrogen is believed to passivate the optical activity of these disks [128]. Calculations have shown that temperatures of around 2200°C are required temperature to break apart the vacancy disks [128], which is in reasonable agreement with the temperature at which the colouration is lost in natural type IIa diamond [124].

References

[1] P. W. Bridgman, J. Chem. Phys. **15**, 92 (1947).

[2] H. P. Bovenkerk, F. P. Bundy, H. T. Hall, H. M. Strong, and R. H. Wentorf, Nature **184**, 1094 (1959).

[3] R. C. Burns and G. J. Davies, in *The Properties of Natural and Synthetic Diamond*, edited by J. E. Field (Academic Press, London, 1992), chap. 10, pp. 396–422.

[4] Wedlake, in *Properties of Diamond*, edited by J. E. Field (Academic Press, London, 1979), chap. 16, pp. 501–535.

[5] R. M. Chrenko, H. M. Strong, and R. E. Tuft, Philos. Mag. **23**, 313 (1971).

[6] R. M. Chrenko, R. E. Tuft, and H. M. Strong, Nature **270**, 141 (1977).

[7] A. T. Collins and S. C. Lawson, Philos. Mag. Lett. **60**, 117 (1989).

[8] H. M. Strong (1978), US Patent 4082185.

[9] H. M. Strong and R. M. Chrenko, J. Phys. Chem. **75**, 1838 (1971).

[10] R. H. Wentorf, J. Phys. Chem. **75**, 1833 (1971).

[11] C. V. H. Stroemann, F. Tshisikhawe, J. O. Hansen, and R. C. Burns, *Synthesis of diamond* (2006), Patent WO2006061672.

[12] Y. Borzdov, Y. Pal'yanov, I. Kupriyanov, V. Gusev, A. Khokhryakov, A. Sokol, and A. Efremov, Diam. Relat. Mater. **11**, 1863 (2002).

[13] R. C. Burns, V. Cvetkovic, C. N. Dodge, D. J. F. Evans, M.-L. T. Rooney, P. M. Spear, and C. M. Welbourn, J. Cryst. Growth **104**, 257 (1990).

[14] H. Kanda and T. Sekine, in *Properties and Growth of Diamond*, edited by G. Davies (INSPEC, London, 1994), chap. 12.5, pp. 415–426.

[15] H. Kanda, T. Ohsawa, O. Fukunaga, and I. Sunagawa, J. Cryst. Growth **94**, 115 (1989).

[16] R. H. Wentorf, Jr. and H. P. Bovenkerk, J. Chem. Phys. **36**, 1987 (1962).

[17] R. M. Chrenko, Phys. Rev. B **7**, 4560 (1973).

[18] A. T. Collins and A. W. S. Williams, J. Phys. C Solid State **4**, 1789 (1971).

[19] R. G. Farrer, Solid State Commun. **7**, 685 (1969).

[20] G. Sittas, H. Kanda, I. Kiflawi, and P. M. Spear, Diam. Relat. Mater. **5**, 866 (1996).

[21] W. G. Eversole and N. Y. Kenmore (1958), US Patent 3030187.

[22] W. G. Eversole and N. Y. Kenmore (1958), US Patent 3030188.

[23] J. C. Angus, H. A. Will, and W. S. Stanko, J. Appl. Phys. **39**, 2915 (1968).

[24] J. E. Butler, R. L. Woodin, L. M. Brown, and P. Fallon, Philos. T. R. Soc. A **342**, 209 (1993).

[25] D. G. Goodwin and J. E. Butler, in *Handbook of Industrial Diamonds and Diamond Films*, edited by M. A. Prelas, G. Popovici, and L. K. Bigelow (Marcel Dekker, New York, 1998), pp. 527–581.

[26] S. Matsumoto, Y. Sato, M. Tsutsumi, and N. Setaka, J. Mater. Sci. **17**, 3106 (1982).

[27] A. Argoitia, C. S. Kovach, and J. C. Angus, in *Handbook of Industrial Diamonds and Diamond Films*, edited by M. A. Prelas, G. Popovici, and L. K. Bigelow (Marcel Dekker, New York, 1998), pp. 797–819.

[28] M. Kamo, Y. Sato, S. Matsumoto, and N. Setaka, J. Cryst. Growth **62**, 642 (1983).

[29] P. K. Bachman, in *Handbook of Industrial Diamonds and Diamond Films*, edited by M. A. Prelas, G. Popovici, and L. K. Bigelow (Marcel Dekker, New York, 1998), pp. 821–850.

[30] A. Denisenko and E. Kohn, Diam. Relat. Mater. **14**, 491 (2005).

[31] J. Isberg, J. Hammersberg, E. Johansson, T. Wikstrom, D. J. Twitchen, A. J. Whitehead, S. E. Coe, and G. A. Scarsbrook, Science **297**, 1670 (2002).

[32] P. M. Martineau, S. C. Lawson, A. J. Taylor, S. J. Quinn, D. J. F. Evans, and M. J. Crowder, Gems. Gemmol. **40**, 2 (2004).

[33] C. Findeling-Dufour, A. Vignes, and A. Gicquel, Diam. Relat. Mater. **4**, 429 (1995).

[34] L. F. Sutcu, C. J. Chu, M. S. Thompson, R. H. Hauge, J. L. Margrave, and M. P. D'Evelyn, J. Appl. Phys. **71**, 5930 (1992).

[35] G. Bogdan, M. Nesldek, J. D'Haen, J. Maes, V. V. Moshchalkov, K. Haenen, and M. D'Olieslaeger, Phys. Status Solidi A **202**, 2066 (2005).

[36] A. Tallaire, J. Achard, F. Silva, R. S. Sussmann, A. Gicquel, and E. Rzepka, Phys. Status Solidi A **201**, 2419 (2004).

[37] N. Lee and A. Badzian, Diam. Relat. Mater. **6**, 130 (1997).

[38] A. Secroun, O. Brinza, A. Tardieu, J. Achard, F. Silva, X. Bonnin, K. D. Corte, A. Anthonis, M. E. Newton, J. Ristein, et al., Phys. Status Solidi A **9999**, NA (2007).

[39] A. Secroun, A. Tallaire, J. Achard, G. Civrac, H. Schneider, and A. Gicquel, Diam. Relat. Mater. **16**, 953 (2007).

[40] D. J. Twitchen, G. C. Summerton, J. O. Friel, I. anf Hansen, K. B. Guy, M. P. Gaukroger, P. M. Martineau, R. C. Burns, S. C. Lawson, and T. P. C. Addison, *High crystalline quality synthetic diamond* (2007), Patent WO2007066215.

[41] J. Achard, A. Tallaire, R. Sussmann, F. Silva, and A. Gicquel, J. Cryst. Growth **284**, 396 (2005).

[42] T. Teraji and T. Ito, J. Cryst. Growth **271**, 409 (2004).

[43] M. Kasu and N. Kobayashi, Diam. Relat. Mater. **12**, 413 (2003).

[44] H. Okushi, Diam. Relat. Mater. **10**, 281 (2001).

[45] H. Okushi, H. Watanabe, S. Ri, S. Yamanaka, and D. Takeuchi, J. Cryst. Growth **237-239**, 1269 (2002).

[46] H. Watanabe, D. Takeuchi, S. Yamanaka, H. Okushi, K. Kajimura, and T. Sekiguchi, Diam. Relat. Mater. **8**, 1272 (1999).

[47] F. Silva, A. Gicquel, A. Tardieu, P. Cledat, and T. Chauveau, Diam. Relat. Mater. **5**, 338 (1996).

[48] A. Tallaire, J. Achard, F. Silva, and A. Gicquel, Phys. Status Solidi A **202**, 2059 (2005).

[49] A. Tallaire, J. Achard, A. Secroun, O. De Gryse, F. De Weerdt, J. Barjon, F. Silva, and A. Gicquel, J. Cryst. Growth **291**, 533 (2006).

[50] L. Bergman, M. T. McClure, J. T. Glass, and R. J. Nemanich, J. Appl. Phys. **76**, 3020 (1994).

[51] A. Tallaire, A. T. Collins, D. Charles, J. Achard, R. Sussmann, A. Gicquel, M. E. Newton, A. M. Edmonds, and R. J. Cruddace, Diam. Relat. Mater. **15**, 1700 (2006).

[52] C. D. Clark and C. B. Dickerson, Surf. Coat. Tech. **47**, 336 (1991).

[53] P. Joeris, I. Schmidt, and C. Benndorf, Diam. Relat. Mater. **5**, 603 (1996).

[54] J. Barjon, E. Rzepka, F. Jomard, J. M. Laroche, D. Ballutaud, T. Kociniewski, and J. Chevallier, Phys. Status Solidi A **202**, 2177 (2005).

[55] R. Samlenski, C. Haug, R. Brenn, C. Wild, R. Locher, and P. Koidl, Appl. Phys. Lett. **67**, 2798 (1995).

[56] R. Samlenski, C. Haug, R. Brenn, C. Wild, R. Locher, and P. Koidl, Diam. Relat. Mater. **5**, 947 (1996).

[57] G. Z. Cao, J. J. Schermer, W. J. P. van Enckevort, W. A. L. M. Elst, and L. J. Giling, J. Appl. Phys. **79**, 1357 (1996).
[58] S. Jin and T. D. Moustakas, Appl. Phys. Lett. **65**, 403 (1994).
[59] W. Muller-Sebert, E. Worner, F. Fuchs, C. Wild, and P. Koidl, Appl. Phys. Lett. **68**, 759 (1996).
[60] E. Kohn and A. Denisenko, Thin Solid Films **515**, 4333 (2007).
[61] A. T. Collins, in *Properties and Growth of Diamond*, edited by G. Davies (INSPEC, London, 1994), chap. 9.7, p. 288.
[62] G. A. Scarsbrook, P. M. Martineau, T. D. J., A. J. Whitehead, and M. A. Cooper (2003), Patent WO03052174.
[63] H. Kawarada, H. Matsuyama, Y. Yokota, T. Sogi, A. Yamaguchi, and A. Hiraki, Phys. Rev. B **47**, 3633 (1993).
[64] S. Koizumi, M. Kamo, Y. Sato, H. Ozaki, and T. Inuzuka, Appl. Phys. Lett. **71**, 1065 (1997).
[65] M. Katagiri, J. Isoya, S. Koizumi, and H. Kanda, Appl. Phys. Lett. **85**, 6365 (2004).
[66] S. Koizumi, T. Teraji, and H. Kanda, Diam. Relat. Mater. **9**, 935 (2000).
[67] H. Sternschulte, K. Thonke, R. Sauer, and S. Koizumi, Phys. Rev. B **59**, 12924 (1999).
[68] M. Nesladek, K. Meykens, K. Haenen, L. M. Stals, T. Teraji, and S. Koizumi, Phys. Rev. B **59**, 14852 (1999).
[69] E. Gheeraert, S. Koizumi, T. Teraji, and H. Kanda, Solid State Commun. **113**, 577 (2000).
[70] S. D. Williams, D. J. Twitchen, P. M. Martineau, G. A. Scarsbrook, and I. Friel (2007), UK Patent Application: GB 2428690 A.
[71] W. V. Smith, P. P. Sorokin, I. L. Gelles, and G. J. Lasher, Phys. Rev. **115**, 1546 (1959).
[72] P. R. Briddon and R. Jones, Physica B **185**, 179 (1993).
[73] O. D. Tucker, M. E. Newton, and J. M. Baker, Phys. Rev. B **50**, 15586 (1994).
[74] A. Cox, M. E. Newton, and J. M. Baker, J. Phys. Condens. Mat. **6**, 551 (1994).
[75] A. T. Collins, M. Stanley, and G. S. Woods, J. Phys. D Appl. Phys. **20**, 969 (1987).
[76] G. S. Woods, J. A. van Wyk, and A. T. Collins, Philos. Mag. B **62**, 589 (1990).
[77] S. C. Lawson, D. Fisher, D. C. Hunt, and M. E. Newton, J. Phys. Condens. Mat. **10**, 6171 (1998).
[78] M. E. Newton, in *Properties, Growth and Applications of Diamond*, edited by M. H. Nazare and A. J. Neves (INSPEC, London, 2001), chap. A5.4, pp. 136–141.
[79] L. du Preez, Ph.D. thesis, University of Witwatersrand (1965).
[80] G. Davies and M. F. Hamer, P. Roy. Soc. Lond. A Mat. **348**, 285 (1976).
[81] G. Davies, S. C. Lawson, A. T. Collins, A. Mainwood, and S. J. Sharp, Phys. Rev. B **46**, 13157 (1992).
[82] J. H. N. Loubser and J. A. van Wyk, Diamond Research **11**, 11 (1977).
[83] N. R. S. Reddy, N. B. Manson, and E. R. Krausz, J. Lumin. **38**, 46 (1987).
[84] D. A. Redman, S. Brown, R. H. Sands, and S. C. Rand, Phys. Rev. Lett. **67**, 3420 (1991).
[85] A. T. Collins and S. C. Lawson, J. Phys. Condens. Mat. **1**, 6929 (1989).
[86] G. Davies, J. Phys. C Solid State **12**, 2551 (1979).
[87] J. E. Ralph, P. Phys. Soc. **76**, 688 (1960).
[88] Y. Mita, Phys. Rev. B **53**, 11360 (1996).

[89] T. A. Kennedy, J. S. Colton, J. E. Butler, R. C. Linares, and P. J. Doering, Appl. Phys. Lett. **83**, 4190 (2003).
[90] R. M. Chrenko, R. S. McDonald, and K. A. Darrow, Nature **213**, 474 (1967).
[91] G. S. Woods and A. T. Collins, J. Phys. Chem. Solids **44**, 471 (1983).
[92] S. J. Charles, J. E. Butler, B. N. Feygelson, M. E. Newton, D. L. Carroll, J. W. Steeds, H. Darwish, C.-S. Yan, H. K. Mao, and R. J. Hemley, Phys. Status Solidi A **201**, 2473 (2004).
[93] F. De Weerdt and I. N. Kupriyanov, Diam. Relat. Mater. **11**, 714 (2002).
[94] I. Kiflawi, D. Fisher, H. Kanda, and G. Sittas, Diam. Relat. Mater. **5**, 1516 (1996).
[95] J. P. Goss, J. Phys. Condens. Mat. **15**, R551 (2003).
[96] R. J. Cruddace, Ph.D. thesis, University of Warwick (2007).
[97] X. Zhou, G. D. Watkins, K. M. M. Rutledge, R. P. Messmer, and S. Chawla, Phys. Rev. B **54**, 7881 (1996).
[98] S. L. Holder, L. G. Rowan, and J. J. Krebs, Appl. Phys. Lett. **64**, 1091 (1994).
[99] D. F. Talbot-Ponsonby, M. E. Newton, J. M. Baker, G. A. Scarsbrook, R. S. Sussmann, A. J. Whitehead, and S. Pfenninger, Phys. Rev. B **57**, 2264 (1998).
[100] D. Talbot-Ponsonby, D. Phil. thesis, University of Oxford (1997).
[101] C. Glover, M. E. Newton, P. Martineau, D. J. Twitchen, and J. M. Baker, Phys. Rev. Lett. **90**, 185507 (2003).
[102] M. J. Shaw, P. R. Briddon, J. P. Goss, M. J. Rayson, A. Kerridge, A. H. Harker, and A. M. Stoneham, Phys. Rev. Lett. **95**, 105502 (2005).
[103] J. P. Goss, P. R. Briddon, R. Jones, and S. Sque, J. Phys. Condens. Mat. **15**, S2903 (2003).
[104] A. Kerridge, A. H. Harker, and A. M. Stoneham, J. Phys. Condens. Mat. **16**, 8743 (2004).
[105] A. M. Zaitsev, V. S. Vavilov, and A. A. Gippius, Sov. Phys. Leb. Inst. Rep. **10**, 15 (1981).
[106] V. S. Vavilov, A. A. Gippius, A. M. Zaitsev, B. V. Deryaguin, B. V. Spitsyn, and A. E. Aleksenko, Sov. Phys. Semicond. **14**, 1078 (1980).
[107] C. D. Clark, H. Kanda, I. Kiflawi, and G. Sittas, Phys. Rev. B **51**, 16681 (1995).
[108] A. T. Collins, private communication.
[109] A. T. Collins, L. Allers, C. J. H. Wort, and G. A. Scarsbrook, Diam. Relat. Mater. **3**, 932 (1994).
[110] J. P. Goss, R. Jones, S. J. Breuer, P. R. Briddon, and S. Oberg, Phys. Rev. Lett. **77**, 3041 (1996).
[111] J. P. Goss, P. R. Briddon, R. Jones, and S. Sque, Diam. Relat. Mater. **13**, 684 (2004).
[112] J. P. Goss, P. R. Briddon, M. J. Rayson, S. J. Sque, and R. Jones, Phys. Rev. B **72**, 035214 (2005).
[113] S. W. Brown and S. C. Rand, J. Appl. Phys. **78**, 4069 (1995).
[114] H. Sternschulte, K. Thonke, J. Gerster, W. Limmer, R. Sauer, J. Spitzer, and P. C. Munzinger, Diam. Relat. Mater. **4**, 1189 (1995).
[115] J. P. Goss, P. R. Briddon, M. J. Rayson, S. J. Sque, and R. Jones, Phys. Rev. B **73**, 199904 (2006).
[116] D. Segev and S. H. Wei, Phys. Rev. Lett. **91**, 126406 (2003).
[117] J. P. Goss, P. R. Briddon, and M. J. Shaw, Phys. Rev. B **76**, 075204 (2007).
[118] P. M. Martineau, private communication.
[119] K. Iakoubovskii, A. Stesmans, K. Suzuki, J. Kuwabara, and A. Sawabe, Diam. Relat. Mater. **12**, 511 (2003).

[120] K. Iakoubovskii and A. Stesmans, Phys. Status Solidi A **186**, 199 (2001).
[121] K. Iakoubovskii and A. Stesmans, Phys. Rev. B **66**, 195207 (2002).
[122] K. Iakoubovskii, A. Stesmans, M. Nesladek, and G. Knuyt, Phys. Status Solidi A **193**, 448 (2002).
[123] L. S. Hounsome, R. Jones, P. M. Martineau, M. J. Shaw, P. R. Briddon, S. berg, A. T. Blumenau, and N. Fujita, Phys. Status Solidi A **202**, 2182 (2005).
[124] R. C. Burns, D. Fisher, and R. A. Spits, *High temperature/high pressure colour change of diamond* (2004), Patent WO0172406.
[125] A. T. Collins, H. Kanda, and H. Kitawaki, Diam. Relat. Mater. **9**, 113 (2000).
[126] D. J. Twitchen, P. M. Martineau, and G. A. Scarsbrook, *Coloured diamond* (2004), Patent WO20040202821.
[127] L. S. Hounsome, R. Jones, P. M. Martineau, D. Fisher, M. J. Shaw, P. R. Briddon, and S. Oberg, Phys. Rev. B **73**, 125203 (2006).
[128] L. S. Hounsome, R. Jones, P. M. Martineau, D. Fisher, M. J. Shaw, P. R. Briddon, and S. berg, Phys. Status Solidi C **4**, 2950 (2007).
[129] A. Pu, T. Bretagnon, D. Kerr, and S. Dannefaer, Diam. Relat. Mater. **9**, 1450 (2000).
[130] V. Avalos and S. Dannefaer, Diam. Relat. Mater. **14**, 155 (2005).
[131] J. M. Maki, F. Tuomisto, C. Kelly, D. Fisher, and P. Martineau, Physica B **401-402**, 613 (2007).

Chapter 3

Theory of EPR

3.1 Introduction

The theory behind electron paramagnetic resonance (EPR) is well established and for an in-depth review the reader is directed towards the textbooks by Weil, Bolton and Wertz [1] or Abragam and Bleaney [2]. Only a relatively short review will be presented here, sufficient to allow the experimental results presented in later chapters to be understood and linked to the underlying theory of the technique.

3.2 Magnetic dipole of the electron

To understand the interaction which arises between an electron and a magnetic field, which is essential to the EPR method, the magnetic dipole of the electron must be considered. In general a circulating mass with charge q produces a current I and gives rise to a magnetic dipole of magnitude μ_d, equivalent to IA, where A is the area enclosed by the current. In the case of an electron (mass $m = m_e$) travelling in a circular orbit of radius r the current is given by $I = qv/2\pi r$. Hence, treating the system classically the magnitude of $\boldsymbol{\mu}_d$ is given by the expression:

$$|\boldsymbol{\mu}_d| = IA = \frac{qv}{2\pi r}\pi r^2 = \frac{q}{2m_e}m_e v r = |\gamma_e \hbar \mathbf{l}| \tag{3-1}$$

where $m_e vr$ is equal to the angular momentum and γ_e is the gyromagnetic ratio. In quantum mechanics the angular momentum, $\mathbf{l}$, is quantised and each integer multiple $\hbar$ has an associated orbital magnetic moment of magnitude $\beta = |\gamma_e \hbar|$. However, the spin, S, which itself gives rise to a magnetic moment, must also be considered. For an electron in an s orbital $l = 0$ and hence the magnetic moment is determined entirely by S; cases where the orbital angular momentum is non-zero will be considered in §3.4.1. In the simplified case of $l = 0$ $\hat{\boldsymbol{\mu}}$ is found to be related

to the spin operator $\hat{\mathbf{S}}$ by the expression:

$$\hat{\boldsymbol{\mu}} = -\frac{e\hbar}{2m_e c} g_e \hat{\mathbf{S}} = -g_e \mu_B \hat{\mathbf{S}} \tag{3-2}$$

μ_B is referred to as the Bohr magneton and g_e is the free-electron "g-factor" which equals 2.002319304386(20) [1].

Classic electromagnetism predicts that the energy, E, of a magnetic moment in a magnetic field $\mathbf{B}$ is given by $E = -\boldsymbol{\mu} \cdot \mathbf{B}$. Hence quantum mechanically, from equation 3-2, an $l = 0$ system can be described by the Hamiltonian:

$$\mathscr{H} = -\hat{\boldsymbol{\mu}} \cdot \mathbf{B} = g_e \mu_B \hat{\mathbf{S}} \cdot \mathbf{B} \tag{3-3}$$

Since the energy is dependent upon the spin eigenstate it is apparent that the application of a magnetic field lifts the degeneracy of the spin states of the electron. It is this fact that provides the basis for the resonance phenomena and the EPR method.

3.3 Resonance conditions and spin relaxation

If the applied magnetic field is chosen to be along the z-axis ($\mathbf{B} \| \mathbf{z}$) then the eigenstates for a single unpaired electron in equation 3-3 are (using Dirac notation) $|M_S\rangle$ where $M_S = \pm\frac{1}{2}$. Two spin-state energy levels therefore result with their energies, E, given by $\pm\frac{1}{2} g_e \mu_B B$. These are often referred to as the electronic Zeeman energies. The separation in energy, corresponding to $|\Delta M_S| = 1$, is proportional to B and is given by $\Delta E = g_e \mu_B B$.

Transitions between the two electronic Zeeman levels may be induced by a magnetic field $\mathbf{B_1}$ ($|\mathbf{B_1}| \ll |\mathbf{B}|$, where $\mathbf{B_1} \perp \mathbf{B}$) component of an electromagnetic (EM) radiation source of appropriate frequency, such that the energy of the photon ($h\nu$) matches ΔE. Therefore the condition for resonance, in its simplest form, is:

$$\Delta E = h\nu = g_e \mu_B B \tag{3-4}$$

From this equation it is evident that there are two approaches for conducting an EPR experiment. One can either keep B fixed (i.e. ΔE is constant) and vary the applied frequency ν, or instead B can be scanned whilst applying a constant frequency of EM radiation. Using the accepted values for the physical constants

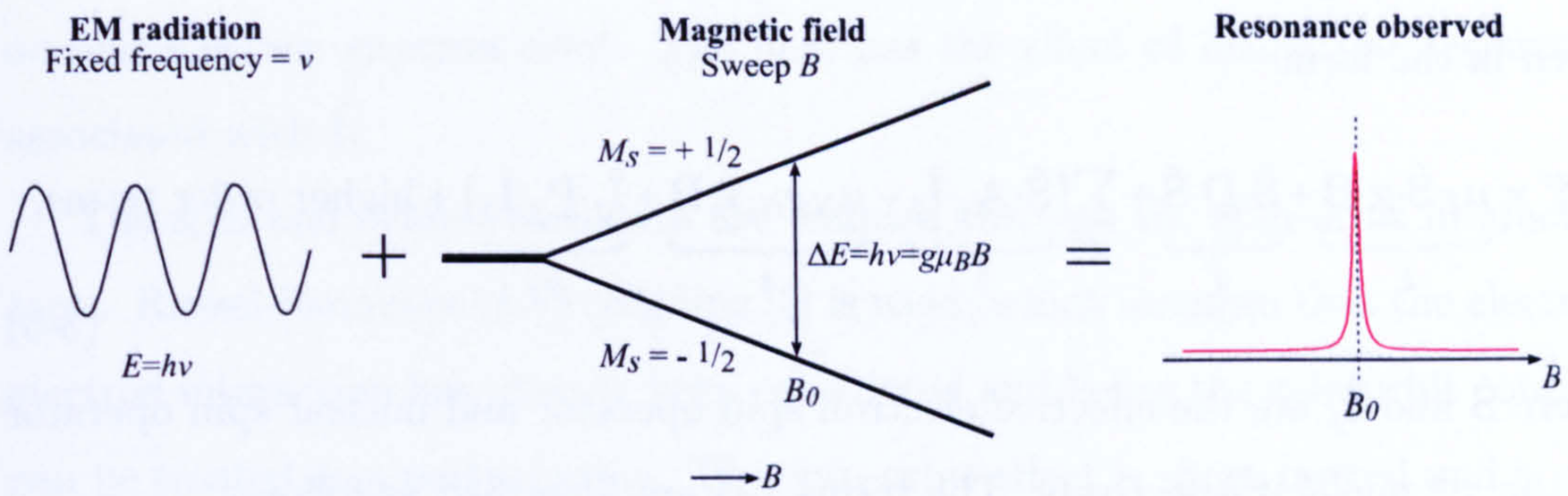

Figure 3-1: An EPR experiment on a single unpaired electron.

in equation 3-4 it is found that the frequency required for resonance is around $28\,\mathrm{MHz\,(mT)^{-1}}$. Thus, for a B field of $0.34\,\mathrm{mT}$ (most frequently used in EPR) the frequency required is around $9.5\,\mathrm{GHz}$. This corresponds to a wavelength of order $30\,\mathrm{mm}$ and is in the microwave region (X-band) of the electromagnetic spectrum.

Experimentally it is much easier to keep the microwave frequency fixed. Consequently in a typical EPR experiment a fixed frequency microwave source is used whilst the magnetic field is scanned, see figure 3-1. The technical aspects of the EPR technique are discussed in chapter 4.

3.4 The spin Hamiltonian

If equation 3-4 provided the complete story then all that would be observed in an EPR experiment is a single resonance line, centred about $g = 2.0023$. In reality the electron is not isolated, it is part of a much more complex and interesting system (in our case diamond). Interactions with the crystal field, other electrons or nearby nuclei (with non-zero spin) must be considered. These perturbations can lead to additional energy levels or a shift in existing levels and such changes can be dependent on the angle between the magnetic field and the crystal axes. As a result, with careful analysis, EPR data can provide a wealth of information regarding the environment of the unpaired electron(s), provided that a simple means of interpreting and representing these interactions is found.

The solution to this is the use of an effective spin Hamiltonian, which conveniently represents the interactions that need to be considered. This is typically

given in the form:

$$\mathscr{H} = \underbrace{\mu_B \hat{\mathbf{S}}\cdot\underline{\mathbf{g}}\cdot\mathbf{B}}_{1} + \underbrace{\hat{\mathbf{S}}\cdot\underline{\mathbf{D}}\cdot\hat{\mathbf{S}}}_{2} + \sum_j [\underbrace{\hat{\mathbf{S}}\cdot\underline{\mathbf{A}}_j\cdot\hat{\mathbf{I}}_j}_{3} - \underbrace{\mu_N g_{N_j}\hat{\mathbf{I}}_j\mathbf{B}}_{4} + \underbrace{\hat{\mathbf{I}}_j\cdot\underline{\mathbf{P}}_j\cdot\hat{\mathbf{I}}_j}_{5}] + \text{higher order terms}, \tag{3-5}$$

where $\hat{\mathbf{S}}$ and $\hat{\mathbf{I}}_j$ are the effective electron spin operator and nuclear spin operator for the j^{th} nuclei, respectively. The terms 1–5 are identified as follows:

1. Electronic Zeeman interaction.
2. Zero-field (electron-electron) interaction (for $S \geq 1$).
3. Hyperfine interaction of electrons with nuclei with non-zero spin ($I > 0$).
4. Nuclear Zeeman interaction for $I > 0$.
5. Nuclear quadrupole interaction (for $I \geq 1$).

3.4.1 Electronic Zeeman interaction

This term arises due to the interaction between the magnetic dipole moment of the electron and the magnetic field. The Hamiltonian for the electronic Zeeman interaction for a *free* electron was given in equation 3-3. However, as will be discussed below, *spin-orbit* interactions can cause a small amount of orbital angular momentum to appear in the ground state. This causes a local **B** field which adds vectorially to the external applied **B** field. The results of this is a change in the effective g-factor and the onset of anisotropy in g. Hence g is written in matrix form and $\mathscr{H}_{\text{Ze}}$ becomes:

$$\mathscr{H}_{\text{Ze}} = \mu_B \hat{\mathbf{S}}\cdot\underline{\mathbf{g}}\cdot\mathbf{B} \tag{3-6}$$

and $(2S+1)$ spin-state energy levels result.

To account for these effects one must consider the fact that electrons bonded to a nucleus may possess orbital angular momentum (L). The total momentum operator, $\hat{\boldsymbol{\mu}}$ is the vector sum of contributions from spin and orbital momentum:

$$\hat{\boldsymbol{\mu}} = \mu_B(\hat{\mathbf{L}} + g_e\hat{\mathbf{S}}) \tag{3-7}$$

Once the nucleus is placed in a crystal the motion of the electron is affected by the electrostatic interactions with the neighbouring atoms (ligands), with the interactions being described by a electrostatic potential introduced in the region

occupied by the electron orbit. The field has the effect of lifting the degeneracy associated with $\hat{\mathbf{L}}$.

The spin and orbital momenta are coupled through the spin-orbit interaction term. Russel-Saunders (LS) coupling [3] is used, which assumes that the electron-electron interaction has already been considered and hence the spin-orbit coupling can be treated as a perturbation. The spin-orbit effect is short-ranged and is only significant close to the nucleus. Using $\mathscr{H}_{\mathrm{Ze}}$ from equation 3-3 and adding the additional term for spin-orbit coupling ($\mathscr{H}_{\mathrm{so}}$) results in the Hamiltonian:

$$\mathscr{H}(\mathbf{r}) = \mathscr{H}_{\mathrm{Ze}} + \mathscr{H}_{\mathrm{so}} = \mu_B \mathbf{B} \cdot (\hat{\mathbf{L}} + g_e \hat{\mathbf{S}}) + \lambda_{\mathrm{so}} \hat{\mathbf{L}} \cdot \hat{\mathbf{S}}, \tag{3-8}$$

where λ_{so} is the Russel-Saunders spin-orbit coupling term. A higher order contribution from diamagnetic terms [4] has been ignored since they are too small to have an effect.

In the absence of spin-orbit coupling the angular momentum is quenched, meaning that the expectation value of its component along the Zeeman field, $\langle L_z \rangle$, is zero. Thus, to first order, $\hat{\boldsymbol{\mu}}$ is given by equation 3-6, with $\mathbf{g}$ replaced by g_e. The quenching is removed by spin-orbit coupling, hence $\hat{\mathbf{L}}$ has a finite expectation value. Off diagonal elements can be finite and the spin-orbit coupling term $\mathscr{H}_{\mathrm{so}}$ can mix excited states $|\psi_n\rangle$ into the original ground state $|\psi_0\rangle_0$:

$$|\psi_0\rangle = |\psi_0\rangle_0 - \sum_{n \neq 0} \frac{|\psi_n\rangle \langle \psi_n | \lambda_{\mathrm{so}} \hat{\mathbf{L}} \cdot \mathbf{S} | \hat{\psi}_0 \rangle_0}{E_n - E_0} \tag{3-9}$$

The Hamiltonian for the Zeeman interaction can then be derived using perturbation theory as [5]:

$$\mathscr{H} = \mu_B^2 \mathbf{B} \cdot \underline{\boldsymbol{\Lambda}} \cdot \mathbf{B} + 2\lambda_{\mathrm{so}} \mu_B \mathbf{B} \cdot \underline{\boldsymbol{\Lambda}} \cdot \hat{\mathbf{S}} + \lambda_{\mathrm{so}}^2 \hat{\mathbf{S}} \cdot \underline{\boldsymbol{\Lambda}} \cdot \hat{\mathbf{S}} \tag{3-10}$$

This has been simplified using the 3×3 spin-orbit coupling matrix, $\underline{\boldsymbol{\Lambda}}$ [1], which is given by:

$$\underline{\boldsymbol{\Lambda}} = -\sum_{n \neq 0} \frac{\langle \psi_0 | \hat{\mathbf{L}} | \psi_n \rangle \langle \psi_n | \hat{\mathbf{L}} | \psi_0 \rangle}{E_n - E_0} \tag{3-11}$$

The first term in equation 3-10 yields a constant contribution to the energy of all spin states and causes no shift between the energy levels. It is therefore of no spectroscopic interest and will not be considered further. However, the second and third terms operate on spin variables; the second term gives the linear Zeeman

effect, i.e. the coupling of the magnetic moment with **B** and the third term represents the zero-field interaction, which is only present for defects with $S \geq 1$. The latter will be discussed in §3.4.2.

Equation 3-10 is generally written in the more compact form:

$$\mathscr{H} = \mu_B \mathbf{B} \cdot \underline{\mathbf{g}} \cdot \hat{\mathbf{S}} + \hat{\mathbf{S}} \cdot \underline{\mathbf{D}} \cdot \hat{\mathbf{S}} \tag{3-12}$$

$$\text{where } \underline{\mathbf{g}} = g_e \underline{\mathbf{1}} + 2\lambda_{so} \underline{\mathbf{\Lambda}} \text{ and } \underline{\mathbf{D}} = \lambda_{so}^2 \underline{\mathbf{\Lambda}},$$

where $\underline{\mathbf{1}}$ is the 3×3 unit matrix.

When the second term in $\underline{\mathbf{g}}$ vanishes (angular momentum *soley* due to spin angular momentum) it is apparent that $\underline{\mathbf{g}}$ is isotropic with the diagonal values all equaling g_e. Any anisotropy or deviation from this value results from the spin-orbit coupling matrix $\underline{\mathbf{\Lambda}}$.

Defects in diamond typically exhibit very small deviations of g from g_e, since both λ_{so} and Λ are quite small. Λ is small due to the fact that is varies inversely with the energy gap separation, which in diamond is large at 5.5 eV.

3.4.2 Zero-field interaction

In systems with $S \geq 1$ the $(2S+1)$-fold degeneracy in the absence of a magnetic field can be lifted via electron-electron interactions. Splittings in the spin-state levels at zero magnetic field are described by the zero-field interaction. This term is given by the expression:

$$\mathscr{H}_{zf} = \hat{\mathbf{S}} \cdot \underline{\mathbf{D}} \cdot \hat{\mathbf{S}} \tag{3-13}$$

D is made traceless ($\text{tr}(\mathbf{D}) = 0$) by subtracting the term which only causes an overall shift in the position of the energy levels, and hence has no affect on the observed spectrum. There are three potential contributions to $\mathscr{H}_{zf}$:

1. The spin-orbit interaction, as described in §3.4.1. This term is usually the dominant contributor to D.
2. The exchange interaction, which describes the direct overlap of the wave-function of the unpaired electrons between neighbouring magnetic ions at a defect site. In the absence of spin-orbit coupling this interaction has no effect on the EPR spectrum. This interaction is discussed fully by Abragham and Bleaney [2].

3. Dipole-dipole interactions, which are the primary contributor to D in the absence of strong spin-orbit coupling.

Combining the equations for $\underline{g}$ and $\underline{D}$ in equation 3-12 leads to the useful relationship that $D_{ij} = \frac{1}{2}\lambda_{so}\delta g_{ij}/g_e$, where ij denotes a particular component of the matrices. This expression allows the contribution to D from spin-orbit coupling to be estimated from the shift of g from g_e. Values for λ_{so} for free atoms are listed in Weil, Bolton and Wertz [1].

Considering dipolar interactions, in the case of a two electron $S = 1$ system with spins $\hat{\mathbf{S}}_1$ and $\hat{\mathbf{S}}_2$ separated by a vector $\mathbf{r}$, this term can be represented by a Hamiltonian of the form:

$$\mathscr{H}_{\text{dip}} = \left(\frac{\mu_0}{4\pi}\right) g_1 g_2 \mu_B^2 \left[\frac{\hat{\mathbf{S}}_1 \cdot \hat{\mathbf{S}}_2}{r^3} - \frac{3(\hat{\mathbf{S}}_1 \cdot \mathbf{r})(\hat{\mathbf{S}}_2 \cdot \mathbf{r})}{r^5}\right] \tag{3-14}$$

Generally $g_1 = g_2 = g$ is assumed and the Hamiltonian is described in terms of a Cartesian coordinate system (x, y, z). Since $\text{tr}(\mathbf{D}) = 0$, only two independent energy parameters are needed. It is common to designate these as:

$$D = \tfrac{3}{2} D_z \tag{3-15}$$

$$E = \tfrac{1}{2}(D_x - D_y) \tag{3-16}$$

By convention D_z is taken to be the principal value with the largest absolute magnitude and D_y has the smallest absolute magnitude in cases where $D_x \neq D_y$, thus producing a set ordered in energy. Equation 3-14 can then be rewritten as:

$$\mathscr{H}_{\text{dip}} = D\left\{S_z^2 - \tfrac{1}{3}S(S+1)\right\} + E(S_x^2 + S_y^2) \text{ where,} \tag{3-17}$$

$$D = \left(\tfrac{\mu_0}{4\pi}\right)\left(\tfrac{3}{4}\right) g^2 \mu_B^2 \left\langle \tfrac{r^2 - 3z^2}{r^5} \right\rangle \tag{3-18}$$

$$\text{and } E = \left(\tfrac{\mu_0}{4\pi}\right)\left(\tfrac{3}{4}\right) g^2 \mu_B^2 \left\langle \tfrac{y^2 - x^2}{r^5} \right\rangle \tag{3-19}$$

Both D and E depend on the distance between two electrons with parallel spins and the angular brackets imply an average over the electronic wavefunction. The equations for these terms above can reveal information regarding the symmetry and dimensions of the defect being observed:

- It is evident that a defect with axial symmetry (x and y axes equivalent) will have $E = 0$, whilst in cases of cubic symmetry ($x \equiv y \equiv z$) $D = 0$.
- If the dipole-dipole term dominates then $|D|$ provides a measurement of the dimensions of the defect.

3.4.3 Hyperfine interaction

One of the most rewarding aspects of EPR data is the analysis of hyperfine interactions, i.e. the interactions between the electronic and nuclear spins, as these provide a local probe for electronic spin density. Since a number of nuclei with $I \neq 0$ may be present the term in the spin Hamiltonian, $\mathscr{H}_{\text{hf}}$, is written as a sum over all such nuclear spins:

$$\mathscr{H}_{\text{hf}} = \sum_j \hat{\mathbf{S}} \cdot \underline{\mathbf{A}}_j \cdot \hat{\mathbf{I}}_j \tag{3-20}$$

This can be understood in terms of local magnetic fields which, to first order, shift the EPR transition by $\Delta E = -m_I A/\mu_B g$ according to the $2I + 1$ possible values for the nuclear spin (m_I).

The hyperfine interaction can be split into an isotropic and anisotropic component. The isotropic (A_s) term, also referred to as the contact or Fermi interaction, is dependent on the unpaired electron density at the nucleus, which arises from the s-electrons. It is given by:

$$A_s = \frac{2\mu_0}{3} g_e \mu_B g_n \mu_n |\psi(0)|^2 \tag{3-21}$$

where μ_N is the nuclear magneton (analogous to μ_B given in equation 3-2, but with m_e replaced by the mass of the proton), g_N is the g-factor of the nucleus and $\psi(0)$ is the wavefunction of the electron at the nucleus.

$|\psi(0)|^2$ is zero for non s-type orbitals and the hyperfine coupling that results arises from the magnetic dipole interaction between the nucleus and the unpaired electron. This is given by the expression stated for the dipolar term in $\underline{\mathbf{D}}$ (equation 3-14), with $\hat{\mathbf{S}}_1 = \hat{\mathbf{S}}$, $\hat{\mathbf{S}}_2 = \hat{\mathbf{I}}$, $g_1 = g$ and $g_2 = g_N$.

Other contributions to the hyperfine structure, referred to as indirect, exist [6]. However, these are generally small compared to the direct contributions discussed, hence such terms are ignored here.

For an axially symmetric hyperfine interaction $\underline{\mathbf{A}}$ may be written in terms of parallel and perpendicular components, $A_\parallel$ and $A_\perp$, where $A_\parallel$ lies parallel to the unique principal axis:

$$\underline{\mathbf{A}} = \begin{pmatrix} A_\perp & 0 & 0 \\ 0 & A_\perp & 0 \\ 0 & 0 & A_\parallel \end{pmatrix} \tag{3-22}$$

The values for $A_{\parallel}$ and $A_{\perp}$ can be directly related to the isotropic and anisotropic parts, thus directly relating the determined parameters to the electronic wavefunction; A_s for the unpaired s-electrons and A_p for the unpaired p-electrons:

$$A_s = (A_{\parallel} + 2A_{\perp})/3 \tag{3-23}$$

$$A_p = (A_{\parallel} - A_{\perp})/3 \tag{3-24}$$

These parameters can be used to provide an estimate of the localisation of the electron at a given nucleus, following the method described by Morton and Preston [7], which is briefly outlined below:

The unpaired electron's wavefunction (Φ) can be constructed from a linear combination of atomic orbitals (LCAO) centred on the atoms in and around the defect. This is a good approximation in diamond due to the strong, highly directional, bonds. In cases where only s and p type orbitals need be considered, the wavefunction (summing over all over all the nuclei (i) in the defect) may be expressed as:

$$\Phi = \sum_i \eta_i \psi_i = \sum_i \eta_i \left[\alpha_i (\psi_s)_i + \beta_i (\psi_p)_i \right], \tag{3-25}$$

Normalisation requires:

$$\alpha_j{}^2 + \beta_i{}^2 = 1 \text{ and } \sum_i \eta_i{}^2 = 1 \tag{3-26}$$

α, β and η may then be related to the measured hyperfine parameters, such that:

$$A_s = a\alpha_i{}^2\eta_i{}^2 \text{ and } A_p = b\beta_i{}^2\eta_i{}^2 \tag{3-27}$$

The constants a and b are the values of A_s and A_p for 100% occupancy of the s and p-type orbitals, respectively. Values for these parameters for nuclei needed for the work in this thesis are listed in table 3-1. A_s and A_p for a given hyperfine interaction can be determined by experiment, thus using equations 3-26 and 3-27 $\alpha_i{}^2$ and $\beta_i{}^2$ may be determined. The localisation of the electron at each site of the nuclei responsible for the considered hyperfine interaction is then given by $\eta_i{}^2$. The hybridisation ratio λ_h can also be calculated, and is given by $\lambda_h = (\beta/\alpha)^2$. For an undistorted sp^3 orbital in diamond this would equal 3.

Table 3-1: Natural abundances, nuclear spins I, g-factors g_N as well as values of a and b (see text) of isotopes relevant to this thesis. Abundances and g_N values are from The CRC Handbook [9], whilst the values for a and b are quoted from the paper by Morton and Preston [7].

Nucleus	Natural abundance	I	g_N	a/MHz	b/MHz
^{1}H	99.9885(70)	$\frac{1}{2}$	5.5857		
^{2}H	0.0115(70)	1	0.8574		
^{13}C	1.07(8)	$\frac{1}{2}$	1.4048	3777	107.4
^{14}N	99.636(20)	1	0.40376	1811	55.52
^{15}N	0.364(20)	$\frac{1}{2}$	-0.5664	-2540	-77.88
^{29}Si	4.685(8)	$\frac{1}{2}$	-1.1106	-4594	-114.2

There are several sources of error in this treatment and Baker and Newton caution that this approach is crude and list the factors which have been omitted [8]. Despite this it remains as a useful starting point for theoretical interpretation of EPR hyperfine data.

3.4.4 Nuclear Zeeman interaction

The nuclear Zeeman interaction results from the interaction between the magnetic moment of a nucleus with the applied magnetic field, akin to the electron Zeeman interaction discussed in §3.4.1, but with g_e and μ_B replaced by the analogous parameters for nuclei:

$$\mathscr{H}_{\mathrm{nZe}} = \sum_j -\mu_N g_{N_j} \hat{\mathbf{I}}_j \mathbf{B} \tag{3-28}$$

Since the mass of the proton is ~ 2000 times greater than that of the electron $\mu_N \ll \mu_B$, (see equation 3-2) and therefore the nuclear Zeeman interaction is much smaller than the electronic Zeeman. The minus sign in equation 3-28 is chosen such that when $g_N > 0$ the stable configuration is the nuclear moment to be parallel to the applied field.

The allowed transitions have the selection rules $\Delta M_S = \pm 1$, $\Delta m_I = 0$ (see §3.5). Since the nuclear Zeeman interaction produces equal shifts in the spin-state energy levels for a given set of levels with the same value of m_I, it is evident that allowed transitions are unaffected by this interaction. However, the value of g_N *will* affect the position of any forbidden electron-nuclear double-spin flip transitions ($\Delta M_S =$

± 1, $\Delta m_I = \pm 1$), hence any observation of resonance lines resulting from such transitions provides the possibility to identify the nuclei responsible for observed hyperfine interactions.

3.4.5 Quadrupole interaction

The direction of the nuclear-spin angular momentum is linked to the actual shape of the nucleus, that is, to the axis of symmetry of its (time-averaged) electrical charge distribution. In cases where a nuclei has $I \geq 1$ any electric-field gradient, resulting from the electron distribution in the immediate neighbourhood, can orient the charge ellipsoid and therefore affect the direction of the spin. The energy of alignment is derivable from the spin-Hamiltonian term, $\mathscr{H}_{\mathrm{qp}}$:

$$\mathscr{H}_{\mathrm{qp}} = \sum_j \hat{\mathbf{I}}_j \cdot \underline{\mathbf{P}}_j \cdot \hat{\mathbf{I}}_j \tag{3-29}$$

In the same way as for $\underline{\mathrm{D}}$ (§3.4.2), the matrix for this interaction is constructed so $\mathrm{tr}(\mathbf{P}) = 0$. The Hamiltonian is often written in terms of Cartesian coordinates:

$$\mathscr{H}_{\mathrm{qp}} = P\left\{I_z^2 - \frac{1}{3}I(I+1)\right\} + \frac{\eta P}{3}\left(I_x^2 - I_y^2\right), \tag{3-30}$$

with P being expressible as:

$$P = \frac{3}{2}P_z = \frac{e^2 q_{\mathrm{efg}} Q}{4I(2I+1)} \tag{3-31}$$

Here q_{efg} is the electric field gradient at the nucleus $\left(\frac{\partial^2 V}{\partial z^2}\right)$. Since s-orbitals are spherically symmetric they do not contribute to q_{efg} but a p-orbital has an asymmetric charge distribution at the nucleus and so has a non-zero contribution. η is referred to as the asymmetry parameter (given by $(P_x - P_y)/P_z$) and describes the deviation of the field gradient from axial symmetry around the z-axis. The quadrupole moment, Q, describes the electrical shape of the nucleus and is hence a means to measure its anisotropy.

It should be noted that adding the term $\mathscr{H}_{\mathrm{qp}}$ to the spin Hamiltonian does not affect the EPR transitions *to first-order*, as all energy levels are shifted equally. Second-order or higher energy contributions can affect the spectrum and lead to a more complex pattern of lines, due to the competition to align the nuclear spin by the local electric-field gradient, the local magnetic field from unpaired electron(s) and the externally applied field.

3.5 Transition probabilities

As discussed in §3.3 the energy driving the transitions between the spin-state energy levels in an EPR experiment is provided by the time varying magnetic component of the microwave field, $\mathbf{B}_1(t)$. This magnetic field interacts with the magnetic moment $\boldsymbol{\mu}$ to produce a perturbation $\mathscr{H}_{\mu w}$, which from equation 3-3 can be expressed as:

$$\mathscr{H}_{\mu w} = -\boldsymbol{\mu} \cdot \mathbf{B}_1(t) \tag{3-32}$$

The transition probability between an initial and final state ($|\psi_i\rangle$ and $|\psi_f\rangle$, respectively) is proportional to:

$$|\langle\psi_f|\mathscr{H}_{\mu w}|\psi_i\rangle|^2 \tag{3-33}$$

Hence knowledge of the eigenvalues of a spin system provides the necessary knowledge to calculate the relative intensities of the possible transitions. The energy matrix of a spin system can be determined by the operation of the spin Hamiltonian ($\mathscr{H}$) on the spin states $|M_S, m_I\rangle$. Each element in the matrix is given by:

$$\langle M_S', m_I'|\mathscr{H}|M_S, m_I\rangle, \tag{3-34}$$

with the eigenvalues of the matrix giving the energy levels of the system between which transitions may occur. Eigenstates of the system $|\psi_k\rangle$ are linear combinations of the states $|M_S, m_I\rangle$. Dependent on the relative sizes of the diagonal elements of the matrix and the off-diagonal components two possibilities regarding the observed transitions arise:

1. If the off-diagonal elements are much smaller the eigenfunctions are simply the spin states $|M_S, m_I\rangle$. In this case only transitions in accordance with the selection rules $\Delta M_S = \pm 1$, $\Delta m_I = 0$ (the allowed transitions) will be observed.
2. If the off-diagonal elements are not negligible the eigenfunctions are no longer pure $|M_S, m_I\rangle$ states, but are instead linear combinations of these states. This is known as *spin-state mixing*. A shift in the energy levels results and the selection rules are relaxed. Therefore transitions where $\Delta M_S \neq \pm 1$, $\Delta m_I \neq 0$ may have non-zero probability.

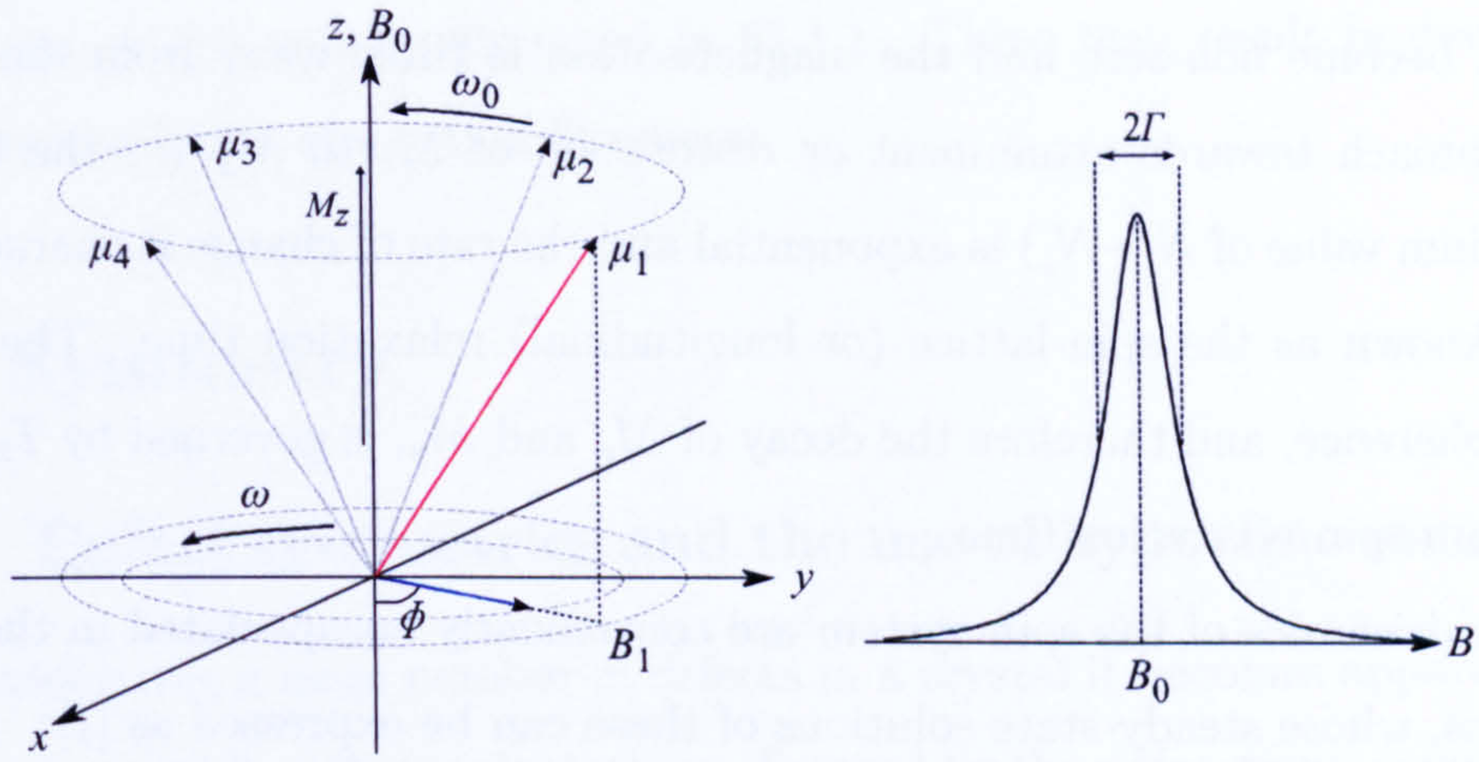

Figure 3-2: Precession of spin magnetic moments (μ) in an applied magnetic field and the Lorentzian lineshape.

3.6 Spin relaxation and the Bloch absorption lineshape

So far in this chapter the interactions in the spin Hamiltonian, which determine the position in field of an EPR resonance line, have been discussed, without thought for the form of the resonance line which is observed. For this spin relaxation must be considered, which determines how a spin system attains and maintains thermal equilibrium and results in finite EPR linewidths.

In a classical treatment of spin resonance the static magnetic field defines the z-axis and the dipole moments of individual spins precess about this axis at the Lamour frequency (ω_0), see figure 3-2. However, since there is no phase coherence between the spins the resulting components of the net magnetisation along x and y (M_x and M_y, respectively) are zero and $\mathbf{M}$ is parallel to the z axis. The thermal equilibrium value of the magnetisation, M_z^0, is determined by the relative populations in the two states ($N_\uparrow$ and $N_\downarrow$) at a temperature T, which is set by a Boltzmann distribution law:

$$\frac{N_\uparrow}{N_\downarrow} = \exp\left(-\frac{\Delta E}{k_B T}\right) \tag{3-35}$$

In an EPR experiment the microwave magnetic field B_1 is precessing in the xy plane (azimuthal angle ϕ) with its own angular frequency ω. At resonance $\omega_0 = \omega$ and phase coherence of the precession of the spins exists. As a result M_x

and M_y become non-zero and the magnetisation is tilted away from the z axis. The approach towards attainment or restoration of M_z to M_z^0 (or the thermal equilibrium value of $N_\uparrow - N_\downarrow$) is exponential and the rate of change is characterised by T_1, known as the spin-lattice (or longitudinal) relaxation time. The loss of phase coherence, and therefore the decay of M_x and M_y, is governed by T_2, which is the spin-spin relaxation time.

Such dynamics of the spin system are conveniently encapsulated in the Bloch equations, whose steady-state solutions of these can be expressed as [1]:

$$M_{x\phi} = -M_z^0 \frac{\gamma_e B_1 (\omega - \omega_0) T_2^2}{1 + (\omega - \omega_0)^2 T_2^2 + \gamma_e^2 B_1^2 T_1 T_2} \tag{3-36}$$

$$M_{y\phi} = +M_z^0 \frac{\gamma_e B_1 T_2}{1 + (\omega - \omega_0)^2 T_2^2 + \gamma_e^2 B_1^2 T_1 T_2} \tag{3-37}$$

$$M_{z\phi} = +M_z^0 \frac{1 + (\omega - \omega_0)^2 T_2^2}{1 + (\omega - \omega_0)^2 T_2^2 + \gamma_e^2 B_1^2 T_1 T_2} \tag{3-38}$$

Note that the response $M_{x\phi}$ is in phase with B_1, whereas $M_{y\phi}$ is 90° out of phase and these terms represent the dispersion and absorption components of the magnetic radiation, respectively. Usually the out-of-phase absorption component is recorded in an EPR experimental under conditions of "slow adiabatic passage", which means that B is swept through resonance conditions *slowly* compared to the characteristic relaxation times T_1 and T_2.

Under field-sweep conditions the lineshape function $Y(B) \propto M_{y\phi}$ is given by:

$$Y(B) \propto M_z^0 \frac{\gamma_e B_1 T_2}{1 + (B - B_0)^2 \gamma_e^2 T_2^2 + \gamma_e^2 B_1^2 T_1 T_2} \tag{3-39}$$

If this is compared to a Lorentzian function, which has the form (where Γ is the half-width at half-maximum linewidth)

$$Y = Y_{\max} \frac{\Gamma^2}{\Gamma^2 + (x - x_0)^2}, \tag{3-40}$$

then it is apparent the EPR lineshape may be considered as a Lorentzian (figure 3-2) with $\Gamma = 1/\gamma_e T_2$ and amplitude $Y(B_0) \propto M_z^0 B_1$, provided $\gamma_e^2 B_1^2 T_1 T_2 \ll 1$. At higher values of B_1 (proportional to the square root of microwave power) the population difference $(N_\uparrow - N_\downarrow)$ and hence |M| is reduced, resulting in a broadening and reduction in amplitude of the EPR resonance line. This effect is known as microwave power saturation and is discussed further in §4.5. In reality the observed lineshape in an experiment is also dependent on additional broadening

mechanisms, which will be discussed in §5.1.1. These may result in deviations away from the Bloch absorption lineshape.

3.7 Symmetry

3.7.1 Defect symmetries and the use of hyperfine structure

When considering a large number of defects in a crystal it becomes apparent that they can occur with various orientations, dictated by the point group symmetry of the defect (this contains all the operators under which the defect is invariant). In cases where the defect distorts the crystal, the number of lines and the distribution in intensity between these lines therefore changes as **B** is rotated with respect to the crystal.

For a general site of low symmetry in diamond, the operations from the T_d symmetry would generate 24 different possible sites, but this number reduces as the symmetry of the defect increases. Table 3-2 shows the number of lines and the pattern of intensities at principal directions of **B** in a {110} plane for possible symmetries of distorted tetrahedral point sites.

To demonstrate these ideas and to introduce the idea of a roadmap a simple example will be considered, that of the single substitutional nitrogen centre (N_s^0). As discussed in §2.2.1.1 this defect has C_{3v} symmetry, with the N-C bond along a ⟨111⟩ direction being elongated compared to the host material. Figure 3-3 illustrates the four possible orientations/sites of this defect. The defect has a single unpaired electron (so $S = \frac{1}{2}$) and nitrogen has $I = 1$ (table 3-1). Although $\underline{\mathbf{g}}$ is close to isotopic the anisotropy in $\underline{\mathbf{A}}$ ($A_\parallel > A_\perp$) means that, as the magnetic field is rotated with respect to the crystal, the hyperfine splitting will vary, dependent on the angle between $A_\parallel$ and **B**. As this angle can be different for the different symmetry-related sites splittings in the lines can be observed.

The symmetry of a defect is investigated by constructing a *roadmap*, obtained by recording a spectra at a number of different orientations of **B** in a given crystallographic plane. The $(1\bar{1}0)$ roadmap and individual simulations for **B** along [100], [111] and [110] for N_s^0 are shown in figure 3-4. This can be interpreted as follows:

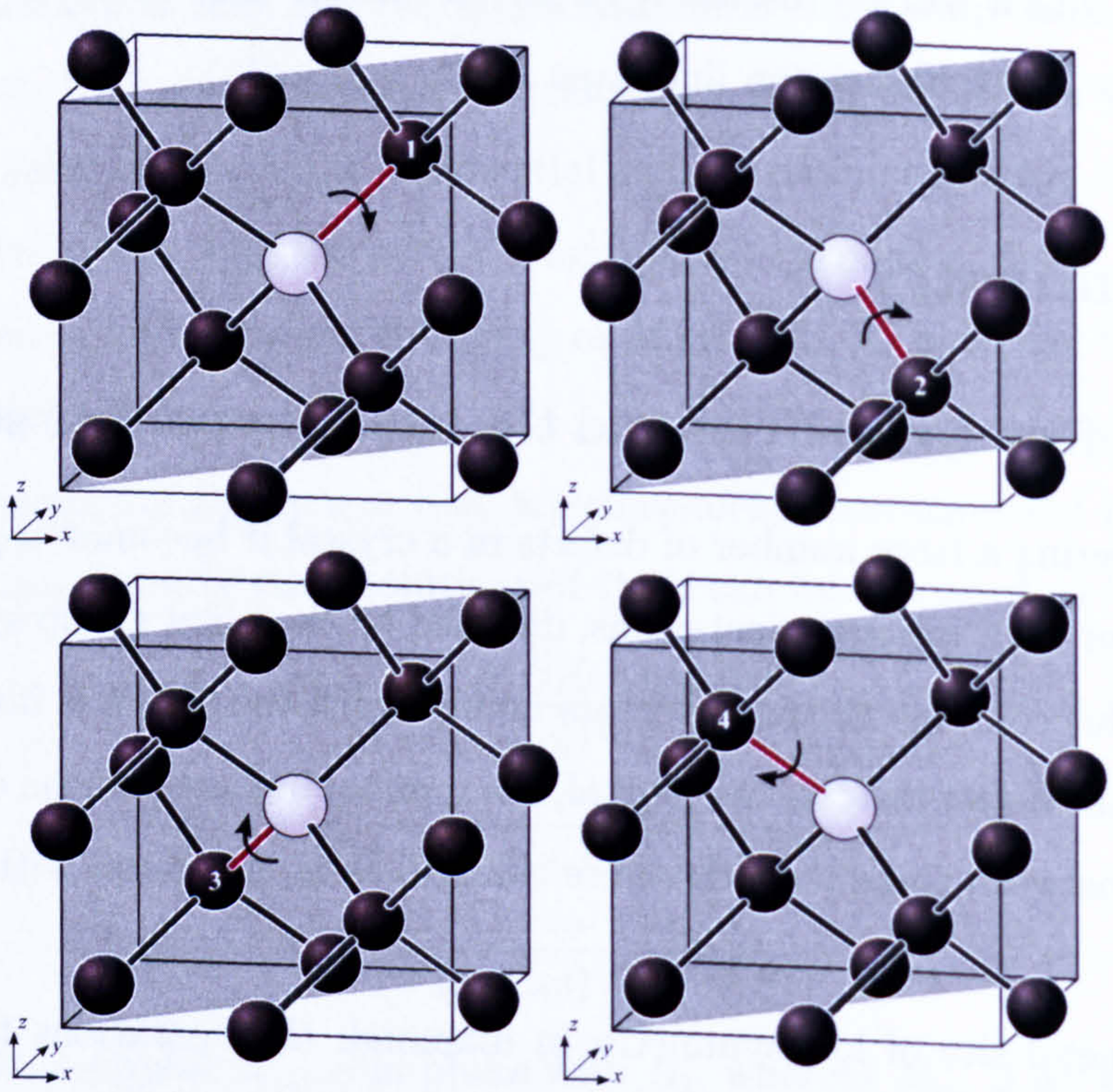

Figure 3-3: The four symmetry-related configurations of the N_s^0 defect. The central lighter atom is the nitrogen atom. The unpaired electron is localised along the shaded bond. This bond is elongated and becomes the C_{3v} rotation axis of the defect. The shaded plane is $(1\bar{1}0)$.

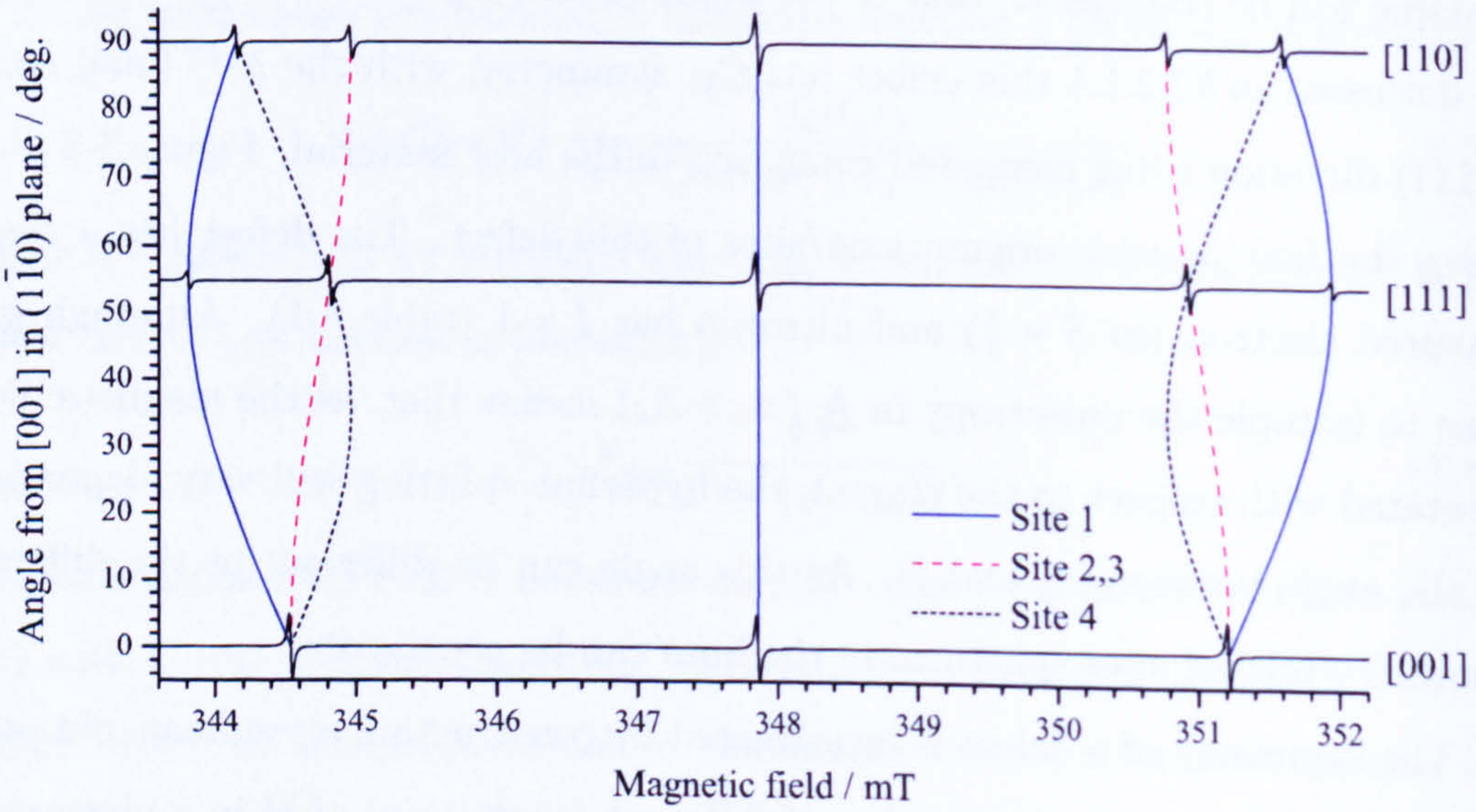

Figure 3-4: A roadmap and simulated intensities for N_s^0, with the magnetic field rotated in the $(1\bar{1}0)$ plane. Simulations obtained at $\nu = 9.75\,\mathrm{GHz}$.

Starting from **B** ∥ [100] in figure 3-3 it is seen that the magnetic field makes the same angle with the four possible orientations of $A_{\parallel}$, hence the same three-lined pattern results from each site. As the magnetic field is rotated in the $(1\bar{1}0)$ plane the same angle will always be made with sites 2 and 3, hence the outer hyperfine satellites from these sites will always overlap. As the magnetic field reaches [111] the splitting is the maximum possible for site 1 ($\mathbf{B} \| A_{\parallel}$), whilst sites 2,3,4 all make the same angle and experience a smaller splitting, A. Hence a ratio of 1:3 for the outer lines is observed. At [110] sites 1 and 4 are equivalent, hence a 2:2 ratio is seen for the outer lines. $A = A_{\perp}$ for sites 2 and 3.

Although the roadmap demonstrates that the centre has trigonal symmetry, how was the model for the defect established? The data indicated that an $I = 1$ nuclei with ~ 100% abundance was present, suggesting ^{14}N was involved, but what about the structure of the surrounding carbon atoms? As there is a small natural abundance of ^{13}C (1.1%), and as this isotope has a nuclear spin of $\frac{1}{2}$, assuming the model is correct there should exist weak additional lines arising from donor electrons in anti-bonding orbitals on ^{14}N-^{13}C pairs. In the measurements of Smith *et al.* [10] one pair of hyperfine satellites were observed.

The intensity of hyperfine satellites, relative to a central transition allows the number of equivalent positions for the nucleus to be determined. In general, for a nucleus with abundance $\mathscr{A}$ and N_{equiv} equivalent positions the intensity of the hyperfine satellites (I_{hf}) can be related to the intensity of the central line (I_{central}) by the equation:

$$I_{\text{hf}} = N_{\text{equiv}} \times \frac{\mathscr{A}}{1-\mathscr{A}} \times I_{\text{central}} \tag{3-41}$$

Hence not only can the number of equivalent sites be determined, but the value obtained for $\mathscr{A}$ can be used to aid in the identification of the nuclei present.

In the case of N_s^0 the hyperfine satellites observed by Smith *et al.* had an intensity consistent with a unique ^{13}C site (i.e. each satellites was $\frac{1}{180}$ of the intensity of the central line). The observation of lines with these relative intensities allowed Smith *et al.* to conclude that the donor electron is mainly confined to the nitrogen atom and one of the nearest-neighbour carbon atoms [10]. The bond between the nitrogen atom and this carbon atom is then elongated, leading to the observed C_{3v} symmetry and the a unique ^{13}C site.

Table 3-2: Possible symmetries for distorted tetrahedral point sites. G is the group of rotation matrices/number of sites required for simulating an EPR spectra (see table 3-4). The relative line intensities are for a $S = \frac{1}{2}$ defect with no hyperfine interaction and accidental coincidences are ignored. This table is based on an original produced by Cox [11].

Symmetry	**Distortion**	G	**Line intensities**		
			⟨100⟩	⟨111⟩	⟨110⟩
T_d $(43m)$	No distortion	1	1	1	1
D_{2d} $(\bar{4}2m)$	[100] axial distortion	3	2,1	3	2,1
D_2 (222)	[100] and [010] axial distortion	6a	2,2,2	6	2,2,2
C_2 (2)	[100] and general non-axial distortion	12a	4,4,4	6,6	4,4,2,2
D_{3d} $(\bar{3}m)$	[111] axial distortion with inversion symmetry	4	4	1,3	2,2
C_{3v} $(3m)$	[111] axial distortion without inversion symmetry	4	4	1,3	2,2
C_{1h} (m)	[111] non-axial distortion, one axis along $[1\bar{1}0]$	12b	8,4	6,3,3	4,2,4,2
C_1 (1)	[111] non-axial distortion, not along $[1\bar{1}0]$	24	8,8,8	6,6,6,6	4,4,4,4,4,4
C_{2v} $(mm2)$	Keep rotation about [001], [110] axial distortion	6b	4,2	3,3	1,1,4
C_{2v} $(mm2)$	Keep rotation about [001], [110] non-axial distortion, one axis along [001]	6b	4,2	3,3	1,1,4
C_{1h} (m)	[110] non-axial distortion, not along [001]	12a	8,4	6,3,3	4,2,4,2
C_1 (1)	Axial distortion, not along axes	24	8,8,8	6,6,6,6	4,4,4,4,4,4
C_1 (1)	Non-axial distortion, not along axes	24	8,8,8	6,6,6,6	4,4,4,4,4,4

3.7.2 Rotation matrices for EPR simulation

In order to reproduce the EPR spectrum for a defect of a given symmetry a way is needed to create the spectrum for each group of defects whose axes make the same angle with the applied magnetic field (each *symmetry-related site*). This can be achieved by generating symmetry-related parameter matrices ($\underline{Y}_i$) for each of the interactions in the spin Hamiltonian (§3.4). By defining one parameter matrix ($\underline{Y}_1$) and rotating this by each of 3×3 rotation matrices[1] $\mathbf{R}_i$ which are permissable in the point group symmetry of the host crystal [12] the required parameter matrices are obtained:

$$\underline{Y}_i = \mathbf{R}_i \cdot \underline{Y}_1 \cdot \mathbf{R}_i^T \tag{3-42}$$

Diamond has tetrahedral symmetry and the 24 different rotations which represent the symmetry operations of this crystal point group are listed in table 3-3, where $\mathbf{R}^n_{hkl}$ denotes a matrix for an n fold rotation about an axis with Miller indices hkl.

For a defect of any symmetry allowed in diamond the overall spectrum can be reproduced using all 24 rotation rotation matrices. However, for a defect of T_d symmetry the system is unchanged under all 24 of these operations and hence only one of the matrices listed in table 3-3 is needed. As the symmetry of a defect is lowered the number of rotation matrices which leave the system unchanged is reduced, and hence the minimum number of operations required to account for all the symmetry-related sites will increase. For example, for a defect of C_{3v} symmetry oriented along [111] (e.g. N^0_s, see §3.7.1), six of the operations will leave the system unchanged. The remaining 18 operations are split equally into groups of six rotations, with each group producing one of the three other possible orientations of the defect ($[1\bar{1}\bar{1}]$,$[\bar{1}\bar{1}1]$ and $[\bar{1}1\bar{1}]$).

The different distortions and the resulting symmetry for a defect in diamond are listed in table 3-2 and for each distortion a name of a group (G) is given. The members of each group G are listed in table 3-4. In this table the operations listed in columns are those which leave the symmetry-related parameter matrices unchanged for a particular site.

[1]The rotation matrices have the property $\mathbf{R}_i^{-1} = \mathbf{R}_i^T$

Table 3-3: The 24 rotation matrices permissable in tetrahedral symmetry. $\mathbf{R}^n_{hkl}$ denotes a matrix for an n fold rotation about an axis with miller indices hkl.

$\mathbf{R}^1$			
$\begin{pmatrix} 1 & 0 & 0 \\ 0 & 1 & 0 \\ 0 & 0 & 1 \end{pmatrix}$			
$\mathbf{R}^2_{100}$	$\mathbf{R}^2_{010}$	$\mathbf{R}^2_{001}$	
$\begin{pmatrix} 1 & 0 & 0 \\ 0 & \bar{1} & 0 \\ 0 & 0 & \bar{1} \end{pmatrix}$	$\begin{pmatrix} \bar{1} & 0 & 0 \\ 0 & 1 & 0 \\ 0 & 0 & \bar{1} \end{pmatrix}$	$\begin{pmatrix} \bar{1} & 0 & 0 \\ 0 & \bar{1} & 0 \\ 0 & 0 & 1 \end{pmatrix}$	
$\mathbf{R}^2_{110}$	$\mathbf{R}^2_{011}$	$\mathbf{R}^2_{101}$	
$\begin{pmatrix} 0 & 1 & 0 \\ 1 & 0 & 0 \\ 0 & 0 & \bar{1} \end{pmatrix}$	$\begin{pmatrix} \bar{1} & 0 & 0 \\ 0 & 0 & 1 \\ 0 & 1 & 0 \end{pmatrix}$	$\begin{pmatrix} 0 & 0 & 1 \\ 0 & \bar{1} & 0 \\ 1 & 0 & 0 \end{pmatrix}$	
$\mathbf{R}^2_{1\bar{1}0}$	$\mathbf{R}^2_{01\bar{1}}$	$\mathbf{R}^2_{10\bar{1}}$	
$\begin{pmatrix} 0 & \bar{1} & 0 \\ \bar{1} & 0 & 0 \\ 0 & 0 & \bar{1} \end{pmatrix}$	$\begin{pmatrix} \bar{1} & 0 & 0 \\ 0 & 0 & \bar{1} \\ 0 & \bar{1} & 0 \end{pmatrix}$	$\begin{pmatrix} 0 & 0 & \bar{1} \\ 0 & \bar{1} & 0 \\ \bar{1} & 0 & 0 \end{pmatrix}$	
$\mathbf{R}^3_{111}$	$\mathbf{R}^3_{1\bar{1}\bar{1}}$	$\mathbf{R}^3_{\bar{1}\bar{1}1}$	$\mathbf{R}^3_{\bar{1}1\bar{1}}$
$\begin{pmatrix} 0 & 0 & 1 \\ 1 & 0 & 0 \\ 0 & 1 & 0 \end{pmatrix}$	$\begin{pmatrix} 0 & 0 & \bar{1} \\ \bar{1} & 0 & 0 \\ 0 & 1 & 0 \end{pmatrix}$	$\begin{pmatrix} 0 & 0 & \bar{1} \\ 1 & 0 & 0 \\ 0 & \bar{1} & 0 \end{pmatrix}$	$\begin{pmatrix} 0 & 0 & 1 \\ \bar{1} & 0 & 0 \\ 0 & \bar{1} & 0 \end{pmatrix}$
$\mathbf{R}^{\bar{3}}_{111}$	$\mathbf{R}^{\bar{3}}_{1\bar{1}\bar{1}}$	$\mathbf{R}^{\bar{3}}_{\bar{1}\bar{1}1}$	$\mathbf{R}^{\bar{3}}_{\bar{1}1\bar{1}}$
$\begin{pmatrix} 0 & 1 & 0 \\ 0 & 0 & 1 \\ 1 & 0 & 0 \end{pmatrix}$	$\begin{pmatrix} 0 & \bar{1} & 0 \\ 0 & 0 & 1 \\ \bar{1} & 0 & 0 \end{pmatrix}$	$\begin{pmatrix} 0 & 1 & 0 \\ 0 & 0 & \bar{1} \\ \bar{1} & 0 & 0 \end{pmatrix}$	$\begin{pmatrix} 0 & \bar{1} & 0 \\ 0 & 0 & \bar{1} \\ 1 & 0 & 0 \end{pmatrix}$
$\mathbf{R}^4_{100}$	$\mathbf{R}^4_{010}$	$\mathbf{R}^4_{001}$	
$\begin{pmatrix} 1 & 0 & 0 \\ 0 & 0 & \bar{1} \\ 0 & 1 & 0 \end{pmatrix}$	$\begin{pmatrix} 0 & 0 & 1 \\ 0 & 1 & 0 \\ \bar{1} & 0 & 0 \end{pmatrix}$	$\begin{pmatrix} 0 & \bar{1} & 0 \\ 1 & 0 & 0 \\ 0 & 0 & 1 \end{pmatrix}$	
$\mathbf{R}^{\bar{4}}_{100}$	$\mathbf{R}^{\bar{4}}_{010}$	$\mathbf{R}^{\bar{4}}_{001}$	
$\begin{pmatrix} 1 & 0 & 0 \\ 0 & 0 & 1 \\ 0 & \bar{1} & 0 \end{pmatrix}$	$\begin{pmatrix} 0 & 0 & \bar{1} \\ 0 & 1 & 0 \\ 1 & 0 & 0 \end{pmatrix}$	$\begin{pmatrix} 0 & 1 & 0 \\ \bar{1} & 0 & 0 \\ 0 & 0 & 1 \end{pmatrix}$	

Table 3-4: The groups (G) of rotation matrices needed [12] for EPR simulations of point defects in diamond. $\mathbf{R}^n_{hkl}$ denotes a matrix for an n fold rotation about an axis with miller indices hkl. In each group the matrices listed in a column yield the same symmetry-related site. Therefore only one rotation matrix from each column is needed. The 24 rotation matrices are given in table 3-3.

G	**Required rotation matrices ($\mathbf{R}^n_{hkl}$)** *Choose one matrix from each column*					
1	System unchanged under all 24 rotation operations ∴ one matrix required					
3	$\mathbf{R}^1$	$\mathbf{R}^4_{100}$	$\mathbf{R}^4_{010}$			
	$\mathbf{R}^2_{001}$	$\mathbf{R}^{\bar{4}}_{100}$	$\mathbf{R}^{\bar{4}}_{010}$			
	$\mathbf{R}^4_{001}$	$\mathbf{R}^2_{011}$	$\mathbf{R}^2_{101}$			
	$\mathbf{R}^{\bar{4}}_{001}$	$\mathbf{R}^2_{01\bar{1}}$	$\mathbf{R}^2_{10\bar{1}}$			
	$\mathbf{R}^2_{100}$	$\mathbf{R}^{\bar{3}}_{111}$	$\mathbf{R}^3_{111}$			
	$\mathbf{R}^2_{010}$	$\mathbf{R}^{\bar{3}}_{1\bar{1}\bar{1}}$	$\mathbf{R}^3_{1\bar{1}\bar{1}}$			
	$\mathbf{R}^2_{110}$	$\mathbf{R}^{\bar{3}}_{\bar{1}1\bar{1}}$	$\mathbf{R}^3_{\bar{1}1\bar{1}}$			
	$\mathbf{R}^2_{1\bar{1}0}$	$\mathbf{R}^{\bar{3}}_{\bar{1}\bar{1}1}$	$\mathbf{R}^3_{\bar{1}\bar{1}1}$			
4	$\mathbf{R}^1$	$\mathbf{R}^2_{001}$	$\mathbf{R}^4_{001}$	$\mathbf{R}^{\bar{4}}_{001}$		
	$\mathbf{R}^2_{1\bar{1}0}$	$\mathbf{R}^4_{100}$	$\mathbf{R}^2_{100}$	$\mathbf{R}^4_{100}$		
	$\mathbf{R}^2_{10\bar{1}}$	$\mathbf{R}^4_{010}$	$\mathbf{R}^{\bar{4}}_{010}$	$\mathbf{R}^2_{010}$		
	$\mathbf{R}^2_{0\bar{1}\bar{1}}$	$\mathbf{R}^2_{110}$	$\mathbf{R}^2_{011}$	$\mathbf{R}^2_{101}$		
	$\mathbf{R}^3_{111}$	$\mathbf{R}^3_{1\bar{1}\bar{1}}$	$\mathbf{R}^3_{\bar{1}1\bar{1}}$	$\mathbf{R}^{\bar{3}}_{1\bar{1}\bar{1}}$		
	$\mathbf{R}^{\bar{3}}_{111}$	$\mathbf{R}^{\bar{3}}_{\bar{1}1\bar{1}}$	$\mathbf{R}^{\bar{3}}_{\bar{1}\bar{1}1}$	$\mathbf{R}^3_{\bar{1}\bar{1}1}$		
6a	$\mathbf{R}^1$	$\mathbf{R}^4_{001}$	$\mathbf{R}^4_{100}$	$\mathbf{R}^4_{010}$	$\mathbf{R}^3_{111}$	$\mathbf{R}^{\bar{3}}_{111}$
	$\mathbf{R}^2_{001}$	$\mathbf{R}^{\bar{4}}_{001}$	$\mathbf{R}^{\bar{4}}_{100}$	$\mathbf{R}^{\bar{4}}_{010}$	$\mathbf{R}^3_{1\bar{1}\bar{1}}$	$\mathbf{R}^{\bar{3}}_{1\bar{1}\bar{1}}$
	$\mathbf{R}^2_{100}$	$\mathbf{R}^2_{110}$	$\mathbf{R}^2_{011}$	$\mathbf{R}^2_{101}$	$\mathbf{R}^3_{\bar{1}1\bar{1}}$	$\mathbf{R}^{\bar{3}}_{\bar{1}1\bar{1}}$
	$\mathbf{R}^2_{010}$	$\mathbf{R}^2_{01\bar{1}}$	$\mathbf{R}^2_{01\bar{1}}$	$\mathbf{R}^2_{10\bar{1}}$	$\mathbf{R}^3_{\bar{1}\bar{1}1}$	$\mathbf{R}^{\bar{3}}_{\bar{1}\bar{1}1}$
6b	$\mathbf{R}^1$	$\mathbf{R}^4_{001}$	$\mathbf{R}^4_{100}$	$\mathbf{R}^{\bar{4}}_{100}$	$\mathbf{R}^4_{010}$	$\mathbf{R}^{\bar{4}}_{010}$
	$\mathbf{R}^2_{001}$	$\mathbf{R}^{\bar{4}}_{001}$	$\mathbf{R}^2_{01\bar{1}}$	$\mathbf{R}^2_{011}$	$\mathbf{R}^2_{101}$	$\mathbf{R}^2_{10\bar{1}}$
	$\mathbf{R}^2_{110}$	$\mathbf{R}^2_{100}$	$\mathbf{R}^{\bar{3}}_{111}$	$\mathbf{R}^{\bar{3}}_{\bar{1}1\bar{1}}$	$\mathbf{R}^3_{1\bar{1}\bar{1}}$	$\mathbf{R}^3_{111}$
	$\mathbf{R}^2_{1\bar{1}0}$	$\mathbf{R}^2_{010}$	$\mathbf{R}^{\bar{3}}_{1\bar{1}\bar{1}}$	$\mathbf{R}^{\bar{3}}_{\bar{1}\bar{1}1}$	$\mathbf{R}^3_{\bar{1}\bar{1}1}$	$\mathbf{R}^3_{\bar{1}1\bar{1}}$
12a	$\mathbf{R}^1$	$\mathbf{R}^4_{001}$	$\mathbf{R}^2_{100}$	$\mathbf{R}^4_{100}$	$\mathbf{R}^2_{011}$	$\mathbf{R}^4_{010}$	$\mathbf{R}^2_{101}$	$\mathbf{R}^2_{110}$	$\mathbf{R}^3_{111}$	$\mathbf{R}^{\bar{3}}_{111}$	$\mathbf{R}^3_{1\bar{1}\bar{1}}$	$\mathbf{R}^{\bar{3}}_{1\bar{1}\bar{1}}$
	$\mathbf{R}^2_{001}$	$\mathbf{R}^{\bar{4}}_{001}$	$\mathbf{R}^2_{010}$	$\mathbf{R}^{\bar{4}}_{100}$	$\mathbf{R}^2_{01\bar{1}}$	$\mathbf{R}^{\bar{4}}_{010}$	$\mathbf{R}^2_{10\bar{1}}$	$\mathbf{R}^2_{1\bar{1}0}$	$\mathbf{R}^3_{\bar{1}1\bar{1}}$	$\mathbf{R}^{\bar{3}}_{1\bar{1}\bar{1}}$	$\mathbf{R}^3_{\bar{1}\bar{1}1}$	$\mathbf{R}^{\bar{3}}_{\bar{1}\bar{1}1}$
12b	$\mathbf{R}^1$	$\mathbf{R}^2_{001}$	$\mathbf{R}^4_{001}$	$\mathbf{R}^{\bar{4}}_{001}$	$\mathbf{R}^4_{100}$	$\mathbf{R}^{\bar{4}}_{100}$	$\mathbf{R}^4_{010}$	$\mathbf{R}^{\bar{4}}_{010}$	$\mathbf{R}^2_{101}$	$\mathbf{R}^2_{10\bar{1}}$	$\mathbf{R}^2_{011}$	$\mathbf{R}^2_{01\bar{1}}$
	$\mathbf{R}^2_{1\bar{1}0}$	$\mathbf{R}^2_{110}$	$\mathbf{R}^2_{100}$	$\mathbf{R}^2_{010}$	$\mathbf{R}^{\bar{3}}_{1\bar{1}\bar{1}}$	$\mathbf{R}^{\bar{3}}_{\bar{1}1\bar{1}}$	$\mathbf{R}^3_{1\bar{1}\bar{1}}$	$\mathbf{R}^3_{\bar{1}1\bar{1}}$	$\mathbf{R}^3_{\bar{1}\bar{1}1}$	$\mathbf{R}^3_{111}$	$\mathbf{R}^{\bar{3}}_{\bar{1}\bar{1}1}$	$\mathbf{R}^{\bar{3}}_{111}$
24	All 24 rotation matrices required					

References

[1] J. A. Weil, J. R. Bolton, and J. E. Wertz, *Electron Paramagnetic Resonance* (Wiley-Interscience, New York, 1994).

[2] A. Abragam and B. Bleaney, *Electron Paramagnetic Resonance of Transition Ions* (Oxford University Press, 1970).

[3] G. K. Woodgate, *Elementary atomic structure* (OUP, Oxford, 1980).

[4] D. Twitchen, D. Phil. thesis, University of Oxford (1997).

[5] A. M. Stoneham, *Theory of defects in solids* (Clarendon Press, Oxford, 1975).

[6] D. Hunt, D. Phil. thesis, University of Oxford (1999).

[7] J. R. Morton and K. F. Preston, J. Magn. Reson. **30**, 577 (1978).

[8] J. M. Baker and M. E. Newton, Appl. Magn. Reson. **7**, 209 (1994).

[9] D. R. Lide, *CRC handbook of chemistry and physics* (CRC Press, Boca Raton, FL, 2006), 87th ed.

[10] W. V. Smith, P. P. Sorokin, I. L. Gelles, and G. J. Lasher, Phys. Rev. **115**, 1546 (1959).

[11] A. Cox, D. Phil. thesis, University of Oxford (1993).

[12] J. A. Weil, T. Buch, and J. E. Clapp, Adv. Magn. Reson. **6**, 183 (1973).

Chapter 4

Experimental details

Electron paramagnetic resonance (EPR) is the main experimental technique which has been utilised for the studies reported in this thesis. After a discussion of the general experimental principles of the EPR technique this chapter will provide a review of the specific experimental setups used on the EPR spectrometers employed in this work.

4.1 General EPR principles

A diagram of a continuous wave EPR spectrometer, representative of those used in this thesis, is shown in figure 4-1. This can be separated out into different sections; the magnetic system, the microwave source and control equipment and the elements responsible for resonance detection.

4.1.1 The magnetic field

The usual source of the static magnetic field in an EPR spectrometer is an iron-core electromagnet, due to the requirement for the magnetic field to be stable and uniform over the sample volume. To acquire a spectrum the magnetic field must be reproducibly scanned over a range of magnetic fields (to average in signals), without the absolute magnetic field drifting over time. The dependence of the magnetic field with the current applied of an iron-core magnet is inherently non-linear and subject to hysteresis, hence measurement and control via a feedback loop is required. This is achieved using a temperature stabilised Hall probe, connected to a magnetic field controller, which is responsible for controlling the current supplied to the magnet. The Hall probe does not provide an absolute field measurement (hence the field controller must be calibrated), but by maintaining a

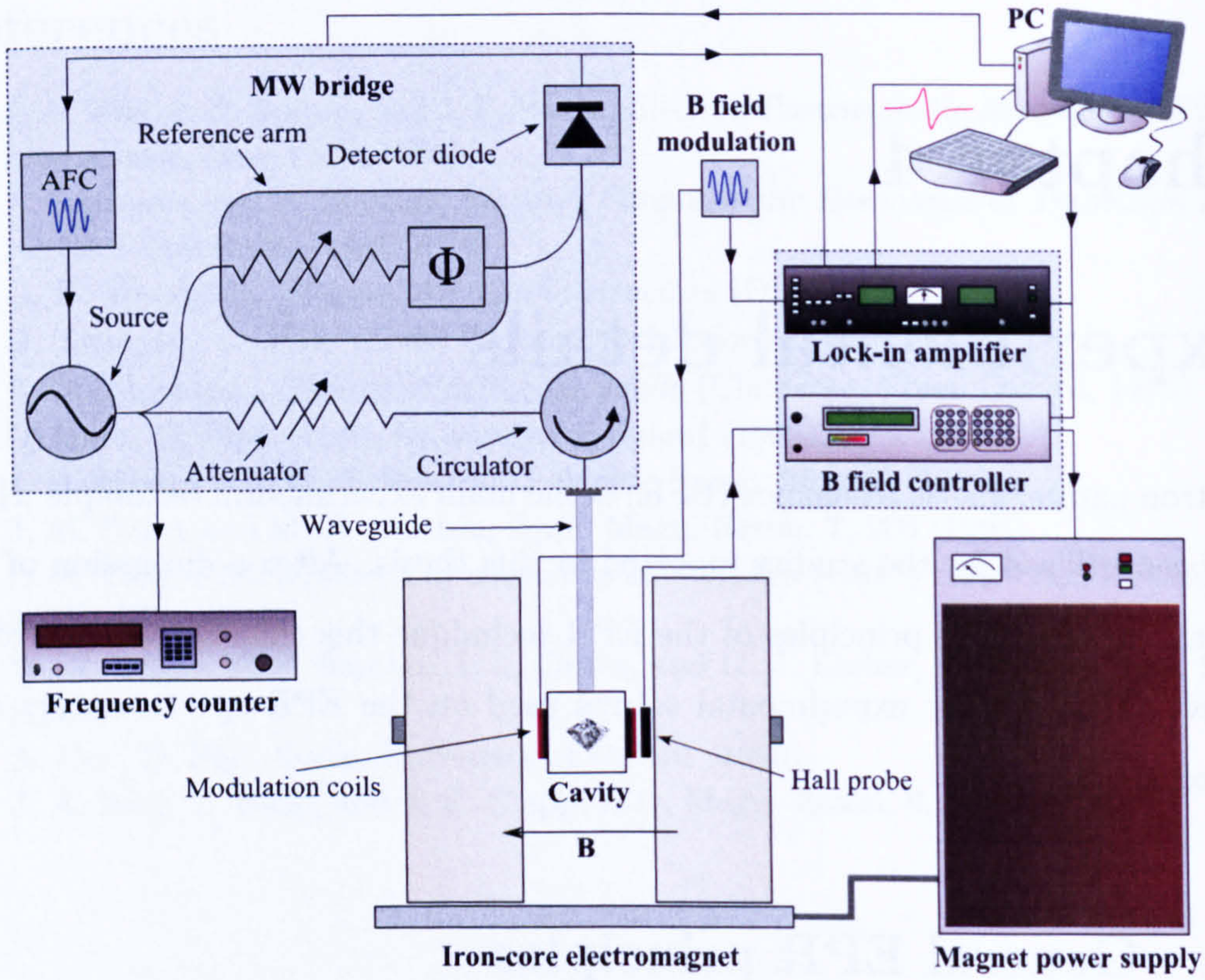

Figure 4-1: Block diagram of an EPR spectrometer, representative of those used in this thesis, including a detailed view of the components in the microwave bridge. The microwave bridge section of the figure is adapted from an illustration provided by Bruker [1].

constant Hall probe voltage at the centre of the scan range the magnetic field can be held constant over a long period of time. The field controller is also responsible for providing a linear scan of the magnetic field around the centre-field.

4.1.2 Microwave source and cavity

In the EPR spectrometers used in this thesis the microwave radiation is provided by a Gunn diode. Microwave sources are classed in *bands*, depending on the frequency of the microwave source. Frequencies between 8–12 GHz are designated as X-band, whilst frequencies between 30–50 GHz fall in the Q-band range. Both these frequency bands are utilised in this work, as comparison between X-band and Q-band spectra can aid in the observation and identification of EPR resonance lines:

- Any line splitting due to g anisotropy (§3.4.1) will be different between

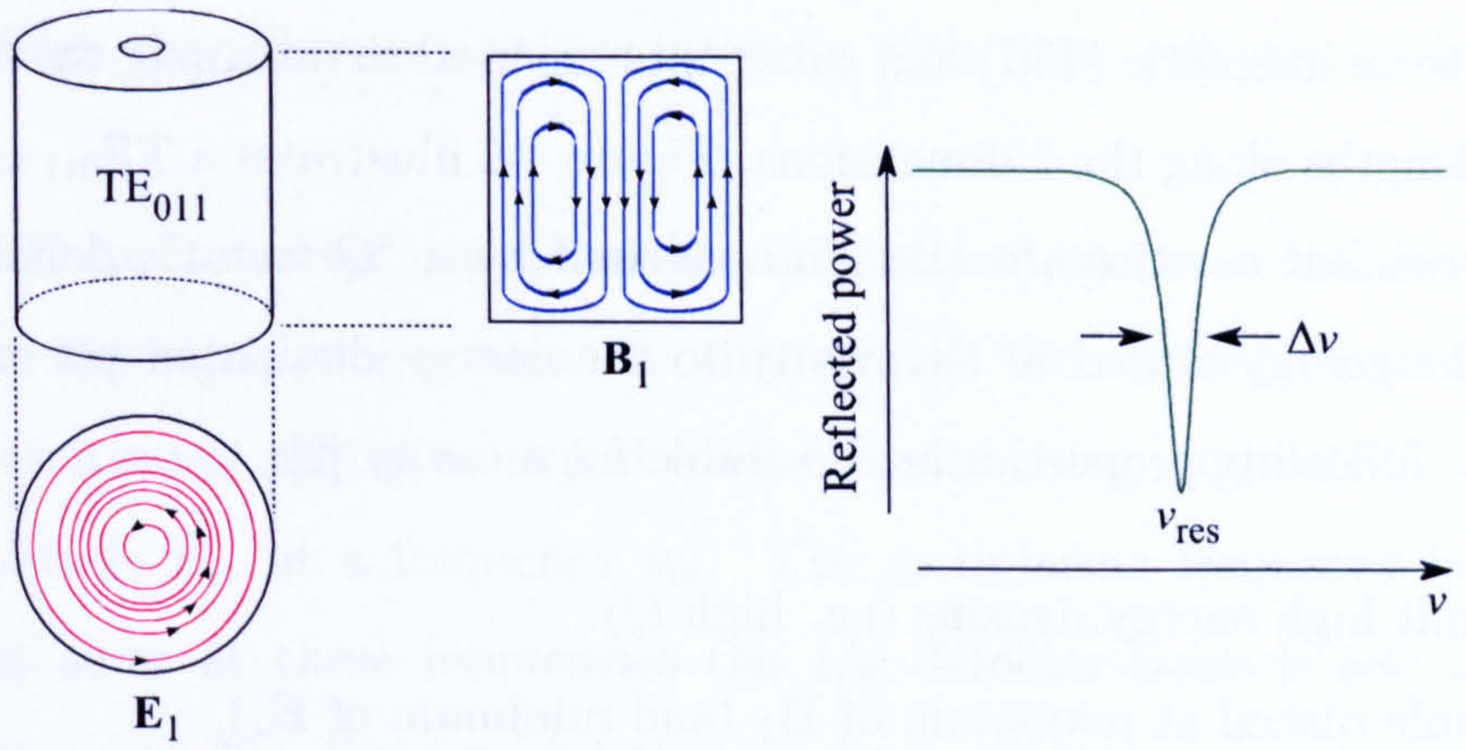

Figure 4-2: Cylindrical TE_{011} mode cavity showing the electric and magnetic fields ($\mathbf{E}_1$ and $\mathbf{B}_1$) respectively. The figure on the right illustrates the observed resonance mode, seen by sweeping the frequency of the microwaves around the centre frequency of the mode (ν_{res}).

the two frequency bands whilst, to first-order, hyperfine splitting (A) terms are frequency-independent (§3.4.3). Thus splittings from g and A can be distinguished by comparing spectra acquired at both frequencies.

- Spectra from defects with slightly different g values will be further separated in field as the frequency is increased and hence may be more easily resolved.
- The intensity of forbidden hyperfine transitions (§3.5) is dependent on the relative size of the hyperfine and nuclear Zeeman interactions. Since the latter depends on the magnetic field, variations in the intensity in these transitions may be observed between different frequency bands.

In commercial EPR spectrometers, such as the Bruker X-band systems used (see §4.2), the microwave source is housed in the microwave bridge. Figure 4-1 provides a illustration of the main components within the bridge. Starting from the microwave source the microwaves are fed into an attenuator which permits the microwave intensity (i.e. $|\mathbf{B}_1|^2$) to be varied. The attenuated output of the bridge passes through the circulator and is then transported by a waveguide to the cavity.

The sample itself is held in a *resonant cavity*, which is used to amplify signals by increasing the energy density at the sample. An EPR cavity is named dependent on the mode that it supports; these are referred to as transverse electric (TE)

and transverse magnetic (TM) and subscripts are used to designate the number of half wavelengths along the 3 dimensions. Figure 4-2 illustrates a TE_{011} cylindrical cavity. Resonant cavities are also characterised by a "Q-factor", defined as the ratio of the energy stored in the cavity to the energy dissipated per microwave cycle. The following properties are desirable for a cavity [2]:

1. Permit high energy density (i.e. high Q).
2. Sample placed at maximum of $\mathbf{B}_1$ (and minimum of $\mathbf{E}_1$).
3. Have $\mathbf{B}_1$ perpendicular to applied magnetic field, $\mathbf{B}$ (§3.5).

Imperfect coupling of the waveguide and the cavity (which results from different impedances) causes the reflection of some fraction of the incident energy. The principle of an EPR experiment is that the detector receives reflected microwave power from the cavity when the sample is at a resonant field, due to the absorption of energy by the sample and a change in the loaded Q-factor or the cavity. It is therefore important to mitigate any sources of reflected power when off resonance. The impedances can be matched by adjusting the size of the iris which is present at the boundary between waveguide and cavity; in this state the system is said to be *critically coupled.*

The frequency of the microwave source needs to match the resonant frequency of the cavity (ν_{res} in figure 4-2) to remain coupled. To avoid drifting away from the centre frequency of the cavity an automatic-frequency control (AFC) system is used, which employs a feedback loop to lock ν around the minimum of the resonance mode. Any drift of the frequency will produce noise in the spectrum and line broadening, hence it is important for the AFC to hold the frequency as stable as possible.

4.1.3 Detection

When at resonance, the reflected microwaves return to the bridge, where the circulator directs the reflected power to the detector diode. For optimal sensitivity and to enter the linear range of the detector (required for quantitative measurements) [1] a reference arm is used to bias the detector with ~ 1 mW of the source microwave power [2]. A phase shifter is therefore required to ensure that the mi-

crowaves from the reference arm are in phase with those reflected back from the cavity.

An EPR spectrometer uses phase-sensitive detection (by a lock-in amplifier) to enhance the signal/noise ratio. In this scheme the applied magnetic field is not just being swept during an experiment, it is also being modulated sinusoidally with amplitude B_{m} at a frequency ν_{m}. The modulation frequency is typically ~ 100 kHz, since at these frequencies the $1/\nu$ detector noise is less than from other sources (see [3]). Field modulation results in the microwave detector output having a component at frequency ν_{m} whose amplitude is proportional to that of the slope of the resonance line at any given point (see figure 4-3); the transfer of modulation from the field to the microwave detector output only occurs at resonance. Hence by comparing the modulated signal with a reference signal having frequency ν_{m} components with different frequencies and phases can be reduced and time-constant filtering can be used to further suppress noise. This necessitates the ability to vary the phase of the reference signal relative to that of the output from the detector diode.

If B_{m} is small compared to the intrinsic linewidth of the resonance line the resulting lineshape can be approximated as the first derivative of the resonance lineshape. However, as illustrated in figure 4-3, higher modulations result in the signal becoming distorted.

4.2 The Bruker EPR spectrometers

In this thesis two commercial Bruker spectrometers were used for X-band measurements; an EMX and EMX-E system. Both these systems permit different microwave bridges and cavities to be used, depending on the type of EPR experiment conducted (discussed in the following sections). Although the magnet on the EMX system (B-E 25) allows fields of up to 1.8 T to be reached this system was only used with an X-band bridge. The EMX-E system employs a smaller magnet (ER070) which is only capable of fields of up to 0.64 T. Both systems use a field modulation frequency of 100 kHz.

The Bruker microwave bridges used have an X-band Gunn diode source with

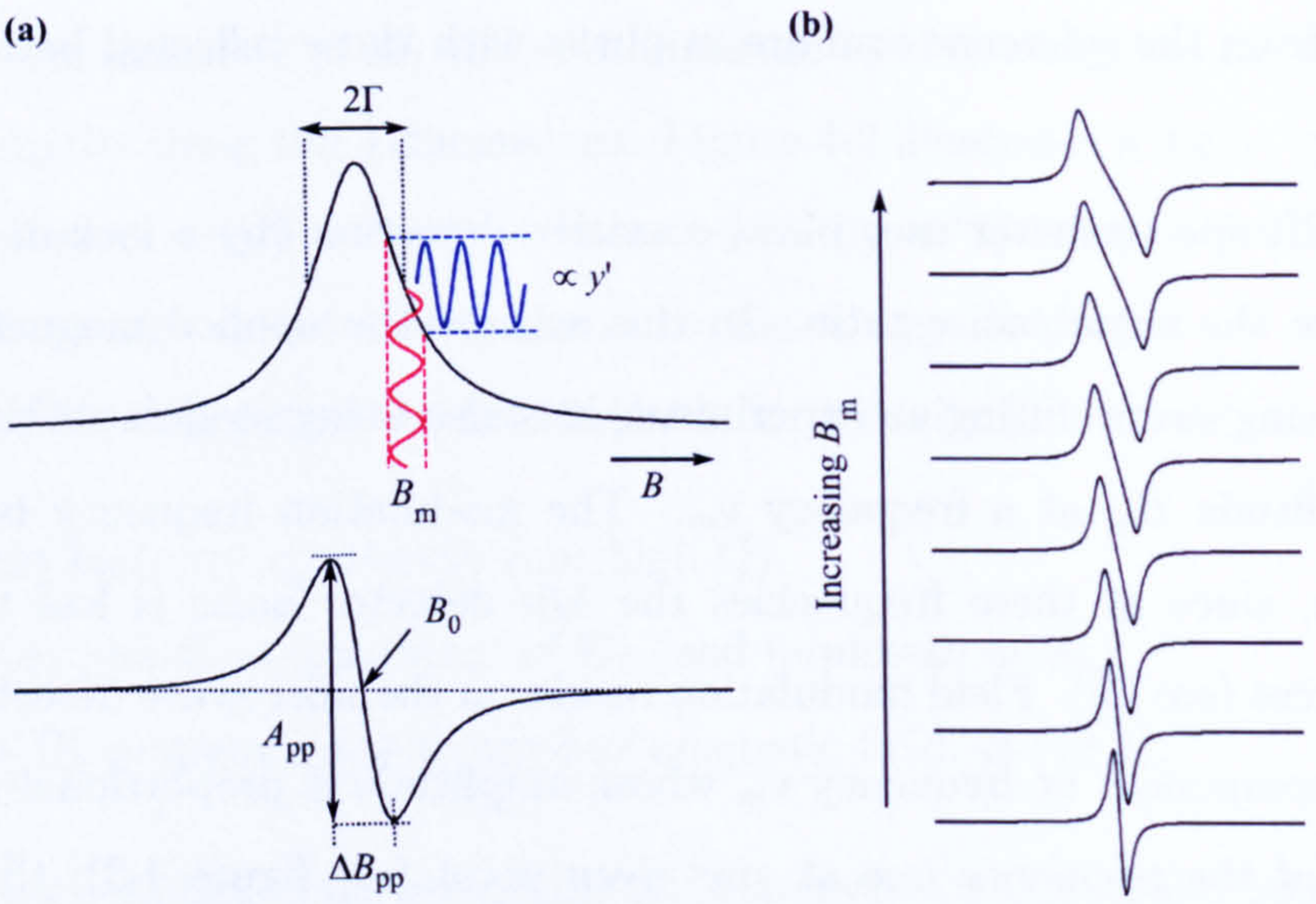

Figure 4-3: (a) Resonant microwave absorption and the corresponding derivative EPR signal detected with a lock-in amplifier using magnetic field modulation. (b) The distortion that occurs as the modulation amplitude (B_m) approaches and exceeds that of the intrinsic linewidth (defined by the half-width at half-maximum, Γ).

a levelled power of 200 mW. For the EMX system a Bruker ER041XG bridge was used for all measurements, which has a maximum attenuation of 60 dB, hence allowing microwave powers of 2×10^{-4}–200 mW to be used. The same model of bridge was used for most measurements on the EMX-E system, but when microwave saturation was a problem even at 2×10^{-4} mW a 90 dB bridge (ER041XG-H) was used. This permitted EPR measurements to be taken at microwave powers as low as 0.2 nW.

On both systems the frequency could be monitored by attaching an EIP-545A microwave frequency counter. By logging the frequency (§4.4.1) during long EPR scans (~ 24 hours) it could be seen that the variation in the frequency over such timescale is typically less than 150 kHz, equivalent to a magnetic field drift of < 0.05 G [4].

The EMX system has been used with three different cavities; a Bruker super-high Q (SHQ) ER4122 spherical (TE_{011}) cavity, a Bruker ER4105DR (TE_{104}) rectangular cavity and an EX-102 cylindrical cavity (TE_{011}) manufactured by the Technical University of Wroclaw (Poland). A cylindrical ER4119HS (TE_{011}) cavity was the only bridge to be used on the EMX-E system.

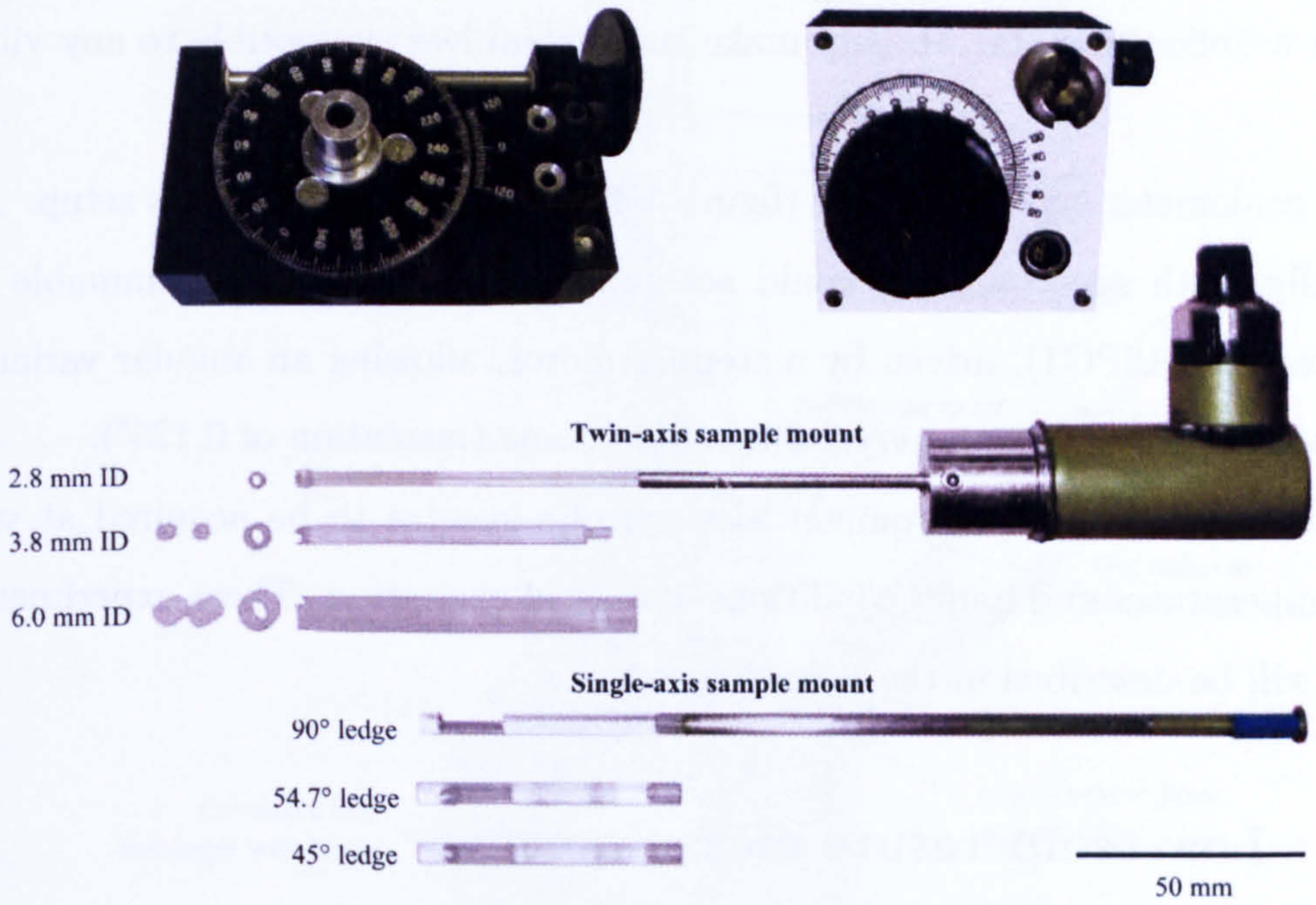

Figure 4-4: The goniometers and sample mounts used in EPR experiments.

To orient a sample within the cavities a collection of single and twin-axis mounts, which could be used on either the Oxford instruments or Bruker goniometers, have been produced (see figure 4-4). The single-axis mounts consist of a german silver and brass rod with a detachable 5 mm diameter Rexalite end-piece with a ledge for the sample (held using vacuum grease). A variety of end pieces with ledges at different angles were made to enable samples to be oriented in different planes. The twin-axis mounts consist of a Rexalite[1] rod and a wheel with a thin piece of cotton, wrapped around the wheel twice, such that samples could be rotated through all azimuthal and polar angles. Three different sized wheels are used, with inner diameters (ID) of 2.8 mm, 3.8 mm and 6.0 mm. For larger samples the single-axis mounts had to be used.

4.2.1 Room-temperature measurements

Room-temperature X-band measurements were conducted using either the EMX system equipped with the ER4122 SHQ cavity or the EMX-E system combined

[1]Rexalite is the trade name for cross linked polystyrene material which has low piezoelectric loss.

with the ER4119HS cavity. In both these configurations the goniometer rests against a Teflon pedestal, to help make the system less susceptible to any vibrations.

All goniometer types and sizes (figure 4-4) are supported with this setup. Additionally, both spectrometers could accommodate a Bruker programmable goniometer (ER218PG1), driven by a stepper motor, allowing an angular variation to be performed in a chosen crystallographic plane (resolution of 0.125°).

The Bruker EMX spectrometer also permits spectra to be acquired at variable temperatures and under conditions of optical excitation. These experimental setups will be described in the following sections.

4.2.2 Low-temperature measurements

Low-temperature measurements (4–300 K) were performed using an Oxford Instruments ESR-900 continuous flow cryostat (figure 4-5) with the Bruker ER4105DR rectangular cavity.

In this system a helium flow from a dewar is drawn through an evacuated Oxford Instruments GFS300 flexible transfer tube. This is fed through a capillary in the cryostat and is delivered directly onto the sample, which is positioned in centre of the EPR cavity. In the region of the cavity the gas is contained within a double walled, high purity quartz tube which is vacuum insulated. The gas is returned back along the transfer tube to shield the incoming helium. For maintaining and controlling the gas flow a small pump is used along with a Oxford Instruments VC30 controller. The flow-rate may be controlled using a needle valve on the transfer tube and by throttling the pump.

To allow the temperature to be varied the cryostat contains a wire wound heater and a gold-iron/chromel thermocouple which is positioned at the end of the feed capillary. An Oxford Instruments ITC503 temperature controller is used to permit the temperature to be measured (using a liquid nitrogen reference), and controlled by varying the current supplied to the heater. The temperature of the system can be logged whilst collecting an EPR spectrum using home-developed software (see §4.4.1).

In cases where optical illumination was not required (§4.2.4) twin or single-

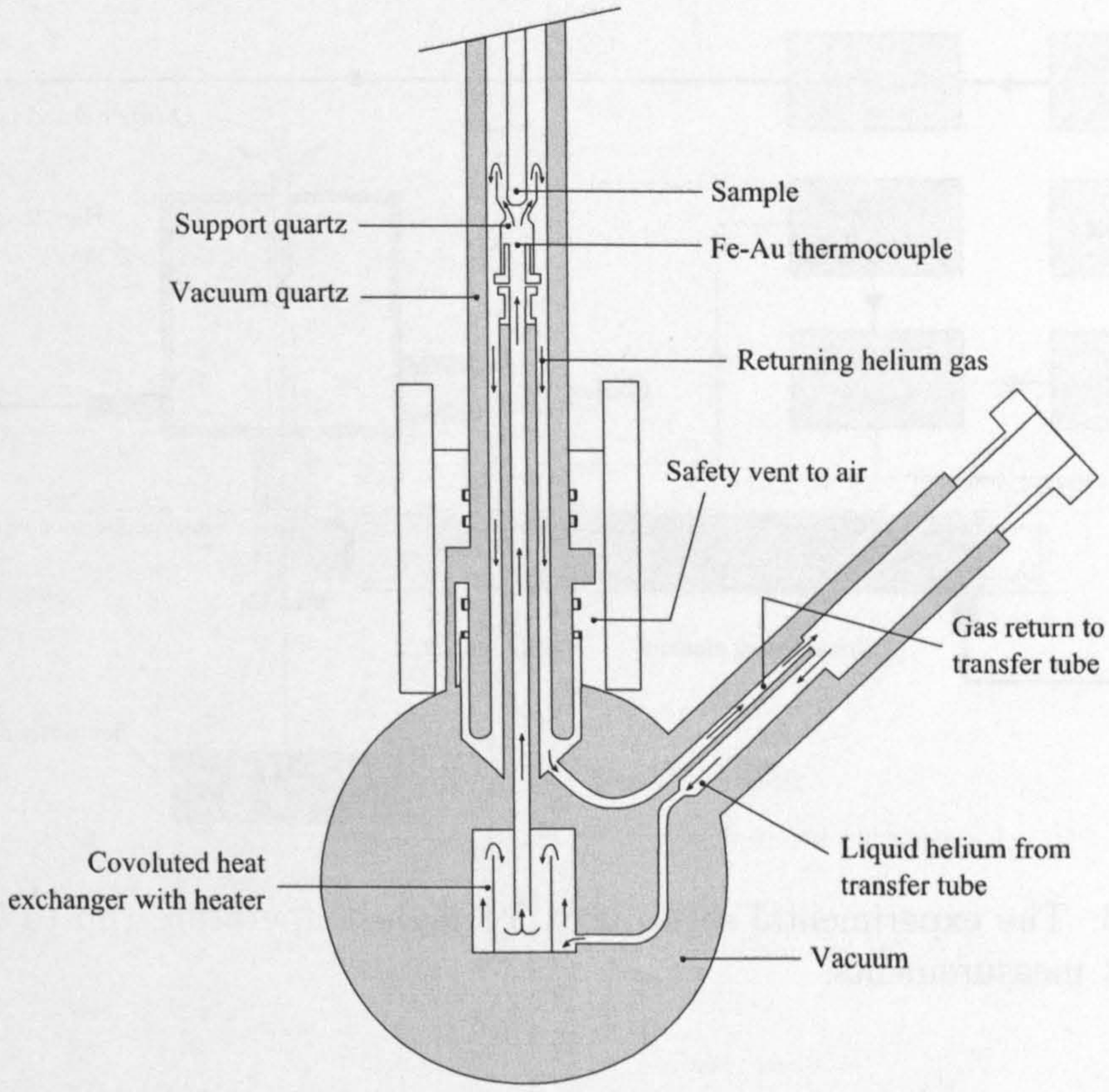

Figure 4-5: The Oxford instruments ESR-900 continuous flow cryostat used for low-temperature EPR measurements.

axis goniometers could be used, as described in §4.2. However, the quartz dewar within the cryostat only accommodates a rod (and sample) of diameters up to 5 mm, hence only the smallest of the twin-axis mounts could be used.

4.2.3 High-temperature measurements

High-temperature measurements (300–750 K) can be performed on the EMX spectrometer using the EX-102 high-temperature cavity and the experimental setup shown in figure 4-6.

The sample temperature is raised by means of a nitrogen flow that is heated by passing it through a transfer dewar containing an Inconel wire heater (Wilmad part numbers WG-836-A and WG-838-A, respectively). The temperature of the sample is monitored by a K-type thermocouple (using an ice-water reference), which is connected to a PID temperature controller. This permits the power delivered by

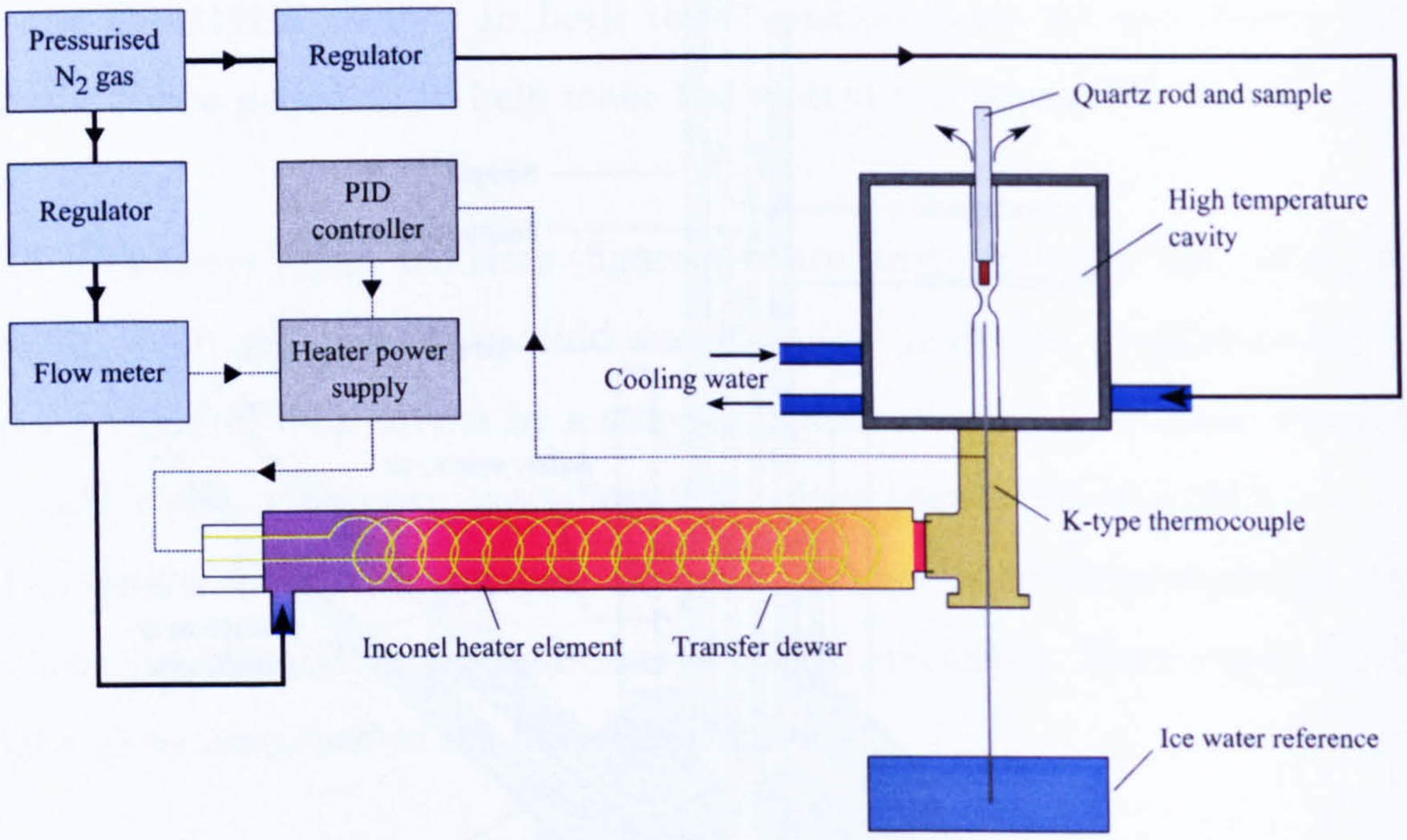

Figure 4-6: The experimental setup used for high-temperature (up to 750 K) X-band EPR measurements.

the heater power supply[2] to be regulated to maintain the desired temperature. The flow rate of nitrogen past the heating element is typically 10–15 l/min and the power supply is designed to cut the power in the event of low flow, to preserve the element. The temperature of the cavity is stabilised by passing cold water through its walls.

To use the PID temperature controller the relationship between the set bias level and the temperature of the sample needed to be determined. This calibration was achieved by introducing a second thermocouple to the sample sample and the results are shown in figure 4-7.

4.2.4 Optically excited EPR

The Bruker ER4105DR rectangular cavity was used for the optically excited EPR measurements presented in this thesis. The optical illumination was provided by a 200 W high pressure Hg-Xe arc-lamp, which was contained within a Spectral Energy LH150 lamp housing and powered by a LPS251SR power supply unit. The lamp housing has a lens which allows the beam to be collimated. Glass long-

[2]built by P Hirst, Clarendon Laboratory

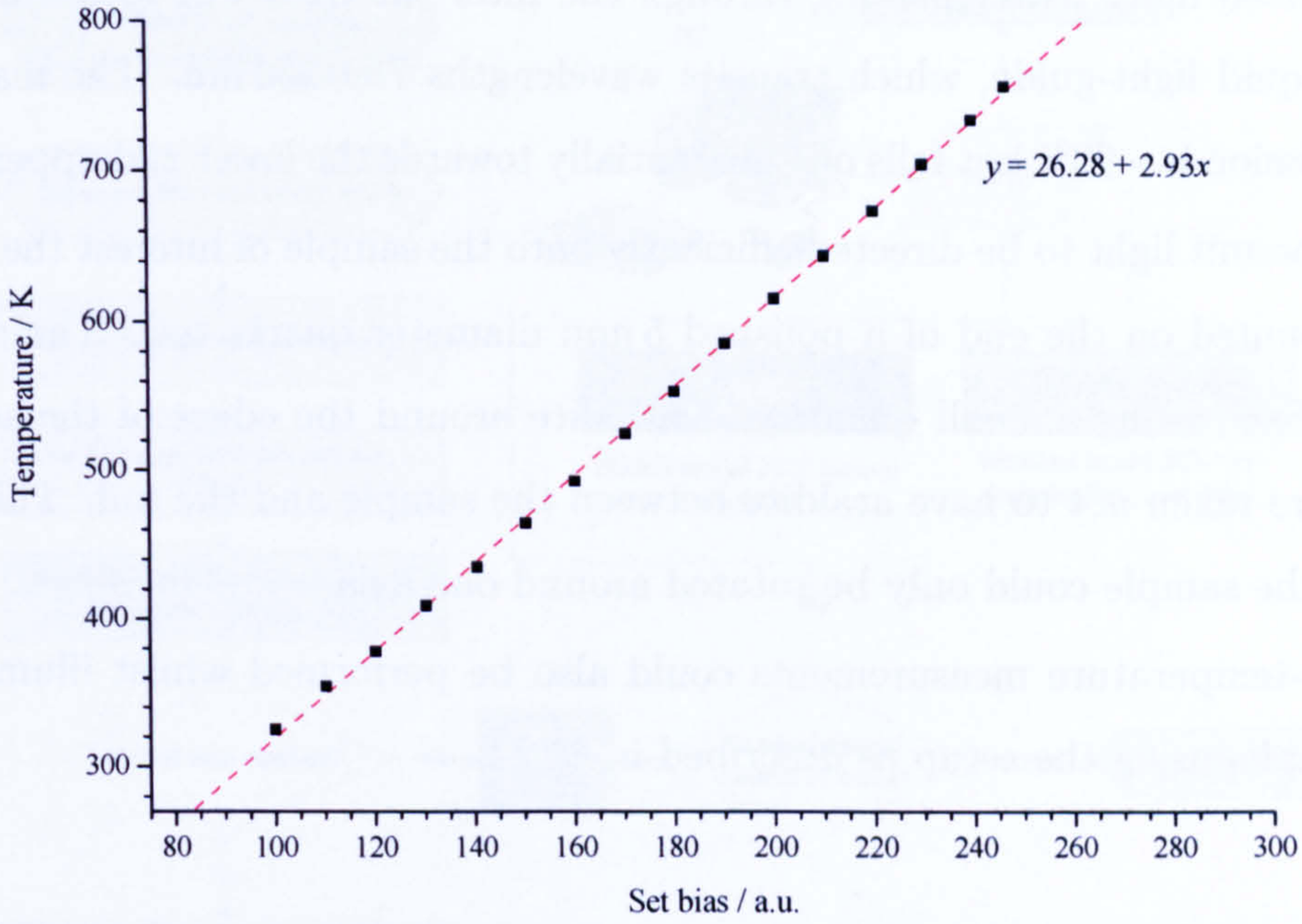

Figure 4-7: Measured temperature against bias set on the PID temperature controller.

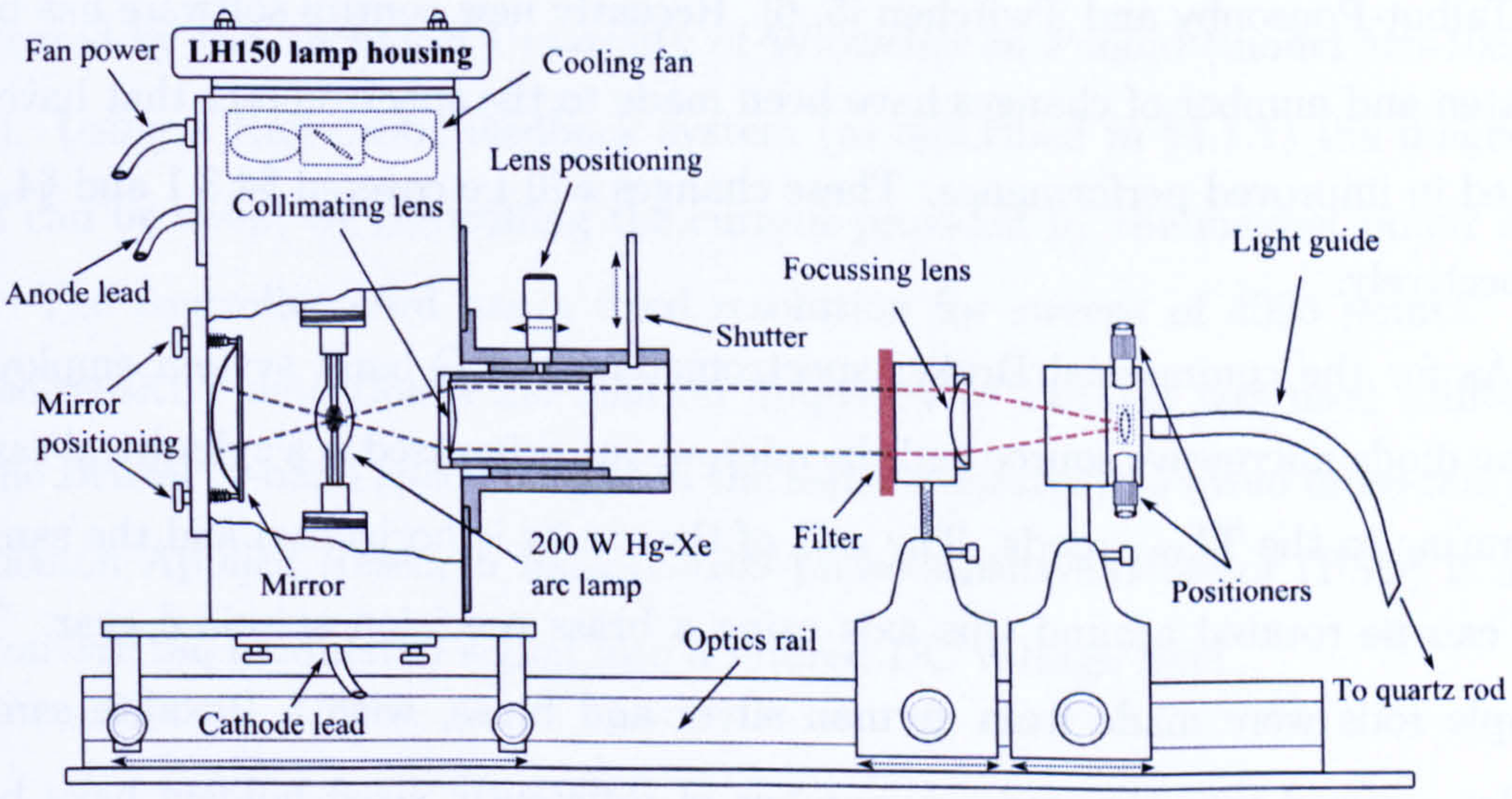

Figure 4-8: The experimental setup used for optically excited EPR, including a detailed view of the Spectral Energy LH150 lamp housing.

pass filters (cooled by a fan) could then be used to vary the energy cut-off of the transmitted light. After passing through the filter the light was focussed onto a 0.5 m liquid light-guide, which transits wavelengths 750–250 nm. The maximum transmission is ~ 90% but falls off substantially towards the lower and upper limits.

To permit light to be directed efficiently onto the sample of interest the sample was mounted on the end of a polished 5 mm diameter quartz rod. The samples were affixed using a small quantity of araldite around the edges of the samples, with care taken not to have araldite between the sample and the rod. This setup meant the sample could only be rotated around one axis.

Low-temperature measurements could also be performed whilst illuminating the sample, using the setup as described in §4.2.2.

4.3 The Q-band EPR spectrometer

Q-band EPR measurements have been obtained using a home-built EPR spectrometer, which was originally constructed at the Clarendon Laboratory under EPSRC funding (grant number GR/H33053) and subsequently relocated at Warwick. A thorough description of the spectrometer can be found in the PhD theses by Talbot-Ponsonby and Twitchen [5, 6]. Recently new control software has been written and number of changes have been made to the spectrometer that have resulted in improved performance. These changes will be covered §4.3.1 and §4.3.2, respectively.

As for the commercial Bruker spectrometers, the Q-band system employs a Gunn diode microwave source and the microwave cavity used is a cylindrical cavity operating in the TE_{011} mode. The axis of the cavity is horizontal and the sample rod can be rotated around this axis using a brass precision spiroidal gear. The sample rods were made from german silver and brass, with a Rexalite sample holder screwed into the end. A number of differently sized holders have been constructed, with both ledges and slits, to permit differently sized samples to be accommodated (held in place using vacuum grease). The applied magnetic field can also be rotated by ~ ±5°, by rotating the magnet on its base.

For the control of the applied magnetic field a magnetic field controller man-

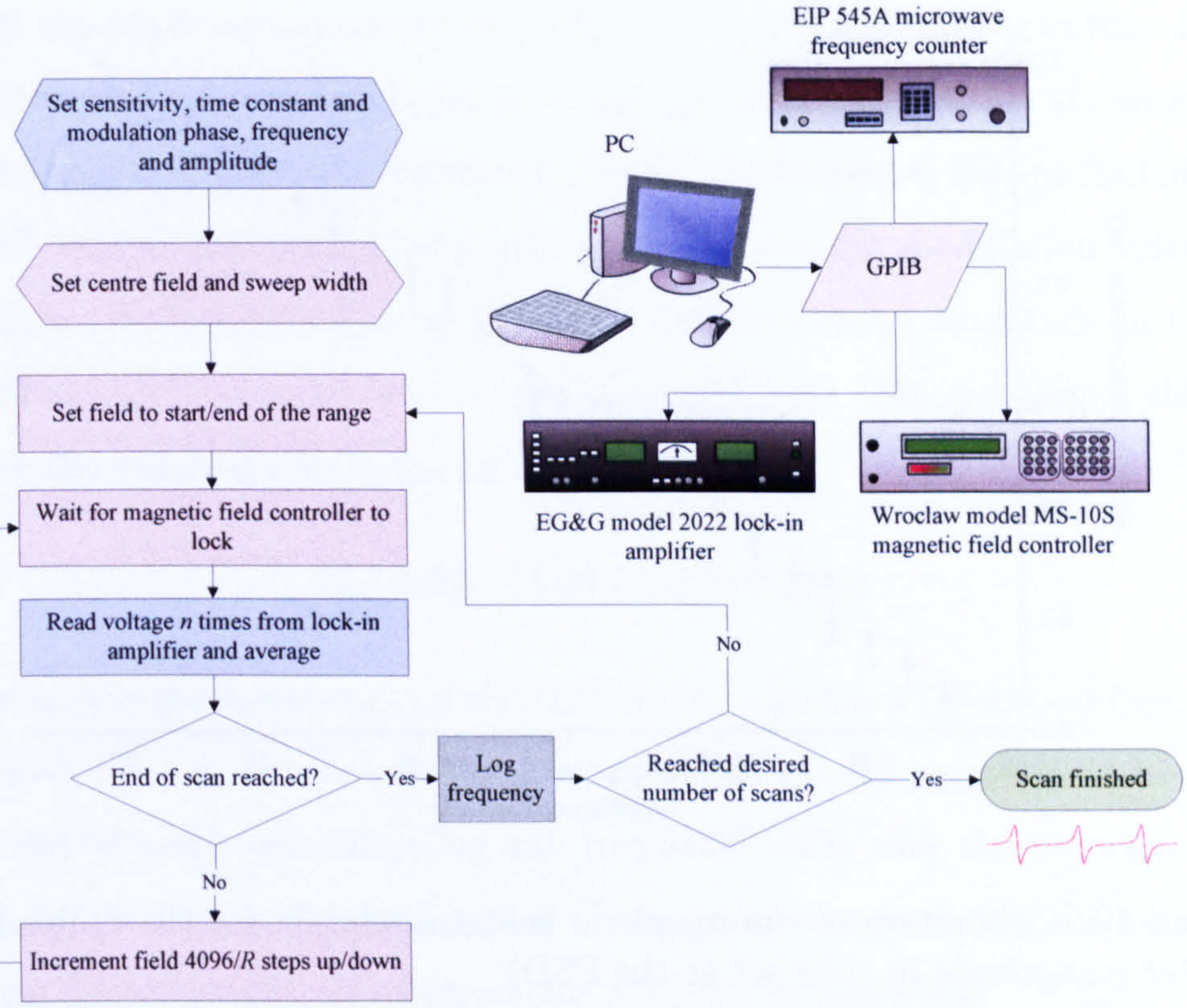

Figure 4-9: Procedure used to collect an EPR spectrum from the Q-band spectrometer. R is the number of points in the scan, which can be 512, 1024, 2048 or 4096. The number of averages (n) of the DC voltage from the lock-in amplifier at each field position is set by the user via the conversion time.

ufactured by the Technical University of Wrowclaw in Poland (model MS-10S) is used. Using a Hall probe feedback system (as described in §4.1.1) the magnetic field can be swept by controlling the current provided by the magnet power supply. The controller used has a fixed resolution for sweeps of 4096 points. For phase-sensitive detection a modulation frequency of 115 kHz was used (different to the Bruker X-band spectrometer in the same laboratory to avoid cross-talk). A Princeton Applied Research EG&G 5209 phase-sensitive detector (PSD) is used to convert the modulated signal into a filtered DC voltage level.

4.3.1 New control software

Both the magnetic field controller and lock-in amplifier both have General Purpose Interface Bus (GPIB/IEEE 488.1) ports. When set up on different channels the interface on each device can be written to and read from by a single interface card

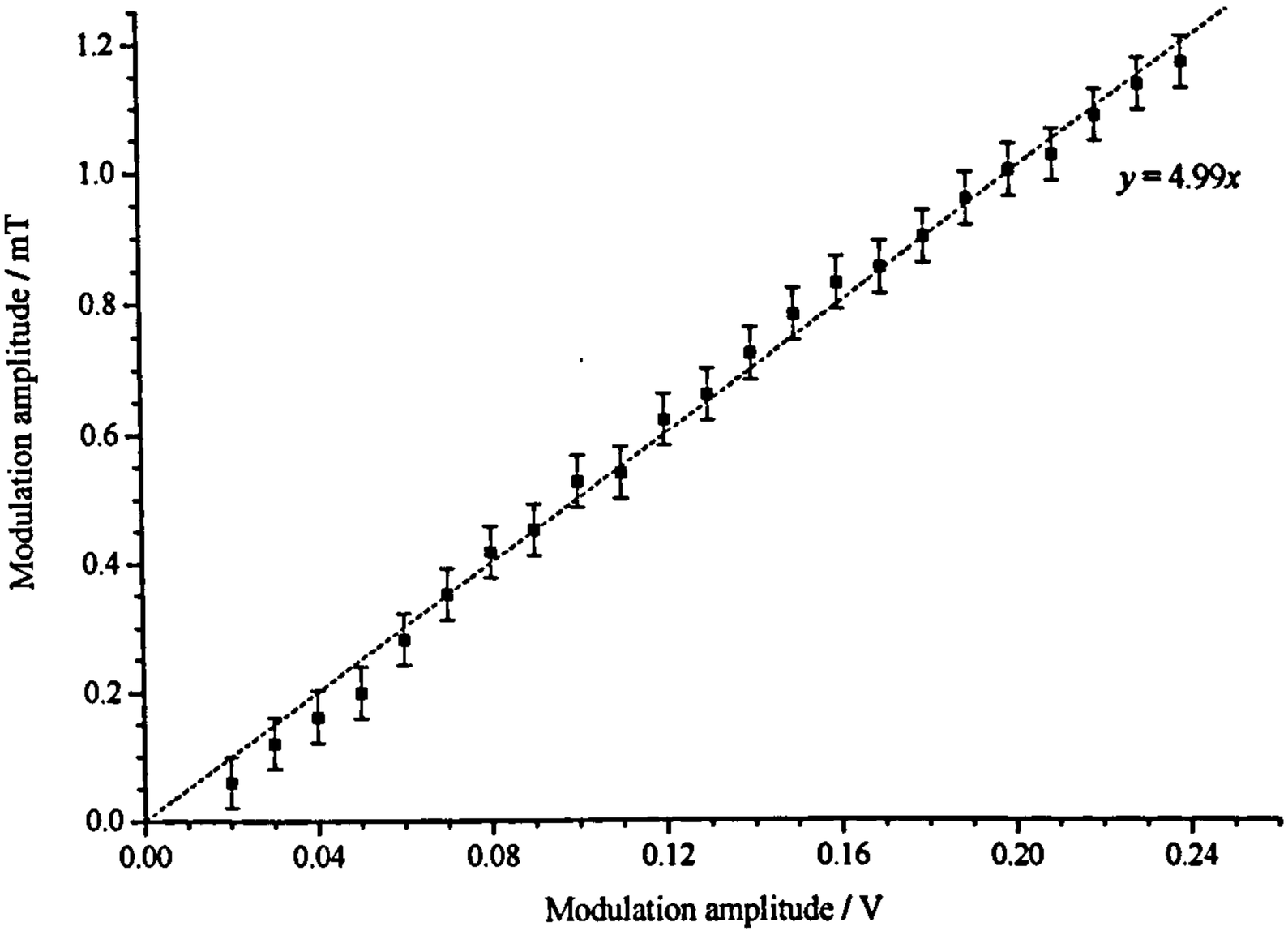

Figure 4-10: Calibration of the magnetic field modulation for the Q-band spectrometer (magnitude in volts set at the PSD).

in a PC. Both devices allow their functions to be controlled via this port and, in the case of the lock-in amplifier a buffer containing the DC voltage levels can be read. Thus by sending the appropriate command to the magnetic field controller to permit the field to be swept (either up or down) and by reading the DC voltage from the lock-in at each point a spectra may be collected.

Previous data collection software, written in Turbo Pascal by Talbot-Ponsonby was available [5], but this has a number of limitations. For example, parameters such as the field modulation amplitude, the resolution of the spectrum and the gain of the PSD cannot be altered by the user. Additionally, the software will only run in a pure MS-DOS environment, severely limiting the programs that can be used on that system. Because of these issues new control software has been written in Visual Basic. In this new program all of the parameters of an EPR experiment (apart from the attenuation, which is changed via a manually controllable attenuator) may be set within the program.

The field modulation amplitude is controlled by the voltage set at the lock-in/PSD, hence in order to choose a modulation amplitude in units of mT the conversion factor between the two needed to be determined. The theoretical ratio

between the peak-to-peak linewidth (ΔB_{pp}) at a given modulation to that at zero modulation $\Delta B_{pp(0)}$ can be plotted as a function of the modulation amplitude B_m [2]. An equivalent plot was constructed using experimental data collected from a HPHT sample containing 240 ppm N_s^0, by varying the modulation voltage at the lock-in. By comparing these two plots the modulation amplitude in mT for each voltage level could be determined, see figure 4-10. The gradient of this plot provides the required conversion factor:

$$B_m(\mathrm{mT}) = (4.99 \pm 0.03) \times B_m(\mathrm{V}) \tag{4-1}$$

The microwave frequency counter (EIP-545A) also has a GPIB interface, hence functionality has been added to the program to permit the frequency to be logged at the end of every scan, allowing any frequency drifts over the duration of the scan to be observed. A flow-diagram of the procedure used to collect an EPR spectrum from the Q-band spectrometer is shown in figure 4-9.

At the end of the data acquisition the collected data (and parameters) can be saved in the same binary format as used by the Bruker EPR spectrometers or a standard tab separated ASCII file. Hence existing software may be used to edit/view the spectra saved from the Q-band spectrometer.

4.3.2 Spectrometer performance and modifications

To test the performance of the Q-band EPR spectrometer a sample with narrow (< 0.1 mT) resonance lines was investigated. The major source of noise in the system appeared to originate from the magnetic field, since the noise level off-resonance was greatly reduced and increasing the number of scans did not yield an increase in the signal/noise ratio.

To investigate the stability of the magnetic field an NMR probe, as described by Robinson [7], was carefully secured between the poles of the magnet. Viewing the position of the proton resonance line on an oscilloscope revealed around 5 μT of noise in the magnetic field. The noise was only apparent when the applied magnetic field was set by the field controller; with the magnetic field set simply by choosing the current supplied to the coils the stability was noticeably improved. This suggested the primary source of the jitter in the magnetic field was the Hall

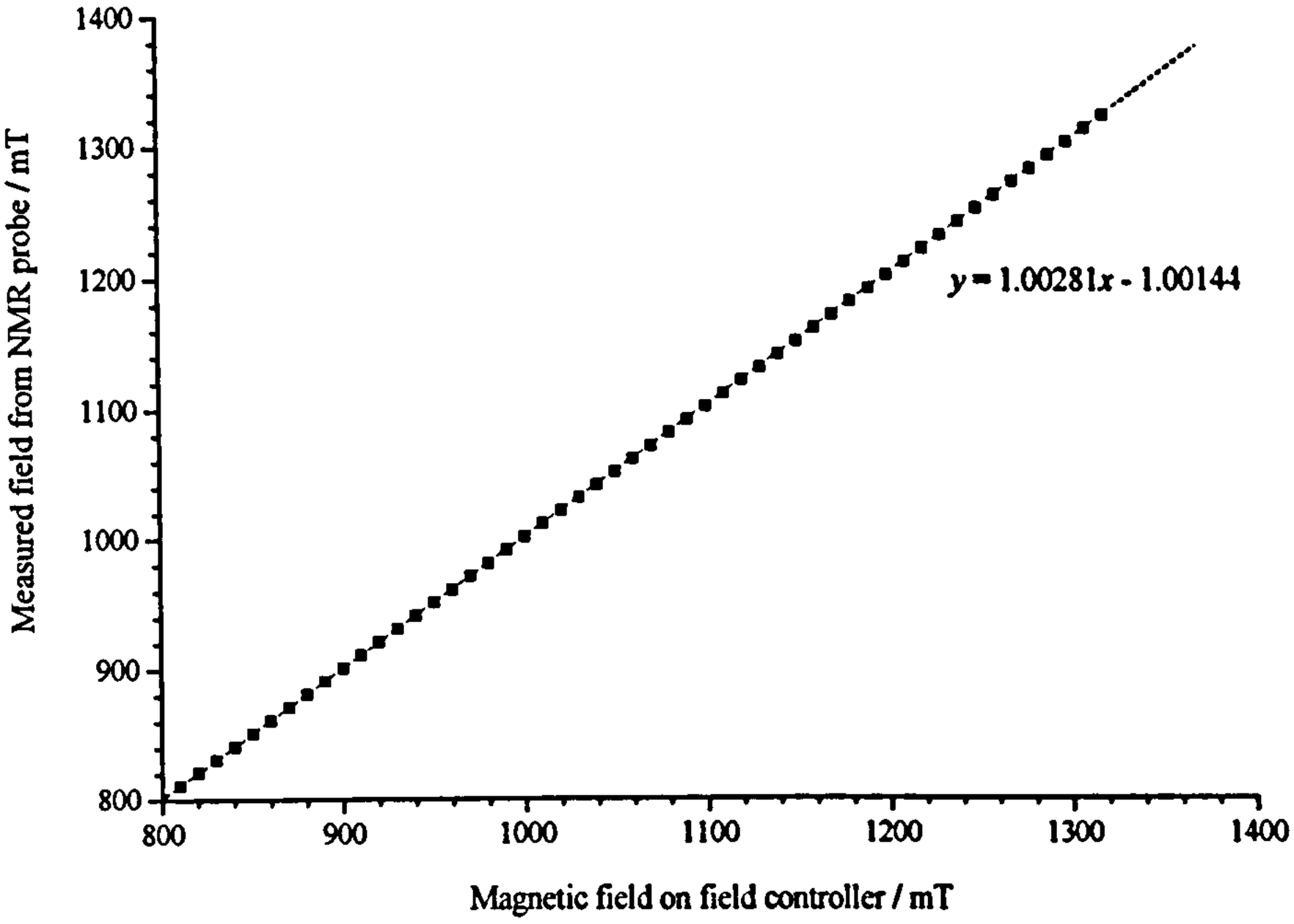

Figure 4-11: Magnetic field measured using a NMR probe compared to the magnetic field set on the Q-band field controller.

probe feedback loop. A number of modifications were made in order to improve the field stability:

1. An earth loop was identified in the feedback signal between the magnetic field controller and power supply. The noise that this introduces was minimised by time-constant filtering and adjusting the loop gain.
2. Any movement in the Hall probe itself would result in noise in the field, as the field controller attempts to hold the field steady. The Hall probe was therefore clamped in place between the poles.
3. Microphonics, which could cause the position of the cavity between the poles to change were suppressed by fitting an additional brace to hold the sample mount more securely between the poles of the magnet.

Applying these changes led to much improved stability of the magnetic field. The field stability is now better than 1 ppm.

The NMR probe also permitted the calibration and linearity of the magnetic field controller to be checked. A plot comparing the measured field to the magnetic field set by the field controller to is shown in figure 4-11.

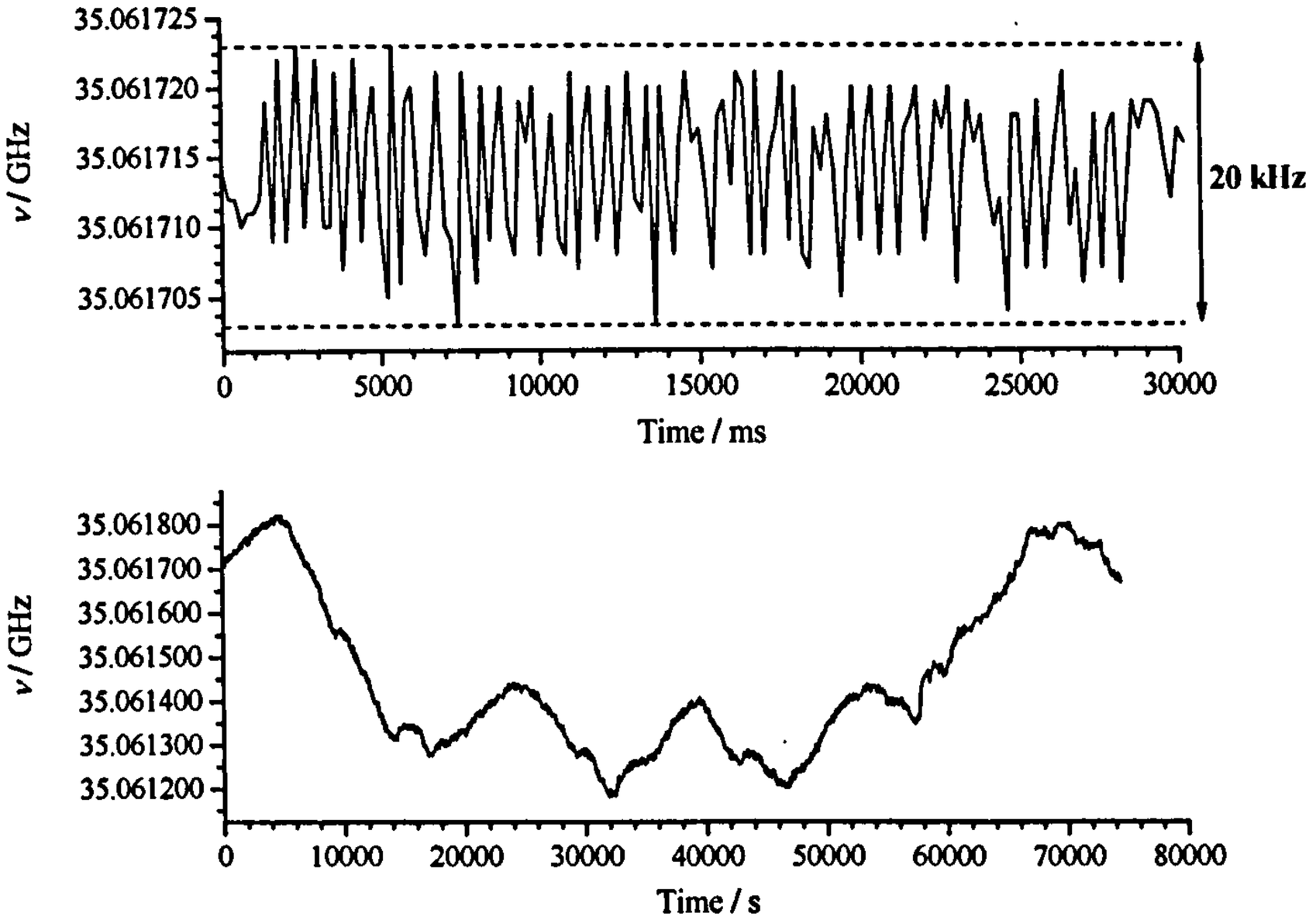

Figure 4-12: The stability of the microwave frequency on the Q-band spectrometer over short and long timescales (upper and lower plots, respectively).

With narrow resonance lines the stability of the microwave frequency is also critical, as any jitter has the potential to introduce noise into the spectrum; for example a field stability of 1 ppm requires a frequency stability of ~ 30 kHz. Since the short-term stability is determined by the AFC (§4.1.2) a new unit was constructed[3]. As shown in figure 4-12 with the new AFC the maximum deviation in the frequency over 30 s is 20 kHz. This figure also illustrates that over long (~ 24 hours) timescales a larger variation is observed; these slow fluctuations arise due to variations in temperature, which cause a change in the cavity size and a proportional change in the wavelength of the standing waves.

4.4 New analysis and logging software

A number of software packages have been written in-house for parameter logging and analysis. A brief summary of these is provided in this section.

[3]Designed and built by Adrian Lovejoy and Mark Newton

4.4.1 Logging of frequency and temperature

Using the software supplied with the Bruker X-band spectrometers it is not possible to record the microwave frequency or the temperature of the sample at regular intervals during the collection of an EPR spectrum. However, since both the EIP-545A microwave frequency counter and the Oxford Instruments VC30 temperature controller had GPIB ports, external software could be written (using Visual Basic .NET) which allows both/either of the microwave frequency and temperature to be logged. This program then displays the average and standard deviation in these parameters.

Rather than simply logging these parameters at a user defined time frequency it was decided to log the parameters at the start of each scan. This is due to the observation that rotating a sample within the cavity often leads to a shift in the frequency of the resonance mode, therefore when collecting sets of scans at different orientations using the automatic goniometer a noticeable change in the frequency is seen for each set of scans. The difficulty with linking the orientation of the sample with the time at which the frequency was logged meant that the average frequency for each set of scans could not be easily determined. However, by logging the frequency at the start of each scan and by registering when the orientation is changed an average and standard deviation can be automatically recorded for each alignment.

The triggering of an external program at the start of a new scan or a new set of scans (e.g. after changing the orientation) is not functionality which is provided in the supplied Bruker software for the EMX spectrometers. Therefore indirect methods of detecting these events had to be found. The currently implemented method in the logging program is to monitor the file modification time of a backup file that the Bruker spectrometer writes to at the start of every new scan; functionality provided to allow recovery of the data in the case of a program crash/power outage. Within this data file the scan number is stored. The logger program waits until the file modification time of the backup file changes, and then reads in the scan number. If this has changed then a new scan has started and if it equals 1 then a new set of scans has begun.

The synchronisation of the actions of an external program with the collection

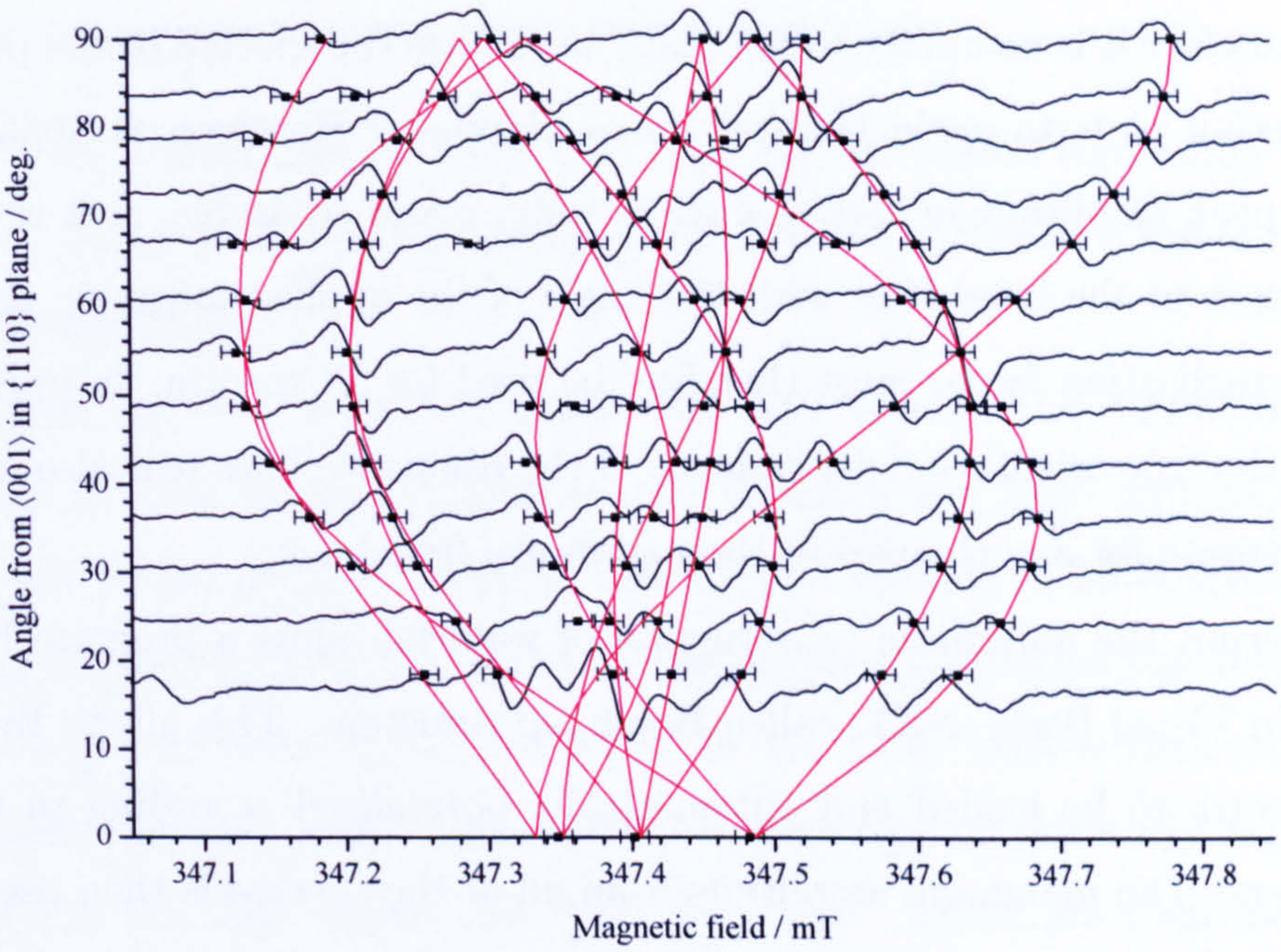

Figure 4-13: An example of the "waterfall" plots produced by the Roadmap Assistant program. From this the symmetry could be determined and the roadmap constructed.

of EPR spectra is also important, as it means it is possible to control additional experimental parameters which the spectrometer software is unaware of. In this way collections of spectra can be obtained which permit comparisons between EPR spectra when an external parameter (e.g. temperature, wavelength of optical excitation, etc) is changed.

4.4.2 Roadmap generation from experimental data

A common experimental procedure is to obtain a collection of EPR spectra at different orientations of the magnetic field and to produce a "waterfall" plot with all the spectra overlaid but offset by the angle of the applied magnetic field, see figure 4-13. This allows patterns in the orientation dependence of the various resonance lines to be observed and ultimately to the construction of a roadmap and the recognition of the symmetry of the defect.

Creating these plots is a tedious process, since the peak amplitude of a resonance line in the different orientation slices may vary due to changes in the experimental parameters (e.g. the number of scans, modulation, microwave power,

etc). Therefore it is necessary to manually normalise the spectra before producing the waterfall plot, to avoid the spectra overlapping. However, normalising the peak-to-peak amplitude in each spectra to unity is not advisable, as it would hide any changes in the intensities with the angle of the applied magnetic field. The same normalisation factor must therefore be used for all spectra. In order to determine the true orientation dependence of the resonance lines it is also necessary to compensate for any changes in the microwave frequency.

To permit the automatic construction of waterfall plots a program has been written in Visual Basic .NET, called Roadmap Assistant. This allows Bruker/Q-band spectra to be loaded and automatically normalised according to the scan parameters. The maximum amplitude from all of the spectra is then used as the same normalisation factor for every slice. The resulting intensities are multiplied by an addition (user specified) factor to determine the peak-to-peak height, relative to the separation in angle between each slice. Finally the spectra are offset by the angle of the applied magnetic field.

The program also allows the magnetic field values to be corrected for changes in microwave frequency (assuming $h\nu = g\mu_B B$). This is done by calculating an average frequency (ν_{avr}) for all the spectra and then offsetting the x-axes accordingly, as if all data sets were obtained at frequency ν_{avr}.

4.4.3 Simulation of EPR spectra

For simulating EPR spectra and for the determination of spin-Hamiltonian parameters a program called EPR-NMR, written by Michael Mombourquette and John Weil is used [8].

For a simulation a text input file has to be created in the correct format. This input file must contain:

1. A header defining the number of sites, transitions, etc.
2. The electronic spin and any nuclei involved in hyperfine interactions.
3. The spin-Hamiltonian matrices, expressed using a cartesian coordinate system.
4. The site rotation matrices (see §3.7.2) appropriate for the defect symmetry.

5. The transitions between energy levels to simulate.

Provided valid inputs are provided an output file is created containing the EPR spectrum. Using similarly formatted input files EPR-NMR also permits roadmaps to be constructed [8].

Creating correctly formatted input files and viewing the output is a time-consuming process, hence a graphical user interface had been written in Visual Basic .NET to permit easy creation, editing and viewing of EPR spectra. This program (named "EPR Sim") allows all the required simulation parameters to be imputed and a correctly formatted input file for EPR-NMR is then guaranteed. Additionally the spin-Hamiltonian parameters may be conveniently expressed in terms of the principal values and their directions. These are then used to automatically produce the spin-Hamiltonian parameters, expressed in a cartesian coordinate system.

The automatically created input file is run through EPR-NMR and the output is intercepted by EPR Sim and the output is displayed. The program allows quick and easy changes to the spin-Hamiltonian parameters, with the result on the EPR spectrum immediately viewable.

4.5 Resonance line intensities and quantitative EPR

In addition to the transition probabilities (§3.5) and temperature (§3.6) several spectrometer and sample-related factors influence the observed signal intensities for a particular paramagnetic defect in an EPR spectrum. These include:

1. The abundance of the paramagnetic defect in the sample.
2. The spin S and electronic g factor.
3. The incident microwave power, $P_{\mu w}$ ($\propto {B_1}^2$).
4. The gain of the microwave detector.
5. The acquisition time, t_{aq}, which determines the length of time the spectrometer spends acquiring data at each magnetic field value.
6. The modulation amplitude, B_m.

7. The number of scans acquired.
8. The Q-factor of the cavity when loaded with the sample and holder.
9. The filling factor, which is proportional to the ratio of the sample volume to the cavity volume.

The first item in the list provides the basis for quantitative measurements; the concentration of a particular paramagnetic defect is proportional to the integrated intensity of all of the EPR absorption resonance lines originating from that centre. This permits the concentration of the defect to be determined by comparing the integrated intensity to that which is observed for a reference sample, which contains a defect of known concentration. However, the list of factors above illustrates that the relationship between the scan conditions and the integrated intensity must be known, since these may vary between the reference sample EPR spectrum and the spectrum of interest.

Provided the detector is not railed the intensity of an EPR spectrum is proportional to the gain, G, of the spectrometer. Additionally, since the Bruker spectrometer simply adds the signal intensities at each magnetic field to those determined after the previous scan, the intensity is also proportional to the number of scans, N. A linear dependence of the integrated intensity with B_{m} was determined, see figure 4-14a.

In the absence of power saturation (§3.6) the EPR signal intensity is proportional to B_1 ($\propto \sqrt{P_{\mu\mathrm{w}}}$), hence if both the reference sample spectrum and spectrum of interest are obtained under non-saturated conditions then the intensities may be easily corrected in the event of differing microwave powers. In this case the concentration of a known defect, [x], may be determined from a reference sample containing known concentration of a paramagnetic defect, [ref], using the following equation [2]:

$$[\mathrm{x}] = [\mathrm{ref}]\frac{I_{\mathrm{x}}}{I_{\mathrm{ref}}}\sqrt{\frac{(P_{\mu\mathrm{w}})_{\mathrm{ref}}}{(P_{\mu\mathrm{w}})_{\mathrm{x}}}}\frac{M_{\mathrm{ref}}}{M_{\mathrm{x}}}\frac{(B_{\mathrm{m}})_{\mathrm{ref}}}{(B_{\mathrm{m}})_{\mathrm{x}}}\frac{g_{\mathrm{ref}}^2}{g_{\mathrm{x}}^2}\frac{S(S+1)_{\mathrm{ref}}}{S(S+1)_{\mathrm{x}}}\frac{(t_{\mathrm{aq}})_{\mathrm{ref}}}{(t_{\mathrm{aq}})_{\mathrm{x}}}\frac{G_{\mathrm{ref}}}{G_{\mathrm{x}}}\frac{N_{\mathrm{ref}}}{N_{\mathrm{x}}}, \qquad (4\text{-}2)$$

where I_{x} and I_{ref} are the integrated intensities from the examined sample and reference, respectively. In the quantitative EPR work presented in this thesis a type Ib single-sector HPHT sample containing 240(10) ppm of $\mathrm{N_s^0}$ (determined from FTIR measurements) has been used as a reference.

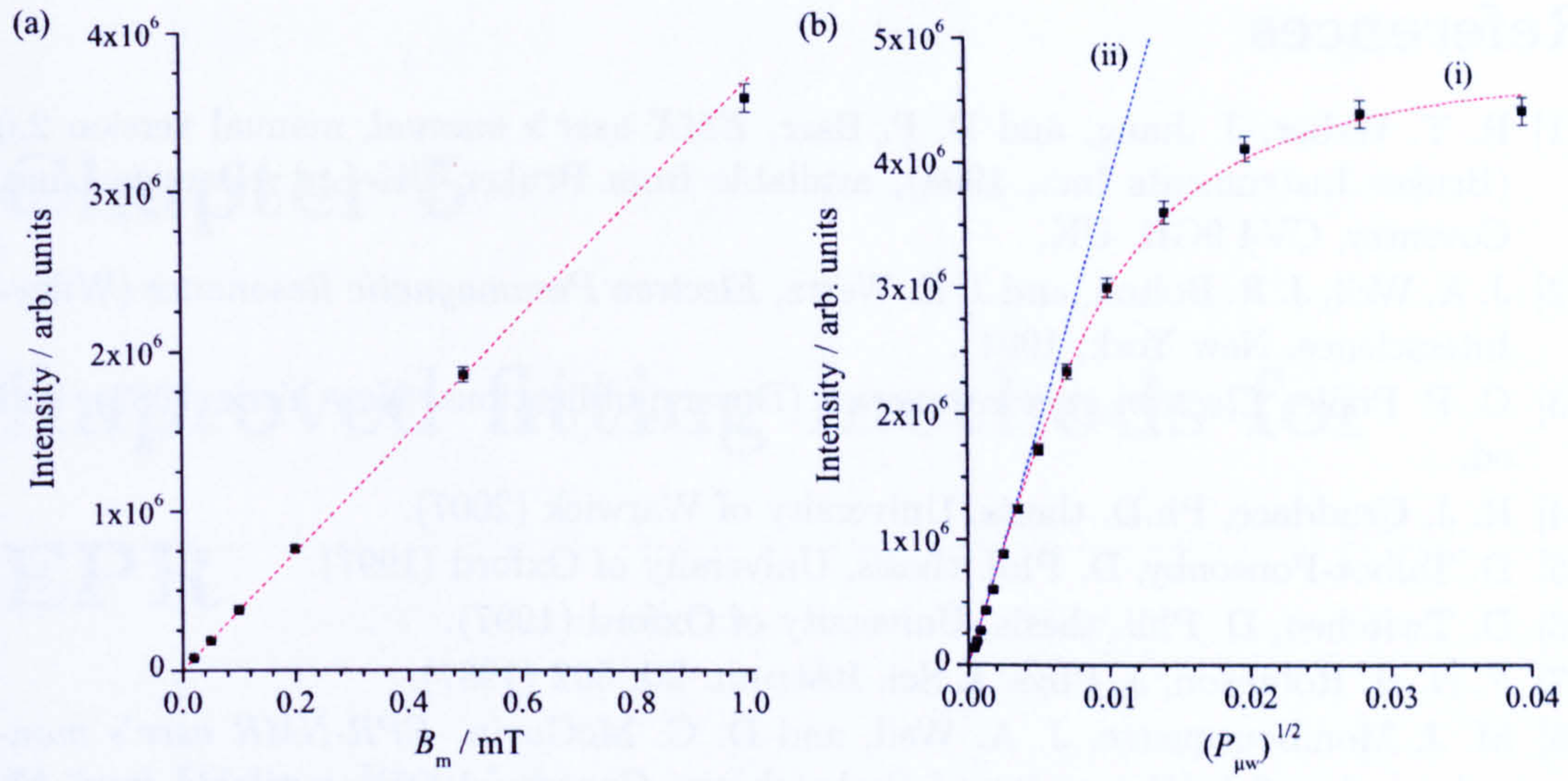

Figure 4-14: Dependence of integrated intensity with (a) modulation amplitude (B_{m}) and (b) microwave power ($P_{\mu\mathrm{w}}$), with lines (i) and (ii) created using equations 4-3 and 4-4, respectively. The data points were collected at room temperature from the reference sample (see text) mounted in the Bruker SHQ cavity.

In the case where microwave power saturation is unavoidable its effect can be modelled using the following equation [9]:

$$I = \frac{\alpha\sqrt{P_{\mu\mathrm{w}}}}{\left(1 + \frac{P_{\mu\mathrm{w}}}{\beta}\right)^{\frac{1}{2}}} \tag{4-3}$$

where α and β are constants. Provided sufficient experimental data points are collected close to the unsaturated region α and β may be determined. The integrated intensity in absence of saturation can then be determined from:

$$I_{\mathrm{corrected}} = \alpha\sqrt{P_{\mu\mathrm{w}}}, \tag{4-4}$$

see figure 4-14b. This corrected intensity can then be used in equation 4-2.

In formulating equation 4-2 it has been assumed that the Q-factor of the loaded cavity and the filling factor are identical between the reference and examined scan. Many additional considerations must be made when conducting quantitative EPR measurements; a comprehensive list of important factors are listed by Mazúr and Valko [10].

References

[1] R. T. Weber, J. Jiang, and D. P. Barr, *EMX user's manual*, manual version 2.0 (Bruker Instruments Inc., 1998), available from Bruker UK Ltd., Banner Lane, Coventry, CV4 9GH, UK.

[2] J. A. Weil, J. R. Bolton, and J. E. Wertz, *Electron Paramagnetic Resonance* (Wiley-Interscience, New York, 1994).

[3] C. P. Poole, *Electron spin resonance* (Dover publications, New York, 1983), 2nd ed.

[4] R. J. Cruddace, Ph.D. thesis, University of Warwick (2007).

[5] D. Talbot-Ponsonby, D. Phil. thesis, University of Oxford (1997).

[6] D. Twitchen, D. Phil. thesis, University of Oxford (1997).

[7] F. N. H. Robinson, J. Phys. E Sci. Instrum. **20**, 502 (1987).

[8] M. J. Mombourquette, J. A. Weil, and D. G. McGavin, *EPR-NMR user's manual*, version 6.1 (University of Saskatchean, Canada, 1997), available from M. J. Morbourquette, Queen's University, Kingston, ON K7L 3N6, Canada (see www.chem.queensu.ca/eprnmr/).

[9] C. Glover, Ph.D. thesis, University of Warwick (2003).

[10] M. Mazur and M. Valko, EPR Newsletter **13**, 27 (2003).

Chapter 5

Improved fitting methods for EPR

5.1 Introduction

At the end of the previous chapter the concept of EPR as a quantitative technique for determining paramagnetic defect concentrations was introduced and the experimental requirements were covered. From this discussion it is evident that a method must found to reliably determine the total integrated intensity of EPR resonance lines from the defect of interest. In practice it is found that numerical integration of the experimental spectrum has a number of limitations/difficulties.

Defects in diamond tend to have electronic g values close to that of the free-electron (2.0023), hence it is common for EPR spectra to overlap. In such situations a method of deconvolving the overlapping resonances from different defects must be found for numerical integration to be successful. It is also vital to determine the total integrated intensity for *all* resonance lines from a defect. For example the single substitutional defect N_s^0 will be dominated by resonance lines from defects incorporating ^{14}N and surrounded by ^{12}C, but additional structure will be present due to the hyperfine interaction with lower abundance nuclei e.g. ^{15}N and ^{13}C. For the total concentration of N_s^0 all these resonances lines would have to be integrated over, or their intensity must be predicted from knowledge of the intensity of the resonance lines which fall within the experimental spectrum.

The calculated intensity can be highly dependent on the choice of baseline used for integration. This choice can be subjective and lead to variation in the determined intensity, with the need for *double* integration of the experimental spectrum exacerbating the problem. Additionally, truncation of an experimental spectrum limits the range of integration and, since the wings of an EPR line can

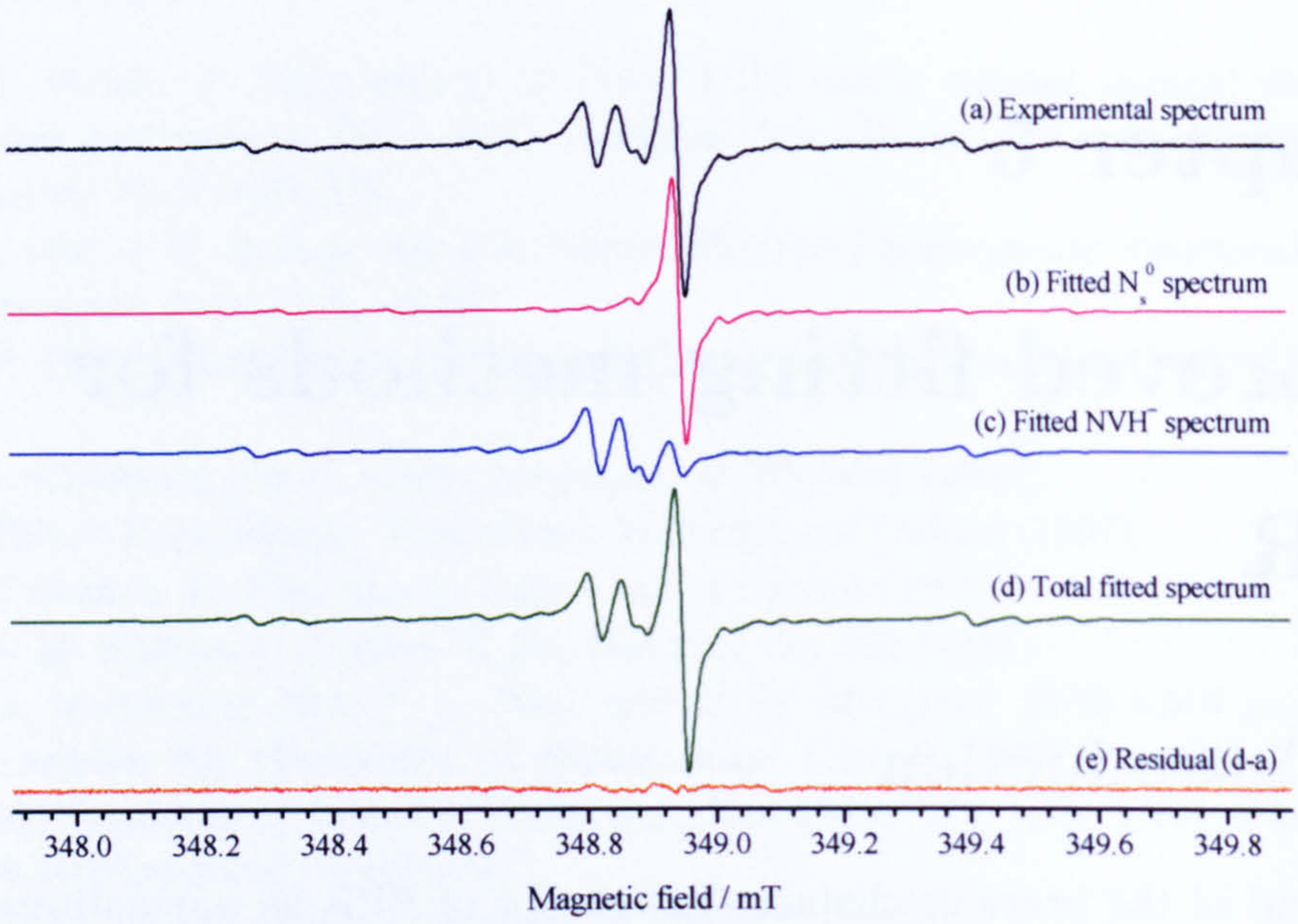

Figure 5-1: Example of deconvolution of N_s^0 and NVH^- spectra observed in a CVD diamond using Tsallis lineshape fitting. The spectrum was recorded at room temperature with $\nu = 9.75\,\mathrm{GHz}$ and $\mathbf{B} \parallel \langle 100 \rangle$.

contain considerable intensity, this can lead to significant underestimation in the integrated intensity [1].

Such difficulties can be mitigated if a theoretical spectrum is generated for the defect(s) of interest and fitted to the experimental spectrum by varying the intensity, linewidth and form of the simulated resonance lines. Providing the experimental spectra are satisfactorily simulated for multiple defects, this method provides a means for deconvolution of overlapping EPR spectra. The integrated intensity of each of the defects in the fitted spectrum can then be used to determine their respective concentrations. As an example figure 5-1 illustrates a typical EPR spectrum for a CVD diamond containing N_s^0 and NVH^-, obtained at X-band and with the applied magnetic field along $\langle 100 \rangle$. Since the two spectra overlap it is difficult to determine the integrated intensity of each defect by numerical integration of the original experimental data. However, fitting using simulations of N_s^0 and NVH^- spectra allows successful deconvolution of the two individual spectral components.

Existing software is available which allows EPR spectra to be simulated from

spin-Hamiltonian parameters. EPR-NMR, written by Michael Momborquette and John Weil [2], is one example and is employed throughout throughout this thesis for simulation and parameter determination (§4.4.3). However, with quantitative EPR analysis in mind, this software does not provide the functionality to fit simulated spectra. In fact, no such software has been found that provides the flexibility to fit multiple spectra for EPR conducted on single-crystal systems where a number of symmetry-related copies (§3.7.2) of point defects are present.

Since EPR-NMR provides the means for the position (in field) and relative intensity of resonance lines for a static paramagnetic defect to be determined all that is required to permit the desired analysis to be conducted is complimentary software designed to accept the output of EPR-NMR and, from this, produce a synthetic spectrum which is fitted to the experimental data. It is the development of such fitting software that is the topic of this chapter. This has required use of suitable lineshape functions and accounting for the effects of magnetic field modulation.

5.1.1 Simulation requirements for the modelling of the EPR lineshape

In §3.6 it was shown that a Lorentzian lineshape is predicted from the Bloch equations for spin-spin relaxation with a single exponential. If this is to be the observed lineshape in an experiment, where resonances are being detected from a large number of identical paramagnetic centres, then it is apparent that all these spins must be interacting with the same net magnetic field, or at least an identical time-averaged field over a sufficiently short time interval. In this case broadening of a resonance line can result from spin-spin interactions, where the linewidth is determined by T_2, or dipolar interactions between like spins. This case is referred to as homogeneous broadening.

Inhomogeneity in the resonance field present at each paramagnetic centre will result in a lineshape being observed which is the superposition of a large number of resonance lines, each slightly shifted in magnetic field position. Such inhomogeneous broadening can occur from inhomogeneities in the external (applied) magnetic field (if this exceeds the natural linewidth), unresolved hyperfine structure

or dipolar interactions with defects with different resonant fields. In this situation central-limit theory can be invoked to justify use of a Gaussian lineshape [3].

The consideration that homogenous or inhomogeneous broadening may be occurring during an experiment clearly demonstrates that a program designed to fit EPR lines needs to have flexibility in the lineshape used. However, experimentally it is often seen that neither a Lorentzian nor a Gaussian lineshape function results in a adequate description of an EPR absorption spectrum; rapid changes in the magnetisation vectors of individual centres can lead to a dynamical averaging of individual distributions leading to a change in the lineshape as a resonance is swept through [4]. This effect is known as motional narrowing [5, 6]. Such an effect means for successful fitting of an EPR spectrum a generalised lineshape function needs to employed.

In addition to broadening effects one must consider the effect of magnetic field modulation (§4.1.3) on the form of the EPR resonance line. As illustrated in figure 4-3, as the modulation amplitude approaches and exceeds the intrinsic width of a resonance line the lineshape is distorted. Whilst such a effect could be prevented by keeping the modulation low, large (e.g. $\gtrsim$ linewidth) modulation amplitudes are useful to increase signal/noise in cases of low defect concentrations and can also aid in preventing microwave power saturation. Hence experimentally it is common to run with field modulation amplitudes comparable with the intrinsic linewidth and, as result, it is important to be able to simulate the distortion in any EPR lineshape fitting.

5.2 The EPR Wizard program

A fitting program called "EPR Wizard" has been developed in Visual Basic to permit the fitting of experimental data using the output from EPR-NMR. This program has the following features:

- Support for opening of 2D/3D EPR data files saved in binary Bruker/ASCII format and recognition of scan parameters.
- Easy to use interface which allows viewing and zooming of EPR spectra.
- Simple analysis of experimental data including field separation measure-

ments and automatic peak-to-peak linewidth determination.

- Import EPR simulation output files from EPR-NMR/EPR Sim (§4.4.3) and permit a database of resonance line positions for different defects, orientations and frequency bands to be built up.
- Automatic scaling of hyperfine satellites with isotope abundance and number of equivalent sites.
- Simulation of EPR spectra using generalised Tsallis lineshapes (§5.2.1.1) and pseudomodulation (§5.2.1.2).
- Optimisation of fit parameters using simplex algorithm (§5.2.1.4).
- Calculation of defect concentration by comparison to a known reference (using equation 4-2).

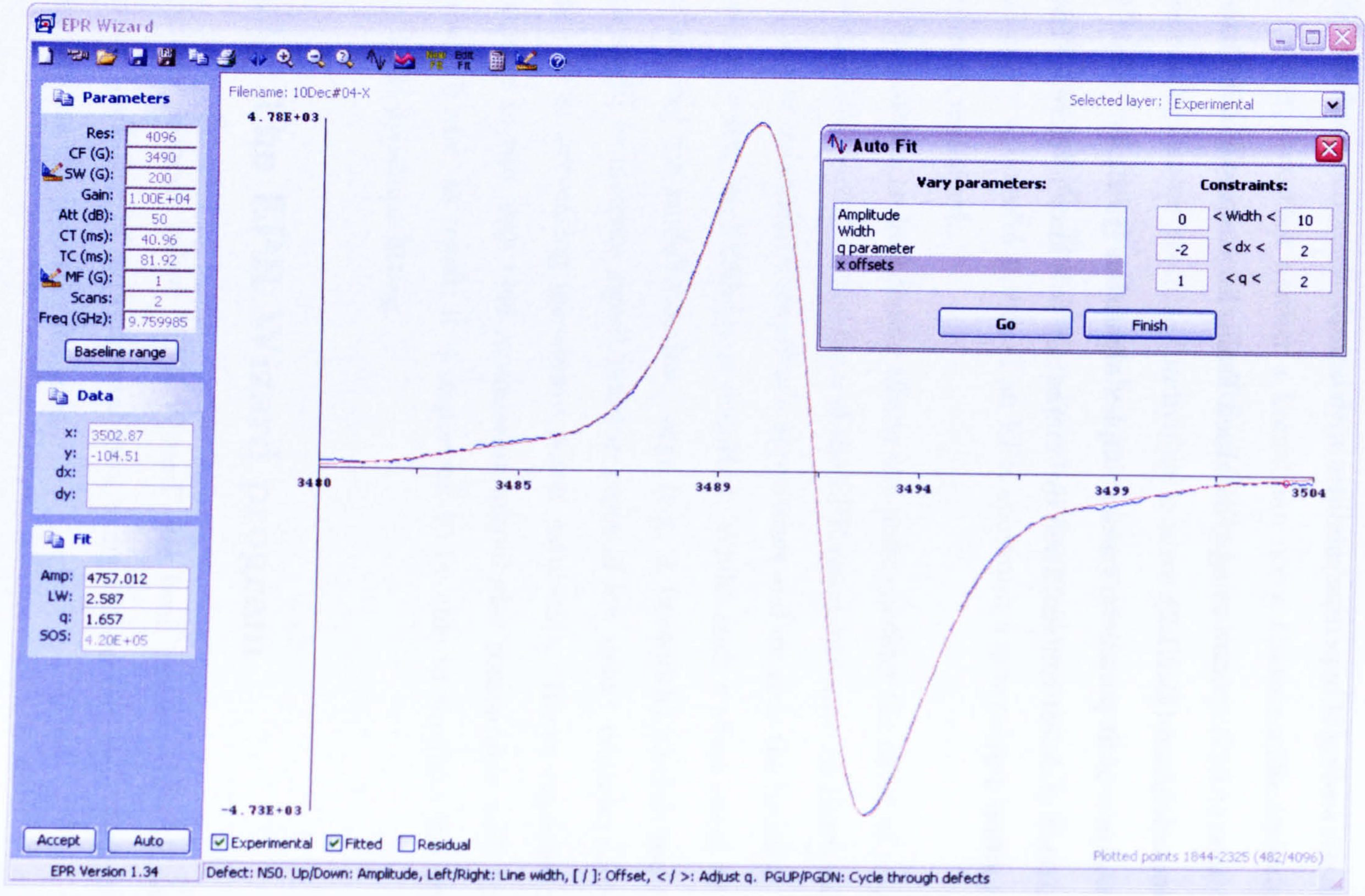

Figure 5-2: The EPR fitting program "EPR Wizard".

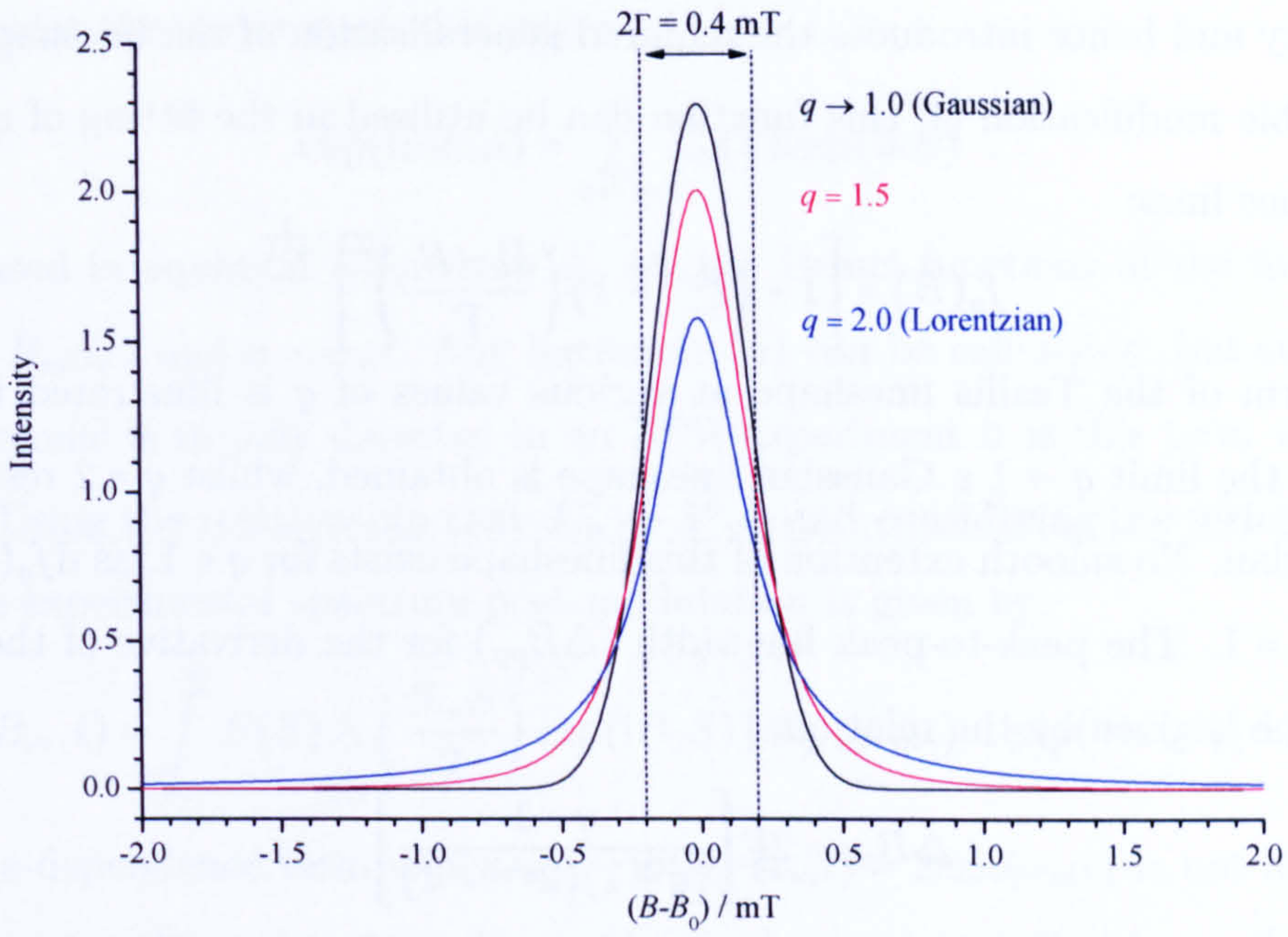

Figure 5-3: Examples of Tsallis absorption lineshapes with identical linewidths (Γ is the half-width at half-maximum). Each data set has been normalised to unit integrated intensity.

5.2.1 Implemented fitting method

5.2.1.1 The Tsallis lineshape

The Voigt lineshape [7], formed by convolving a Gaussian with a Lorentzian, is an example of a suitable lineshape for the simulation of experimental EPR spectra, as both the Gaussian and the Lorentzian appear as limiting cases. In the case of inhomogeneous broadening the Gaussian lineshape can be constructed by the convolution of an infinitesimally narrow Lorentzian with a Gaussian lineshape describing the positions of the lines. Conversely if the variance of the Gaussian distribution is zero a Lorentzian (homogeneously broadened) lineshape results. In the case of non-zero variance of both components of the Voigt a general lineshape is produced.

An alternative is the Tsallis function, which was first derived for solutions to the entropy-maximisation principle [8]. In addition to the half-width at half-maximum linewidth parameter, Γ, the Tsallis lineshape utilises one additional variable q, which determines the contribution of the line wings to the integrated

intensity and hence introduces the required generalisation of the lineshape. With a suitable modification [4] this function can be utilised in the fitting of magnetic resonance lines:

$$f_q(B) = \left[1 + \left(2^{q-1} - 1\right)\left(\frac{B - B_0}{\Gamma}\right)^2\right]^{-\frac{1}{q-1}} \tag{5-1}$$

The form of the Tsallis lineshape at various values of q is illustrated in figure 5-1. In the limit $q \to 1$ a Gaussian lineshape is obtained, whilst $q = 2$ results in a Lorentzian. No smooth extension of this lineshape exists for $q < 1$, as $\mathrm{d}f_q(B)/\mathrm{d}q = \infty$ at $q = 1$. The peak-to-peak linewidth (ΔB_{pp}) for the derivative of the Tsallis lineshape is given by the relation:

$$\Delta B_{pp} = 2\Gamma\left[\frac{q-1}{(q+1)(2^{q-1}-1)}\right]^{1/2} \tag{5-2}$$

The Tsallis function provides the required flexibility in the EPR lineshape in a single function and the form can be described by one parameter (q). As a result the function is easier to implement and less computationally expensive compared to a Voigt lineshape. For these reasons the Tsallis lineshape has been utilised in the EPR fitting program created for quantitative EPR analysis.

5.2.1.2 Pseudomodulation

Before constructing the synthetic spectrum from Tsallis lineshapes and fitting this to the experimental data the effects of magnetic field modulation are simulated by applying pseudomodulation, as described [9] by Hyde *et al.* This method and its implementation in EPR Wizard will be outlined briefly here.

Magnetic field modulation can be described using the equation:

$$B = B_0 + \left(\frac{B_m}{2}\right)\sin(\omega_m t), \tag{5-3}$$

where B_m is the modulation amplitude. Taking $f(B)$ as the modelled EPR absorption lineshape (equation 5-1), the Fourier transform of this is written as:

$$F(S) = \frac{1}{\sqrt{2\pi}}\int_{-\infty}^{\infty} f(B)\exp(-\mathrm{i}BS)\mathrm{d}B, \tag{5-4}$$

where S is a dummy variable. Then, if the inverse Fourier transform is calculated and equation 5-3 is used for the time-dependence of B:

$$f(B_0, B_m, t) = \frac{1}{\sqrt{2\pi}}\int_{-\infty}^{\infty} F(S)\exp(\mathrm{i}B_0 S)\exp\left[\frac{\mathrm{i}B_m S}{2}\sin(\omega_m t)\right]\mathrm{d}S \tag{5-5}$$

At this point the mathematical identity:

$$\exp(\mathrm{i}x\sin\alpha) = \sum_{n=-\infty}^{\infty} J_n(x)\exp(\mathrm{i}n\alpha) \tag{5-6}$$

can be used in equation 5-5, where J_n are the Bessel functions of the first-kind [10], $x = B_m S/2$ and $\alpha = \omega_m t$. Any harmonic (n) can be calculated, but since the first harmonic is usually detected in an EPR experiment it is this term which is chosen. Using the relationship that $J_{-n} = -1^n J_n$ and considering the terms $n = \pm 1$ only, the experimental spectrum post-modulation is given by:

$$\dot{f}(B_0, B_m, t) = \int_{-\infty}^{\infty} F(S) J_1\left(\frac{B_m S}{2}\right) \exp(\mathrm{i}B_0 S)\left[\exp(\mathrm{i}\omega_m t) - \exp(-\mathrm{i}\omega_m t)\right] \mathrm{d}S \tag{5-7}$$

The time-dependence term $\exp(\mathrm{i}\omega_m t) - \exp(-\mathrm{i}\omega_m t) = 2\mathrm{i}\sin(\omega_m t)$ is not apparent after phase-sensitive detection, hence the final experimentally observed form is given by:

$$\dot{f}(B_0, B_m) = \int_{-\infty}^{\infty} F(S) J_1\left(\frac{B_m S}{2}\right) \exp(\mathrm{i}B_0 S)\mathrm{d}S \tag{5-8}$$

It is evident from this expression that a pseudomodulated spectrum can be obtained by taking the inverse Fourier transform of $F(S)J_1(B_m S/2)$ i.e. the Fourier transform of the Tsallis lineshape function $f(B)$ multiplied by the appropriate Bessel function. Transforming the modulation amplitude in magnetic field units (e.g. mT) to the dummy variable S can be achieved by multiplying $B_m(B)$ by $2\pi/W$, where W is the scan width expressed in the same units. J_1 is then calculated from $S = 0 \rightarrow N_p/2$ where N_p is the number of points in the theoretical spectrum. Since J_1 is an odd function the negative half in S can be calculated at the same time.

In the created fitting program the required code to calculate values of the Bessel function and the Fourier transforms (using fast Fourier transforms or FFTs) is based on the routines provided in Numerical Recipes [11].

5.2.1.3 Construction of the simulated spectrum

To produce the simulated EPR spectrum the pseudomodulated Tsallis lineshape must be combined with knowledge of the position and relative intensity of all the resonance lines in the EPR spectrum. In the created program this is achieved by convolving the lineshape with a "stick" spectrum for the defect being simulated,

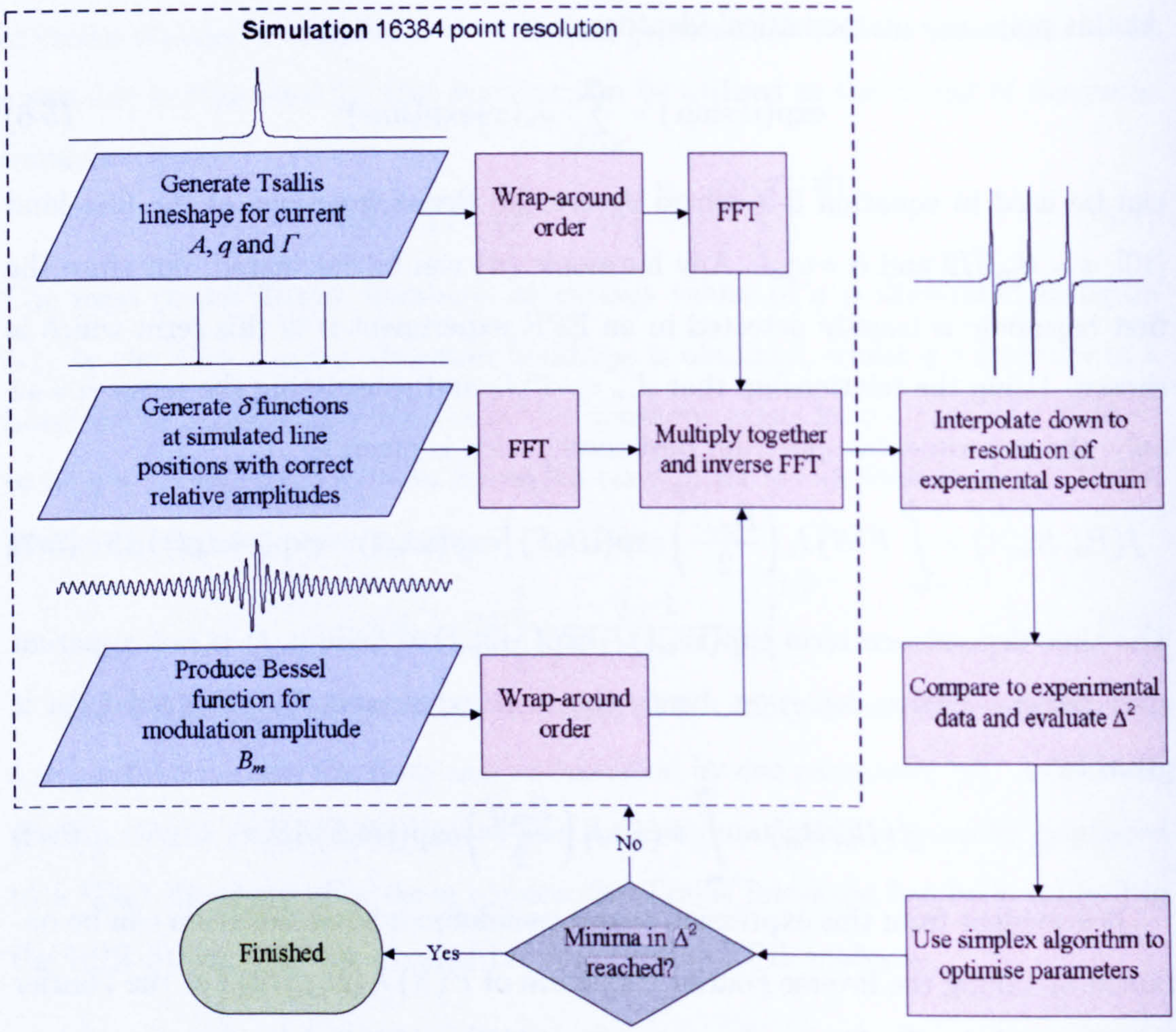

Figure 5-4: Block diagram of procedures used to obtain optimum fit to experimental EPR spectra.

which consists of δ-functions at the correct position in magnetic field and with intensities proportional to the probability for the transition giving rise to each resonance line. To do this the EPR Wizard fitting program reads output files from EPR-NMR/EPR Sim where the appropriate spin-Hamiltonian parameters, rotation matrices and transitions have been defined.

Considering a defect such as N_s^0, to obtain the most accurate fit and measurement of the total integrated intensity, it is necessary to consider the hyperfine EPR structure from all isotopes of nitrogen and carbon with non-zero spin. These satellites must be scaled by the isotope abundance and the number of equivalent sites. To meet this requirement EPR Wizard allows groups of EPR-NMR simulations to be defined for each defect, with the user able to define the abundance of the isotope responsible for each set of lines and the number of equivalent sites.

The sum of the transition probabilities from each simulation is normalised to unity and is then multiplied by the corrected intensity as determined by equation 3-41.

From the read-in positions of all the required resonance lines EPR Wizard creates a stick spectrum consisting of N points (or "bins") which spans the same magnetic fields as the loaded experimental data. The resonance lines positions are interpreted to determine which bin they need to be placed into. If multiple resonance lines are found to fall within the same bin then the intensities are added together.

For the convolution operation, if $\dot{f}(B)$ is the pseudomodulated Tsallis lineshape and $r(B)$ consists of the appropriately positioned and sized δ-functions, then convolution theory states that the Fourier transform of the convolution $\dot{f} * r$ is simply the product of the individual Fourier transforms, $\dot{F}(S) \times R(S)$. From §5.2.1.2 it is known that $\dot{F}(S)$ is given by the product $F(S)J_1(B_m S/2)$. In the case of producing a synthetic EPR spectrum to compare to experimental data discrete convolution theorem [11] needs to be used. In the context of the simulation of EPR spectra this states that the discrete convolution of the stick spectrum with the EPR lineshape is a member of the discrete Fourier transform pair:

$$\sum_{k=-N/2+1}^{N/2} r_{j-k}\dot{f}_k \Leftrightarrow R_n \dot{F}_n \tag{5-9}$$

Here N is the number of data points in each data stream (must be equal for both data sets and 2^z, where z is an integer for the FFTs). F_n is the discrete Fourier transform of the y values for the Tsallis lineshape and R_n is the discrete Fourier transform of the stick spectrum data r_k. The values $\dot{f}_k$ in the range $k = -N/2+1, ..., N/2$ are expressed in wrap-around order. This means for a data set consisting of N points the values are reordered such that the second half (values $N/2+1 \rightarrow N$) is followed by the first half (values $1 \rightarrow N/2$). This reordering of the Tsallis lineshape data is therefore completed before Fourier transforming the data. An identical reordering is required for the Bessel function data (§5.2.1.2). A summary of the steps taken to construct the simulated EPR spectrum is shown in figure 5-4.

The advantage of the employed convolution method to construct the synthetic data is that the computation time required for the operation is independent of

the number of resonance lines being simulated, since the stick spectrum data r always contains the same quantity of data (N data points). The disadvantage of this method is that, to allow accurate positioning of the lines, a large number of points must be used to create the stick spectrum. In the method employed the Tsallis lineshape, Bessel function and stick spectrum are all constructed using 16384 points (must be 2^n for the FFTs), which for a commonly used 20 mT scan width allows the lines to be moved by ±1.2μT. Lower resolutions can be chosen by the user, but N = 16384 was found to provide a good balance between magnetic field resolution and computation time.

5.2.1.4 Least squares fitting

For each defect being simulated in the fitting program there are four parameters that can be varied to permit the fit to the experimental data to be optimised:

1. Amplitude scaling factor.
2. Peak-to-peak linewidth (related to Γ by equation 5-2).
3. Tsallis lineshape parameter (q).
4. Magnetic field offset.

By default all the resonance lines from a particular defect are assumed to have identical parameters, although it is possible to regroup the resonance lines into separate simulations which then permits (for example) different linewidths for particular EPR lines.

In general, for M adjustable parameters a_j, $j = 1,...,M$, the quality of fit between a model and experimental data consisting of N data points (x_i, y_i) can be evaluated by means of a sum of the squares calculation:

$$\Delta^2 = \sum_{i=1}^{N} [y_i - y(x_i; a_1 ... a_M)]^2 \qquad (5\text{-}10)$$

For Δ^2 to be calculated it is apparent that the x_i columns for both the fitted data and the experimental data must be identical. Since the synthetic data in EPR Wizard is produced at high resolution to permit accurate placement of the resonance lines this data must be interpolated down (simple linear interpolation suffices) to the resolution of the experimental data before calculating the sum of the squares.

Parameter determination via maximum likelihood estimation [11] involves minimising Δ^2 by varying the adjustable parameters. After the user has adjusted the parameters manually to obtain a reasonable starting fit EPR Wizard will then attempt to optimise the parameters systematically to find the minimum Δ^2 value. Instead of always being summed over all N data points the sum in EPR Wizard is extended over the current range as selected by the user. In this way it is possible to consider only a portion of the spectrum for fitting.

The Nelder-Mead downhill simplex method [12] is a commonly used non-linear optimisation algorithm. The simplex procedure derives its name from the use of a simplex, which is a polytope of $M+1$ vertices in M dimensions, which is moved and transformed in the parameter space whilst iteratively shrinking around the minimum (see Olasson and Nelson [13] for an example of its operation). It is a so-called "direct" procedure in that no derivatives of the objective function (in this case Δ^2) are required, and, as a result it can be readily implemented in complex non-linear problems where computation of $\mathrm{d}(\Delta^2)/\mathrm{d}a_j$ is non-trivial. This is clearly the case in the fitting of synthetic EPR spectra, hence this optimisation method has been utilised within the created fitting program, with the code based on the implementation presented in Numerical Recipes [11].

A limitation of the classic Nelder-Mead method is that it provides no direct means for linear constraints to be imposed on the adjustable parameters a_j. This is a problem in this application, since the requirement for bounded parameters is important in the case of the Tsallis line parameter, which requires the constraint $2 \geq q > 1$. It is also sensible to impose boundaries on the extent to which the position in magnetic field that resonance lines from a defect can be offset by as well as the linewidths, to ensure a physically reasonable minimum in Δ^2 is obtained.

There is, however, a very simple way of handling bounds for the simplex method through the transformation of the parameters a_j into a bounded search space. In EPR Wizard the parameters a'_j are varied by the simplex routine, which are related to the unbounded parameters by the following expression:

$$a_j = L + \frac{U - L}{2}\left[1 + \cos(a'_j)\right], \tag{5-11}$$

where L and U are the lower and upper bounds for the variable a_j. As a result, irrespective of the value of a'_j, the parameter will always comply to the desired

constraints.

The downhill simplex method must be started not just with a single point in the M dimensional parameter space but with $M + 1$ points, defining an initial simplex. One vertex will consist of the fit parameters as estimated by the user, the other two need to be generated within the program. If no assumptions are made about how close the user defined simplex point is to the global minimum in Δ^2 then it is valid to permit the other simplex points to be formed by any values of a_j that fall within the defined constraints. The bounded parameter space as defined in equation 5-11 simplifies matters, since one can choose a random number for the a'_j variables; $0 \leq a'_j \leq \pi$.

When the simplex routine in the fitting program has reached a minimum in Δ^2 the program presents a summary of the starting and ending values of Δ^2 and allows the user to decide whether to accept or reject the current fit and whether to restart minimisation using the current parameter values.

5.2.1.5 Concentration determination

Given the complexities in determining the integrated intensity of a Tsallis lineshape of general Γ and q algebraically [4] the integrated intensity of the fitted defect simulation(s) in EPR Wizard are calculated numerically from the individual (x_i,y_i) values, using a simple trapezium based integration method [10].

Since numerical integration is used the same truncation issues that would apply for numerical integration of the experimental data, as discussed in §5.1, must be considered. However, for the simulated data the potential exists to numerically integrate over the single generated pseudomodulated Tsallis lineshape and then, through knowledge of the relative intensities of each resonance line, the overall integrate intensity can be calculated. Since the single resonance line which is convolved with the stick spectrum is generated over the same scan range as the entire spectrum truncation problems will only appear when the scan width approaches that of a single resonance line. It is good experimental practice to scan sufficiently wide such that the baseline level can be observed, so this should not be an issue. Another related situation is when a scan is being conducted over *part* of spectrum, such that only a subset of the resonance lines from a particular defect are being

observed (e.g. using half-field spectra for quantitative measurements of NV^-). In this case determining the overall integrated intensity using the above method ensures that the correct overall intensity is obtained.

EPR Wizard allows the integrated intensity and scan parameters to be saved for a sample of known concentration. Once the integrated intensity for a different defect and/or sample has been determined the concentration can then be determined from equation 4-2.

5.3 Analysis

In this section three questions will be addressed with regards to the fitting method:

1. To what extent does generalising the EPR lineshape and accounting for modulation impact on the quality of fit and the determined integrated intensities (hence concentrations)?
2. How good is the program at deconvolving multiple EPR spectra which overlap?
3. How reproducible are quantitative EPR measurements when considering the fitting method and experimental factors?

When analysing the quality of fit of a synthetic EPR spectrum to experimental data a consideration of the degree of noise in the experimental data must be taken into account. A simple sum of the squares measurement does not this so, although it is still valid to obtain the best model by minimising this quantity, it does not provide a true picture of how well the model fits the experimental data. For this reason it is common to evaluate the sum of the squares normalised by the standard deviation (σ_i) of each data point in the experimental data set:

$$\chi^2 = \sum_{i=1}^{N} \left[\frac{y_i - y(x_i; a_1 \ldots a_M)}{\sigma_i} \right]^2 \tag{5-12}$$

The number of data points being fitted and the number of parameters being varied in the fit must also be considered. Increasing the number of points (N) would be expected to increase χ^2, whilst increasing the number of variables (M) raises the chance of obtaining a lower average deviation from the experimental values. Hence χ^2 is compared to the degrees of freedom, given by $\nu = N - M$ (in the case of

fitting an experimental EPR spectrum $N \gg M$, hence $\nu \approx N$). It is therefore helpful to define the *reduced* χ^2 measurement:

$$\chi^2_\nu = \frac{\chi^2}{N - M} \tag{5-13}$$

An "ideal" fit would be considered as one where the only source of deviation between data and calculation is normally distributed spectral noise. In this case χ^2_ν should be distributed about unity with a standard deviation of $\sqrt{2/(N-M)}$. As a result χ^2_ν provides a semi-quantitative measure of the goodness-of-fit.

To evaluate the effect of generalising the EPR lineshape on the goodness-of-fit and determined intensities a typical EPR spectrum obtained from the single-sector HPHT sample used for quantitative EPR measurements (§4.5), will be examined. Figures 5-5a and 5-5b illustrate the fits obtained using Lorentzian and Tsallis lineshapes respectively for the central N_s^0 resonance line observed with $\mathbf{B} \| \langle 100 \rangle$. χ^2_ν values were determined using equation 5-12, with the standard error (σ) determined from the standard deviation of 400 experimental data points which were situated far away from any EPR lines. To investigate the dependence of χ^2 with q in more detail figure 5-6a has been constructed by fixing q at a particular value and then allowing EPR Wizard to optimise the amplitude, width and magnetic field offset of the resonance lines. From this data it is apparent that neither a Lorentzian nor a Gaussian provides a satisfactory fit to the experimental spectrum. Allowing q (i.e. the form of resonance line) to vary leads to a significant improvement in the quality of fit; χ^2_ν is reduced by more than a factor of ten compared to a Lorentzian line.

From the fits obtained to construct figure 5-6a it is possible to determine the integrated intensity as a function of the lineshape parameter, q. As shown in figure 5-6b there is a strong dependence of the intensity with the q parameter and assuming a Lorentzian lineshape would lead to an overestimation of the integrated intensity by ~ 30%. One could envisage the situation where the reference sample intensity was determined assuming $q = 2$ and this intensity was used to obtain the concentration of defect in a different sample that had a true Lorentzian form. This would lead to a systematically low result for the concentration of the paramagnetic centre of interest. The strong dependence of the intensity with q also demonstrates the importance of good signal to noise in the wings of the EPR spectrum, since

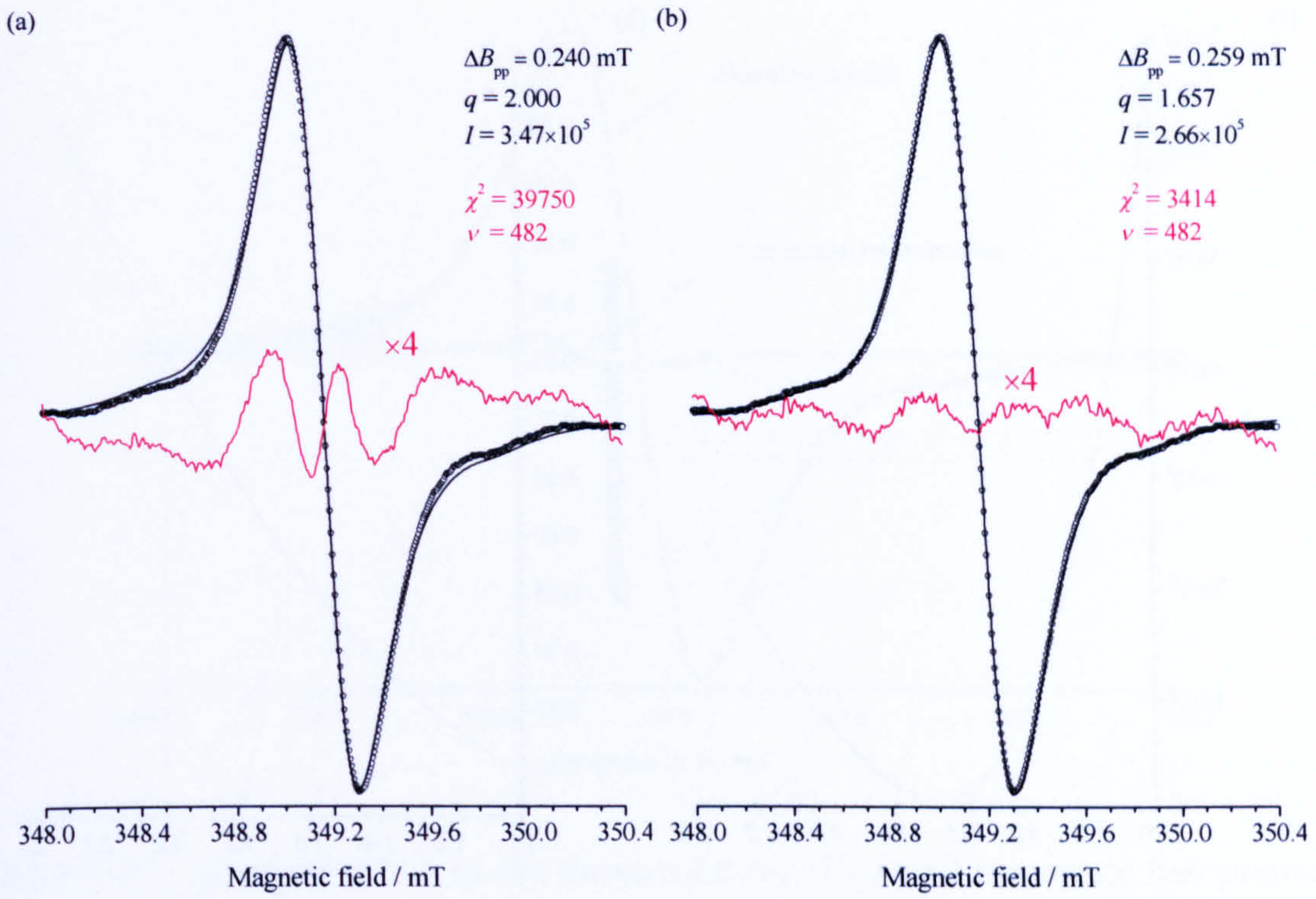

Figure 5-5: Comparison of quality of fit obtained using (a) Lorentzian and (b) Tsallis lineshapes obtained for the central N_s^0 line observed in the HPHT reference sample (240 ppm) used for quantitative EPR measurements. In both (a) and (b) the residual has been magnified by a factor of four.

these are required in order to accurately determine the true form of the resonance lines.

Even with the variation of the form of the EPR lineshape the value of χ^2_ν is greater than unity ($\chi^2_\nu \approx 7$ from figure 5-5b), so from the earlier discussions of this goodness-of-fit parameter the best fit obtained would still not be regarded as ideal, since the discrepancies between the data and model cannot be explained by normally distributed experimental noise. A simple $y = mx + c$ type baseline is permitted to account for any broad cavity background signals but even with such correction the fit is not improved. The deviation away from the model is caused by a slight asymmetry in the experimentally observed resonance lines, which is visible due to the good signal/noise. One possible explanation for this is the presence of additional EPR signals resulting from defect(s) with similar g values. However, since all the N_s^0 resonance lines show a similar asymmetry it is more likely to arise from a slight mixture of dispersion components into the signal.

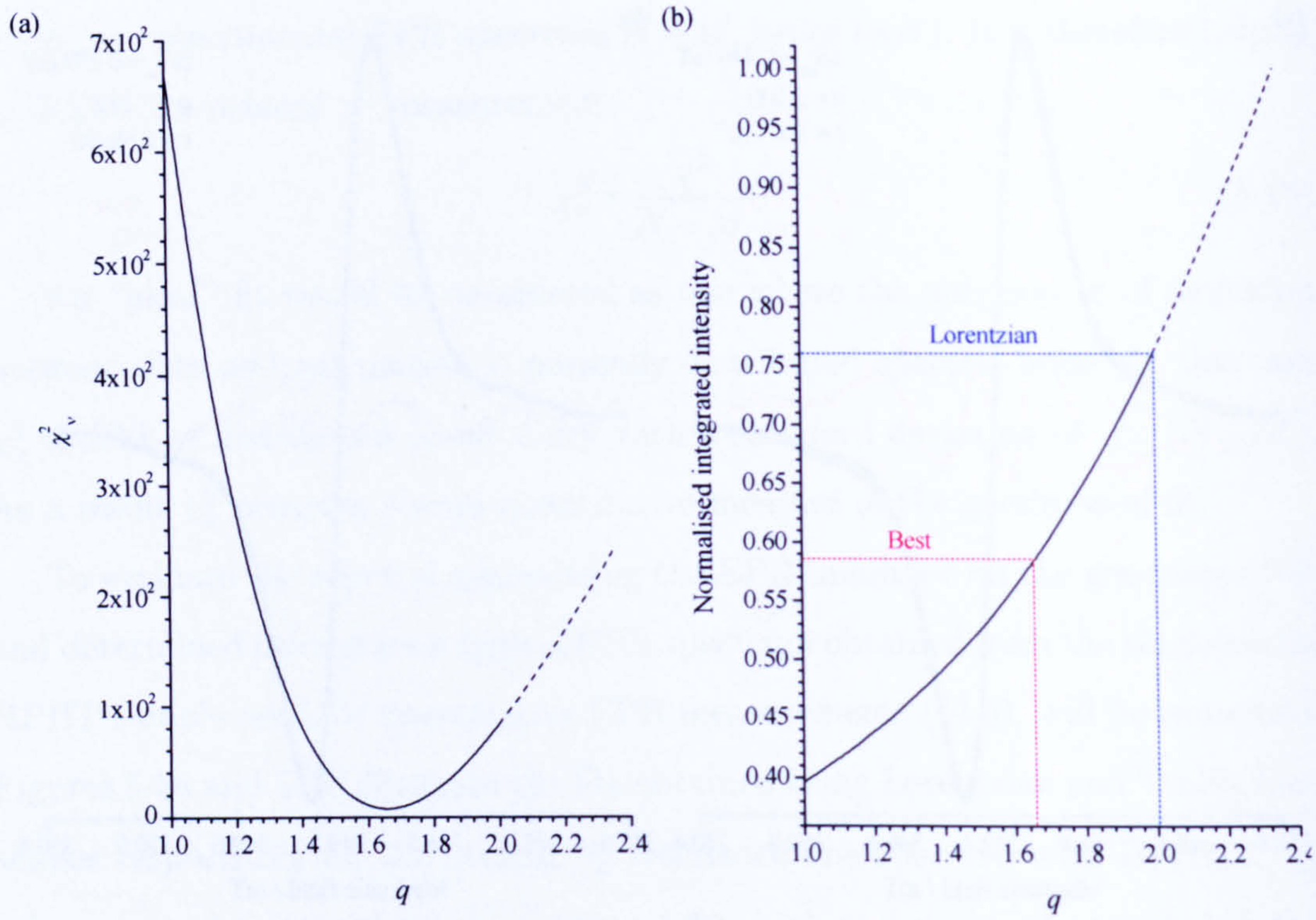

Figure 5-6: (a) Dependence of χ^2_ν with the Tsallis line parameter q. At each point q was fixed and the other parameter (linewidth, offset and amplitude) were allowed to vary. (b) Normalised integrated intensity as a function of q. Both plots were obtained from the fitting of the central N_s^0 resonance line observed in the HPHT reference sample (see figure 5-5).

The discussion of the potential for smaller resonance lines to be hidden under other broad resonances raises the question regarding the ability of the fitting algorithms to deconvolve multiple EPR spectra which partially, or entirely overlap. It was shown in figure 5-1 that partially resolved spectra can be successfully fitted in the case where the spectra are of comparable size, but what about the case when a small resonance line is entirely covered by a much larger background signal?

To test the ability of the program to deconvolve such a resonance line a single Lorentzian line of linewidth 0.15 mT and peak-peak amplitude which is 5% of the central resonance line has been added to the experimental reference sample spectrum shown in figure 5-5. The Nelder-Mead fitting algorithm was then used to attempt to find the best fit to this created spectrum using the simulations of N_s^0 and a single resonance line. The starting simulation had the two fitted spectra centred on the central N_s^0 resonance line in the experimental data and

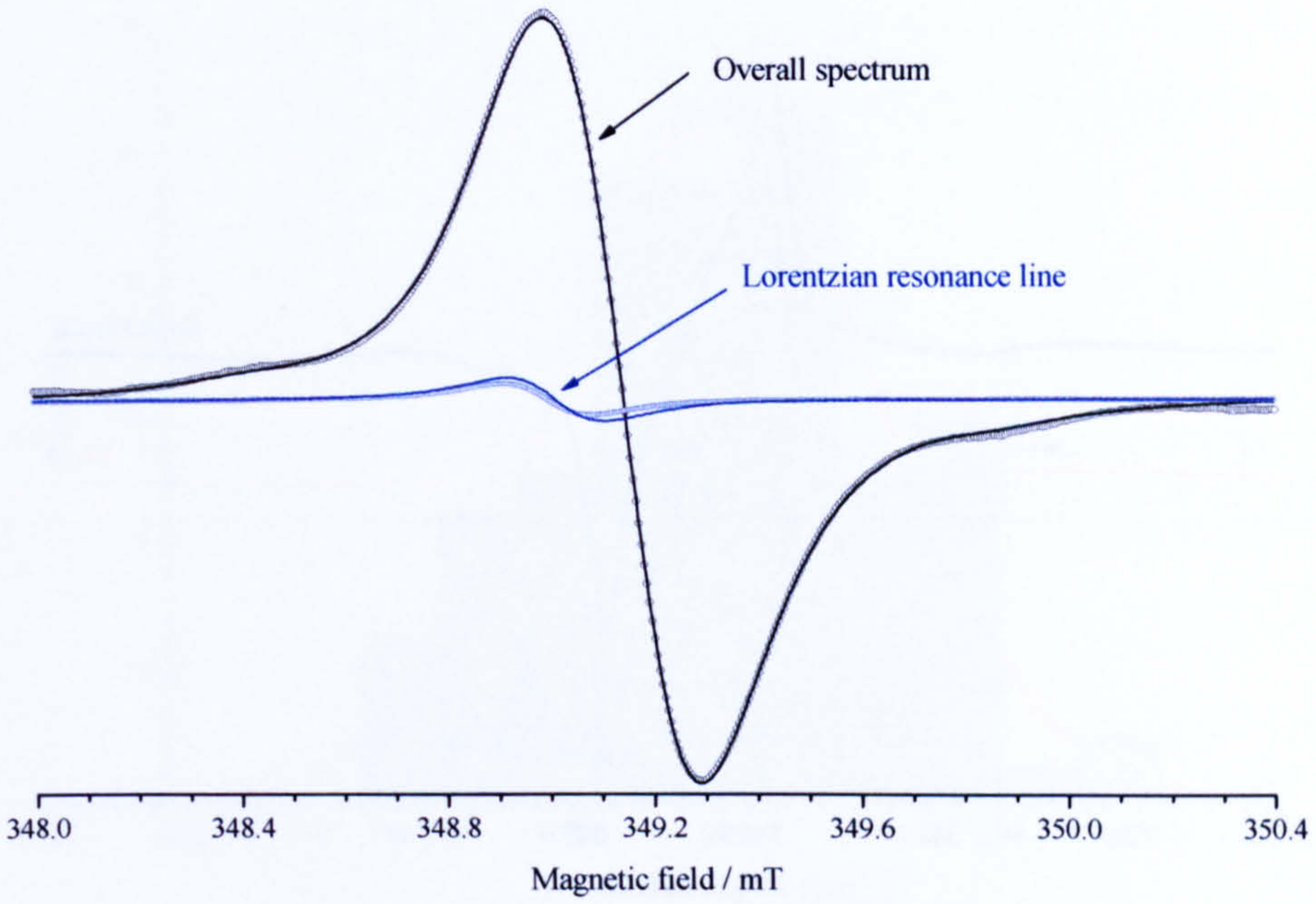

Figure 5-7: Demonstration of the deconvolution of a small resonance line present underneath a large background signal using pseudomodulated Tsallis lineshapes. In this example a synthetic resonance line of linewidth 0.15 mT and a peak-peak amplitude 5% of the central N_s^0 resonance line has been added to an experimental spectrum obtained from the reference sample. The points represent the created spectrum and the solid lines illustrate the fit obtained to this data using least-squares fitting.

both simulated spectra had equal peak-peak amplitudes.

As shown in figure 5-7 the fitting algorithm managed to locate the small resonance line and a reasonable fit is obtained. The deviation between the position of the synthetic and fitted resonance lines can be explained by the slight asymmetry of the original experimental N_s^0 resonance line, as discussed above. However, it is apparent that the generalisation of the EPR lineshape is critical to the success of the recovery of such small resonance lines; the added resonance line is comparable to the size of the residual seen when fitting the reference sample spectra assuming a Lorentzian form to the resonance lines (figure 5-5a) and hence such a signal could never be recovered using this lineshape.

For the reference sample $\Delta B_{pp} \rightarrow 0.264(4)\,\mathrm{mT}$ as $B_m \rightarrow 0$. Hence, with a modulation amplitude of 0.1 mT distortion in the shape of the resonance line is not readily apparent and one would expect a lineshape approaching that of the first

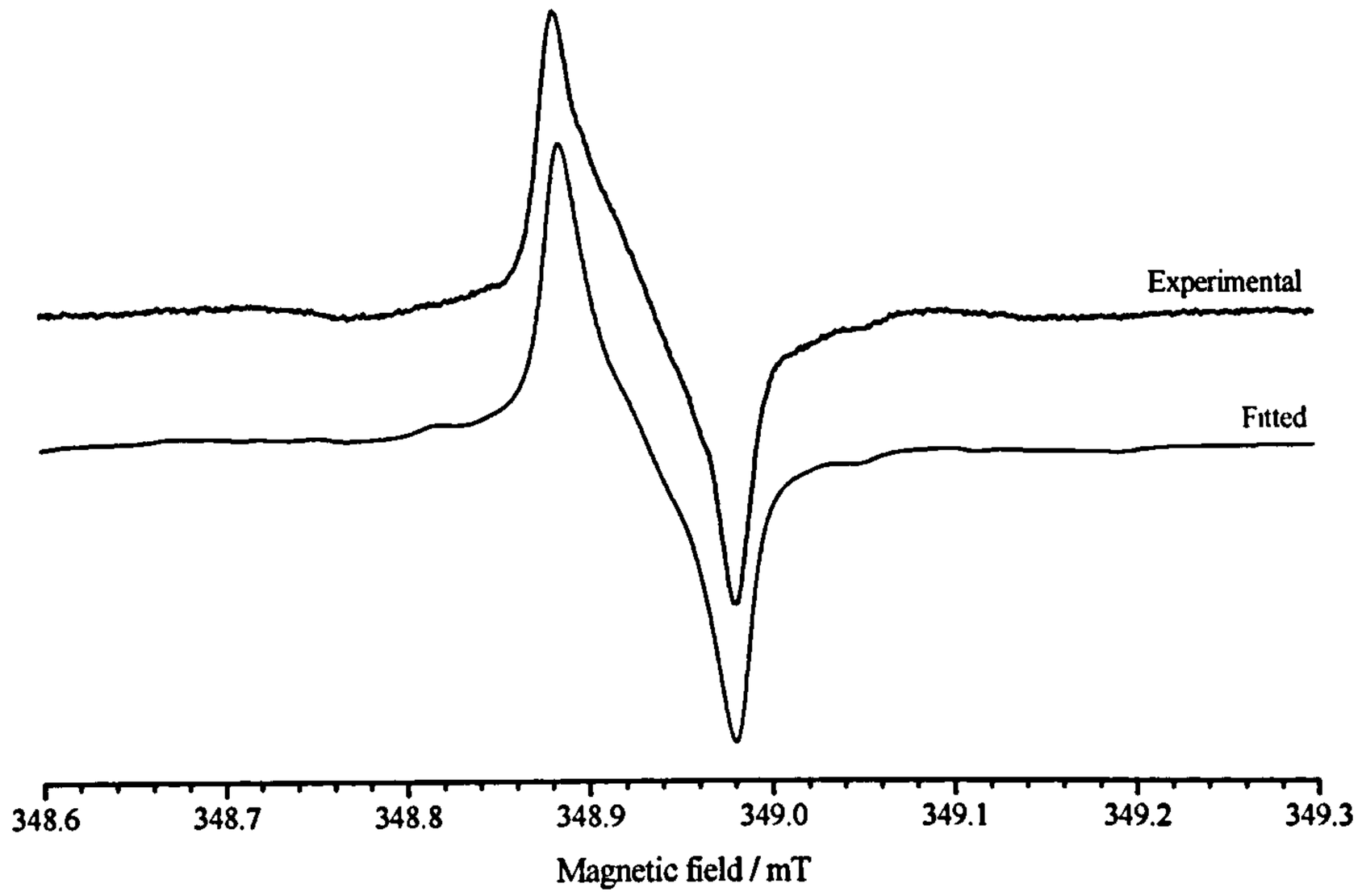

Figure 5-8: Example of fit obtained with an over-modulated EPR resonance line ($B_{\mathrm{m}}/\Delta B_{\mathrm{pp}(0)} \approx 10$) using pseudomodulation of a Tsallis lineshape.

differential of the simulated Tsallis lineshape. Even so, if pseudomodulation is not utilised for the fitting of the reference sample spectra shown in figure 5-5 then χ^2_ν increases by 10%. A more dramatic example of the success of pseudomodulation is shown in figure 5-8.

So far it has been shown that the pseudomodulated Tsallis lineshape fitting procedure results in a improved fit to the EPR reference sample spectra and hence gives a more accurate measurement of the integrated intensity of the N_s^0 resonance lines for quantitative EPR. However, the *reproducibility* of such concentration measurements, now that a systematic fitting method is in place, have not been discussed. One must consider both experimental errors and the robustness of the minimisation algorithm used for fitting.

To investigate the magnitude of the errors associated with quantitative measurements a large number (> 100) of room-temperature spectra have been collected over a period of one year. All data was obtained using an identical experimental setup; the Bruker EMX spectrometer (9.75 GHz) was used with the spherical SHQ cavity and the sample was mounted in a twin-axis goniometer and centred using the teflon inserts (see §4.2). In this way the experimental errors should be

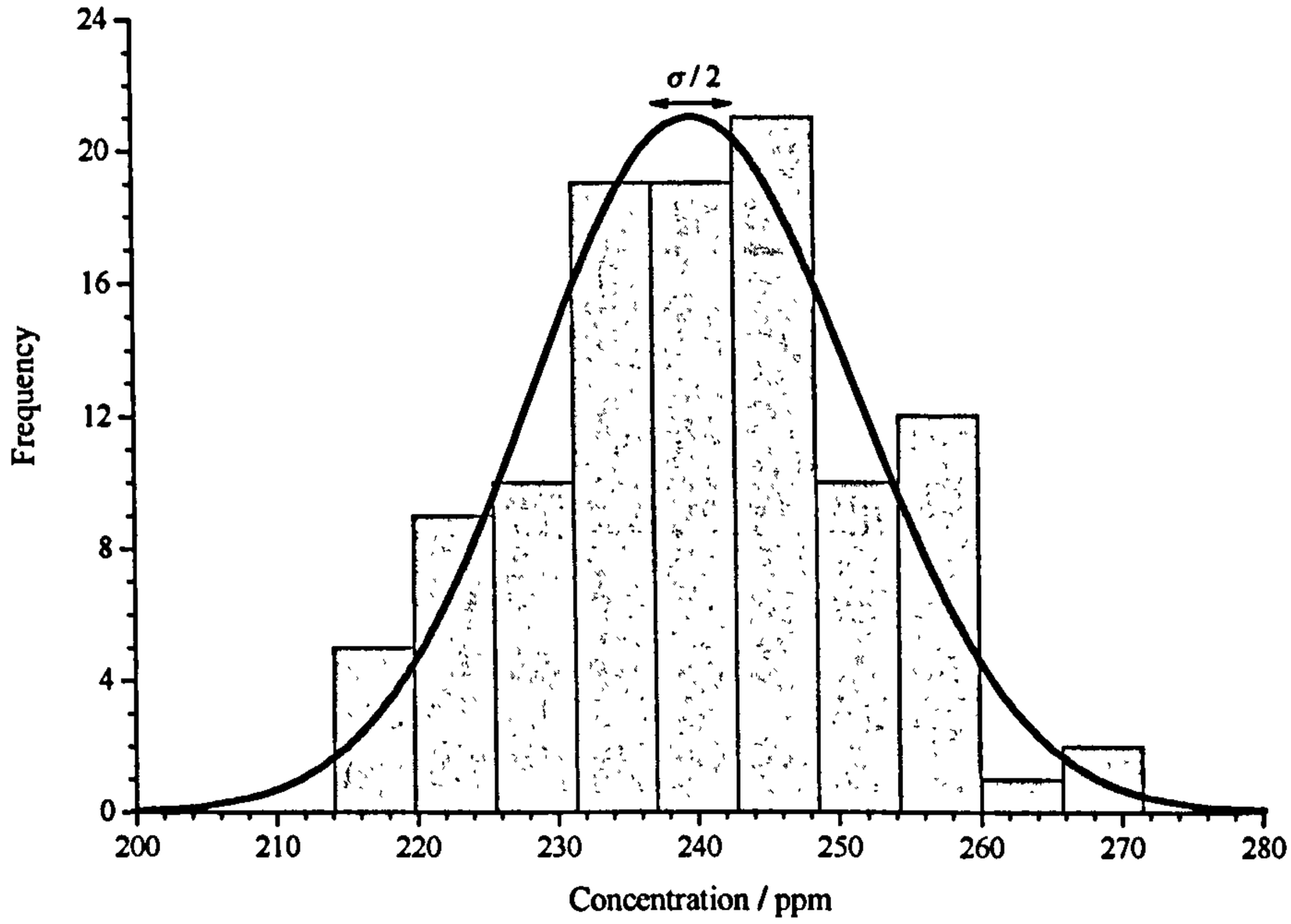

Figure 5-9: Histogram showing the reproducibility of quantitative EPR measurements on the reference sample using the developed fitting program. The mean of the integrated intensities are normalised such that the concentration of N_s^0 is 240 ppm (§4.5). The width of each bar has been set to half the standard deviation (σ). The curve shows a normal distribution (Gaussian) lineshape.

minimised.

Both the linewidth (ΔB_{pp}) and q were found to be consistent; $\overline{\Delta B_{pp}} = 0.258$ mT and $\bar{q} = 1.657$, with both having a standard deviations (σ) of 0.004. Figure 5-9 shows a histogram which has been constructed to illustrate the distribution in determined concentrations. The concentration of the reference sample is known to be 240 ppm, hence the mean was set to this value. The standard deviation, σ, was found to be ~ 12 ppm and the outlying data points were within 11% of the mean. This establishes that, with a constant experimental setup and the fitting program developed, the standard error of quantitative EPR measurements on a given sample is around 5%.

The Nelder-Mead simplex algorithm was found to perform well in the case of varying the four parameters that can be adjusted for a single defect; the amplitude, q, ΔB_{pp} and the magnetic field offset. Even in the case where the starting solution is a long way from the global χ^2 minimum (e.g. $\chi^2_{start} \sim 10^3 \times \chi^2_{min}$) the routine is able to successfully locate the optimum fit, typically in < 100 iterations. Since

differentials of χ^2 with respect to the different varied parameters do not need to be calculated in the simplex method iterations are quick; 100 iterations take around 30 seconds on a "typical" office PC. However, in the case of > 4 variables, i.e. when fitting multiple defects the number of iterations required increases dramatically and it is sometimes observed that the simplex algorithm becomes stuck in a local mimima, due to increased complexity in the χ^2 parameter space. As a result it is a good idea to restart the fitter from the determined best-fit point, to check to see if this is truly the global-minimum.

5.4 Conclusions

The developed EPR spectrum fitter, "EPR Wizard", which utilises a Tsallis lineshape and pseudomodulation, has been shown to produce significant improvements in the quality of fit when examining experimental data collected from a single-sector HPHT diamond containing N_s^0. This is important as it results in an integrated intensity which more closely reflects that of the experimental data, hence improving the accuracy of quantitative measurements. It has also been demonstrated that the generalisation of the EPR lineshape allows small overlapping resonance lines to be more readily resolved from large background signals.

Using spectra collected over a period of one year the reproducibility in quantitative results on a given sample is excellent, with a standard error of just 5%. This not only reflects the reproducibility in the experimental setup, but also the robustness of the Nelder-Mead simplex algorithm which is utilised to obtain the optimum fit to the EPR spectrum (by minimising the sum of the squares). Although the reproducibility for any given sample is excellent systematic errors due to experimental factors may be present when using the reference sample integrated intensity to determine the concentration of a paramagnetic defect in a *different* sample (see §4.5).

The methods presented here have allowed quantitative EPR measurements to become routine for this research group. The EPR spectrum fitting program has been used for the quantitative EPR measurements presented in this thesis and has been used extensively recently to investigate relationships between defect concen-

trations in CVD diamond [14]. However, it is evident that there are situations where the approach described here will not lead to an accurate reproduction of an EPR spectrum:

- If a sample contains regions with different concentrations of a particular defect then the resulting spectrum may be comprised of overlapping resonance lines which have differing widths and/or form. Previously a relationship between the linewidth and concentration has been established [15], but no dependence of the lineshape with the concentration has been identified. With systematic fitting possible for a generalised lineshape function this is a subject which could now be investigated.
- In cases where motional averaging between different configurations of a defect occurs. In this situation, dependent on the symmetry of the defect and the orientation of the applied magnetic field, the static spin-Hamiltonian parameters for a defect may no longer give rise to the experimentally observed position and intensities of the resonance lines. This subject is discussed in chapter 9.
- In cases where there are unidentified EPR spectra which overlap with the resonance lines of interest. However, with the improvement in the quality of fit the ability to uncover resonance lines which reside under previously identified spectra is increased.

There are also aspects of the program which could be improved from a functional and performance standpoint. Currently the fitting program is separate to EPR Sim (§4.4.3) and, as a result, it is time-consuming to obtain the required data in terms of the position in field and relative amplitude of resonance lines and import these into EPR Wizard each time a new orientation/defect or frequency band is used. Therefore it is planned for the functionality of both EPR Sim and EPR Wizard to be combined into a *joint* simulation and fitting program.

The ease of implementation of the Nelder-Mead routine into the fitting program made this an obvious first choice, but investigation of its convergence properties in this application compared to other optimisation methods would be helpful.

References

[1] J. A. Weil, J. R. Bolton, and J. E. Wertz, *Electron Paramagnetic Resonance* (Wiley-Interscience, New York, 1994).

[2] M. J. Mombourquette, J. A. Weil, and D. G. McGavin, *EPR-NMR user's manual*, version 6.1 (University of Saskatchean, Canada, 1997), available from M. J. Morbourquette, Queen's University, Kingston, ON K7L 3N6, Canada (see www.chem.queensu.ca/eprnmr/).

[3] P. R. Bevington and D. K. Robinson, *Data Reduction and Error Analysis for the Physical Sciences* (McGraw-Hill, New York, 1969), 3rd ed.

[4] D. F. Howarth, J. A. Weil, and Z. Zimpel, J. Magn. Reson. **161**, 215 (2003).

[5] P. W. Anderson, J. Phys. Soc. Jpn. **9**, 316 (1954).

[6] P. W. Anderson and P. R. Weiss, Rev. Mod. Phys. **25**, 269 (1953).

[7] B. H. Armstrong, J. Quant. Spectrosc. Ra. **7**, 61 (1967).

[8] C. Tsallis, S. V. F. Levy, A. M. C. Souza, and R. Maynard, Phys. Rev. Lett. **75**, 3589 (1995).

[9] J. S. Hyde, M. Pasenkiewicz-Gierula, A. Jesmanowicz, and W. E. Antholine, Appl. Magn. Reson. **1**, 483 (1990).

[10] K. F. Riley, M. P. Hobson, and S. J. Bence, *Mathematical methods for physics and engineering* (Cambridge University Press, Cambridge, 2000).

[11] W. H. Press, S. A. Teukolsky, W. T. Vetterling, and B. P. Flannery, *Numerical Recipes in C* (Cambridge University Press, 1996), 2nd ed.

[12] J. A. Nelder and R. Mead, The Computer Journal **7**, 308 (1965).

[13] D. M. Olsson and L. S. Nelson, Technometrics **17**, 45 (1975).

[14] R. J. Cruddace, Ph.D. thesis, University of Warwick (2007).

[15] J. A. van Wyk, E. C. Reynhardt, G. L. High, and I. Kiflawi, J. Phys. D Appl. Phys. **30**, 1790 (1997).

Chapter 6

Silicon-related defects in diamond

6.1 Background and motivation for study

Silicon is a frequent accidental contaminant in CVD diamond. Despite this, to-date the only optical or EPR feature in diamond which has been conclusively shown to involve silicon is the optical centre observed at 1.682 eV (737 nm) in photoluminescence and absorption, discussed in §2.2.3.1. Goss *et al.* have shown that a negatively charged split-vacancy structure, with the silicon atom at the centre of a divacancy (figure 6-1), referred to here as (V-Si-V)$^-$, is compatible with the fine structure observed around 1.682 eV [1, 2].

Polarised PL [3], uniaxial stress [4] and Zeeman splitting [4] measurements on the 1.682 eV band have suggested that the defect responsible has tetragonal or lower symmetry. Both the positive and negative charge states of (V-Si-V) are subject to a Jahn-Teller distortion which would lower the symmetry [2]. Hence the band may indeed originate from (V-Si-V)$^-$, but further experimental and theoretical work is required to confirm this association. Due to the remaining debate over the symmetry of the centre it will be referred to as the 1.682 eV defect in this chapter.

In previous studies using EPR three defects have been detected in CVD diamond and attributed to the incorporation of silicon; an $S = 1$ defect referred to as KUL1, and two $S = \frac{1}{2}$ centres labelled KUL8 and KUL3 (§2.2.3.1). These were assigned to (V-Si-V)^0, (V-Si-V)$^-$ and a neutral divacancy, where one of the six basal carbon atoms is replaced by silicon and one dangling bond (remote to the silicon atom) is passivated by a hydrogen atom, respectively [5–7]. KUL1, KUL3 and KUL8 have been observed in polycrystalline CVD diamond deposited on silicon substrates. KUL1 and KUL3 have also been observed in single-crystal CVD films grown on iridium [8].

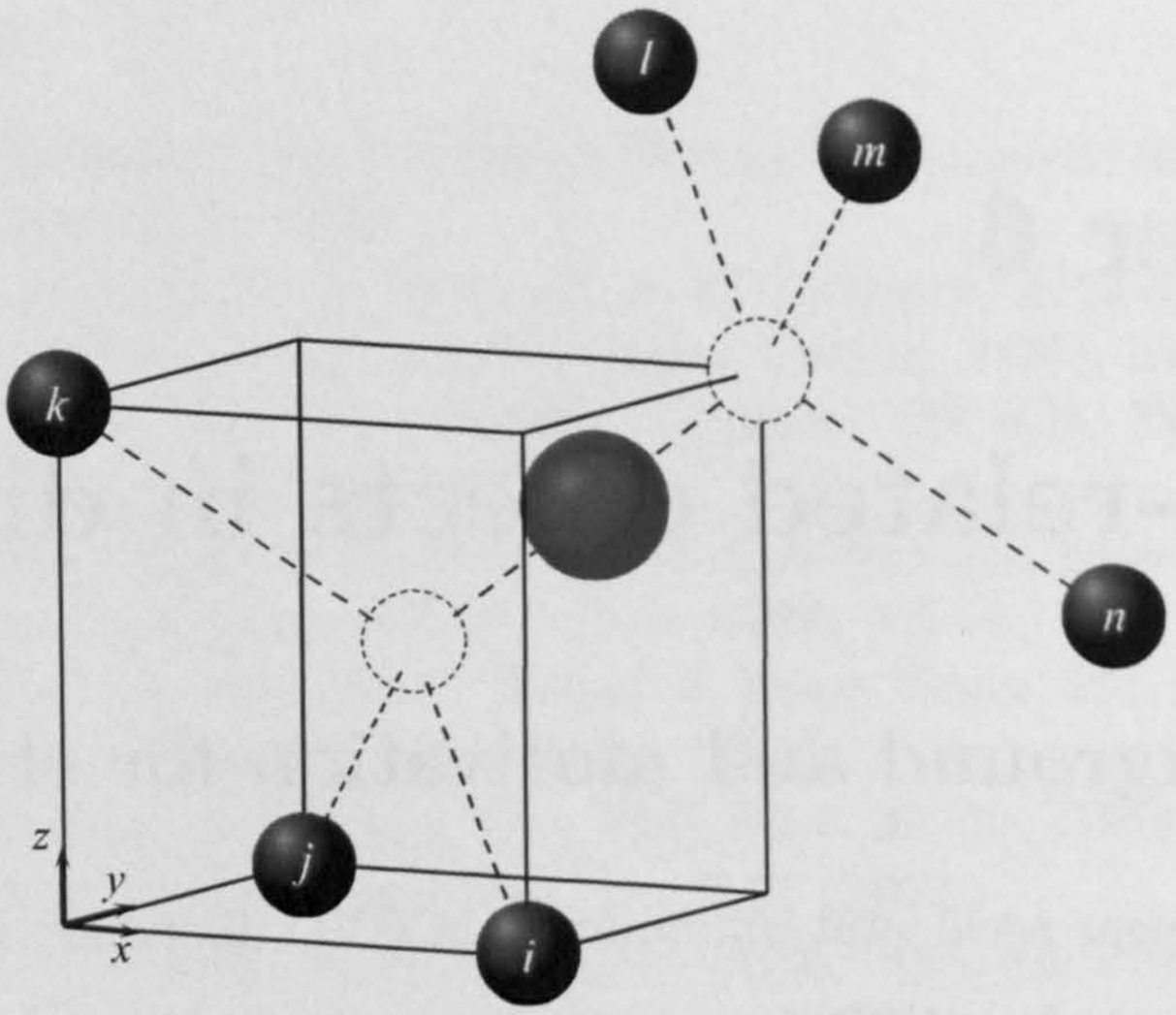

Figure 6-1: The structure of the silicon split-vacancy centre (V-Si-V). The black spheres (labelled i–n) represent carbon atoms, the central blue sphere the relaxed silicon site, and the dashed circles indicate the positions of the vacancies.

The $(\text{V-Si-V})^0$ model for KUL1 permits definite predictions regarding the hyperfine structure of this defect to be made. As apparent from figure 6-1, there are six equivalent nearest-neighbour carbon atoms and a single silicon atom. Both ^{13}C and ^{29}Si (with natural abundances 1.1% and 4.7%, respectively) have $I = \frac{1}{2}$, hence satellites from the hyperfine interactions of these two isotopes (centered on transitions from ^{28}Si, ^{30}Si and ^{12}C defects) would be expected. With the applied magnetic field ($\mathbf{B}$) in a {110} plane a maximum of three pairs of ^{13}C satellites would be expected and, since there is only one possible site for the ^{29}Si atom, a single pair of satellite lines from ^{29}Si would be observed.

The experimental data for the hyperfine structure of KUL1 in the literature [5, 8] does not match with the predictions for the $(\text{V-Si-V})^0$ model. Tentative assignment of one pair of hyperfine satellites was made to ^{29}Si, but the remaining satellites did not suggest six equivalent carbon atoms; instead a unique site and two equivalent sites were reported. Due to the apparent trigonal symmetry of KUL1 it is difficult to construct a defect that is consistent with the previously reported ^{13}C hyperfine structure [5, 8]. The uncertainty regarding the assignment of the hyperfine structure of this defect also means that the main evidence for the involvement of silicon in this defect is the observation that polishing the substrate

side of diamond deposited on silicon substrates led to a reduction in intensity of the KUL1 spectra. Hence it is apparent that further EPR investigations are required to prove the involvement of silicon in this defect and unambiguously identify its structure. Additionally, since no hyperfine satellites have been resolved for KUL8 the assignment of this defect to the negative charge state of (V-Si-V) [6, 7] (and therefore to the theoretical model for the 1.682 eV defect) should be regarded as tentative.

Recent theoretical modelling of silicon-related defects in diamond have provided predictions for the ^{13}C and ^{29}Si hyperfine parameters for $(V\text{-}Si\text{-}V)^-$ and $(V\text{-}Si\text{-}V)^0$ [2]. These studies have also assigned KUL3 to $(V\text{-}Si\text{-}V)^0$ decorated with a nearby hydrogen atom, in contrast to the model suggested by Iakoubovskii *et al.* [5, 8].

Interest in the 1.682 eV defect has been reinvigorated by the use of colour centres in diamond as single photon sources. Time-resolved and high-resolution photoluminescence (PL) measurements have shown that the 1.682 eV band has a very short photoluminescence lifetime of 1–4 ns (compared to the theoretical value of ~ 3 ns [1]) and a narrow emission bandwidth of about 5 nm [9]. The combination of these two properties means that this defect is potentially an attractive centre with which to produce a single photon source. Recently stable single photon emission has been observed from single 1.682 eV centres produced by controlled implantation of Si^{2+} ions in type IIa diamond [10].

Work has also demonstrated that controlled silicon-doping of CVD diamond (see §2.1.2.3) can be used for production of near-colourless synthetic gem-quality diamond for which the 1.682 eV luminescence line is readily detected [11]. This could be used as an easily detectable "fingerprint" for the identification of synthetic diamond, without having to physically mark the diamond itself. Such doping experiments have also demonstrated that the controlled incorporation of silicon in diamond, at least under certain growth conditions, can be advantageous as it reduces the uptake of nitrogen [12]. Both these findings demonstrate the importance of gaining a greater understanding of the incorporation of silicon in diamond and the impact that it has on the CVD growth mechanism.

In this chapter results obtained by multi-frequency EPR on SC-CVD diamond

samples which have been deliberately doped with silicon by the addition of silane to the growth gases are reported. Isotopic enrichment of the silane was used to conclusively identify silicon as a constituent of the defects studied, via observation of the ^{29}Si hyperfine structure. Analysis of the orientation dependence and relative intensities of the ^{13}C and ^{29}Si hyperfine satellites has enabled conclusive determination of defect symmetries and structures. Additional measurements obtained from photoluminescence, UV/visible/NIR absorption and secondary-ion mass spectroscopy are also used to infer further information regarding the incorporation of silicon in diamond.

6.2 Experimental details

The SC-CVD diamond samples used for the studies presented in this chapter have been homoepitaxially grown by Element Six Ltd on {100} or {110} oriented single-crystal diamond substrates. During growth the samples were doped with silicon by the addition of silane to the reactor gases. Silane containing ^{29}Si in natural abundance (4.7%) or enriched to 90% (supplied by Voltaix Inc. USA) was used in a series of growth runs. After deposition the substrates were removed to leave freestanding plates, which were then cut and polished to remove twinned and poor quality material from the edges.

Room-temperature EPR measurements have been performed on these samples using the EMX/EMX-E Bruker X-band spectrometers, described in §4.2 and the custom-built Q-band spectrometer (§4.3). The concentrations of all paramagnetic defects found in the examined samples have been determined from room-temperature X-band EPR spectra, using the fitting method outlined in chapter 5. To negate the problem of microwave power saturation, spectra at various powers between 0.2 nW and 3 mW have been obtained.

To investigate changes in the intensity of the observed EPR spectra as well as the variation of the spin-Hamiltonian parameters, scans have been made at a range of temperatures between 7 K and 300 K, using the low-temperature X-band experimental setup (§4.2.2).

For initial characterisation of the sample PL measurements were made us-

ing a commercial Renishaw Raman In-via microscope with a 514.5 nm (2.410 eV) Argon-ion laser. Measurements were also made using 785 nm (1.579 eV) excitation, provided by a solid-state diode laser. Spectra were obtained at ~ 10 K in a continuous flow cryostat (Oxford Instruments LHe microstat).

For an estimate of the concentration of the 1.682 eV defect UV/visible/NIR absorption measurements were performed at the Diamond Trading Company (Maidenhead, UK), using a Perkin Elmer Lambda-19 spectrometer with a 0.7 mm aperture, with the sample at ~ 90 K in a liquid nitrogen cryostat. Results from secondary-ion mass spectroscopy (SIMS) measurements of the total silicon concentration were provided by the Diamond Trading Company.

For an additional estimate of the N_s^+ concentration Fourier transform infrared (FTIR) absorption measurements were acquired over the mid infra-red region at a resolution of 1 cm^{-1} using a Perkin Elmer Spectrum-GX spectrometer equipped with a beam condenser. All measurements were made at room temperature. Analysis of the absorption spectra enabled the concentration of N_s^+ to be estimated using the previously determined absorption coefficient [13] (5.5±1 ppm of N_s^+ gives rise to an absorption coefficient of 1 cm^{-1} at 1332 cm^{-1}).

6.3 Results

6.3.1 Sample characterisation

The results obtained from three SC-CVD diamonds will be discussed in this chapter, which will be referred to as samples A, B and C. Sample A was grown on a {110} oriented substrate and doped with silicon using silane containing the natural abundances of silicon isotopes. Samples B and C were both grown with the addition of silane isotopically enriched to ~ 90% ^{29}Si. Sample B was grown on a {100} substrate, whilst a {110} oriented substrate was used for the growth of sample C. All three samples were examined as grown, after cutting and polishing.

The 1.682 eV ZPL, observed in PL measurements using 514.5 nm (2.40 eV) excitation, was found to be strong in all the samples examined (see figure 6-2 for a representative spectrum). In all three samples it was observed that $NV^0 \gg$

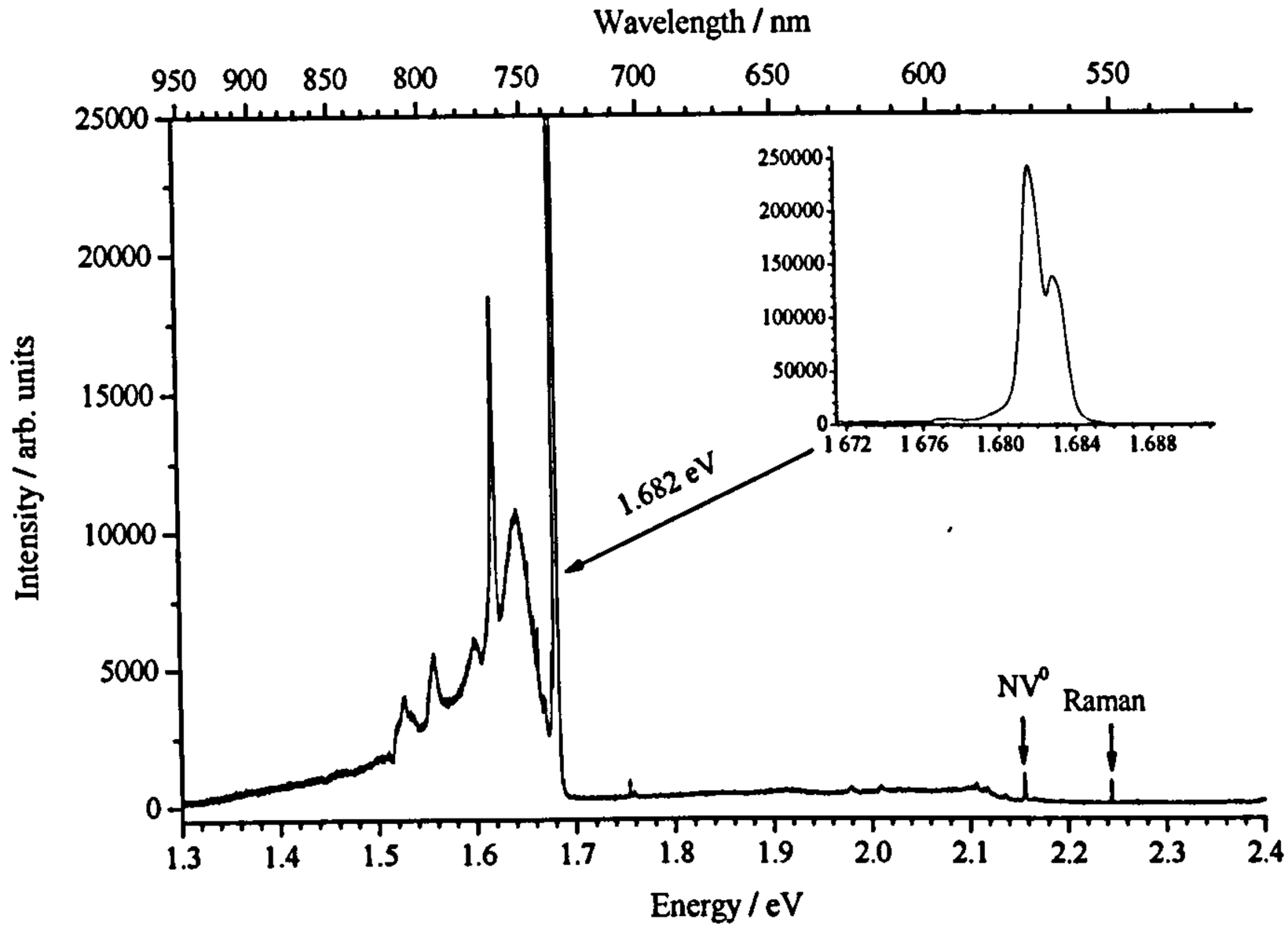

Figure 6-2: A PL spectrum obtained from sample C at 10 K using 514.5 nm (2.410 eV) excitation. The ZPLs at 1.682 eV (associated with silicon incorporation) and 2.156 eV (associated with NV^0) are labelled. At this excitation energy the Raman line occurs at 2.245 eV.

NV^-, inferred from the presence of a ZPL at 2.156 eV (NV^0) and the lack of any detectable photoluminescence at 1.945 eV (NV^-). Near infra-red measurements using the 785 nm (1.579 eV) laser revealed an additional pair of lines in the near infra-red region of the spectrum, at 1.310 eV (946.5 nm) and 1.303 eV (951.3 nm) (see figure 6-3). These features were present in all the samples examined and are further discussed in §6.4.3.

Initial X-band EPR room-temperature measurements were taken with the applied magnetic field (**B**) oriented along ⟨111⟩. With this orientation the spectra were dominated by a four lined EPR spectra, with the smallest, outermost lines, split by around 71.3 mT (see figure 6-4 for an example spectrum, obtained from sample A). Comparing the EPR spectra with the published data for KUL1 [8] revealed that this set of resonance lines could be assigned to this defect. An additional, weaker spectrum, observed around $g = 2$ (348 mT) could be identified as KUL3. In all three samples KUL1 and KUL3 were present in detectable concentrations. KUL8, however, was not detected in any of the samples examined.

With **B** ∥ ⟨100⟩ N_s^0 could also be readily detected by EPR in samples B and C ,

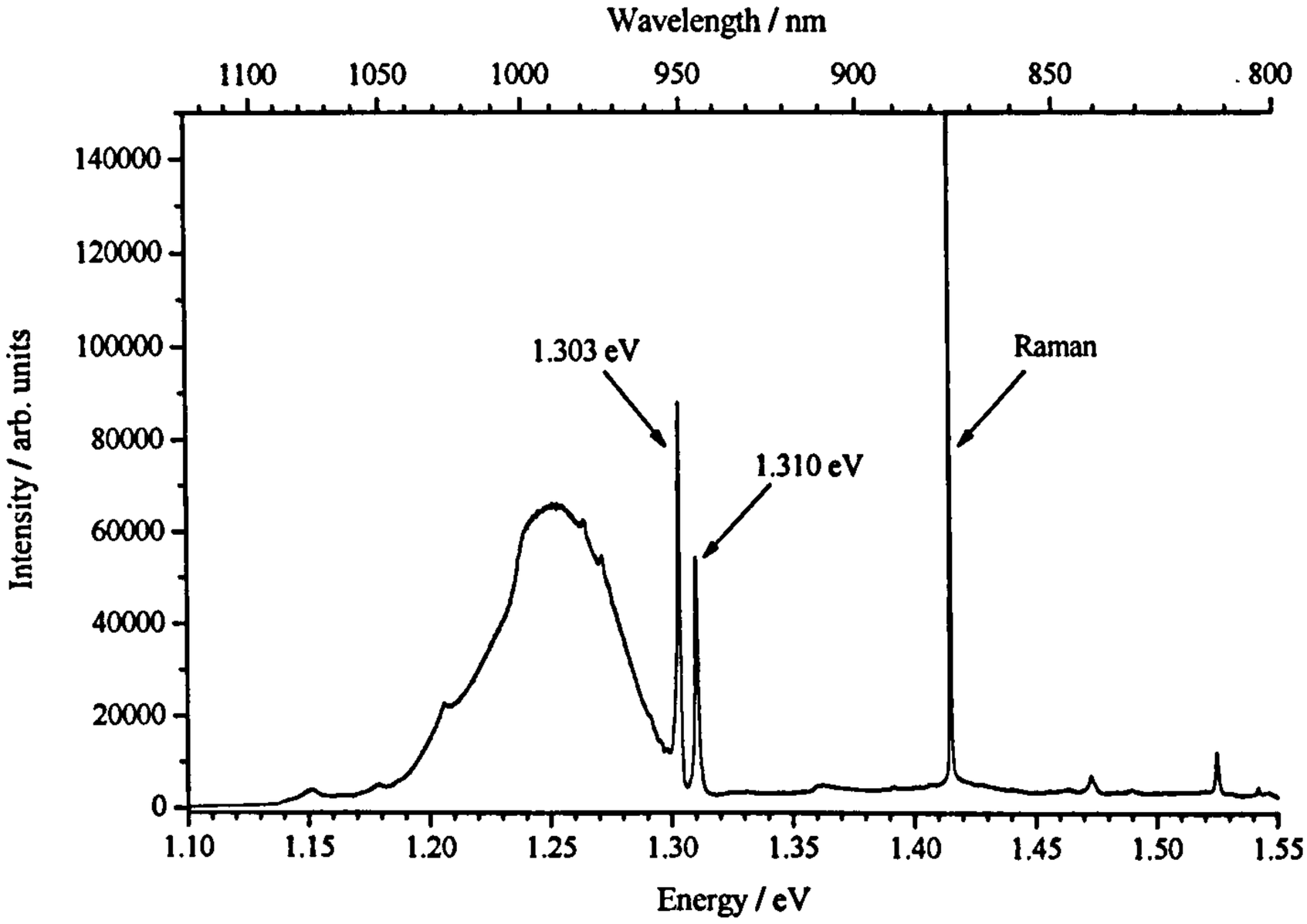

Figure 6-3: A PL spectrum obtained from sample C at 10 K using 785 nm (1.579 eV) excitation clearly showing lines at 1.310 eV and 1.303 eV.

whilst in sample A no signal from N_s^0 was apparent, hence only an upper limit can be quoted for the concentration in this sample. Scans at this orientation were also taken at half field (170 mT) to check for the presence of NV^- and other defects with $S \geq 1$. No resonance lines attributed to NV^- could be observed during long scans, imposing an upper limit for the concentration of ~ 1 ppb. This is consistent with the lack of a ZPL at 1.945 eV in the PL measurements. Concentrations for the different defects in the samples are given in table 6-1.

Absorption at 1332 cm^{-1} was not observed in sample A, but in samples B and C the absorption peak was sufficiently large to permit an estimation of the concentration of N_s^+. In both these samples $[N_s^+]$ was of the order of 1 ppm, hence $[N_s^+] \gg [N_s^0]$. Given the concentration of $[N_s^0]$ from EPR it is not surprising that no absorption at 1130 cm^{-1} could be detected in any of the examined samples. The variation in the nitrogen content between the sample A compared to B and C can be explained by the degree of nitrogen contamination in the two sources of methane (one containing natural abundance of silicon isotopes and one enriched with ^{29}Si). In the case of the ^{29}Si enriched source it is known that the nitrogen content was significantly higher.

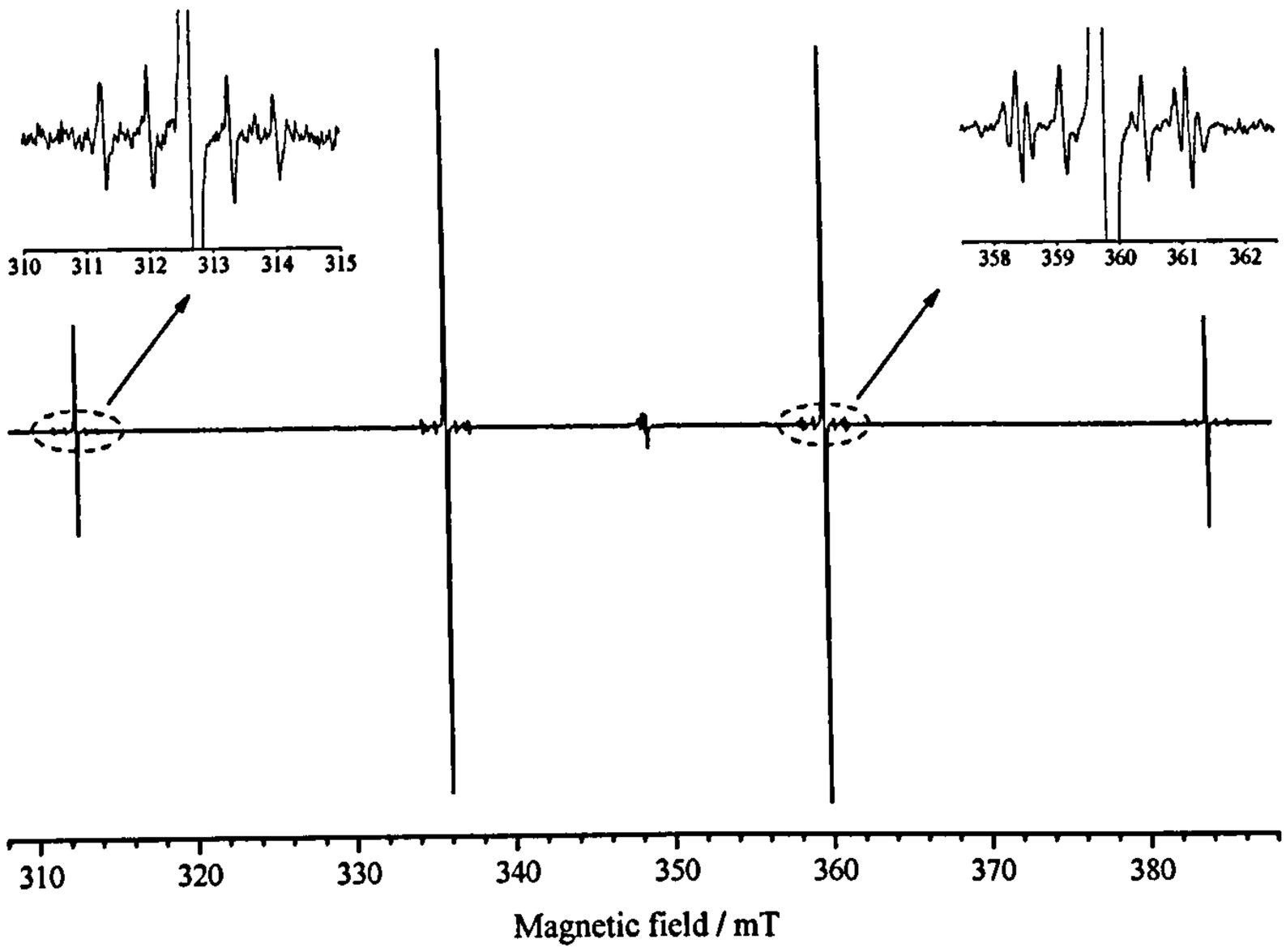

Figure 6-4: Room-temperature X-band spectrum obtained from sample A, with the applied magnetic field oriented along ⟨111⟩. The insets show the hyperfine structure resolved around the resonance lines. KUL3 can be observed around $g = 2$ (348 mT).

Secondary ion mass spectroscopy (SIMS) measurements on sample A were conducted to measure the concentration of silicon. An average over the sample of approximately 600 ppb was determined, but it was noted that the local concentration varied by more than a factor of six. Hence an average value across the surface was determined.

Table 6-1 summarizes the concentrations obtained from EPR, FTIR and SIMS measurements, as well as the integrated absorptions for the 1.682 eV ZPL. The results presented in this table will be discussed in §6.4.3, where the information that this data provides regarding the incorporation of silicon in diamond is covered.

Since both KUL1 and KUL3 were present in readily detectable concentrations in all three samples further investigation of these defects by EPR was possible.

6.3.2 KUL1

To investigate the orientation dependence of the main KUL1 EPR scans were obtained at 5° increments from $\theta = 0°$ (parallel to [001]) to $\theta = 90°$ (parallel to

Table 6-1: Summary of the quantitative results obtained regarding the concentration of the major nitrogen-related defects and those thought to be silicon-related. N_s^0, KUL1 and KUL3 concentrations were determined using EPR and $[N_s^+]$ was estimated using FTIR. In sample A N_s^+ was below detection limits (~ 100 ppb). The concentrations that can be inferred from the integrated absorption of the 1.682 eV centre are discussed in §6.4.3. The final column indicates the total silicon concentration, as determined by SIMS.

Sample	Substrate	$[(N_s{}^0)]$	$[(N_s{}^+)]$	[KUL1]	[KUL3]	1.682 eV	[Si]
		ppb	ppb	ppb	ppb	meVcm^{-1}	ppb
A	{110}	< 0.5		100(10)	6(3)	~ 0.93	~ 600
B	{100}	20(10)	~ 1200	30(5)	1.0(5)	~ 24.1	
C	{110}	20(10)	~ 800	400(20)	5(2)	~ 24.8	

[110]), equating to a rotation of the applied magnetic field (B) in a $(1\bar{1}0)$ plane. The position at X-band of the observed resonance lines in the ^{28}Si sample (A), as a function of angle, are plotted in figure 6-5. The lines centred around $g = 2$ are labelled (i)-(vi) to aid future referencing.

A number of hyperfine pairs were visible around each KUL1 resonance line (see figure 6-4). To view the effect that isotopic enrichment with ^{29}Si has on the hyperfine structure narrow scans, with $\mathbf{B} \parallel \langle 111 \rangle$, were obtained around the KUL1 resonance lines for the sample containing 4.7% ^{29}Si and those where this isotope was enriched to 90%. Figure 6-6 shows the hyperfine structure around line (i). This figure establishes that the outermost satellites can be assigned to a ^{29}Si hyperfine interaction, with the ratio of the intensity of these satellites to the central line in figure 6-6 equalling ~9:1, in agreement with the quoted enrichment of ^{29}Si in the silane. These findings confirm the involvement of silicon in this defect. The remaining pair of satellites were assigned to ^{13}C, since they evidently arise from an $I = \frac{1}{2}$ isotope with a low natural abundance (^{13}C is 1.1% abundant). Further confirmation of this assignment is provided in §6.4.1.

To examine the orientation dependence of these hyperfine satellites and to determine the number of equivalent positions for ^{29}Si and ^{13}C atoms in this defect, scans at both X and Q-band were made with **B** at different orientations in a $(1\bar{1}0)$ plane. Rotating away from $\langle 111 \rangle$ revealed that the ^{29}Si satellites did not split, whilst the ^{13}C satellites split into a maximum of two sets around the lines labelled

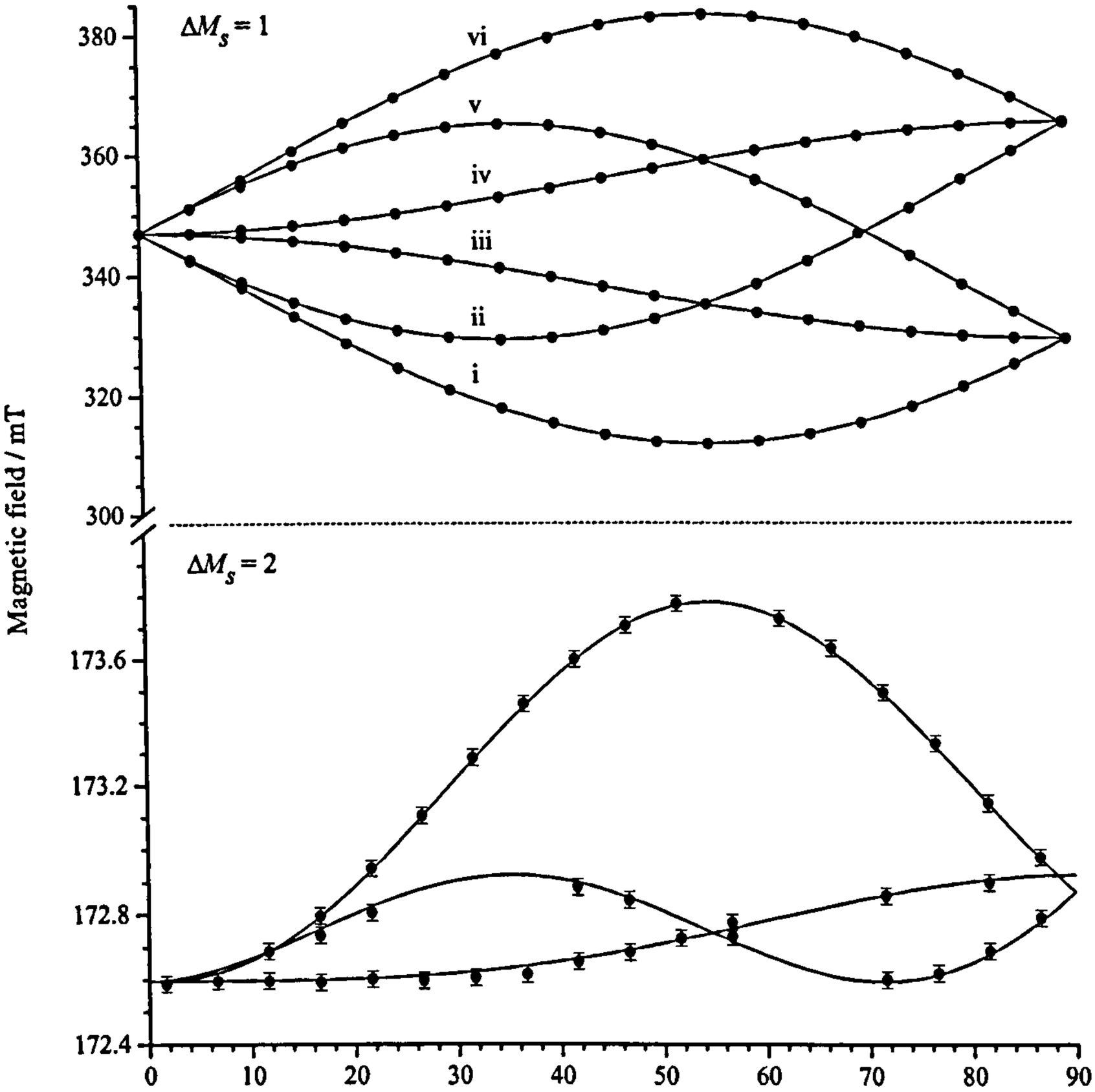

Figure 6-5: The EPR roadmap for KUL1. The points indicate the determined positions, as a function of angle in the $(1\bar{1}0)$ plane, of the KUL1 EPR lines at X-band. The solid curves show the best fit to the experimental data and were used to determine the parameters g and D (see text).

(i),(ii),(v) and (vi) in figure 6-5 and three sets around the lines labelled (iii) and (iv) in figure 6-5. Figure 6-7 shows an example of the hyperfine structure observed at X-band with the applied magnetic field 80° from [001] in the $(1\bar{1}0)$ plane for the sample containing ^{29}Si in its natural abundance. The resonances labelled $^{29}Si_a$ and $^{13}C_{a-c}$ are not observed at Q-band (see §6.4.1). The orientation dependence in the $(1\bar{1}0)$ plane of the lines assigned to ^{13}C and ^{29}Si satellites is plotted in figure 6-8.

In order to investigate the impact of different temperatures on the KUL1 resonance lines X-band spectra were obtained at temperatures from 10 K to 300 K, with $\mathbf{B} \parallel \langle 111 \rangle$. As the temperature was varied between 300 K and 30 K the splitting of

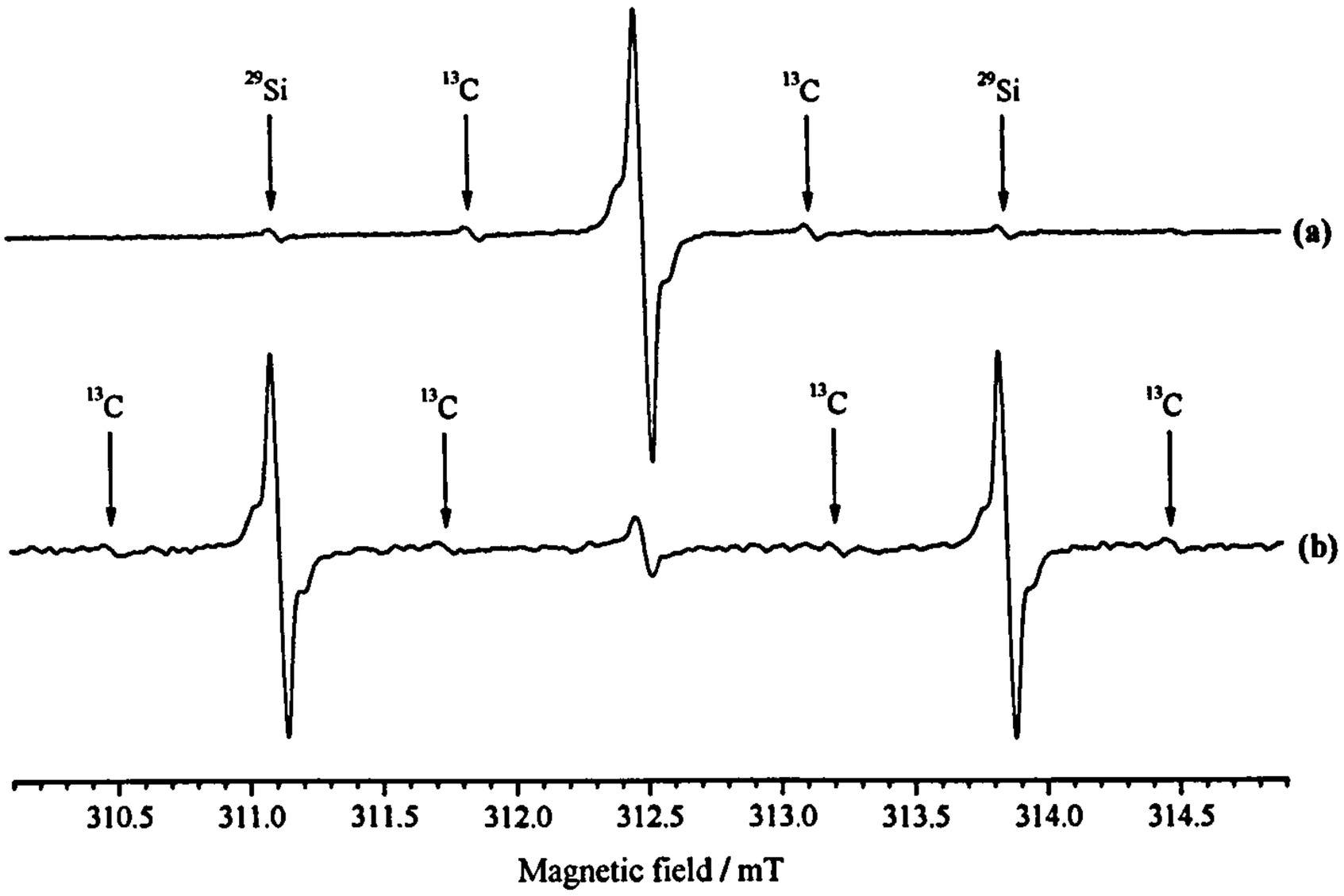

Figure 6-6: A comparison between the KUL1 hyperfine structure observed around line (i) (see figure 6-5) for a sample with ^{29}Si in its natural abundance (a) and one enriched to 90% ^{29}Si (b). The spectra were recorded at X-band with B ∥ ⟨111⟩.

the outermost KUL1 resonance lines was seen to decrease from 71.2(1) mT at 300 K to 67.4(1) mT at 30 K. Over this temperature range the linewidth was constant and the intensity of the spectrum was seen to follow Curie's law, i.e. proportional to T^{-1} (see figure 6-9). Below 30 K the intensity of KUL1 decreased rapidly, as microwave power saturation became unavoidable, with 0.3 μW the lowest microwave power achievable with the setup used for cryogenic temperature EPR (see §4.2.2). EPR lines from KUL1 could still be observed below 30 K, but only under rapid-passage conditions, making quantitative measurements impossible. No changes in symmetry were apparent at reduced temperatures.

6.3.3 KUL3

Narrow EPR scans around $g = 2$ were obtained at ~ 5° increments in a $(1\bar{1}0)$ plane for sample A at both X and Q-band, to permit a roadmap of the KUL3 resonance lines to be constructed. From table 6-1 it is apparent that KUL3 is present in much lower concentrations than KUL1, hence close to ⟨100⟩ the resonance lines from KUL1 dominated the spectra, meaning that the positions of the KUL3 lines could

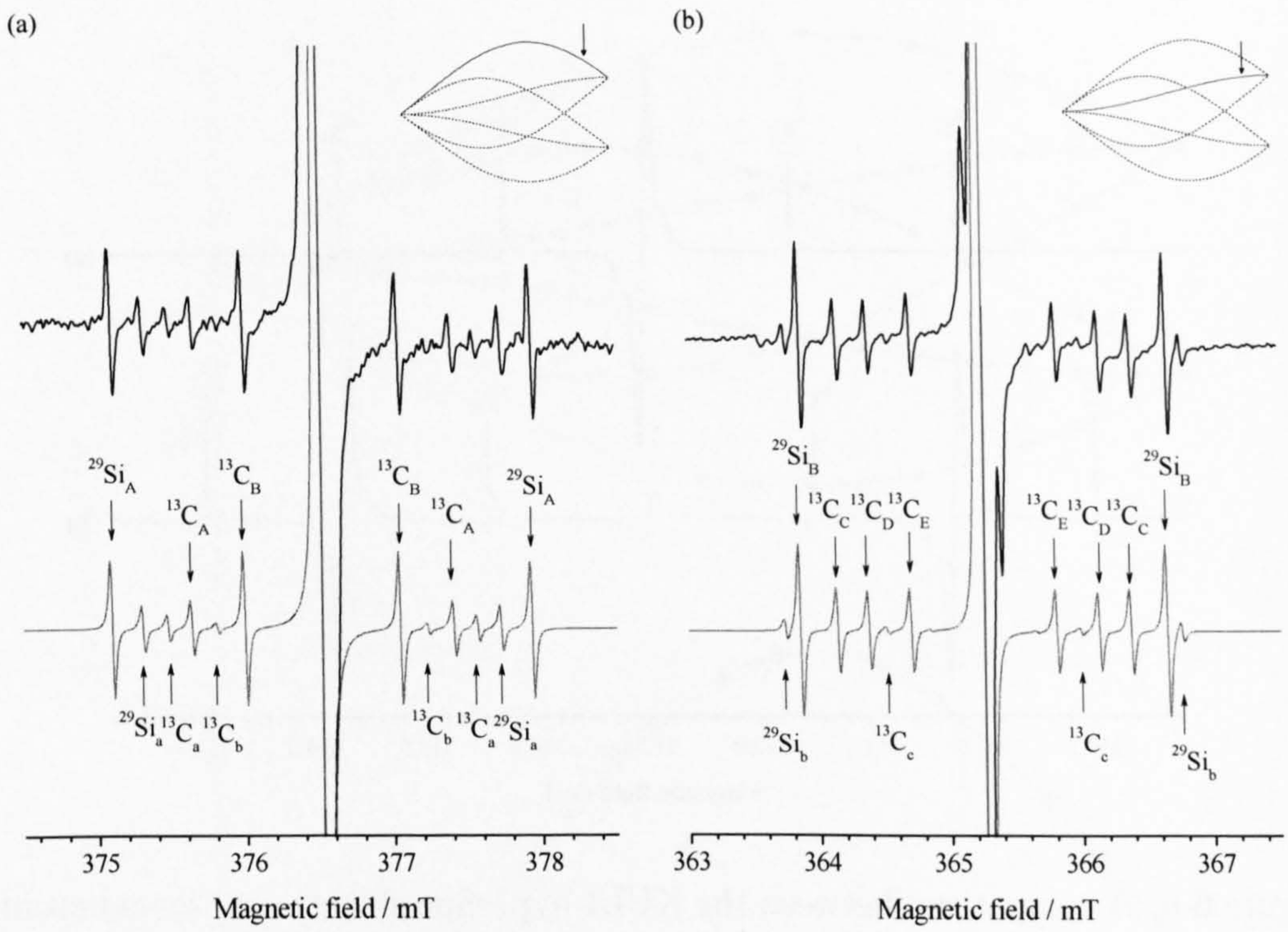

Figure 6-7: KUL1 hyperfine structure observed at X-band with $\theta = 80°$ in a $(1\bar{1}0)$ plane. The plots beneath illustrate the simulated data obtained using the determined spin-Hamiltonian parameters and equations 6-1 and 6-2. Lower case labels denote lines which are absent at Q-band. (a) displays the structure around resonance line vi and (b) shows the hyperfine satellites seen around line iv (see insets and figure 6-5).

not be accurately determined. Figure 6-10 illustrates the roadmaps constructed from sample A (4.7% ^{29}Si).

Small pairs of hyperfine satellites were observed around the central KUL3 resonance lines in sample A. Hence, in order to assist in their identification, equivalent X and Q-band scans were obtained for the samples containing 4.7% and 90% ^{29}Si (A and B respectively). The effect of enrichment is shown in figure 6-11, for X-band EPR spectra with $\mathbf{B} \parallel \langle 111 \rangle$. Since the intensity of the satellites is increased such that the ratio of intensity of these to the centre line is 9:1, this unambiguously identifies the lines as ^{29}Si hyperfine satellites and confirms the presence of silicon in this centre. A number of spectra at different orientations in a $(1\bar{1}0)$ plane were obtained for the ^{29}Si enriched samples to permit the hyperfine parameters for this isotope to be determined.

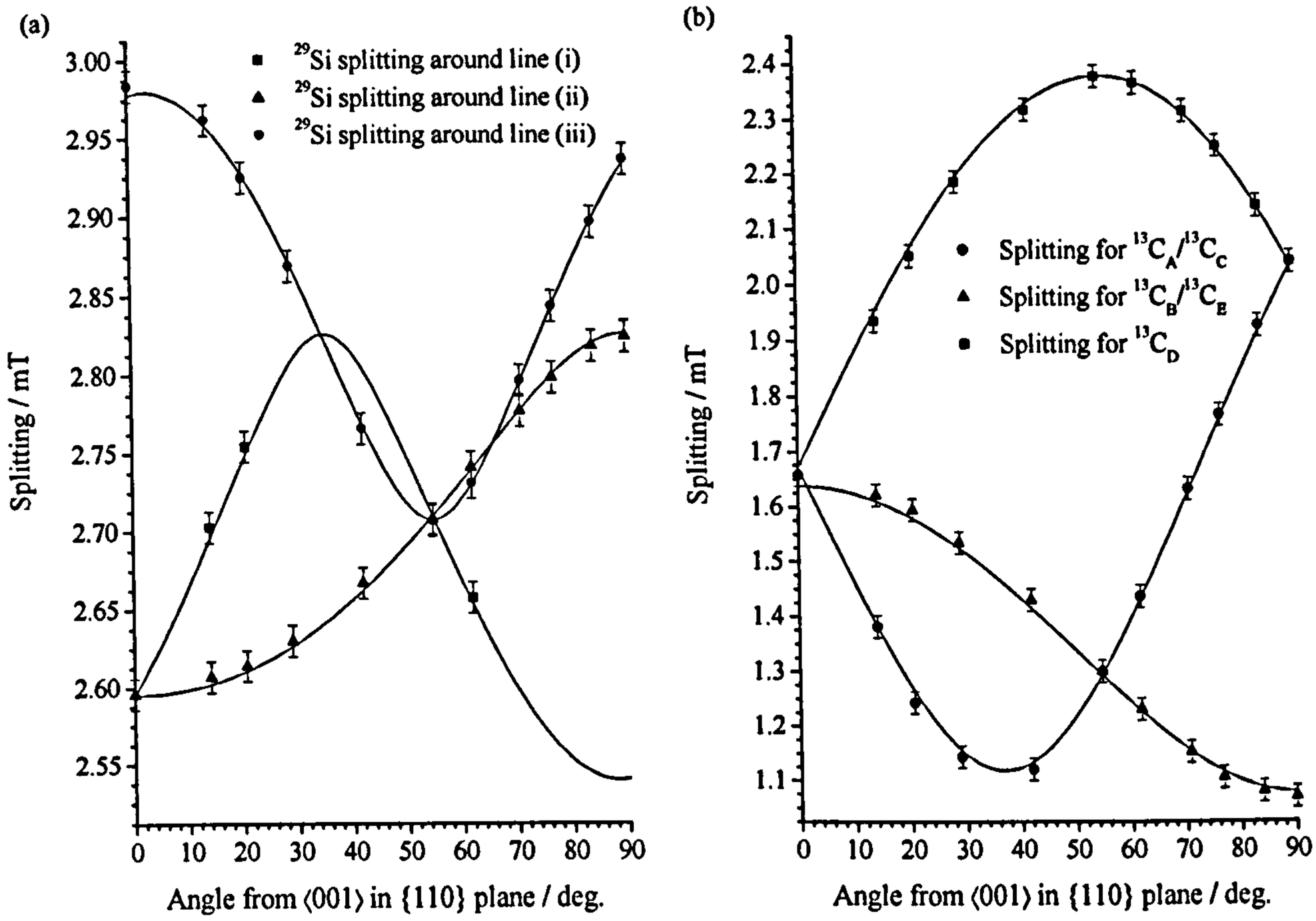

Figure 6-8: (a) Splitting of the ^{29}Si hyperfine satellites around KUL1 resonance lines (see figure 6-5) as a function of angle in the $(1\bar{1}0)$ plane. (b) Splitting of the ^{13}C satellites as a function of angle in the $(1\bar{1}0)$ plane, with the three data sets labeled as in figure 6-7. The plotted lines were obtained using the determined spin-Hamiltonian parameters and equations 6-1 and 6-2.

6.4 Discussion

6.4.1 KUL1

The large splitting of the outermost KUL1 resonance lines observed with $\mathbf{B} \parallel \langle 111 \rangle$ suggests that a zero-field splitting (D) is primarily responsible for the orientation dependence of the lines shown in figure 6-5, therefore implying that the defect has $S \geq 1$. Weak resonance lines, present at half field originating from a $|-1\rangle \rightarrow |+1\rangle$ transition, and the absence of any lines from $\left|-\frac{1}{2}\right\rangle \rightarrow \left|+\frac{1}{2}\right\rangle$ transitions confirms that the defect has $S = 1$. The Curie-law variation of intensity with temperature (figure 6-9) shows that this is the ground state, well separated from any excited states.

The results of the angular variation study have therefore been fitted using a spin Hamiltonian of the form of equation 6-1 and the temperature dependence of the large splitting of the lines could be interpreted as a change in the magnitude

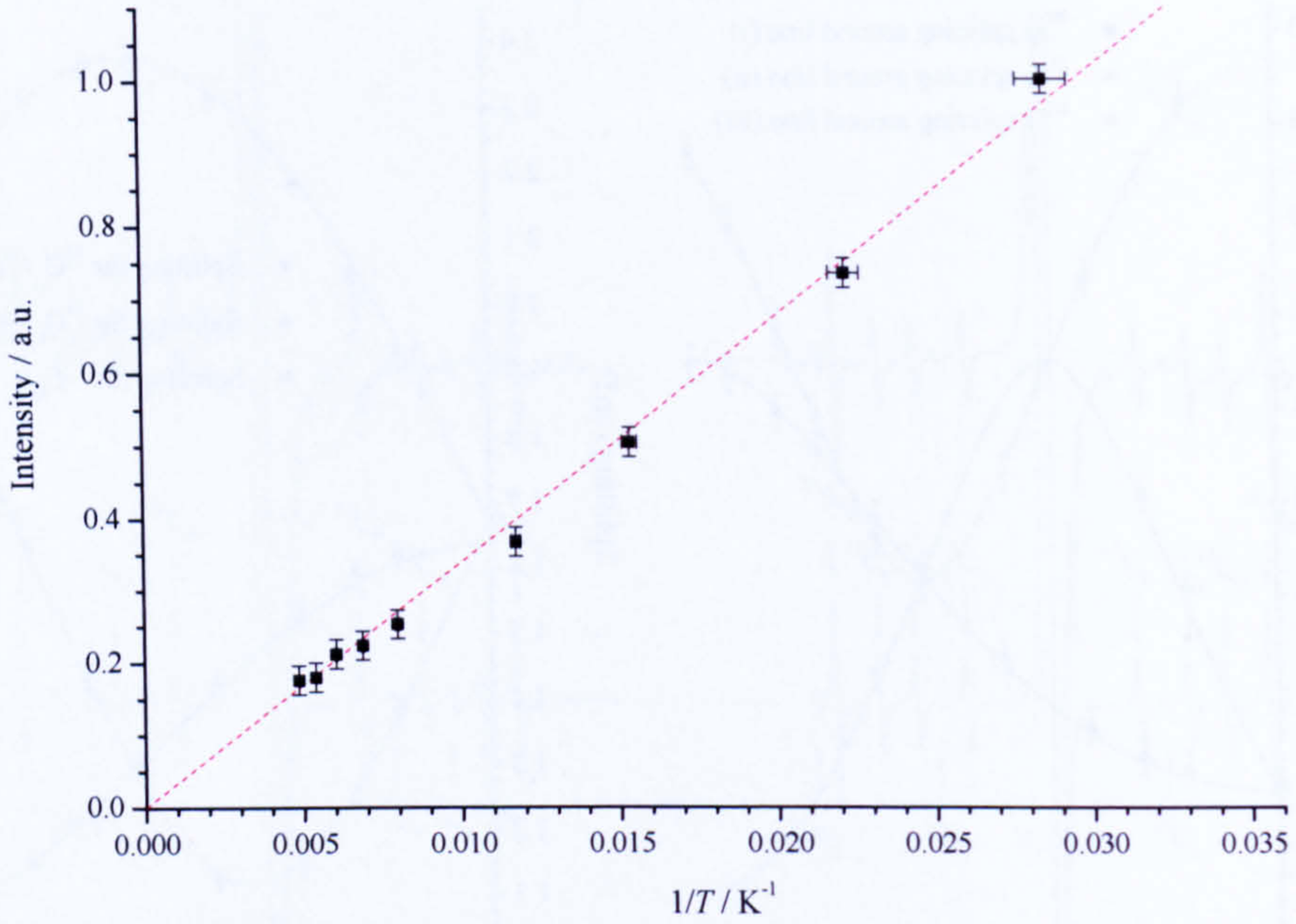

Figure 6-9: Intensity of the KUL1 resonance lines (normalised to the maximum observed) plotted as a function of $1/T$. The fitted line is constrained to pass through the origin.

of D:

$$\mathscr{H}_{\text{electronic}} = \mu_B \hat{\mathbf{S}} \cdot \underline{\mathbf{g}} \cdot \mathbf{B} + \hat{\mathbf{S}} \cdot \underline{\mathbf{D}} \cdot \hat{\mathbf{S}}. \tag{6-1}$$

Using the experimentally observed positions of the resonance lines optimum values for the electronic Zeeman ($\underline{\mathbf{g}}$) and zero-field ($\underline{\mathbf{D}}$) terms (§3.4.1 and §3.4.2, respectively) could be found. It was assumed that $\underline{\mathbf{g}}$ and $\underline{\mathbf{D}}$ are axially symmetric about the [111] trigonal axis of the defect; relaxing this constraint did not improve the quality of the fit. The parameters for $\underline{\mathbf{g}}$ were calculated relative to g for N_s^0, which was taken to be $g = 2.0024$ [14]. $g_\parallel$ and $g_\perp$ for KUL1 were determined as 2.0042(2) and 2.0035(1) respectively, with $g_\parallel$ along [111], whilst $D = +1000(1)\,\text{MHz}$ at 300 K (again with the principal axis along [111], where D is defined as $\frac{3}{2}D_{zz}$). These results are in agreement with those previously published for KUL1 [8]. Figure 6-12 illustrates the determined dependence of D with temperature.

From the change in intensity of the outmost hyperfine satellites in samples enriched with ^{29}Si (see figure 6-6), it was apparent that these could be assigned to ^{29}Si. The splitting of this pair with orientation, illustrated in figure 6-8a, can

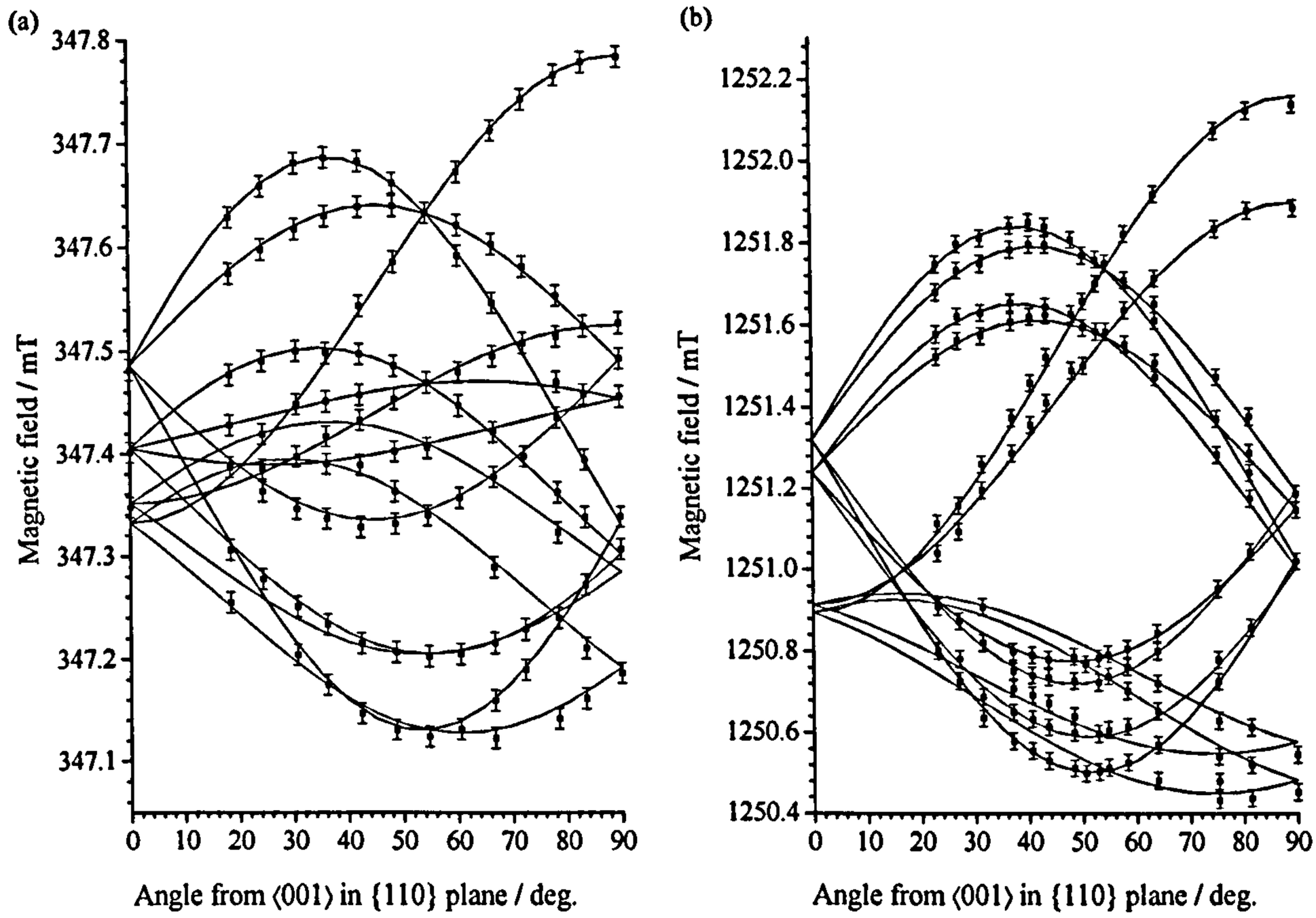

Figure 6-10: The determined positions, as a function of angle in the $(1\bar{1}0)$ plane, of the KUL3 EPR lines observed at (a) X-band and (b) Q-band. The plotted lines were obtained using the determined parameters for g and A (see table 6-3).

be used to extract the hyperfine (A) parameters, using an additional term in the spin Hamiltonian shown in equation 6-1:

$$\mathscr{H}_{\text{nuclear}} = \sum_j \hat{\mathbf{S}} \cdot \underline{\mathbf{A}}_j \cdot \hat{\mathbf{I}}_j - \mu_N g_{N_j} \hat{\mathbf{I}}_j \mathbf{B}, \tag{6-2}$$

where g_{N_j} is the nuclear g factor (g_N) for nuclei j.

The hyperfine interaction for ^{29}Si was found to be axially symmetric, with $A_\parallel$ oriented along the [111] trigonal axis (see table 6-2), although it should be noted that the orientation dependence illustrated in figure 6-8a is dominated by the second-order terms in D. Since the ^{29}Si satellites did not split when the orientation of **B** was changed it is apparent that a *single* silicon atom is incorporated in the defect at a unique site. A silicon atom at the centre of a di-vacancy, as in (V-Si-V), would explain both the hyperfine symmetry and the single observable site.

The data in figure 6-5 is consistent with a defect that has either D_{3d} or C_{3v} symmetry and hence, in itself, is insufficient to confirm the (V-Si-V)^0 model. The data shown in figure 6-7 is important, since the intensity of ^{13}C satellites, relative

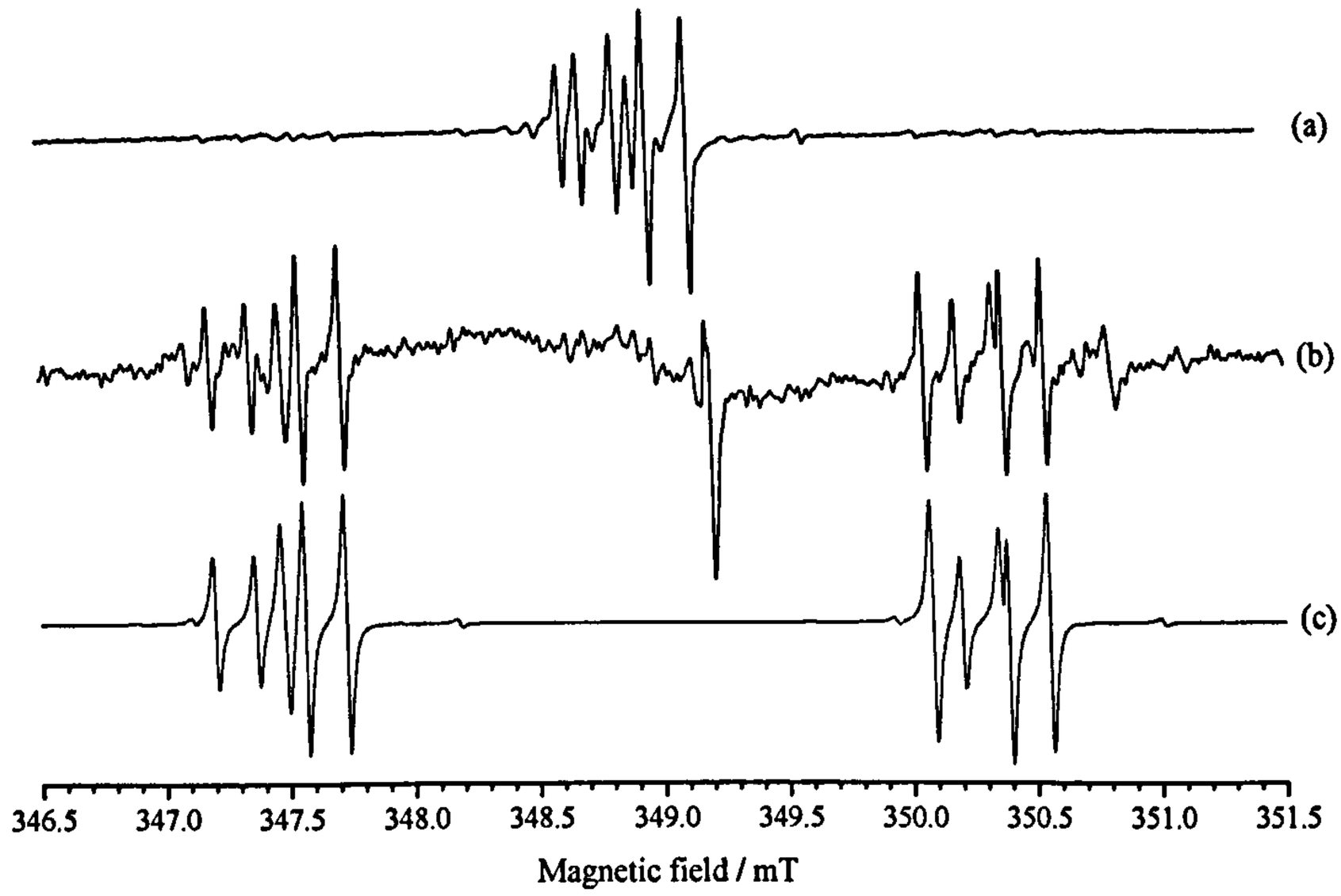

Figure 6-11: EPR lines observed around $g = 2$ at X-band with B along ⟨111⟩ for (a) sample A (^{29}Si in natural abundance) and (b) sample B (enriched with 90% ^{29}Si). The central resonance line in (b) arises due to the presence of N_s^0 in this sample. (c) shows a spectrum simulated using the determined parameters for KUL3, given in table 6-3.

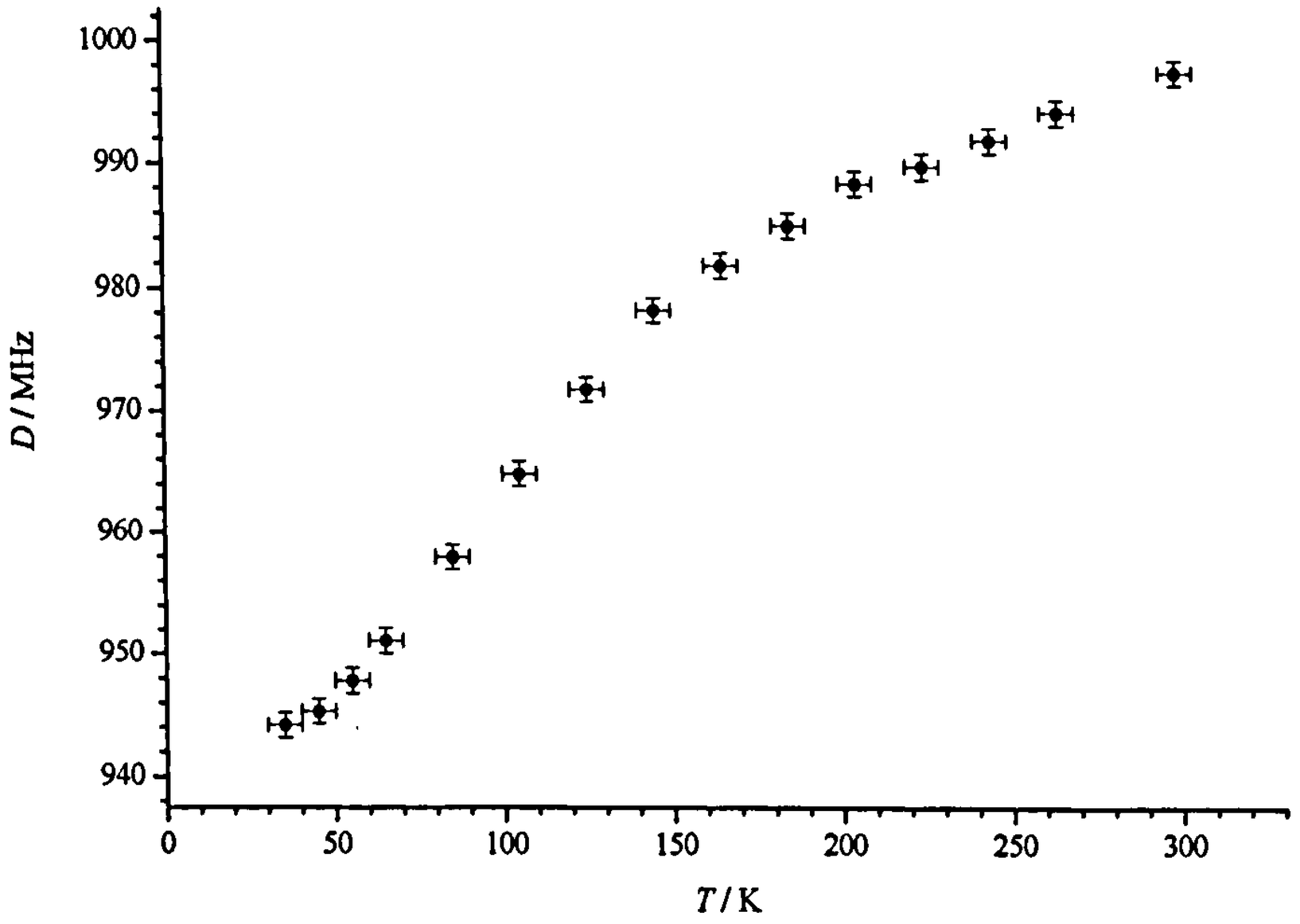

Figure 6-12: The magnitude of the zero-field (D) interaction for KUL1, as a function of temperature.

Table 6-2: Experimentally determined (at 300 K) ^{13}C and ^{29}Si hyperfine (A) parameters (see §3.4.3 for definitions) for KUL1, compared to those predicted from theory [2].

Interaction	$A_\parallel$ MHz $[hkl]$	$A_\perp$ MHz	A_s MHz	A_p MHz	η^2	λ_h
$^{13}C_{experiment}$	66.2(2) ∥ $[\bar{1}\bar{1}1]$	30.2(2)	42.2(1)	12.3(1)	0.123(6)	10.0(7)
$^{13}C_{theory}$	51 ∥ $[\bar{1}\bar{1}1]$ (2°)	12	25	13	0.13	18
$^{29}Si_{experiment}$	76.3(1) ∥ [111]	78.9(1)	78.0(1)	−0.867(47)		
$^{29}Si_{theory}$	78 ∥ [111]	82	80.6	−1.3		

to the central transition allows the number of equivalent atom positions to be determined (see §3.7.1). A defect with C_{3v} symmetry (e.g. NV^-) would have two distinct sets of three equivalent carbon atoms, with the addition of the inversion symmetry in $(V\text{-}Si\text{-}V)^0$ increasing the symmetry to D_{3d}, leading to a set of six equivalent carbon atoms (see figure 6-1).

The intensity of the simulated data in figure 6-7 has been set using equation 3-41, assuming that there are *six* nearest-neighbour carbon atoms ($N_{equiv} = 6$), with ^{13}C being present in its natural abundance ($\mathscr{A} = 0.011$). A good match to the experimental data is found, confirming that KUL1 has D_{3d} symmetry, supporting the assignment of KUL1 to $(V\text{-}Si\text{-}V)^0$. The orientation dependence data for the ^{13}C satellites (figure 6-8b) was used to extract the hyperfine parameters for this interaction (see table 6-2). $A_\parallel$ was found be directed along a ⟨111⟩ axis which is not parallel to the D_{3d} symmetry axis (e.g. $[\bar{1}\bar{1}1]$); with the silicon atom located along [111] this result is to be expected for the (V-Si-V) model.

The distributions in intensity between the ^{13}C hyperfine satellites illustrated in figure 6-7 can be explained using the $(V\text{-}Si\text{-}V)^0$ model, considering all the possible ⟨111⟩ orientations of this defect. Rotating the applied magnetic field **B** in a $(1\bar{1}0)$ plane in figure 6-1 (trigonal symmetry axis in the plane) four of the possible orientations of $A_\parallel$, arising from a ^{13}C atom at positions i,j,l,m, make the same angle with **B**. A different angle is made to the other two possible orientations of $A_\parallel$, arising from a ^{13}C atom at positions k or n. Hence, ^{13}C satellites for $(V\text{-}Si\text{-}V)^0$ defects with their D_{3d} axis along [111] would be expected to split with relative intensities 4:2. For defects oriented along different ⟨111⟩ directions a splitting into

three pairs with intensities 2:2:2 would arise. This is the behavior observed in figure 6-7a and 6-7b, respectively.

It was noted in §6.3.2 that the lines labelled $^{29}Si_{a-b}$ and $^{13}C_{a-c}$ were not observed at Q-band. These could therefore be assigned to the forbidden electron-nuclear double-spin flip ($\Delta M_S = 1$, $\Delta m_I = 1$) transitions. Whilst their presence complicates the initial interpretation of the spectra, their position, relative to the allowed lines depends on the value of g_{N_j}, therefore allowing the nucleus responsible to be identified. The good fit to the experimental data further supports the assignment of the hyperfine structure to ^{29}Si and ^{13}C. These transitions are also sensitive to the relative sign of A and D. The absolute sign of D can be determined via depopulation of the higher energy spin states at lower temperature, but, as stated in §6.3.2 below 30 K saturation became a problem, hence this was not possible. However, providing assumptions are made regarding the unpaired electron wave-function localisation, the signs of D as well as A for the ^{29}Si and ^{13}C hyperfine interactions can be found via position of lines resulting from the electron-nuclear double-spin flip transitions.

In previously published work on KUL1 [8], where it was initially proposed that KUL1 could be $(V\text{-}Si\text{-}V)^0$, the sign of the zero-field interaction was assumed to be negative, presumably to agree with the finding that $D < 0$ for the di-vacancy in diamond [15]. However, assigning KUL1 to $(V\text{-}Si\text{-}V)^0$ means that real localisation of the electron probability density on the basal carbon atoms is expected. Since g_N is positive for ^{13}C (see table 3-1) this necessitates a positive value for A. D must then be positive, to successfully match the experimentally observed positions of the satellites labeled $^{13}C_{a-c}$ in figure 6-7. Using this sign for D requires that the ^{29}Si hyperfine interaction is positive to match the positions of the $^{29}Si_{a-b}$ resonance lines.

The ^{13}C hyperfine interactions can be interpreted in the usual way in terms of an unpaired electron wave function, as discussed in §3.4.3. The experimental wave-function parameters determined for ^{13}C are given in table 6-2. Approximately 74% of the unpaired electron probability density is located on the six nearest-neighbour carbon atoms. It is also apparent in figure 6-7b that there are additional hyperfine satellites around the central KUL1 resonance line which are partially resolved.

These are likely to arise from next-nearest-neighbour ^{13}C atoms, hence accounting for some of the remaining unpaired electron probability density.

The nuclear g factor for ^{29}Si is negative (table 3-1), therefore the determined positive hyperfine interaction implies a *negative* spin density at the nucleus. This suggests an indirect interaction (e.g. configuration interaction [16], exchange polarisation [17], etc) is responsible for the observed hyperfine interaction. Taking $a_0 = -4594\,\text{MHz}$ for the $3s$ orbital [18], the isotropic part of the ^{29}Si hyperfine interaction could be produced by $\sim 2\%$ $3s$ character. A similar result was found for the tin-vacancy complex in silicon [19].

Recent theoretical work by Goss *et al.* has provided estimations of the hyperfine interaction parameters for ^{29}Si and ^{13}C in $(V\text{-}Si\text{-}V)^0$ [2]. The ^{29}Si interaction was predicted to be axial along [111] and dominated by the isotropic component; $A_\parallel = 78\,\text{MHz}$ and $A_\perp = 82\,\text{MHz}$, in excellent agreement with the determined values. The ^{13}C interaction for the six nearest-neighbour carbon atoms was also predicted to be axial and within 2° of ⟨111⟩. Values of $A_\parallel = 51\,\text{MHz}$ and $A_\perp = 12\,\text{MHz}$ were calculated. The localisation of the unpaired electron probability density on each ^{13}C atom (η^2) calculated from the experimentally determined hyperfine parameters is in good agreement with theory, although the ratio between the localisation in s and p type orbitals differs.

The shift of the g value from the free-spin value g_e and the anisotropy for KUL1 is large ($\delta g_\parallel = 0.0019$) compared to most defects in diamond. This arises from a spin-orbit admixture of excited states which, in a free atom, leads to a contribution to D of the form $D = \frac{1}{2}\lambda_{so}\delta g/g_e$, where λ_{so} is the spin-orbit coupling constant (§3.4.2). Assuming $\lambda_{so} \sim 4.5\times10^5\,\text{MHz}$ for a carbon atom in a $S = 1$ defect [20], the contribution to D in KUL1 from spin-orbit coupling is $\sim 640\,\text{MHz}$. More detailed analysis of the size and temperature dependence of the zero-field splitting is complicated, but the simple estimate shows that the large positive value of D can be explained by spin-orbit coupling.

6.4.2 KUL3

The orientation dependence of the KUL3 resonance lines, shown in figure 6-10, indicates a defect with C_{1h} (monoclinic-I) symmetry with small splittings around

$g = 2$, implying that $S = \frac{1}{2}$. The weak hyperfine satellites visible in the sample containing ^{29}Si in its natural abundance suggest a low abundance $I = \frac{1}{2}$ nuclei is involved. The data in figure 6-11 for a ^{29}Si enriched sample confirms that these arise due to the presence of ^{29}Si. The intensity of the hyperfine satellites in the unenriched samples, relative to the central KUL3 resonance lines indicate that the satellites arise from a unique ^{29}Si atom.

The hyperfine interaction for ^{29}Si was found to be non-axial, with A_1 tilted approximately 2° away from [111] (towards [001]) in a $(1\bar{1}0)$ plane; constraining $\underline{A}$ to be axial along [111] led to a statistically significant degradation in the quality of the fit. To produce the central pattern of resonance lines another $I = \frac{1}{2}$ nuclei must be involved, with ~ 100% abundance. Due to its prevalence in CVD diamond hydrogen is a natural choice, with the assignment being confirmed by the observation of electron-nuclear double-spin flip transitions, as found in previous studies [5].

From the roadmap for KUL3 (figure 6-10) the values describing $\underline{g}$, as well as $\underline{A}$ for the hydrogen atom were determined. The principal values of g were found to be along [110], $[00\bar{1}]$ and $[1\bar{1}0]$. Allowing these to deviate from these directions did not improve the fit. The hydrogen hyperfine interaction is also non-axial and is tilted ~ 4° from $[\bar{1}\bar{1}1]$ towards [001] in a {110} plane. Due to the low abundance of ^{13}C and the low concentration of KUL3 the hyperfine parameters for nearest or next-nearest-neighbour ^{13}C could not be found.

Table 6-3 provides a comparison between the spin-Hamiltonian parameters determined in this study and those previously published [8]. It is apparent that there is disagreement between the two. Using the previous parameters for KUL3 to fit the experimental X-band data points in figure 6-10 resulted in a poor fit. This can be explained by that fact that these parameters were determined at Q-band. Since the g anisotropy of this defect is relatively large (c.f. $(V\text{-}Si\text{-}V)^0$), at higher frequencies the change of position of the resonance lines as the direction of **B** is changed will be dominated by this term in the spin Hamiltonian. In contrast the hyperfine term from the hydrogen atom will have a relatively small effect, hence it is challenging to accurately determine at this frequency band. Additionally, it has previously been assumed that the principal axes for both g and A are along

Table 6-3: Comparison between the previously published parameters [8] for KUL3 and those determined in this study (at 300 K). θ is the angle from [001], ϕ is the angle from [100] in a (001) plane. The hyperfine (A) parameters are quoted in MHz. In this study the parameters for $\underline{\mathbf{g}}$ were determined relative to g for N_s^0, which was taken to be $g = 2.0024$ [14].

Parameter	**Previously published [θ,ϕ]**	**Determined [θ,ϕ]**
g_1	2.00506(3) ‖ [75,45]	2.0054(2) ‖ [90,45]
g_2	2.00426 ‖ [165,45]	2.0048(2) ‖ [0,45]
g_3	2.00254 ‖ [90,315]	2.0030(2) ‖ [90,315]
A_1 (^{29}Si)		±76.1(2) ‖ [53(1),45]
A_2 (^{29}Si)		±81.1(2) ‖ [143(1),45]
A_3 (^{29}Si)		±79.1(2) ‖ [90,315]
A_1 (^{1}H)	−2.8(6) ‖ [75,45]	∓7.9(1) ‖ [50(1),225]
A_2 (^{1}H)	0 ‖ [165,45]	±4.7(1) ‖ [140(1),225]
A_3 (^{1}H)	7.3 ‖ [90,315]	±7.3(1) ‖ [90,315]

the same direction which, as shown in table 6-3, is not the case if the axes of the two interactions are allowed to vary independently. The modified parameters, used in figure 6-10, provide an excellent fit to the EPR data at both microwave frequencies. An example fit to an X-band spectrum with $\mathbf{B} \parallel \langle 111 \rangle$ is shown in figure 6-11.

It was suggested that KUL3 is a neutral di-vacancy, where one of the six basal carbon atoms is replaced by silicon, and one dangling bond (remote to silicon atom) is passivated by a hydrogen atom [8]. The data obtained in this study has confirmed the suggested involvement of hydrogen and silicon in this defect, but the new experimental data and recent theoretical modelling [2] of hydrogen in the vicinity of (Si_s-V) both suggest an alternative structure; (V-Si-V:H)^0.

The magnitude of the ^{29}Si hyperfine parameters determined for KUL1 and KUL3 in this study are almost identical, but KUL3 has lower symmetry. This suggests that the silicon atom is in a similar environment, with the basic (V-Si-V) unit being common to both defects, but KUL3 is decorated with a single hydrogen atom; (V-Si-V:H). The determined directions for the hyperfine interactions for ^{29}Si is consistent with this assignment, as the principal axis is close to the [111] axis containing the di-vacancy, as found for KUL1. This is in agreement with the theoretical predictions for the (V-Si-V:H) centre; a stable defect with

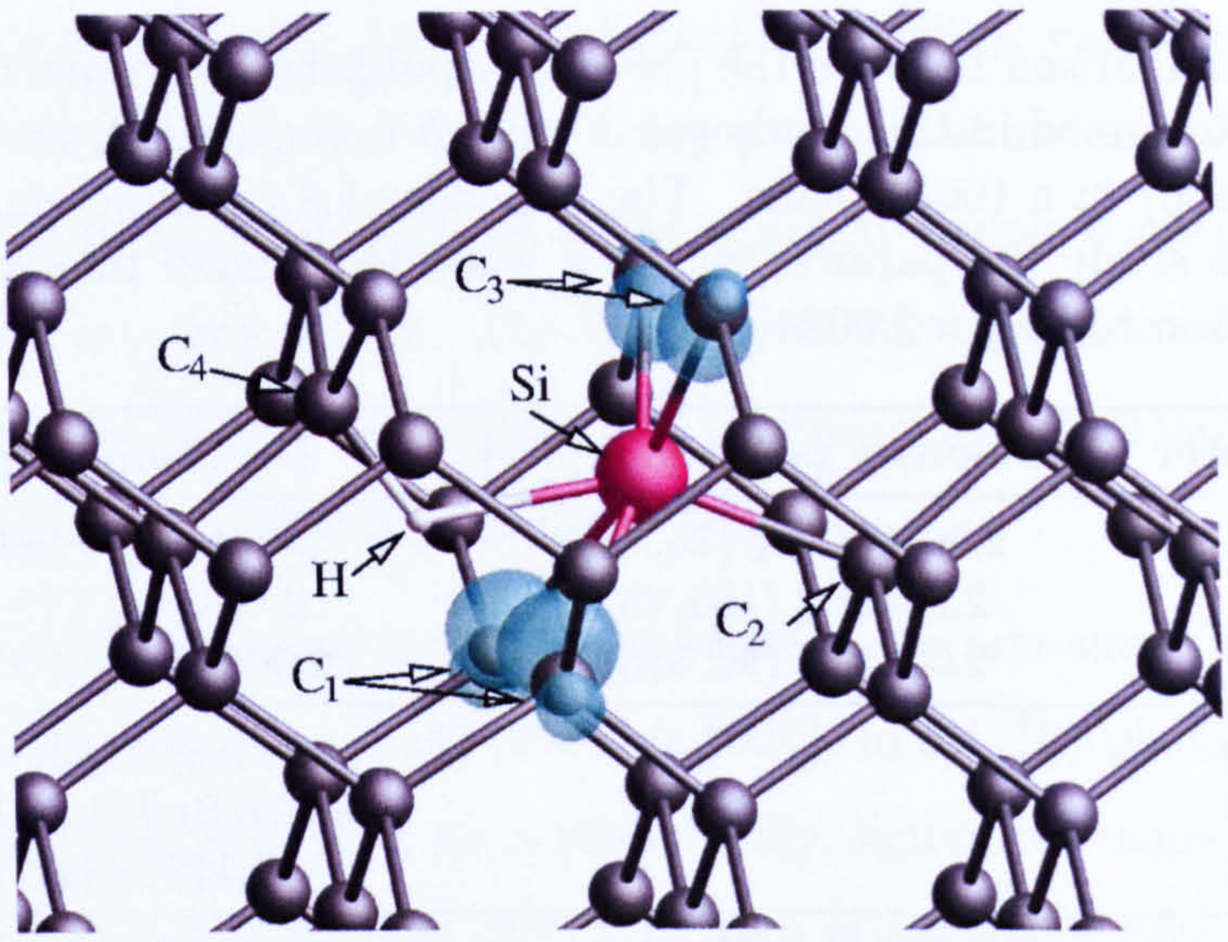

Figure 6-13: The (V-Si-V:H)^0 defect structure [2], as determined from theory, illustrating the electron localisation on the surrounding carbon atoms.

C_{1h} symmetry where the hydrogen atom is bonded close to the relaxed (V-Si-V) structure, see figure 6-13 [2].

The absolute sign of the hyperfine parameters for ^{29}Si and ^{1}H for (V-Si-V:H)^0 could not be determined experimentally by EPR, although A for the ^{29}Si interaction is likely to be positive, in agreement with the sign determined for (V-Si-V)^0. Theoretical predictions for the ^{29}Si hyperfine interaction support this with A_1, A_2 and A_3 all determined to be positive [2]. The theoretically calculated ^{29}Si hyperfine interaction is within 3° of [111], in a $(1\bar{1}0)$ plane, in good agreement with the value determined from experiment. The predictions from theory for the magnitudes for the hydrogen hyperfine interaction ($A_1 = -7\,\mathrm{MHz}$, $A_2 = 3\,\mathrm{MHz}$ and $A_3 = 6\,\mathrm{MHz}$) are also in good agreement with the values from EPR, and are consistent with the localisation of the unpaired electron probability density on the surrounding carbon atoms, as shown in figure 6-13. Considering this model the experimentally determined 4° deviation of A_1 from $[\bar{1}\bar{1}1]$ (towards [001]) for the hydrogen hyperfine interaction is reasonable.

6.4.3 Incorporation of silicon in diamond

It is known that the intensity of the 1.682 eV silicon-related absorption band can be dramatically increased by irradiation damage and annealing at temperatures where vacancies are mobile [21, 22]. This result is consistent with the assignment of the 1.682 eV centre to a (V-Si-V) structure and the incorporation of silicon in another form which is converted to (V-Si-V) by vacancy capture.

The SIMS data in table 6-1 indicates that more silicon is incorporated in sample A than is accounted for by the EPR defects KUL1/KUL3, but as stated in §6.3.1 the silicon incorporation is highly inhomogeneous. Optical absorption intensities are reported for the 1.682 eV doublet but, because of the lateral inhomogeneity in the silicon concentration of these samples, these measurements should be treated with caution.

The conversion factor relating the absorption intensity under the zero phonon line at 77 K (A_{737}) in units of meV cm^{-1} to a concentration ([737]) in cm^{-3} is not known; however, an estimation can be made by considering the data from other defects in diamond. A typical conversion factor [23] at 77 K is $\sim 2 \times 10^{16}$ meV cm^2 for defects with a Huang-Rhys factor (which is a measure of the vibronic coupling) of ~ 3 [24]. Using the published value of 0.05 for the Huang-Rhys factor of the 737 nm system [25] one would expect the conversion factor for this defect to be a factor of ~ 60 higher; $\sim 10^{18}$ meV cm^2. In this way we can crudely estimate the concentration of the defect giving rise to the 737 nm system from the data in table 6-1 using the expression $A_{737} = 10^{18}[737]$. A concentration of ~ 1 ppb is estimated for sample A and ~ 12 ppb for samples B and C (1 ppb equates to a defect density of 1.77×10^{14} cm^{-3}).

Due to the very low concentration of nitrogen in sample A one would expect the majority of silicon defects to be neutral. Using the concentration estimates a significantly higher ratio of [KUL1] to [1.682] is found in this sample compared to both samples B and C, which contain nitrogen. However, despite samples B and C being grown under identical conditions, it appears that the ratio of [KUL1] to [1.682] is different between the two samples. Although the concentration of N_s^+ obtained from FTIR should be treated with caution in the same way as the results inferred from the 737 nm absorption measurements, it appears that a higher

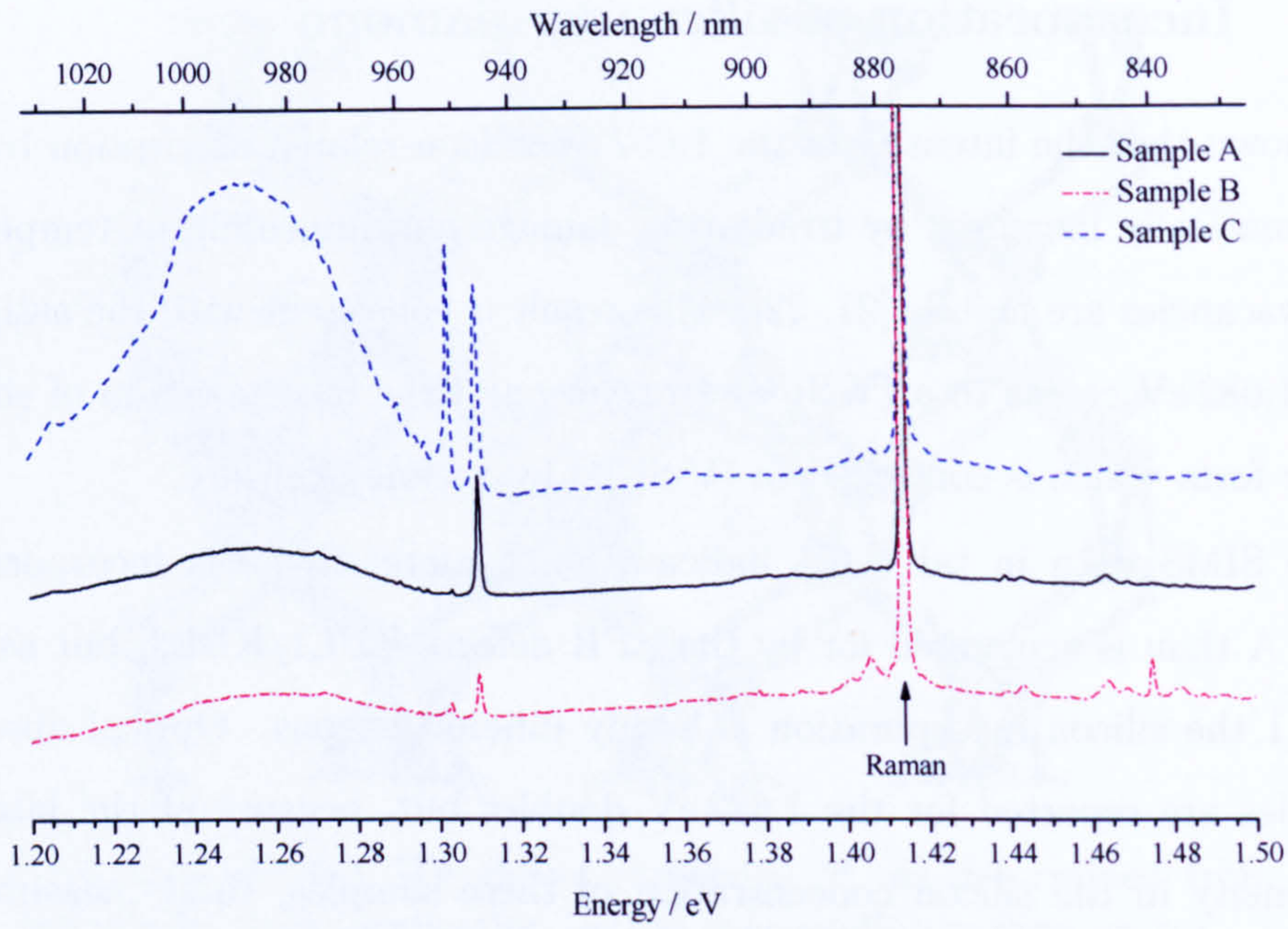

Figure 6-14: Comparison between the PL spectra (normalised to the intensity of the Raman line at 1.414 eV) observed in the three samples in the 1.2–1.5 eV region. All spectra were acquired at 10 K using 785 nm (1.579 eV) excitation.

proportion of the nitrogen in sample B is in the positive charge state, N_s^+. This could explain the higher fraction of [1.682] in this sample, compared to sample C.

The combined concentration of (V-Si-V)^0, (V-Si-V:H)^0 and the 1.682 eV defect in samples B and C suggests that silicon, at least in these forms, is more readily incorporated in {110} surfaces than {100}.

In §6.3.1 it was stated that two additional sharp lines were observed at 1.303 eV (951.3 nm) and 1.310 eV (946.4 nm) when examining the NIR region of PL spectra acquired using 785 nm excitation. A line at 946.4 nm has also been observed in absorption measurements of these samples [26]. This feature has previously been observed in absorption measurements on polycrystalline CVD diamond and this work indicated that one defect is responsible for the line at 946 nm, as well as additional lines at 857 nm and 830 nm [27]. This line, however, has never been reported in single-crystal CVD diamond grown without silane addition, inviting the suggestion that it is silicon-related.

Absorption measurements suggest that the line at 946 nm is strongest in samples grown in the absence of nitrogen and for the samples examined by EPR an

approximate correlation between its intensity and the concentration of $(V\text{-}Si\text{-}V)^0$ has been noted [26]. A similar correlation is observed in the photoluminescence measurements shown in figure 6-14, although due to the inhomogeneous incorporation of silicon this result should be treated with caution.

The line at 1.303 eV observed in the photoluminescence measurements of these samples has not been previously reported. Figure 6-14 also suggests that the vibronic sideband visible between 1.2–1.3 eV is likely to be associated with this feature. Further study is needed before any correlations between the intensity of this feature and the uptake of silicon can be inferred.

6.5 Conclusions and further work

EPR has been used to study defects present in SC-CVD samples intentionally doped with silicon by the addition of silane to the growth gases. It is concluded that the EPR spectra for KUL1 are consistent only with the neutral silicon split-vacancy model, $(V\text{-}Si\text{-}V)^0$, and KUL3 has been shown to be the same defect, but decorated with a hydrogen atom bonded in the vicinity of the $(V\text{-}Si\text{-}V)^0$ structure; $(V\text{-}Si\text{-}V{:}H)^0$, as proposed by Goss *et al.* [2]. These models were confirmed from the intensities and orientation dependence of the ^{13}C and ^{29}Si hyperfine satellites in KUL1 and the ^{1}H and ^{29}Si hyperfine satellites for KUL3. The presence of silicon in both defects has been proved by examining samples enriched with ^{29}Si; in such samples the intensity of the hyperfine satellites assigned to ^{29}Si increased such that the ratio of these to the central (^{28}Si) resonance line matched the quoted isotopic enrichment of the silane used in the growth. There is excellent agreement between the hyperfine parameters determined for $(V\text{-}Si\text{-}V)^0$ and $(V\text{-}Si\text{-}V{:}H)^0$ and those calculated from local density functional theory [2].

The symmetry of the $\underline{g}$ and $\underline{D}$ matrices determined for KUL1 are consistent with the $(V\text{-}Si\text{-}V)^0$ model. Although a detailed interpretation of the magnitudes of these parameters has not yet been attempted it has been shown that a simple spin-orbit coupling estimate of the magnitude of D from the g shift suggests that the zero-field interaction is dominated by this term. The observed temperature variation of the $\underline{D}$ matrix is interesting and deserves further study.

The KUL8 defect, suggested [6, 7] to be (V-Si-V)$^-$ has not been detected in any of the samples examined and to-date no additional spectra have been observed that can be assigned to (V-Si-V)$^-$, despite the presence of absorption/PL features at 1.682 eV. The concentration of the 737 nm defect was estimated from the absorption measurements to be ~ 12 ppb in two of the samples examined, which is well above the detection limit in EPR. Hence the apparent absence of an EPR spectrum that can be attributed with the $S = \frac{1}{2}$ ground state of (V-Si-V)$^-$ is intriguing.

It is possible that the EPR spectra from the (V-Si-V:H)^0 defect overlaps with EPR lines from (V-Si-V)$^-$. It is apparent that additional, as yet unidentified, EPR lines are present in these sample (see for example figure 6-11, where an additional resonance line is observed at 350.8 mT). In previous work KUL3/(V-Si-V:H)^0 has been observed to annealed out 1400°C, at the same time as another (likely hydrogen-related defect) was seen to increase in intensity [5]. Annealing studies are therefore planned to further investigate the stability of (V-Si-V:H)^0 and to aid in the identification of any additional EPR spectra which remain or are formed during annealing.

The lack of detection of (V-Si-V)$^-$ by EPR may be due to dynamic Jahn-Teller coupling of the ground state, giving rise to an averaging between different configurations which is fast compared to the timescale of an EPR experiment. Such averaging could result in the ground-state EPR signal becoming very broad, hence making it hard to detect. It should be noted that, in the samples examined which have a high concentration of the 1.682 eV defect, a very broad signal (~ 1 mT) is observed around $g = 2$. This is absent in a sample which contained an order of magnitude lower 1.682 eV. Applying uniaxial stress to the sample whilst conducting an EPR experiment could lift the degeneracy and allow the ground state to be detected. The experimental equipment to make such studies possible is currently being developed.

References

[1] J. P. Goss, R. Jones, S. J. Breuer, P. R. Briddon, and S. Oberg, Phys. Rev. Lett. **77**, 3041 (1996).

[2] J. P. Goss, P. R. Briddon, and M. J. Shaw, Phys. Rev. B **76**, 075204 (2007).

[3] S. W. Brown and S. C. Rand, J. Appl. Phys. **78**, 4069 (1995).

[4] H. Sternschulte, K. Thonke, J. Gerster, W. Limmer, R. Sauer, J. Spitzer, and P. C. Munzinger, Diam. Relat. Mater. **4**, 1189 (1995).

[5] K. Iakoubovskii and A. Stesmans, Phys. Status Solidi A **186**, 199 (2001).

[6] K. Iakoubovskii and A. Stesmans, Phys. Rev. B **66**, 195207 (2002).

[7] K. Iakoubovskii, A. Stesmans, M. Nesladek, and G. Knuyt, Phys. Status Solidi A **193**, 448 (2002).

[8] K. Iakoubovskii, A. Stesmans, K. Suzuki, J. Kuwabara, and A. Sawabe, Diam. Relat. Mater. **12**, 511 (2003).

[9] H. Sternschulte, K. Thonke, R. Sauer, P. C. Munzinger, and P. Michler, Phys. Rev. B **50**, 14554 (1994).

[10] C. L. Wang, C. Kurtsiefer, H. Weinfurter, and B. Burchard, J. Phys. B At. Mol. Opt. **39**, 37 (2006).

[11] D. J. F. Evans, C. J. Kelly, P. Leno, P. M. Martineau, and A. J. Taylor, *Silicon doped single crystal CVD diamond grown using silane*, The 57^{th} Diamond Conference, Cambridge, oral presentation by P. M. Martineau (2006).

[12] S. D. Williams, D. J. Twitchen, P. M. Martineau, G. A. Scarsbrook, and I. Friel (2007), UK Patent Application: GB 2428690 A.

[13] S. C. Lawson, D. Fisher, D. C. Hunt, and M. E. Newton, J. Phys. Condens. Mat. **10**, 6171 (1998).

[14] W. V. Smith, P. P. Sorokin, I. L. Gelles, and G. J. Lasher, Phys. Rev. **115**, 1546 (1959).

[15] D. J. Twitchen, M. E. Newton, J. M. Baker, T. R. Anthony, and W. F. Banholzer, Phys. Rev. B **59**, 12900 (1999).

[16] A. Abragam, J. Horowitz, M. H. L. Pryce, and K. W. Morton, Proc. Roy. Soc. Lond. A Mat. **230**, 169 (1955).

[17] J. H. Wood and G. W. Pratt, Phys. Rev. **107**, 995 (1957).

[18] J. R. Morton and K. F. Preston, J. Magn. Reson. **30**, 577 (1978).

[19] G. D. Watkins, Phys. Rev. B **12**, 4383 (1975).

[20] M. Gerloch, *Orbitals, terms and states* (Wiley, Chichester, 1986).

[21] C. D. Clark and C. B. Dickerson, Surf. Coat. Tech. **47**, 336 (1991).

[22] A. T. Collins, L. Allers, C. J. H. Wort, and G. A. Scarsbrook, Diam. Relat. Mater. **3**, 932 (1994).

[23] G. Davies, Physica B **273-274**, 15 (1999).

[24] G. Davies, Rep. Prog. Phys. **44**, 787 (1981).

[25] K. Iakoubovskii, G. J. Adriaenssens, N. N. Dogadkin, and A. A. Shiryaev, Diam. Relat. Mater. **10**, 18 (2001), diam. Relat. Mat.

[26] P. M. Martineau, private communication.

[27] L. Allers and A. T. Collins, J. Appl. Phys. **77**, 3879 (1995).

Chapter 7

Preferential orientation of silicon-related defects

7.1 Background and motivation for study

In §3.7.1 it was discussed how a point defect in diamond may be aligned along a number of different directions which are crystallographically equivalent, dependent on the symmetry of the centre. If the defect is assumed to be *statistically oriented* then the probability of defect being aligned along all equivalent directions is equal. In this chapter the term *preferential orientation* will be used to describe a defect which displays a non-equal distribution over crystallographically equivalent directions.

In previous studies a number of preferentially-oriented defects have been observed in HPHT diamond:

- The H3 centre, which is a defect of C_{2v} symmetry which consists of a vacancy trapped at an A-centre aggregate (see figure 7-1), are only found in {100} growth sectors and are exclusively aligned with the ⟨100⟩ growth direction for a particular sector [1].
- The 1.40 eV [2] and 1.22 eV [3] optical centres are both predominantly aligned to the [111] axis in {111} growth sectors. The 1.40 eV centre has been associated with the $S = \frac{1}{2}$ EPR defect NIRIM2 [4], which has been suggested to consist of a Ni^+ ion situated at the centre of a split vacancy [5] (D_{3d} symmetry, analogous to $(V\text{-}Si\text{-}V)^0$). The 1.22 eV centre is thought to be a different charge state of the same defect [3] and has been assigned to the NIRIM5 EPR spectrum [5].

For the H3 centre a model has been put forward by Dodge to explain the

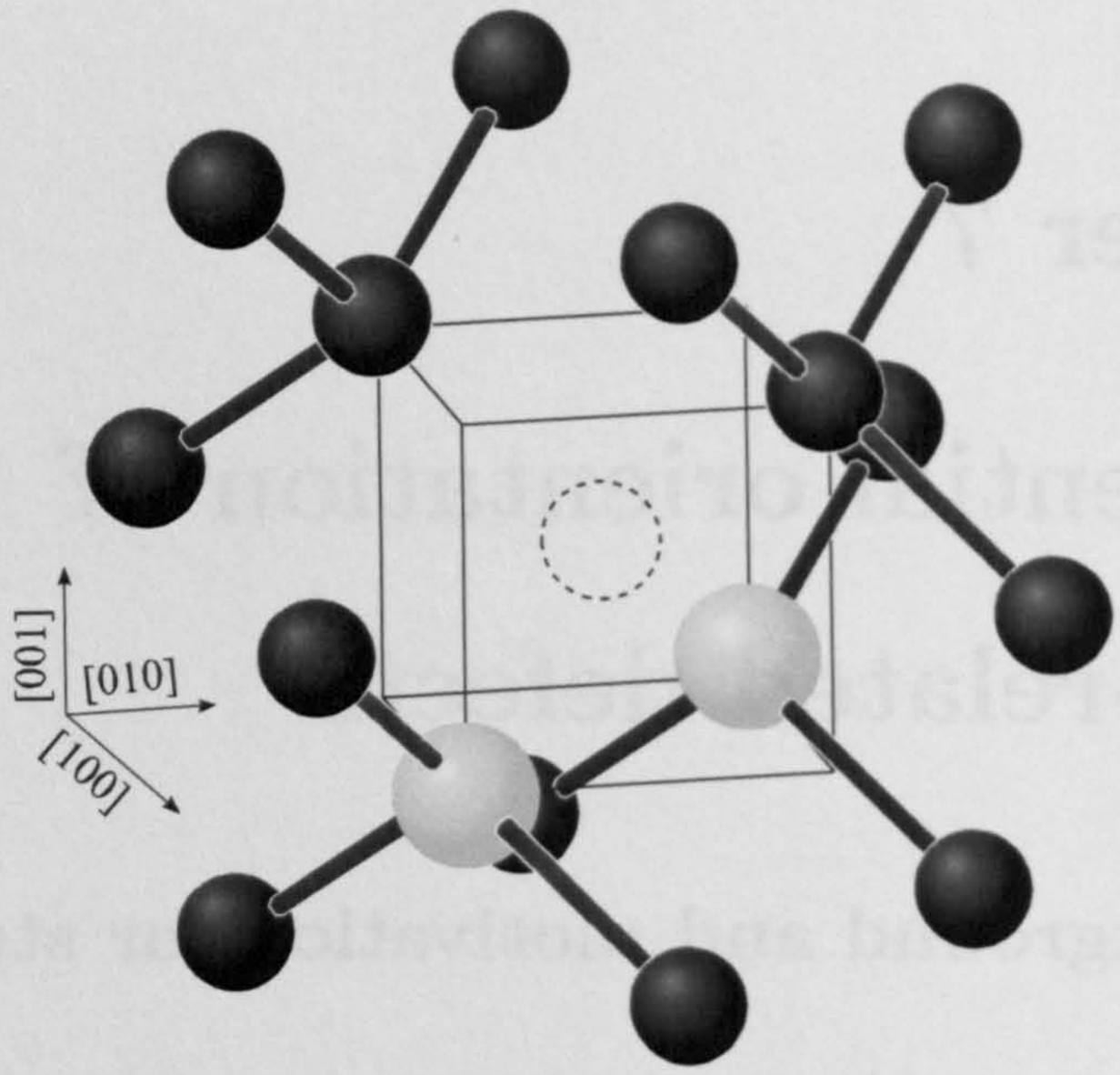

Figure 7-1: The structure of the H3 centre. The black spheres represent carbon atoms, the lighter spheres the nitrogen atom and the dashed circle indicates the position of the vacancy.

formation and preferential orientation of H3 [6]. At high temperatures (1200–1800°C) there is a possibility that two single nitrogen atoms will form an in-plane nearest-neighbour pair in a {100} growth sector. The vacancy must then be located in the next {100} layer, to preserve the continuity of the growth, hence the defect is exclusively aligned along the ⟨100⟩ axis parallel to the growth direction of the sector. The nitrogen atoms and vacancies are grown in as a *unit*. H3 can also be formed in type Ia diamond by irradiation damage, followed by annealing at temperatures in excess of 550°C [7]. In these cases no preferential orientation is reported, consistent with the formation of the defect by the capture of a mobile vacancy by an A-centre.

The above example demonstrates how preferential orientation can be used to infer information regarding the production of a defect during growth, or subsequent sample processing. However, in diamond grown by the CVD method there is very little published material concerning preferential orientation of defects. The observation of a preference of alignment for any defect in as-grown CVD diamond would be significant, as it means the defect incorporation provides a "finger-print" of the growth direction.

The $(V\text{-}Si\text{-}V)^0$ defect revealed in the previous chapter has D_{3d} symmetry, hence there are four possible orientations of this defect (along [111], $[\bar{1}\bar{1}1]$, $[1\bar{1}\bar{1}]$ and $[\bar{1}1\bar{1}]$). Therefore with the applied magnetic field (**B**) parallel to ⟨111⟩ four groups of EPR resonance lines would be expected. If $(V\text{-}Si\text{-}V)^0$ is assumed to statistically orient itself, then these groups will have relative intensities 1:3:3:1. Any deviation away from this ratio will indicate, providing care is taken to check for saturation effects, that the defect displays a preference as to which direction it is oriented along.

In this chapter experimental results are presented which demonstrate that the previously identified $(V\text{-}Si\text{-}V)^0$ defect displays preferential orientation in SC-CVD diamond deliberately doped with silicon during growth. The significance of this is discussed with reference to what it may reveal regarding the formation of the defect and the incorporation efficiency of silicon on differently oriented diamond surfaces.

7.2 Experimental details

The results presented in this chapter have been obtained from the three silicon-doped SC-CVD diamond samples which were used to identify the $(V\text{-}Si\text{-}V)^0$ and $(V\text{-}Si\text{-}V\text{:}H)^0$ defects in the previous chapter. As before these will be referred to as samples A, B and C (see §6.3.1). For the purposes of this chapter the important difference between these samples is the orientation of the diamond substrate that these samples were grown on. Samples A and C were grown on {110} oriented substrates, whilst sample B was grown on a {100} substrate.

Room-temperature EPR spectra were obtained using the EMX/EMX-E Bruker X-band spectrometers (described in §4.2), with **B** oriented along the different ⟨111⟩ directions. These could be easily identified using the roadmap for $(V\text{-}Si\text{-}V)^0$ (figure 7-2) and with knowledge of the crystallographic orientations of the faces of the sample. To accurately determine the ratio of the intensities of the $(V\text{-}Si\text{-}V)^0$ resonance lines high resolution scans were collected over half the $(V\text{-}Si\text{-}V)^0$ spectrum, as shown in figure 7-2. These spectra were then obtained at a range of microwave powers between 0.2 nW and 3 mW, to ensure that saturation did not

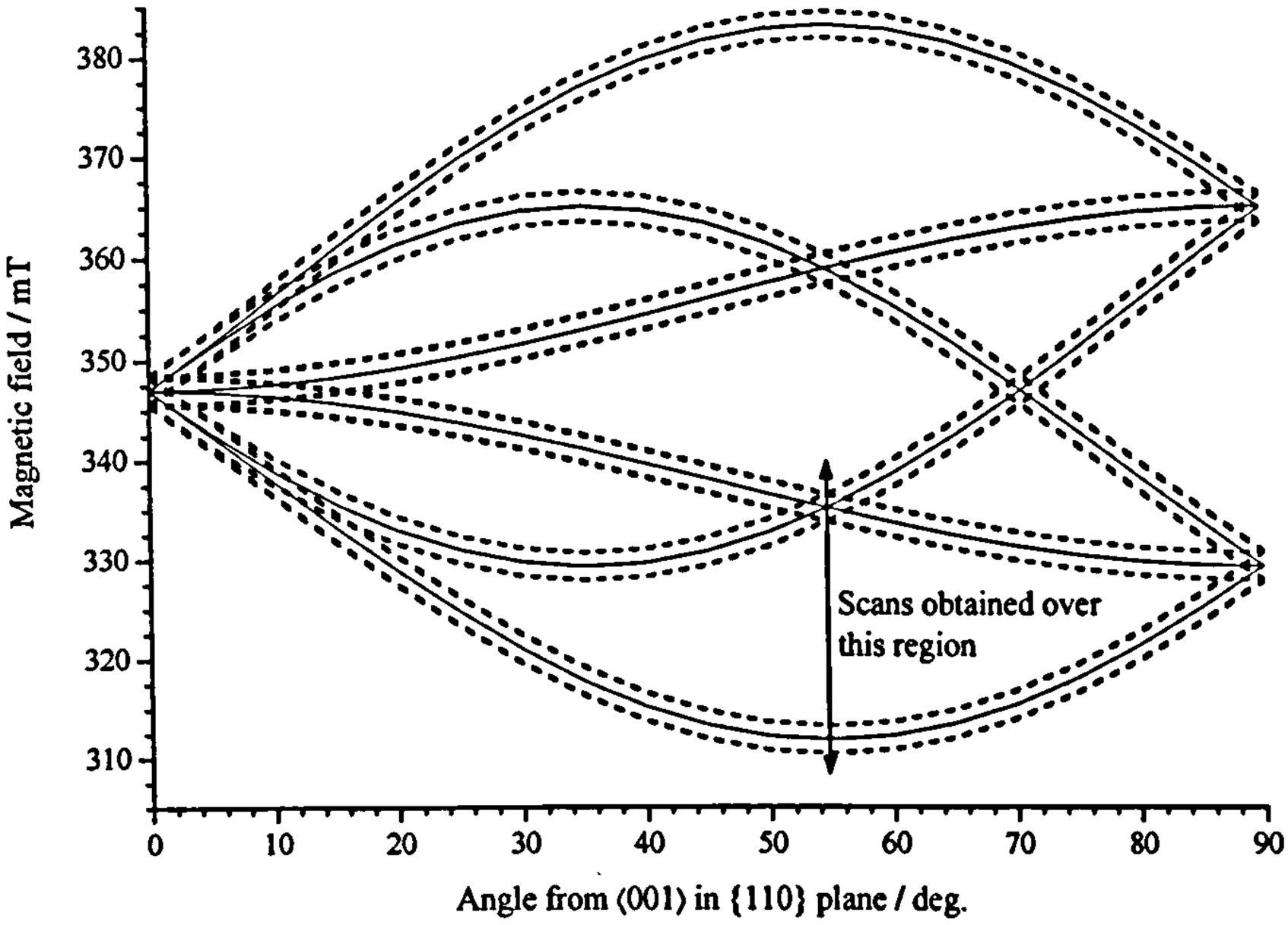

Figure 7-2: Roadmap for $(V\text{-}Si\text{-}V)^0$, generated using the parameters presented in §6.4.1. The solid lines map the orientation dependence of the resonance lines from $(V\text{-}^{28}Si\text{-}V)^0$, whilst the dotted lines represent $(V\text{-}^{29}Si\text{-}V)^0$. The region over which the scans were obtained in this chapter is indicated.

distort the ratio of line intensities expected for a given distribution of centres amongst equivalent orientations.

For clarity and consistency when discussing the results obtained from the samples grown on {110} oriented substrates ⟨111⟩ directions will be referred to with reference to the specific {110} plane in which they are found. If the direction of growth is taken to be [110] two groups of ⟨111⟩ orientations are present; two of the ⟨111⟩ directions lie in the (110) growth plane, whilst the remaining two are found in the $(\bar{1}10)$ plane which is perpendicular to this. This is clearly shown in figure 7-3.

7.3 Results

The EPR spectrum obtained from sample B (grown on a {100} substrate) with $B \parallel \langle 111 \rangle$ is shown in figure 7-4. The simulated data was created assuming that the ratio, R, of the intensities (I_2 and I_1) under the two sets of $(V\text{-}Si\text{-}V)^0$ lines shown, equals 3.

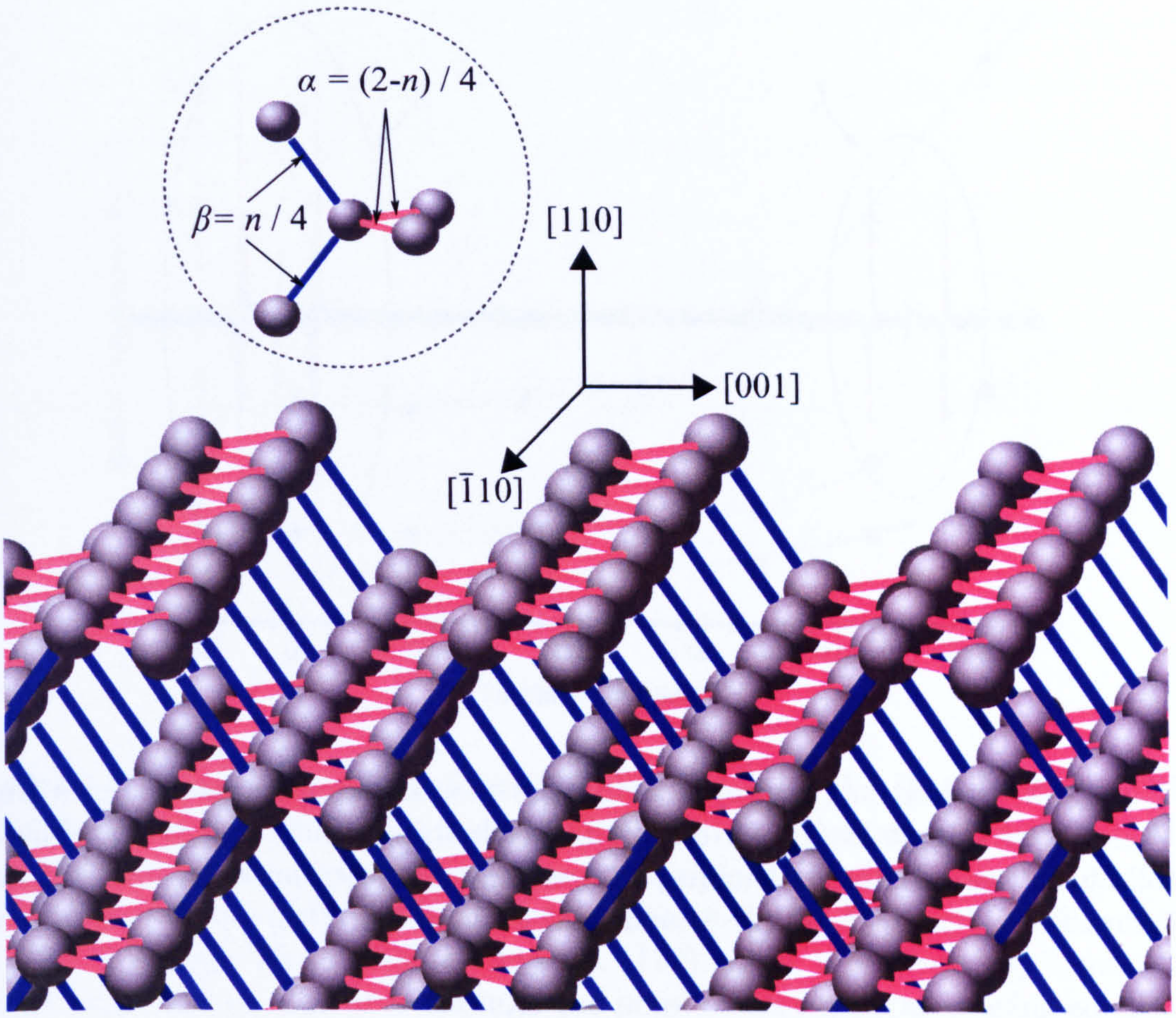

Figure 7-3: View along a (110) growth plane, displaying the atomic scale roughness of the surface. Bonds that lie in the growth plane (type α) are coloured red (—) and those that are in the ($\bar{1}$10) plane (type β) are indicated by blue (—) lines.

Figure 7-5 shows that R is dependent on the microwave power ($P_{\mu w}$), with the ratio rising as $P_{\mu w}$ is increased, illustrating the importance of conducting such scans at a range of microwave powers. As the power approached zero R leveled off to the value of 3 ($R_0 = 3$), inferred from the experimental data shown in figure 7-4. This value (and the dependence of R with microwave power) remained unchanged when looking at the spectra along all four ⟨111⟩ directions.

However, as is also illustrated in figure 7-5, *two* values of R_0 were obtained for sample C (grown on a {110} substrate), depending on which ⟨111⟩ direction **B** was parallel to. For both the ⟨111⟩ orientations in the (110) plane of growth a ratio, $R_{0(\alpha)} = 7.3(1)$ was determined, compared to $R_{0(\beta)} = 1.6(1)$ for the two ⟨111⟩ directions pointing out of the growth surface (in ($\bar{1}$10) plane). For the other {110} sample (sample A) the difference between the ratios was smaller; $R_{0(\alpha)} = 3.9(1)$

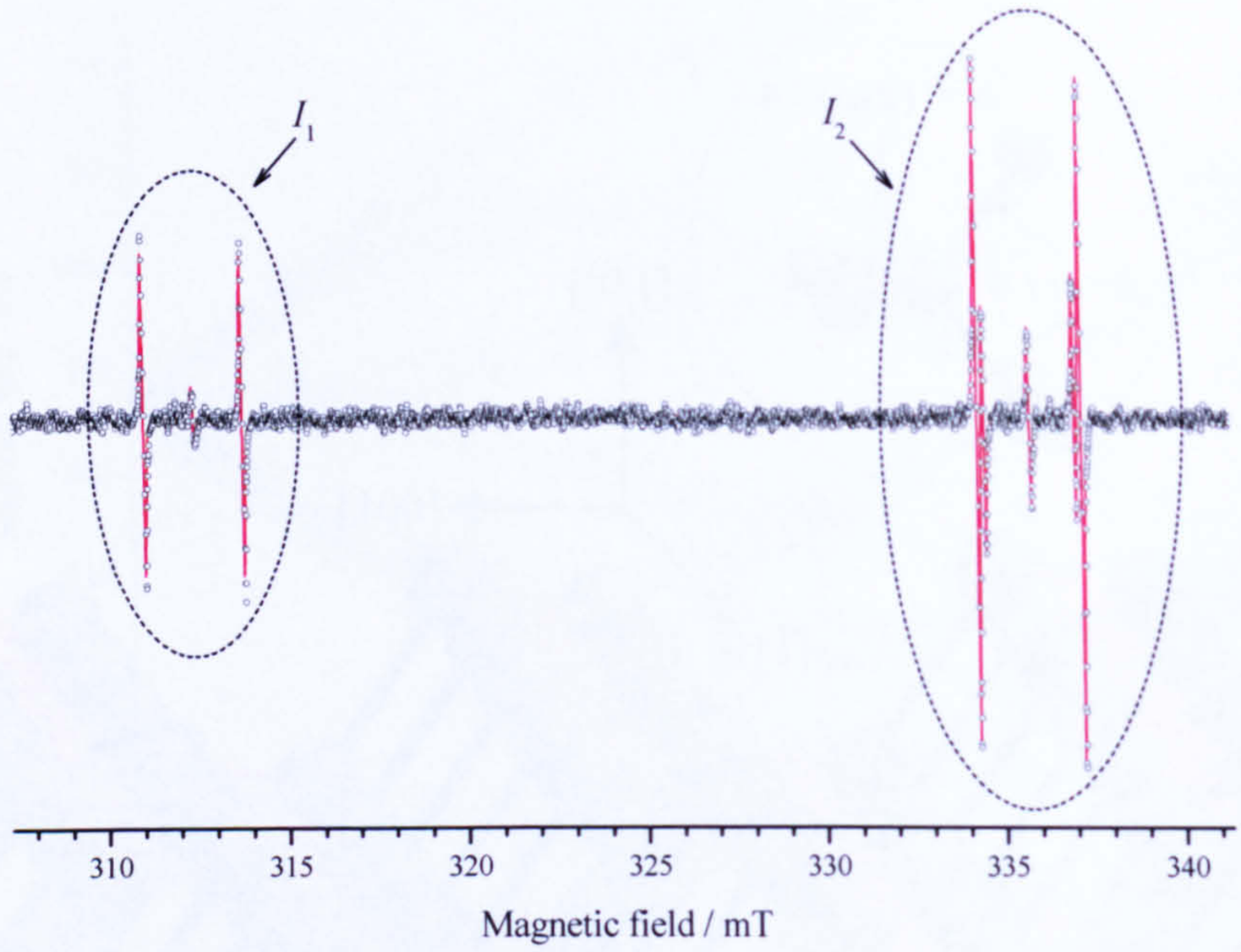

Figure 7-4: Spectrum (points) showing the two lowest field sets of lines from $(\text{V-Si-V})^0$ in sample B (grown on a {100} substrate) when $\mathbf{B} \parallel \langle 111 \rangle$. The fit (solid line) was generated assuming no preferential orientation of $(\text{V-Si-V})^0$ (ratio of intensities, $R = I_2/I_1$, equals 3) and a 9:1 ratio of $^{29}\text{Si}/^{28}\text{Si}$.

and $R_{0(\beta)} = 2.3(1)$.

The low concentrations of $(\text{V-Si-V:H})^0$ in the three samples (maximum 6 ppb, see table 6-1) means that a detailed study of the relative intensities of these resonance lines with $\mathbf{B}$ along different $\langle 111 \rangle$ orientations has not been completed to-date.

7.4 Discussion

7.4.1 Microwave power dependence of line intensities

It is apparent from the data in figure 7-5 that the observed distribution of intensity between EPR lines originating from different sites of $(\text{V-Si-V})^0$ is dependent on the microwave power. Resonance lines originating from sites parallel to the magnetic field saturate at lower microwave powers than those along other, equivalent, $\langle 111 \rangle$ directions. This results in R being increased at higher values of $P_{\mu w}$.

The variation in the degree of microwave saturation of different alignments

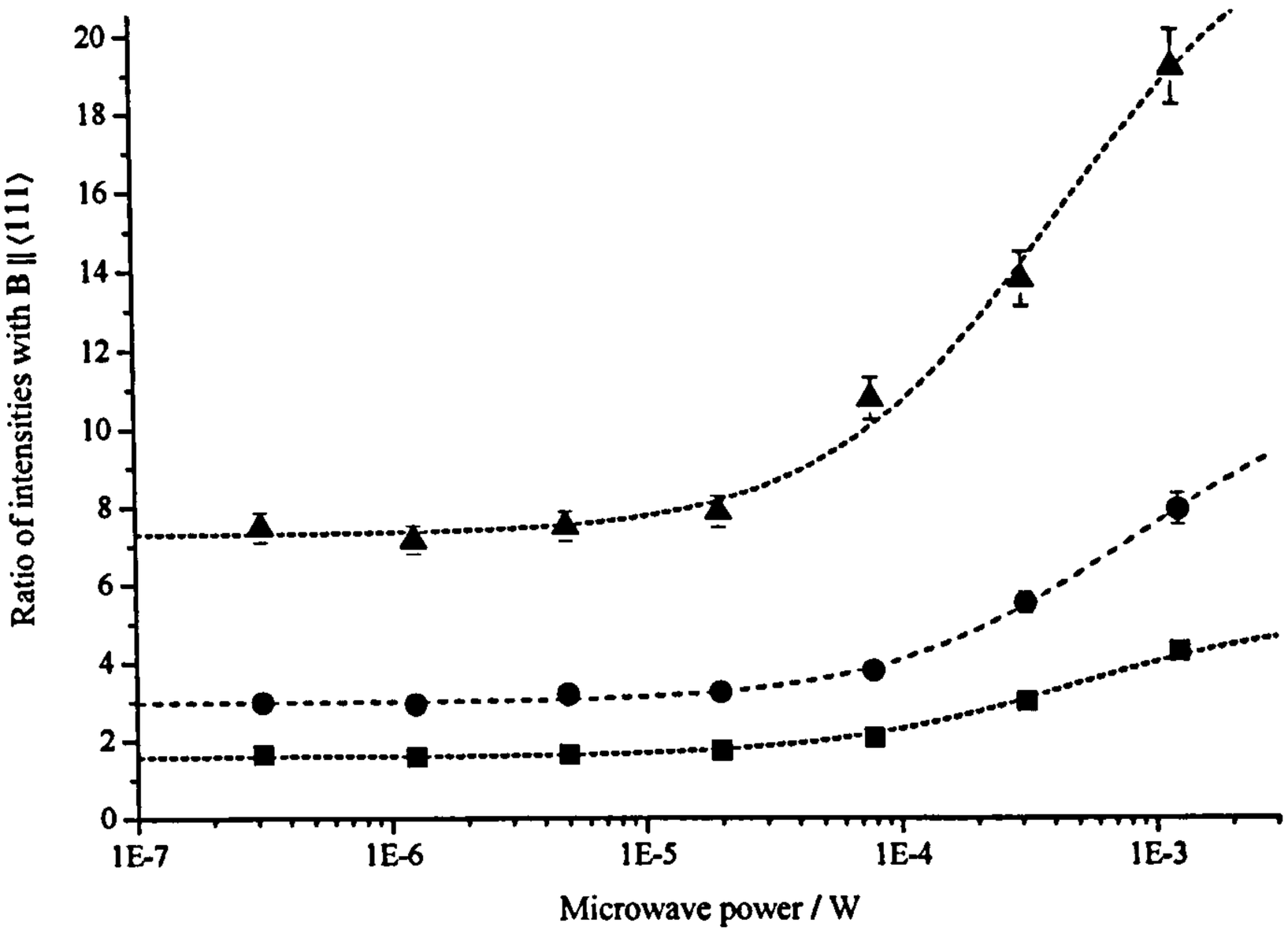

Figure 7-5: Ratio of intensities of the (V-Si-V)^0 lines with B ∥ ⟨111⟩ (see figure 7-4) observed for samples B and C (grown on {100} and {110} substrates, respectively), as a function of microwave power. Data for sample B is indicated by the circular data points (•). For sample C data has been obtained with B along ⟨111⟩ directions in the (110) plane (growth plane) and the ($\bar{1}$10) plane, represented by symbols ▲ and ■, respectively. The lines through the points where generated using equation 7-2.

of (V-Si-V)^0 is understandable if one considers the matrix of elements formed by operating the spin Hamiltonian on the spin states of the system. As discussed in §3.5, the eigenvalues of this matrix describe the probability of a transition occurring between the eigenstates. Considering the case where **B** is applied along ⟨111⟩ the matrix for (V-Si-V)^0 sites that lie parallel to the magnetic field will have zero off-diagonal elements, which means only transitions in accordance with the selection rules $\Delta M_S = \pm 1$, $\Delta m_I = 0$ are permitted (§3.5). Conversely, for the other three orientations the off-diagonal elements are non-zero and hence the selection rules are relaxed.

Saturation occurs when the microwave power is high enough that the spin-lattice relaxation rate ($1/T_1$) is no longer sufficient to maintain the population difference between the spin states at resonance. From the discussion above it is apparent that, for the sites that lie parallel to B, only one relaxation pathway is permitted ($\Delta M_S = \pm 1$, $\Delta m_I = 0$), whereas for the other three sites, due to the

mixing between eigenstates, multiple pathways are allowed. This means the value of T_1 will vary, dependent on the alignment of **B** relative to the D_{3d} symmetry axis. If T_{1_a} and T_{1_b} are defined as the electron spin-lattice relaxation times for sites lying parallel to **B** and those which make an angle of 70.5° with **B**, respectively, then it would be expected that $T_{1_a} > T_{1_b}$.

To predict the dependence of R with microwave power an expression relating the integrated intensity to the microwave power is required. From the Lorentzian form of the EPR lineshape obtained from the Bloch equations (equation 3-39) it is evidence that the integrated intensity, I, is given by the expression:

$$I = A\frac{B_1\pi}{\gamma_e T_2}\frac{1}{\sqrt{{\Gamma_0}^2 + {B_1}^2\left(\frac{T_1}{T_2}\right)}}, \tag{7-1}$$

where A is a constant, Γ_0 is the half-width at half-maximum as $P_{\mu w} \rightarrow 0$ and T_2 is the spin-spin relaxation time (see §3.6). Hence the ratio, R, between two sets of resonance lines values can be written (in general form) as:

$$R(P_{\mu w}) = R_0\sqrt{\frac{\Gamma_{0_a}T_{2_a} + T_{1_a}P_{\mu w}}{\Gamma_{0_b}T_{2_b} + T_{1_b}P_{\mu w}}}, \tag{7-2}$$

The highest curve in figure 7-5 for $R(P_{\mu w})$ for the sample grown on a {110} substrate was fitted using equation 7-2, with $\Gamma_{0_a} = \Gamma_{0_b}$ and $T_{2_a} = T_{2_b}$. The data corresponding to the saturation behaviour observed in this sample for the other type of ⟨111⟩ direction was then plotted using the same value for Γ_0, T_2, T_{1_a} and T_{1_b}; only R_0 was allowed to vary. The same function was used to fit the experimental data from the sample grown on a {100} substrate. This function provides an excellent fit to the observed dependence of R with microwave power for all three data sets.

7.4.2 Preferential orientation of (V-Si-V)^0

As the microwave power is reduced, one would expect the ratio to level off and approach $R = 3$ if all ⟨111⟩ orientations of (V-Si-V)^0 are equally probable. This is not the case in sample C, as it was shown that, when the magnetic field is oriented along a ⟨111⟩ direction in the $(\bar{1}10)$ plane $R_{0(\alpha)} = 1.6(1)$, compared to a value of $R_{0(\beta)} = 7.3(1)$ for the ⟨111⟩ orientations in the (110) growth plane. This finding

demands further scrutiny, as it implies that (V-Si-V)^0 incorporates itself unequally in the four different ⟨111⟩ directions, demonstrating preferential orientation.

To model the apparent preferential orientation of (V-Si-V)^0 the probability of the defect's D_{3d} symmetry axis being oriented along one of the ⟨111⟩ directions in the $(\bar{1}10)$ plane (β in figure 7-3) is set to $\frac{n}{4}$. The probability for the other two possible ⟨111⟩ orientations of (V-Si-V)^0 (α) is therefore set to $\frac{2-n}{4}$, such that the probabilities sum to unity. $R_{0(\alpha)}$ and $R_{0(\beta)}$ can then be expressed as:

$$R_{0(\alpha)} = \frac{2\beta + \alpha}{\alpha} = \frac{2+n}{2-n} \tag{7-3}$$

$$R_{0(\beta)} = \frac{2\alpha + \beta}{\beta} = \frac{4-n}{n} \tag{7-4}$$

In the case of no preferential orientation a value of $n = 1$ would be expected, since this would yield the result $R_{0(\alpha)} = R_{0(\beta)} = 3$.

The result obtained for sample C that $R_{0(\alpha)} = 7.3$ implies that $n = 1.5$. Using this value in equation 7-4 yields a predicted ratio of 1.6, in excellent agreement with the experimentally observed ratio of 1.6 ± 0.1. The results are therefore consistent with (V-Si-V)^0 being preferentially oriented with equal probability in the two ⟨111⟩ directions pointing out of the growth plane; referring to figure 7-3 site type β is approximately three times more prevalent than type α. Sample A also displayed preferential orientation, but to a lesser extent; $n = 1.2$. Since $n = 1$ for sample B no preferential orientation was observed in this sample.

The finding that (V-Si-V)^0 displays preferential orientation allows one to elucidate possible formation mechanisms for the defect during growth. However, the variation in the degree of preferential orientation in the three samples must be accounted for.

It is known that the concentration of (V-Si-V)$^-$ can be dramatically increased by irradiation damage and annealing at temperatures where vacancies are mobile (> 700 K [8]) [9, 10]. This suggests that (V-Si-V) can be formed by mobile vacancies being captured by silicon, present in a different form. If such a mechanism is the primary source of (V-Si-V) formation during growth preferential orientation of the defect is unlikely, since vacancy migration is likely to be equally probable along crystallographically equivalent directions. The finding of preferential orientation

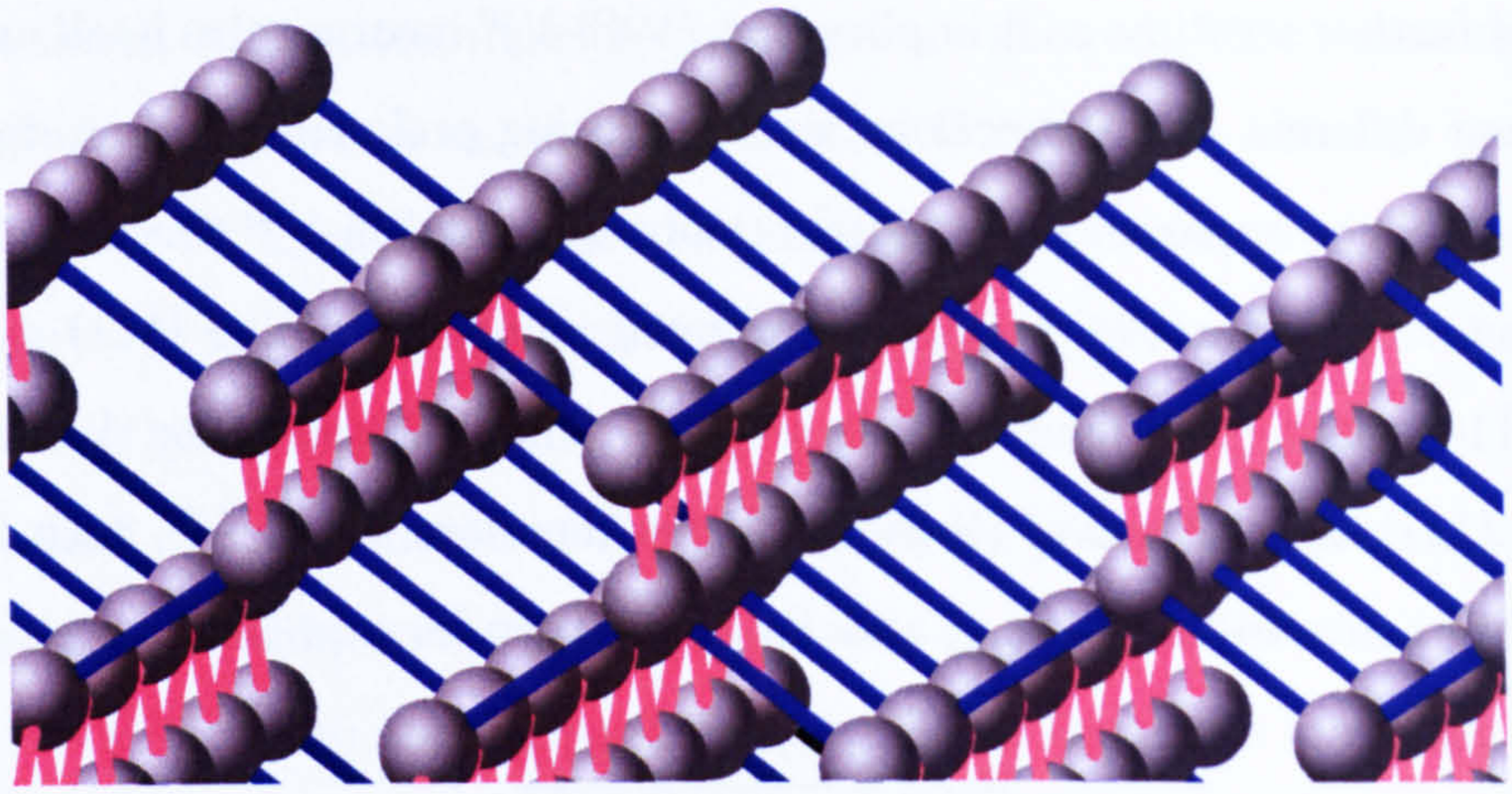

Figure 7-6: View along a (100) growth plane displaying the alternating planes in which the bonds along ⟨111⟩ are found in each layer.

therefore implies the defect is growing in (or at least a substantial fraction) as a *unit*.

For growth on a {100} substrate all possible ⟨111⟩ directions make the same angle with the growth direction; the layers formed during growth display alternating pairs of possible ⟨111⟩ orientations (see figure 7-6). It is therefore evident that no obvious mechanism exists for preferential orientation of (V-Si-V) in CVD diamond grown on {100} substrates, even if the defect is grown in as a unit. This explains the lack of observable preferential orientation of $(\text{V-Si-V})^0$ in sample B. Also, since {100} oriented diamond substrates are the most widely used in SC-CVD growth, the lack of data in previous literature demonstrating the existence of preferentially oriented trigonal defects (i.e. ⟨111⟩ symmetry axis) in CVD diamond is not surprising.

It is possible that $(\text{V-Si-V})^0$ is formed both as a unit *and* via vacancy capture during growth. If the former process dominates over the latter then preferential orientation can be displayed, but the degree will depend upon the balance between these two processes. This will be dependent on the production and availability of isolated vacancies during growth and the presence of competing traps. Such factors will vary with the growth conditions (such as the temperature of the substrate) as well as the presence of other impurities.

It is noted that an E6 patent suggests that a typical substrate temperatures

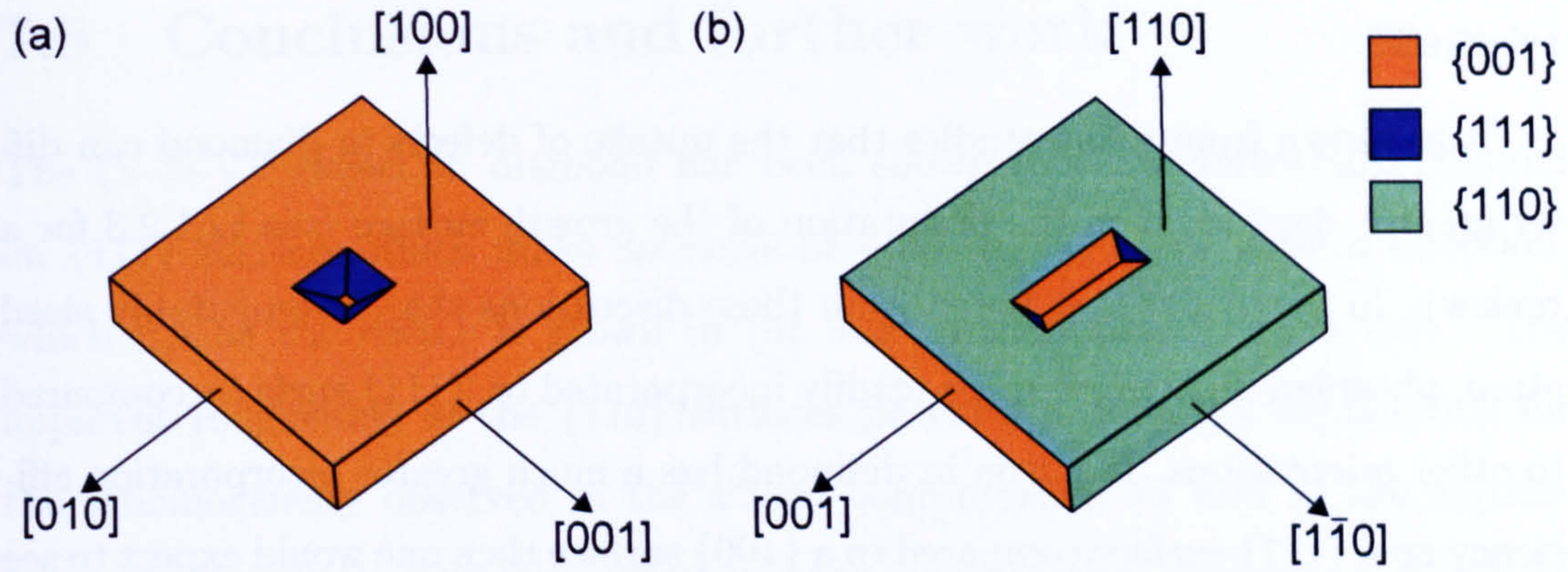

Figure 7-7: Schematic illustrating the micro-faceting observed on (a) {100} and (b) {110} surfaces of silicon-doped samples.

for silicon-doped CVD diamond (albeit on {100} substrates) is ~ 800°C [11]. This implies that the temperature of the samples will to be sufficiently high to permit vacancy migration during growth, thus if silicon is the primary trap for vacancies only *partial* preference of two ⟨111⟩ orientations would be expected in these samples. Although differences in the growth conditions between the two samples are likely, due to the different degrees of nitrogen contamination in the methane source gas (see §6.3.1), no specific information is available. The lack of observation of NV^- in either sample (by EPR) suggests silicon is indeed the primary trap for vacancies.

In contrast to a {100} surface {110} surfaces are rough on an atomic scale (compare figures 7-3 and 7-6). To examine the morphology of the surface of the samples differential interference contrast microscopy (DIC) images have been obtained by the Diamond Trading Company (Maidenhead, UK). These images show that both samples have a rough {110} surface, with long groves/micro-facets running along the surface which have their longest length parallel to [001] [12]. This makes it probable that their side facets are close to (100) and (010), as shown in figure 7-7a. The groves were observed to be bounded by ⟨111⟩ facets.

In §6.3.1 it was noted that the concentration of silicon in these samples was highly inhomogeneous, with a variation of a factor six across the surface. The apparent micro-faceting during growth provides a means to explain this observation as well as providing an explanation for the appearance (and variation in the degree) of preferential orientation of $(V\text{-}Si\text{-}V)^0$ in samples grown on {110}

substrates.

It is known from many studies that the uptake of defects in diamond can differ greatly, dependent in the orientation of the growth surface (see §2.1.2.3 for a review). In particular it is noted from these discussions that a comparably sized atom, phosphorus, is much more readily incorporated on {111} surfaces compared to other orientations. If silicon in diamond has a much greater incorporation efficiency on a {111} surface compared to a {100} surface then one would expect to see greatly increased concentrations in regions where micro-facets (bounded by {111} faces) occurred. Critically for the consideration of preferential orientation only two of the four ⟨111⟩ orientations (those contained in the $(\bar{1}10)$ plane perpendicular to the growth direction) are presented. Hence, with a sufficiently large difference in incorporation efficiency between the {110} growth surface and the {111} micro-facets, a preferential orientation could be built up provided $(V\text{-}Si\text{-}V)^0$ is grown in as a unit: Considering the incorporation of substitutional silicon on a {111} surface the overgrowth of the next layer may result in a vacancy incorporated above the silicon atom. On the bulk {110} surface this may also occur, but it is not clear why preferential orientation would be observed.

The fact that two {110} growths show different degrees of preferential orientations is likely to be related to different surface roughening, rather than some "intrinsic" growth process.

In contrast to the roughening occurring on a bulk {110} surface, micro-faceting visible on the surface of a sample grown on a {100} oriented substrate will likely to display all four ⟨111⟩ faces, as shown in figure 7-7b. The presence of such micro-facets would still permit a highly inhomogeneous uptake of silicon, but since all ⟨111⟩ faces are presented there is no means for preferential orientation of $(V\text{-}Si\text{-}V)^0$.

Considering the formation of $(V\text{-}Si\text{-}V\text{:}H)^0$, it is probable that $(V\text{-}Si\text{-}V)^0$ is formed in the vicinity of an incorporated hydrogen atom, with the hydrogen atom then relaxing to the position inferred for $(V\text{-}Si\text{-}V\text{:}H)^0$ (see figure 6-13). With the initial (V-Si-V) structure common to both defects it appears likely be likely that $(V\text{-}Si\text{-}V\text{:}H)^0$ would display the same degree of preferential orientation, although further experimental study of {110} grown samples is needed to ascertain whether this is the case.

7.5 Conclusions and further work

The (V-Si-V)^0 defect in diamond has been shown to be preferentially oriented on {111} surfaces which make an angle of ~ 35° to the ⟨110⟩ growth direction, which means the defect is grown in (at least predominantly) as a unit. The apparent roughening of the {110} surfaces provides a potential explanation for the inhomogeneity observed in the silicon concentration as well as the appearance of preferential orientation, providing the incorporation efficiency of silicon on {111} surfaces is higher than on {110}-oriented surfaces. To-date no independent experimental data concerning the relative incorporation efficiency on silicon on differently oriented diamond surfaces exists, hence this is an area which demands further experimental work.

The production of vacancies by irradiation and subsequent annealing would be expected to reduce the degree of preferential orientation, assuming a reservoir of residual silicon exists in another form that vacancies can migrate to. This is an obvious follow-up experiment. Preliminary annealing results suggest that annealing (at 1200°C) an as-grown sample (grown on a {110} substrate) containing (V-Si-V)^0 is insufficient to change the degree of preferential orientation [13], implying that most vacancies are trapped by silicon or another impurity in a stable form at these temperatures.

The recognition that preferential orientation of trigonal defects in CVD diamond is only likely to be observable in samples grown on {110} substrates is intriguing, as it permits the suggestion that other, previously identified vacancy-related centres in diamond (e.g. (NV)$^{-/0}$) may also be grown in as a unit rather than being formed predominately by vacancy capture by an impurity atom. Further investigation of defects in CVD samples grown on {110} substrates is therefore planned.

References

[1] A. T. Collins, Diam. Relat. Mater. **1**, 457 (1992).

[2] A. T. Collins, J. Phys. Condens. Mat. **1**, 439 (1989).

[3] S. C. Lawson, H. Kanda, and M. Sekita, Philos. Mag. B **68**, 39 (1993).

[4] P. W. Mason, F. S. Ham, and G. D. Watkins, Phys. Rev. B **60**, 5417 (1999).

[5] K. Iakoubovskii, Phys. Rev. B **70**, 205211 (2004).

[6] C. Dodge, Ph.D. thesis, University of Reading (1986).

[7] C. D. Clark, R. W. Ditchburn, and H. B. Dyer, Proc. Roy. Soc. Lond. A Mat. **237**, 75 (1956).

[8] G. Davies, S. C. Lawson, A. T. Collins, A. Mainwood, and S. J. Sharp, Phys. Rev. B **46**, 13157 (1992).

[9] C. D. Clark and C. B. Dickerson, Surf. Coat. Tech. **47**, 336 (1991).

[10] A. T. Collins, L. Allers, C. J. H. Wort, and G. A. Scarsbrook, Diam. Relat. Mater. **3**, 932 (1994).

[11] S. D. Williams, D. J. Twitchen, P. M. Martineau, G. A. Scarsbrook, and I. Friel (2007), UK Patent Application: GB 2428690 A.

[12] P. M. Martineau, private communication.

[13] U. F. S. D'Haenens-Johansson, private communication.

Chapter 8

The nitrogen-vacancy centre in diamond

8.1 Background and motivation for study

The negatively charged nitrogen-vacancy centre, NV^-, is a much studied colour centre in diamond which has a ZPL at 1.945 eV (637 nm) [1] and an $S = 1$ ground state with long spin-coherence time [2]. These properties have led to a great deal of interest in NV^-, focused primarily on its potential use in quantum information technologies. For example, NV^- has been suggested as a possible qubit in solid state quantum computation [3] and a single photon source for quantum communication [4]. A detailed understanding of the properties of the NV centre is important for such applications.

As discussed in §2.2.1.2 (where details regarding the identification of this defect are given), the nitrogen-vacancy consists of a substitutional nitrogen impurity and a nearest-neighbour lattice vacancy, resulting in a colour centre with C_{3v} symmetry, as shown in figure 8-1. This can be modelled using the defect-molecule approach [5], which assumes that the properties of the defect are determined by electrons in the dangling orbitals on the carbon and nitrogen atoms neighbouring the vacancy.

From group theory it is known that the three resulting linear combinations of orbitals must transform as a_1, a_1 and e. For the negative charge state of this defect there will be six electrons occupying the dangling bonds and, assuming the order of these energy levels is $a_{1N} < a_{1C} < e$ (subscripts N and C indicate singlet levels derived from nitrogen and carbon dangling orbitals respectively), the lowest energy configuration $a_{1N}^2 a_{1C}^2 e^2$ gives rise to the many-electron states $^1A_1$, $^3A_2$ and ^1E. The optically excited state found by promoting an electron from a singlet to

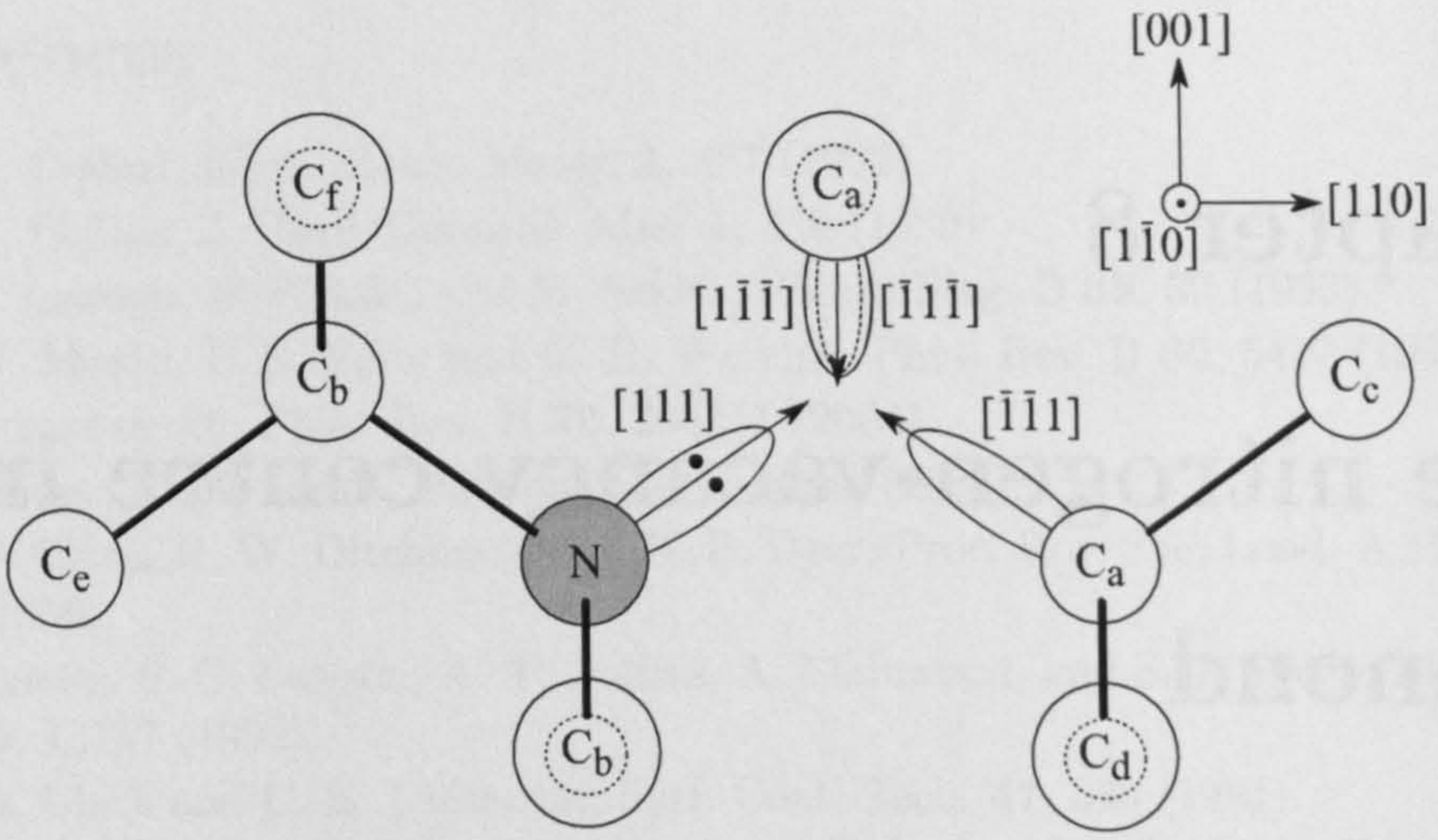

Figure 8-1: Projection of the nitrogen-vacancy centre in diamond on the (1$\bar{1}$0) plane. The grey circle represents a nitrogen atom and the other circles indicate the position of carbon atoms. The larger circles represent carbon atoms located above the plane of the paper, while the smaller, dashed circles represent those below this plane.

the doublet has the configuration $a_{1N}^2 a_{1C}^1 e^3$ and many-electron states ^{1}E and ^{3}E. Hole burning [6], optically-detected magnetic resonance [7], EPR [8] and Raman heterodyne [9] measurements have established that the ground state is a spin triplet. Combining this with results from optical measurements where uniaxial stress has been applied [1] the 1.945 eV ZPL can be associated with a $^3A_2 \rightarrow ^3$ E transition (figure 8-2).

The EPR signals associated with NV^- were first observed under conditions of optical illumination with energies greater than ~ 2 eV [10]. This is due to the fact that optical excitation causes preferential population of one of the ground state triplet levels; with a larger difference in spin populations compared to a Boltzmann distribution this leads to an increase in signal intensity and also results in the observation of EPR signals in both emission and absorption, as shown in figure 8-3b. This effect is referred to as *spin polarisation* and is attributable to inter-system crossing (permitted due to spin-orbit coupling) from the ^{3}E excited state to meta-stable singlet levels(s) (^{1}A, ^{1}E) and back preferentially to one of the spin levels of the triplet ground state [11, 12].

The observation of optically induced spin polarisation for NV^- is significant, as for quantum computing it is important that the qubit can be initialised such

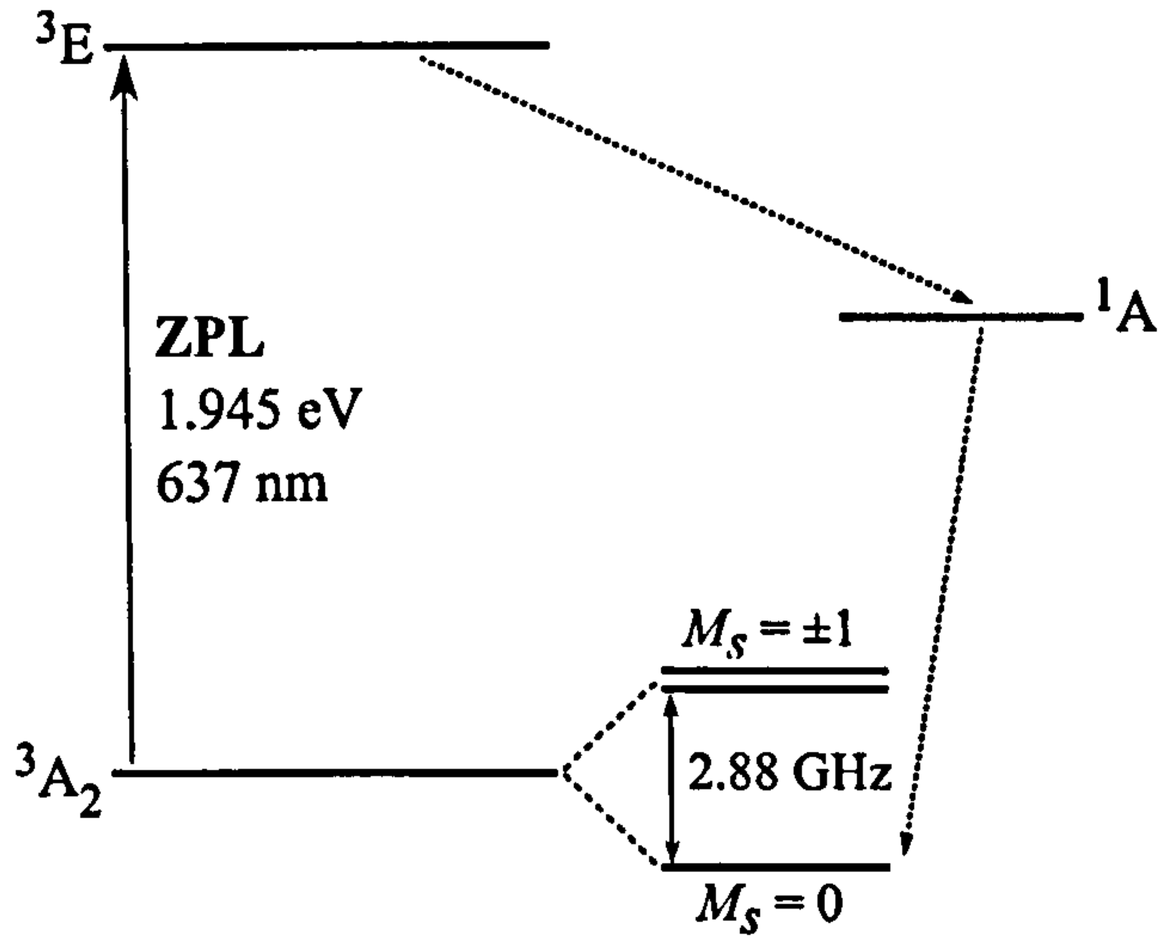

Figure 8-2: Schematic representation of the energy levels of the negative nitrogen-vacancy centre in diamond. The dashed arrows indicate the inter-system crossing allowed by the spin-orbit interaction.

that there is near 100% probability that an electron has a particular spin state. Hence previous investigations have been concerned with determining which M_S state is preferentially populated and the degree of spin polarisation.

EPR measurements at 2 K have enabled the sign of the zero-field interaction (D) to be determined and hence it has been possible to determine which of the ground spin states is preferentially populated [11]. The $M_S = 0$ state was found to be preferentially populated and measurements have estimated the population of the $M_S = 0$ state at 2 K to be ~ 80% [13].

From the discussions above it is apparent that optical excitation with energies > 1.945 eV can result in a large increase in signal intensity, especially compared to dark room-temperature measurements where the difference in population between the levels is small. Therefore the illumination of a sample containing NV^- provides a good experimental setup to resolve both the $^{14}N/^{15}N$ and weak ^{13}C satellites and therefore experimentally determine the unpaired electron localisation on the nitrogen atom and the surrounding carbon atoms. These interactions of the electron spin with the surrounding nuclei are of particular interest, since it has been suggested that they could be used to extend the number of qubits per node for quantum computation with NV centres [14]. Such investigations also allow the degree of spin polarisation to be calculated and compared to previous

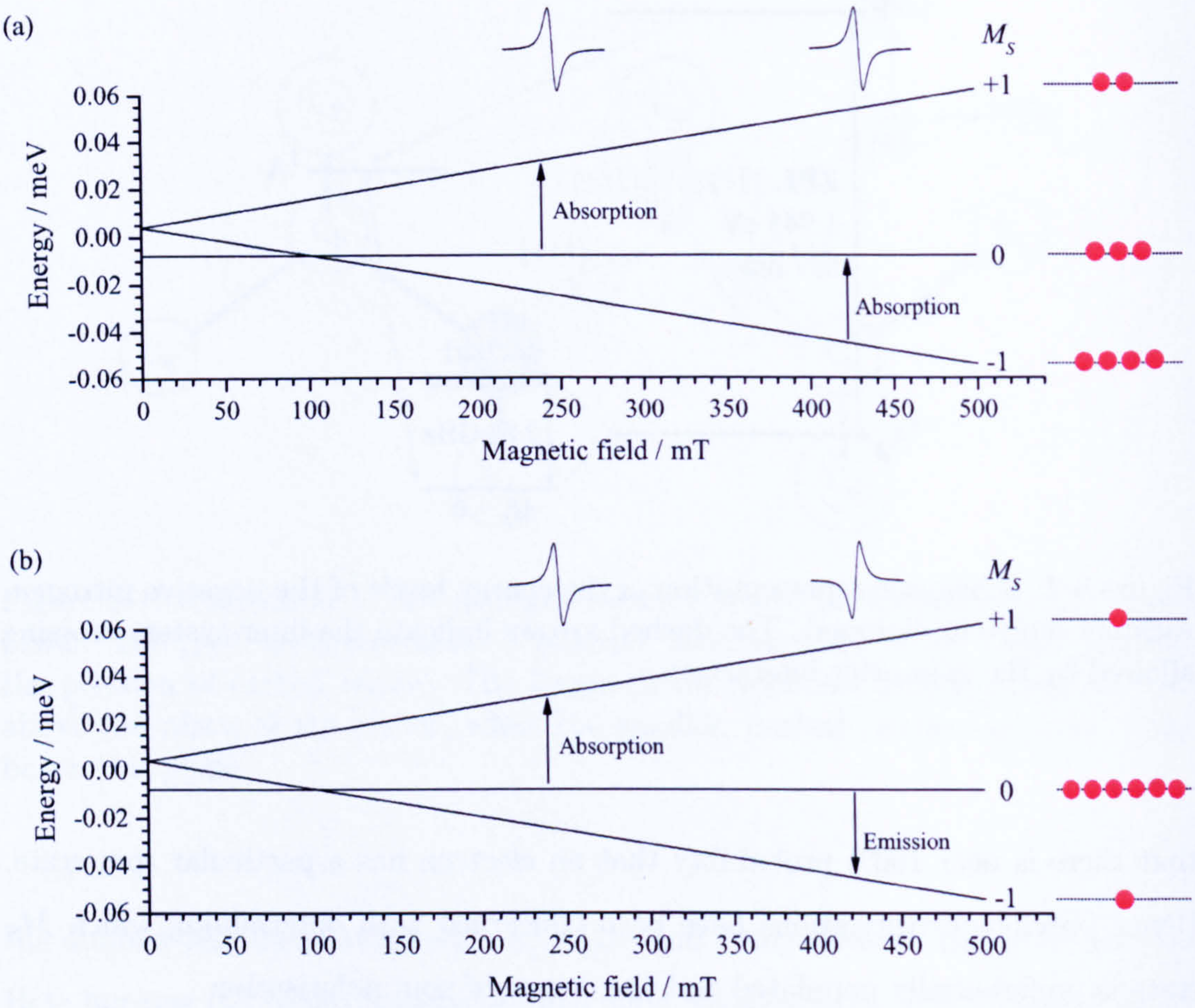

Figure 8-3: Schematic of the ground state spin levels of the NV^- centre in the dark (a) and under conditions of optical illumination with energy > 1.945 eV (b). The solid circles illustrate the populations in the three levels. In (b) optical pumping leads to preferential population of the $M_S = 0$ state, hence EPR lines are seen in emission and absorption as the spectrum is scanned.

published data. The results of such studies form part of this chapter.

Considering the neutral charge state of the nitrogen vacancy, NV^0, which is known to give rise to a ZPL at 2.156 eV (575 nm) [15], there are five electrons with which to populate the one-electron levels and the $a_{1N}^2 a_{1C}^2 e^1$ configuration gives rise to the many-electron ground state ^{2}E. Promoting an electron from a singlet to the doublet gives the configuration $a_{1N}^2 a_{1C}^1 e^2$ and the many-electron states $^2A_1$, $^4A_2$ and ^{2}E. The NV^0 ZPL at 2.156 eV has been shown to arise from a transition between an E ground and an A excited state [15]. The spin of these states was not determined in the uniaxial stress splitting study of the ZPL, but the assignment of these states to ^{2}E (ground) and $^2A_1$ follows from the simple electronic structure

Table 8-1: Summary of sample preparation and quantitative EPR results for the samples investigated.

	Sample A	**Sample B**	**Sample C**
Synthesis method	HPHT	HPHT	CVD
Nitrogen isotope distribution	99.6% ^{14}N	~ 95% ^{15}N	~ 90% ^{15}N
HPHT annealed	No	Yes	No
Irradiation type	1.9 MeV e^-	1.5 MeV e^-	1.9 MeV e^-
Irradiation dose	3×10^{18} cm^{-2}	4×10^{17} cm^{-2}	10^{18} cm^{-2}
Post irradiation annealing	4 hr @ 1100 K	4 hr @ 1100 K	>1 hr @ 1100 K
As-grown [N_s^0] / ppm	~ 10	~ 150	
Post treatment [N_s^0] / ppm	1.2(1)	17(1)	0.8(1)
Post treatment [NV^-] / ppm	1.0(1)	0.6(1)	0.12(1)

arguments.

The $S = \frac{1}{2}$ ^{2}E ground state has not been detected by EPR and, as a result, NV^0 has not attracted attention amongst the quantum information processing community. On first inspection the lack of detection by EPR is surprising. An electronic Zeeman g value (g) close to that of the free spin and a small hyperfine coupling (since there is no unpaired electron probability density on the nitrogen) would be expected, so it is possible that the EPR spectrum is obscured by other paramagnetic defects, such as N_s^0. Overlapping spectra would make detection more difficult but it is hard to believe that this explains the lack of detection, especially given the improvements in fitting of signals from N_s^0 (chapter 5) and the lack of evidence for remaining EPR resonances. Hence other possible reasons for the lack of detection need to be considered and investigated.

This chapter presents EPR data for a previously unobserved nitrogen-related trigonal defect in diamond with an $S = \frac{3}{2}$ excited state populated via optical excitation. Analysis of the spin-Hamiltonian parameters and the dependence of the intensity of the EPR spectrum with the wavelength of the optical excitation leads to the assignment of this $S = \frac{3}{2}$ state to the $^4A_2$ excited state of NV^0.

8.2 Experimental details

Three synthetic single-crystal diamonds were used in this study. In this chapter these samples are labeled A, B and C and a summary of sample preparation and

properties is given in table 8-1. Sample A was grown by conventional HPHT synthesis using a cobalt-containing solvent-catalyst and titanium as a nitrogen getter. The residual nitrogen contained the natural abundance of isotopes (99.6% ^{14}N). The sample was cut predominately from a cube growth sector, although it contains small volumes of other growth sectors. IR absorption measurements indicated that the sample, as grown, contained 9(1) ppm N_s^0. The sample was subsequently irradiated with 1.9 MeV electrons to a dose of $3 \times 10^{18}\,cm^{-2}$ yielding a vacancy concentration [16] of ~ 20 ppm. Finally the sample was annealed at 1100 K in a non-oxidising atmosphere for 4 hours.

Sample B was synthesised using a modified HPHT process [17]: The growth capsule with the carbon source and solvent/catalyst reaction mixture was pre-treated at high temperature in a vacuum to remove the vast majority of the atmospheric gases. The removed gas was replaced with ^{15}N enriched gas at a reduced temperature and the capsule was sealed. The reaction mixture was then subjected to HPHT conditions in the diamond stable region producing material with ~ 150 ppm N_s^0, as measured using EPR. The sample was HPHT annealed leading to >80% aggregation of the nitrogen to A-centres and then irradiated with 1.5 MeV electrons to a dose of $4 \times 10^{17}\,cm^{-2}$ leading to a vacancy concentration [16] of ~ 5 ppm. This sample contains different growth sectors with differing N_s concentrations, so that in some sectors it is likely that the vacancy concentration was of the same order of magnitude as the N_s concentration. After the irradiation the sample was annealed for 4 hours at 1100 K in a non-oxidising atmosphere.

Sample C was homoepitaxially grown on a {100} substrate using a CVD method. The sample was doped with ^{15}N by the addition of ^{15}N enriched N_2 to the source gases (EPR measurements suggest ~ 90% ^{15}N). The sample was irradiated with 1.5 MeV electrons to a dose of $10^{18}\,cm^{-2}$, yielding a vacancy concentration [16] of ~ 10 ppm and was subsequently annealed at 1100 K in a non-oxidising atmosphere.

EPR measurements have been conducted on all three samples after the processing described above, with the measurements made using the Bruker EMX (X-band) spectrometer §4.2. Low-temperature measurements under conditions of optical illumination were conducted using the 200 W high pressure Hg-Xe arc-lamp

experimental setup, as described in §4.2.4. Long-pass filters (280–780 nm) were employed to permit the energy cut-off to be varied.

Quantitative measurements of the average bulk NV^- and N_s^0 concentrations were obtained from room-temperature EPR spectra taken in the dark using the fitting method outlined in chapter 5.

For sample B optical absorption measurements were conducted at the Diamond Trading Company (Maidenhead, UK), using a Perkin Elmer Lambda-19 spectrometer with a 0.7 mm aperture, with the sample at ~ 90 K in a liquid nitrogen cryostat. This enabled the relative concentration of NV^0 and NV^- to be estimated from the integrated absorptions of the 2.156 eV and 1.945 eV ZPLs, respectively.

8.3 Results

The results from quantitative EPR measurement of N_s^0 and NV^-, together with a summary of the preparation steps for the three samples, are presented in table 8-1. Absorption measurements conducted on sample B implied comparable concentrations of NV^0 and NV^-.

To study the nitrogen hyperfine interaction of NV^- EPR spectra showing the half-field forbidden ($\Delta M_S = \pm 2$) transitions were recorded in the dark for all the samples, with the applied magnetic field (B) parallel to ⟨001⟩, ⟨110⟩ and ⟨111⟩. Half-field spectra were used since, to first order, the orientation dependence of the position of these resonance lines (B_0) is independent of the large zero-field interaction ($dB_0/d\theta$ is much lower). Figure 8-4 illustrates data for samples A and C, obtained with $\mathbf{B} \parallel \langle 100 \rangle$.

Spectra were obtained for the $\Delta M_S = \pm 1$ resonance lines under conditions of optical illumination. Figure 8-5 shows a room-temperature EPR spectrum obtained from sample B with the full output of the lamp (300–700 nm). In this spectrum the spin-polarised nature of NV^- evident; the first two lines (1 and 2) are in absorption, whilst 3 and 4 are in emission.

Glass filters were then used to control the energy cut-off of the incident light. This allowed the intensity of the NV^- resonance lines to be investigated as a

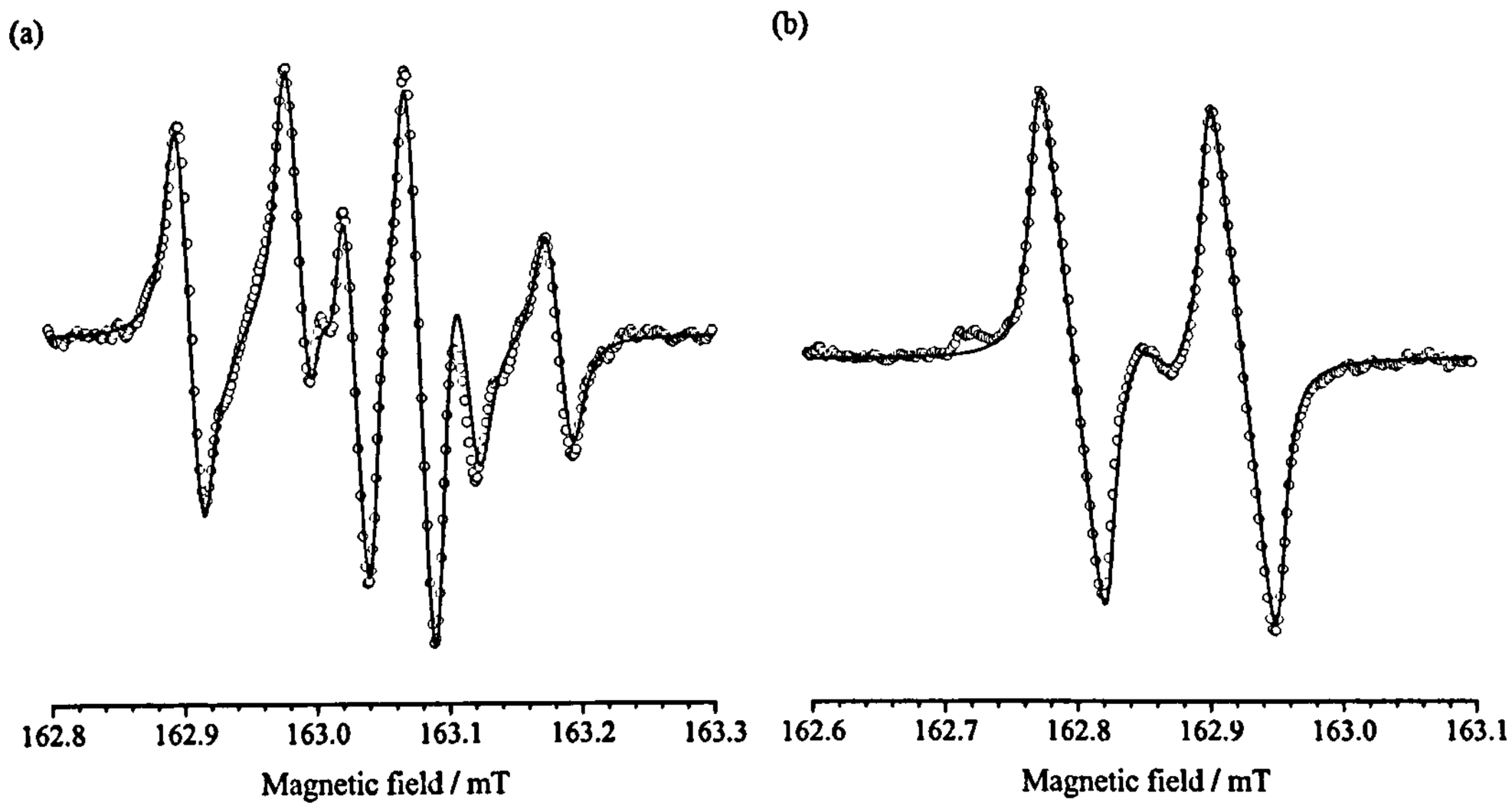

Figure 8-4: X-band EPR spectra (300 K) showing the half-field ($\Delta M_S = \pm 2$) transitions of (a) $^{14}NV^-$ (sample A) and (b) $^{15}NV^-$ (sample C). Both spectra were obtained with the applied magnetic field along ⟨100⟩. The lines through the points show the simulated spectra, obtained using the new hyperfine parameters listed in table 8-2.

function of excitation energy. Figure 8-6 shows the intensity of resonance lines 1 and 4, i.e. the resonance lines originating from sites with their C_{3v} trigonal axis parallel to **B**. The intensity of both resonance lines appears to increase above ~ 1.9 eV. The ratio of signal intensity of NV^- under conditions of broadband illumination by the lamp, compared to dark measurements, was determined at room temperature (~ 300 K) and also at 100 K and 10 K using the low-temperature cryostat. Under conditions of full illumination at room temperature with the lamp set up for use with filters the NV^- resonance line arising from the $M_S = -1 \rightarrow 0$ transition for the site with its C_{3v} axis along **B** (line 4 in figure 8-5) increased in intensity by a factor of −143 (negative since the signal changed from being in absorption to emission). At 100 K and 10 K microwave power saturation was unavoidable for measurements in the dark, leading to an underestimation of the of the intensity of the EPR signals.

To check the dependence of the intensity of the NV^- resonance line intensity with the power of the lamp measurements were also conducted at room temperature with the lamp set up so as to maximise the intensity of light focused onto the optical light-guide. The intensity of the illumination was then varied by changing

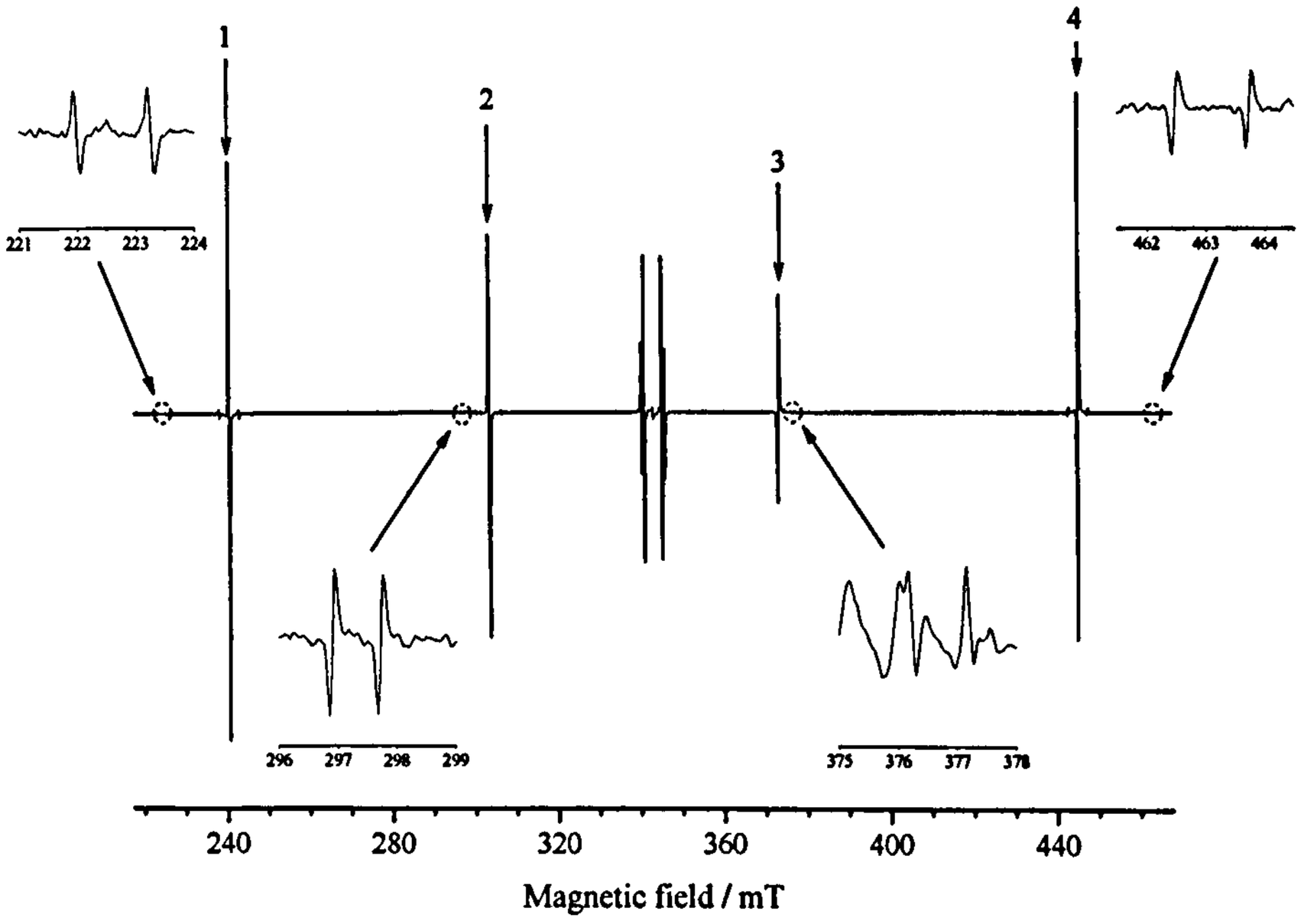

Figure 8-5: X-band (9.6 GHz) EPR spectrum obtained from the ^{15}N-doped HPHT sample at room temperature under conditions of optical illumination with energy > 2.2 eV and the applied magnetic field along ⟨111⟩. EPR lines from NV^- are labelled 1–4; lines 1 and 2 are in absorption whilst 3 and 4 are in emission. Sections of the plot are expanded to show the four pairs of new resonance lines observed with this orientation of the magnetic field. Resonance lines around $g = 2$ (340 mT) arise from N_s^0.

the voltage applied; the lamp power could be determined from the product of the measured voltage and current. Figure 8-7 displays the dependence of NV^- signal intensity with lamp power.

With the greatly increased intensity of the NV^- resonance lines it was possible to readily resolve the ^{13}C hyperfine satellites around the main resonance lines of NV^- for both $^{14}NV^-$ and $^{15}NV^-$. Figure 8-8 shows spectra collected from sample B with $\mathbf{B} \parallel \langle 111 \rangle$ for the $\Delta M_S = \pm 1$ transitions. Similar spectra were collected with $\mathbf{B} \parallel \langle 110 \rangle$ and for sample A an additional scan with $\mathbf{B} \parallel 35°$ from [001] in a $(1\bar{1}0)$ plane was obtained.

In wide (~ 250 mT) EPR scans of sample B with full lamp illumination additional spin-polarised resonance lines were observed that could not be accounted for by NV^- or N_s^0. In figure 8-5, where $\mathbf{B} \parallel \langle 111 \rangle$, four pairs of additional resonance lines are apparent. These resonance lines were not seen in samples A or

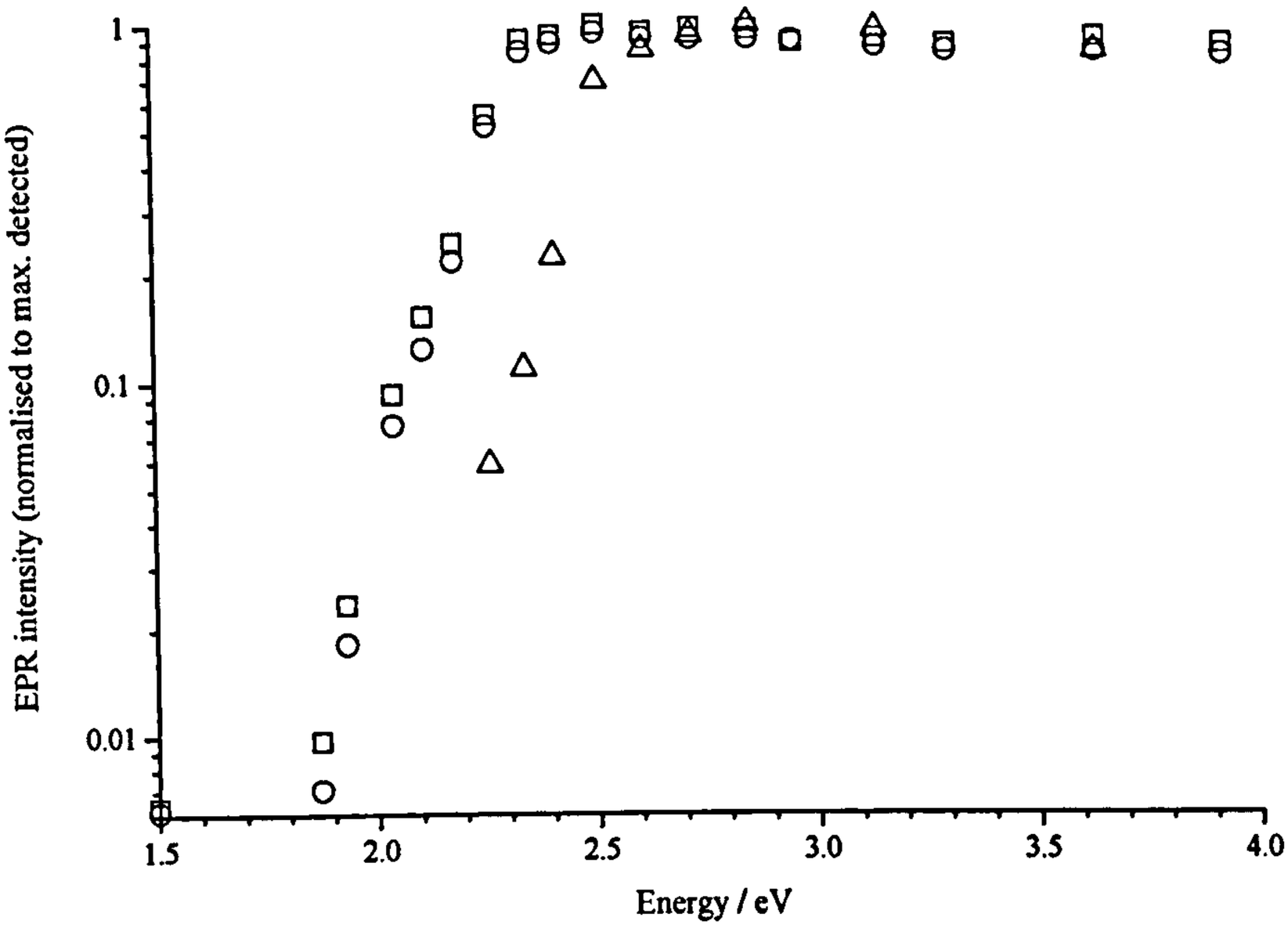

Figure 8-6: Room-temperature EPR signal intensity as a function of optical excitation energy for the $M_S = \frac{1}{2} \rightarrow \frac{3}{2}$ transition of the $S = \frac{3}{2}$ defect (△) and the $M_S = 0 \rightarrow 1$ (□) and $M_S = -1 \rightarrow 0$ (○) transitions of NV^- (both observed in sample B). The data were recorded with $\mathbf{B} \parallel \langle 111 \rangle$ for the defects with their axes parallel to the applied field. Below 2.2 eV no EPR signal for the $S = \frac{3}{2}$ defect could be detected. The error in the cut-off energy is ±0.1 eV.

C. The intensity of the lowest pair of new resonance lines observed in sample B with $\mathbf{B} \parallel \langle 111 \rangle$ was measured as a function of the cut-off energy of the lamp. These results are shown in figure 8-6, alongside the results determined for NV^-, as previously described. The signal intensity was observed to drop rapidly towards zero at around 2.2(1) eV. The new resonance lines were not observed during dark measurements, even after considerable signal averaging.

The number of orientations that could be found in a $(1\bar{1}0)$ plane was limited, due to the fact that the sample was mounted onto the end of a quartz rod. However, measurements with the applied magnetic field along $\langle 111 \rangle$, ~ 65° (in a $\{110\}$ plane) and $\langle 110 \rangle$ were possible. The position of the new resonance lines at these orientations of $\mathbf{B}$ are shown in figure 8-9.

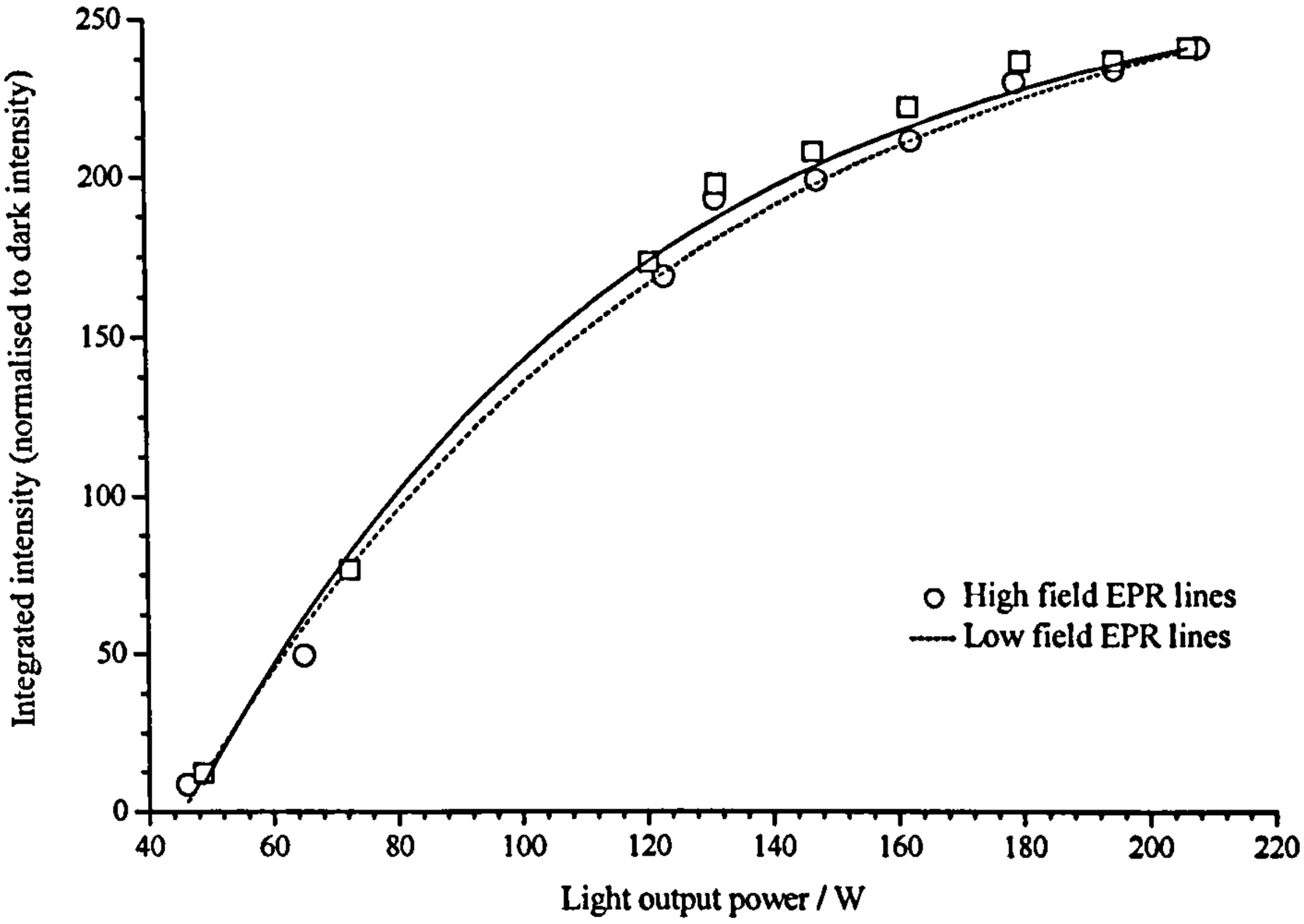

Figure 8-7: Room-temperature EPR signal intensity for NV^- in sample B, for defects with their C_{3v} axes parallel to **B**, as a function of lamp power. The sample was illuminated using the full output of the lamp (200–700 nm). At maximum power (~ 200 W) the intensity of the NV^- resonance lines was increased by a factor of 240 compared to measurements in the dark. The lines through the points have been fitted using an exponential of the form $y = y_0 + k_1 \exp(-x/k_2)$.

8.4 Discussion

8.4.1 The NV^- centre

8.4.1.1 Spin-Hamiltonian parameters

The main EPR resonance lines observed in both samples for NV^- were fitted to a spin Hamiltonian of the form:

$$\mathcal{H} = \mu_B \hat{\mathbf{S}} \cdot \underline{\mathbf{g}} \cdot \mathbf{B} + \hat{\mathbf{S}} \cdot \underline{\mathbf{D}} \cdot \hat{\mathbf{S}} + \sum_j \left[\hat{\mathbf{S}} \cdot \underline{\mathbf{A}}_j \cdot \hat{\mathbf{I}}_j - \mu_N g_{N_j} \hat{\mathbf{I}}_j \mathbf{B} \right] \qquad (8\text{-}1)$$

From the angular variation data **g** and **D** could be determined. Values of D = 2.87(1) GHz, $g_\parallel$ = 2.0029(1) and $g_\parallel$ = 2.0031(1) (D and $g_\parallel$ along ⟨111⟩) were determined, in agreement with previously published parameters [10, 18].

For samples B and C, which are isotopically enriched to > 90% ^{15}N, a simple two line NV^- spectrum is obtained from half-field scans with the applied magnetic field along ⟨100⟩ (figure 8-4b shows the spectrum from sample C), as would be

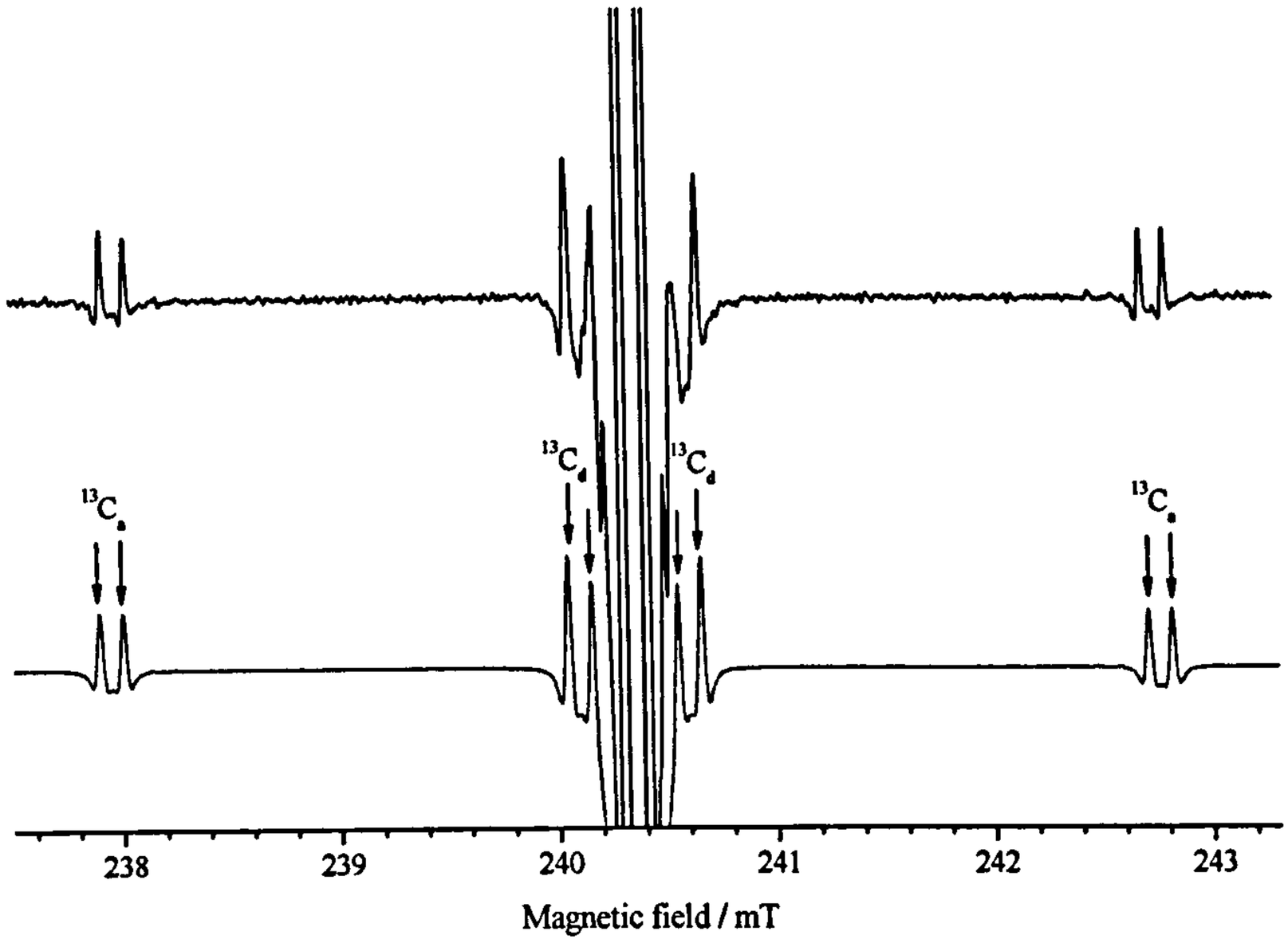

Figure 8-8: ^{13}C hyperfine structure for NV^- observed around line 1 (figure 8-5) in sample B, with the applied magnetic field along ⟨111⟩. The spectrum was acquired at 10 K with the unfiltered output of the lamp. The plot underneath the experimental data sets illustrate the fitted spectra obtained using the ^{13}C hyperfine parameters determined in §8.4.1.1. The satellites are labelled according to the position of the ^{13}C atom as shown in figure 8-1.

expected with a hyperfine interaction along ⟨111⟩ for an $I = \frac{1}{2}$ nuclei. The sample containing ^{14}N in natural abundance reveals a considerably more complicated spectrum (figure 8-4a). Since $I = 1$ for ^{14}N a nuclear quadruple interaction (§3.4.5) is present, hence an additional term in the spin Hamiltonian of the form:

$$\mathscr{H}_{qp} = \sum_j \hat{\mathbf{I}}_j \cdot \underline{\mathbf{P}}_j \cdot \hat{\mathbf{I}}_j, \tag{8-2}$$

is required. The complex spectrum for $^{14}NV^-$ suggests that the hyperfine and nuclear quadrupole have comparable magnitudes, resulting in considerable mixing between the eigenstates and hence increased transition probability for $\Delta m_I \neq 0$ transitions. From half-field spectra with **B** along ⟨100⟩, ⟨110⟩ and ⟨111⟩ parameters for the hyperfine interactions for ^{14}N and ^{15}N could be determined along with the magnitude of the quadrupole interaction for ^{14}N. These parameters are shown in table 8-2.

Harrison *et al.* have experimentally determined the sign D for NV^- to be positive [11]. This information allows the absolute sign of the hyperfine interaction

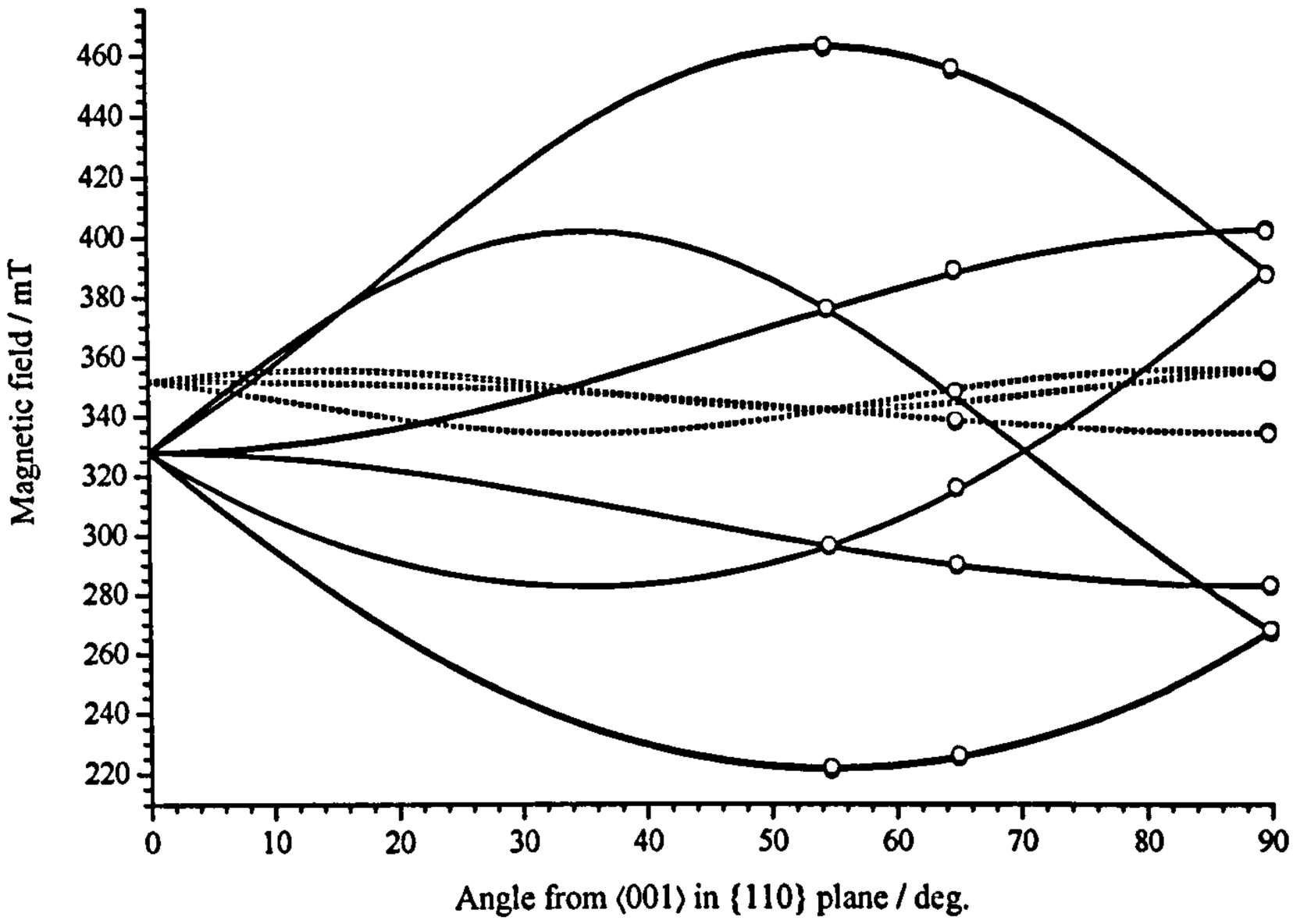

Figure 8-9: The EPR roadmap (300 K) for the new $S = \frac{3}{2}$ defect. The points indicate the determined positions of the resonance lines at X-band (9.7 GHz), as a function of angle in the $(1\bar{1}0)$ plane . The lines through the points were generated using the values for g, D and A given in table 8-5, where solid and dotted lines indicate resonances originating from $M_S = \pm\frac{1}{2} \leftrightarrow \pm\frac{3}{2}$ and $M_S = -\frac{1}{2} \leftrightarrow \frac{1}{2}$ transitions, respectively.

Table 8-2: Nitrogen hyperfine parameters for ^{14}N and ^{15}N in the NV$^-$ defect. $A_\parallel$ and P are parallel to [111] (see figure 8-1). † denotes results of He *et al.* [18].

Isotope	$A_\parallel$ MHz	$A_\perp$ MHz	P MHz	A_s MHz	A_p MHz
^{14}N	−2.14(7)	−2.70(7)	−5.01(6)	−2.51(5)	0.19(3)
^{14}N†	2.30(2)	2.10(10)	−5.04(5)	2.17(7)	0.07(3)
^{15}N	3.03(3)	3.65(3)		3.44(5)	−0.21(3)

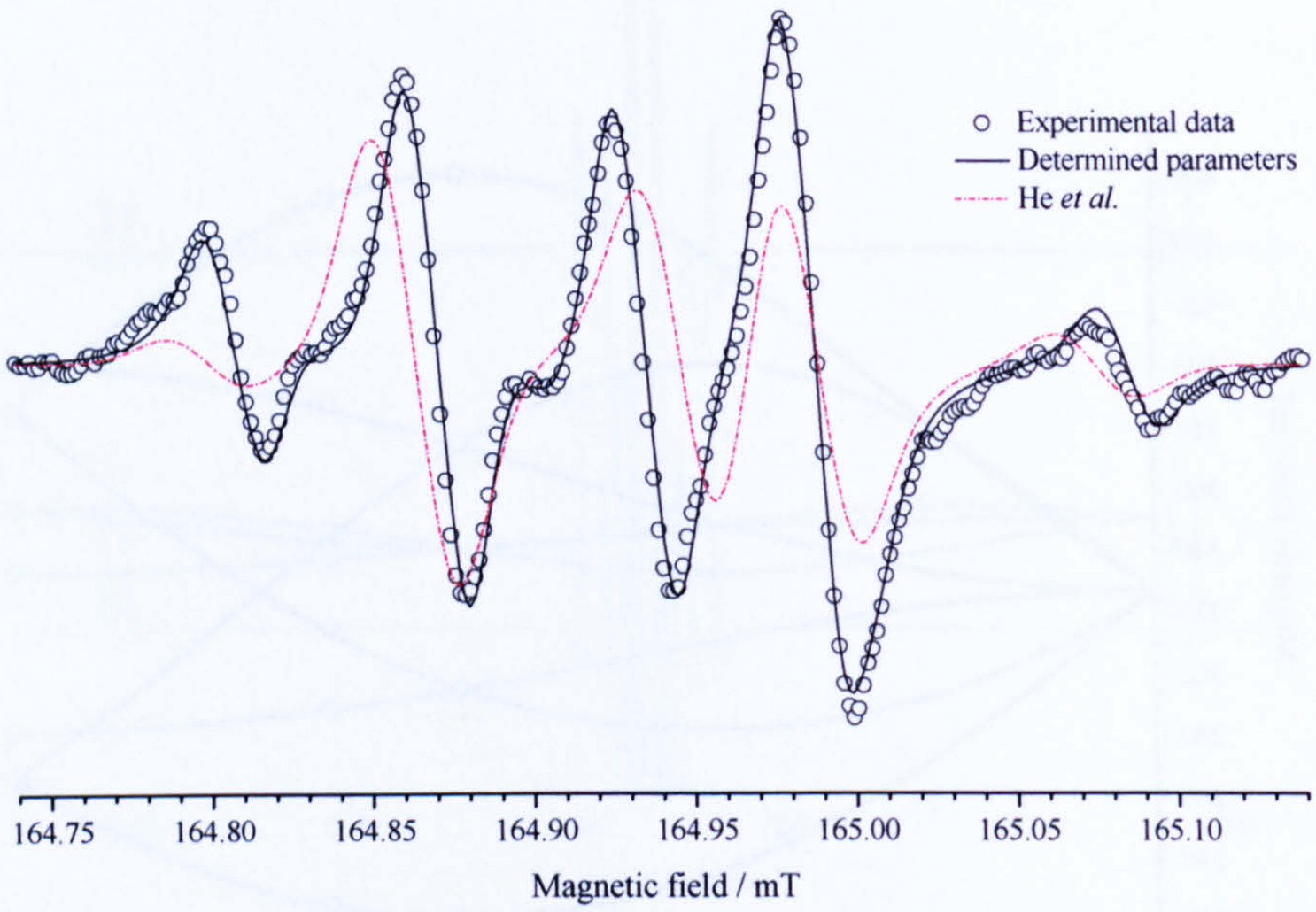

Figure 8-10: X-band EPR spectra showing the half-field transitions of $^{14}NV^-$ (from sample A) with the applied magnetic field along ⟨110⟩. The circles show the experimental data points and the lines illustrate the fits obtained using the determined parameters (table 8-2) and the published parameters determined by He *et al.* [18] (see legend).

to be determined from the position of the electron-nuclear double-spin flip transitions ($\Delta M_S = 1$, $\Delta m_I = 1$). The nuclear g value for ^{14}N is positive, and for this isotope the sign of the hyperfine interaction has been determined to be negative in this investigation. Since g_N for ^{15}N is of opposite sign to ^{14}N a positive sign of the hyperfine interaction for ^{15}N is assumed. The experimentally determined magnitudes of the hyperfine interactions for ^{15}N and ^{14}N scale with the g_N values of these two isotopes (see table 3-1).

The results obtained in this investigation are in contrast to those of He *et al.* who argue that, since g_N for ^{14}N is positive, so is the hyperfine interaction for this isotope [18]. A comparison between the fit obtained with $\mathbf{B} \parallel \langle 110 \rangle$ in sample A (99.6% ^{14}N) using the previously published values and those determined here is presented in figure 8-10. The previously published parameters do not satisfactorily reproduce the experimental data.

The data shown in figure 8-8 reveals two sets of ^{13}C satellites. Using the data collected with different orientations of $\mathbf{B}$ for samples A and B the hyperfine

Table 8-3: ^{13}C hyperfine parameters for the NV^- defect with directions $[\theta,\varphi]$, where θ is the angle from the crystallographic [001] direction and φ is the angle in degrees from [100] measured towards [010] in the (100) plane, as shown in figure 8-1.

Defect	$A_\parallel$ MHz	$A_\perp$ MHz	A_s MHz	A_p MHz	η^2
^{14}N $^{13}C_a$ @ 10K	199.7(2) ‖ [125.26(3),45]	120.3(2)	146.8(2)	26.5(1)	0.285(1)
^{15}N $^{13}C_a$ @ 10K	199.1(1) ‖ [125.26(2),45]	121.1(1)	147.1(1)	26.0(1)	0.281(1)
^{15}N $^{13}C_a$ @ RT	198.2(3) ‖ [125.26(5),45]	120.8(2)	146.6(2)	25.8(1)	0.279(1)
^{15}N $^{13}C_d$ @ 10K	18.49(5) ‖ [125.3(1),45]	13.26(5)	15.00(4)	1.74(2)	0.0202(2)

parameters could be be determined by fitting these (separately) to equation 8-1. Both hyperfine interactions were constrained to have two principal axes in a {110} plane not containing the C_{3v} axis of the defect. Removing this constraint did not improve the fit. The determined ^{13}C hyperfine parameters for NV^- are summarised in table 8-3.

The larger ^{13}C hyperfine interaction (labelled $^{13}C_a$) is axially symmetric, with $A_\parallel$ directed along a ⟨111⟩ direction which is not the C_{3v} axis of the defect. The intensities of the ^{13}C satellites in figure 8-8 resulting from this interaction, relative to the central ^{12}C resonance lines, have been set using equation 3-41, assuming three equivalent carbon atoms ($N_{equiv} = 3$), with ^{13}C present in natural abundance. This, combined with direction of $A_\parallel$, means this interaction is assigned to the carbon atoms neighbouring the vacancy (the atoms labelled C_a in figure 8-1). The parameters obtained are in agreement with the ^{13}C hyperfine interaction reported by Loubser and van Wyk [10].

The intensities of the hyperfine satellites labelled $^{13}C_d$ are reproduced assuming six equivalent ^{13}C neighbours. For this interaction $A_\parallel$ is also directed along a ⟨111⟩ direction which is not the C_{3v} axis of the defect. The number of equivalent sites for the ^{13}C atom, the magnitude and direction for the hyperfine interaction all invite the assignment of this interaction to the next-nearest-neighbour carbon atoms labelled C_d in figure 8-1.

Interpreting the ^{13}C hyperfine parameters in terms of an unpaired electron probability density in the usual manner (§3.4.3), it is found that the two sets of carbon neighbours account for ~ 96% of the unpaired electron probability density

for NV^-, with ~ 84% on the three carbons nearest the vacancy.

Table 8-2 shows the isotropic (A_s) and anisotropic (A_p) components of the nitrogen hyperfine components. Since A_s is small and of opposite sign to that expected for the case of real localisation of the electron probability density on a nitrogen atom (see table 3-1) this suggests an indirect interaction (e.g. configuration interaction [19], exchange polarisation [20], etc), as was found for ^{29}Si in $(V\text{-}Si\text{-}V)^0$ (§6.4.1). The small anisotropic hyperfine interaction for $^{14}N/^{15}N$ in the NV^- defect can be explained by a dipolar interaction between the unpaired electron probability density, assumed localised on the three carbon atoms neighbouring the vacancy and the nitrogen atom (see above), as outlined in Glover [21]. Theoretical values for A_p of 0.18 MHz and -0.25 MHz are determined for ^{14}N and ^{15}N, respectively. Given the approximations which are inherent in this simple model the agreement between the experimental and calculated values is fortuitous.

8.4.1.2 Spin polarisation of NV^-

Assuming a positive value for D [11] the EPR spectra collected in this investigation with optical illumination agree with the previous finding that it is the $M_S = 0$ level that is preferentially populated [11] (see figures 8-3 and 8-5). From the data the degree of spin polarisation of the $M_S = 0$ spin level can also be calculated.

For a Boltzmann distribution the probability (p_i) of an electron at temperature T occupying a spin state with energy E_i can be written as:

$$p_i = \frac{\exp\left(\frac{E_i}{k_B T}\right)}{\sum_j \exp\left(\frac{E_j}{k_B T}\right)} \tag{8-3}$$

Values for E_i for the three spin-state levels of NV^- with $\mathbf{B} \parallel \langle 111 \rangle$ for the defects with their C_{3v} axis parallel to $\mathbf{B}$ were determined using EPR-NMR using the calculated parameters for g and D (see §8.4.1.1). The relative populations of the $M_S = -1$ and $M_S = 0$ spin states of NV^- at the $M_S = -1 \rightarrow 0$ transition ($\nu = 9.7$ GHz) at different temperatures are shown in table 8-4.

The intensity of an EPR transition ($\mathscr{I}$) is proportional to the population difference (η) between the spin levels between which it occurs. Hence:

$$\frac{\mathscr{I}^{\text{light}}}{\mathscr{I}^{\text{dark}}} = \frac{\eta^{\text{light}}}{\eta^{\text{dark}}} \tag{8-4}$$

Table 8-4: Energy, E, and population probabilities in the dark, p, for the $M_S = -1$ and $M_S = 0$ spin states of NV^- at the $M_S = -1 \rightarrow 0$ transition ($\nu = 9.7\,GHz$). The results are determined at 300 K, 100 K and 10 K for defects with their axes parallel to the applied field ($\mathbf{B} \parallel \langle 111 \rangle$).

M_S	E		p		
	GHz	meV	300 K	100 K	10 K
−1	−11.5	0.0476	0.3339	0.3352	0.3518
0	−1.90	−0.00786	0.3334	0.3336	0.3360

$\mathscr{I}^{light}/\mathscr{I}^{dark}$ is known experimentally and η^{dark} can be calculated using the probabilities shown in table 8-4. Therefore η_{light} can be determined from equation 8-4. However, to calculate the spin polarisation (occupation of the $M_S = 0$ spin state) the populations, not simply the differences, need to be known. This requires an assumption to be made.

In the calculation of the spin polarisation of NV^- at 2 K from Q-band measurements Harrison *et al.* made the assumption that population is lost equally from both the $M_S = \pm 1$ levels [13]. However, given that at 2 K at 35 GHz the population of the $M_S = -1$ and $M_S = 1$ levels ($p_{\pm 1}$) are ~ 60% and ~ 10%, respectively, this assumption cannot be valid for large spin polarisation effects. A more reasonable assumption is that the populations of the $M_S = \pm 1$ levels are equal under conditions of optical illumination, which relies upon the optical pumping being fast enough to dominate over the spin-lattice relaxation (T_1) process. Using the assumption that $p_{-1}^{light} = p_1^{light}$ leads to the determination of p_0^{light} as:

$$p_0^{light} = \frac{1}{3} + \frac{2}{3}\left|\frac{\mathscr{I}^{light}}{\mathscr{I}^{dark}}\right|\eta^{dark} \tag{8-5}$$

Using this expression and assuming no microwave power saturation spin polarisations of 78% and 88% are determined from the measurements of Harrison *et al.* conducted at 1.9–2 K on two irradiated and annealed HPHT type Ib diamonds [13].

From the value of $\mathscr{I}^{light}/\mathscr{I}^{dark} = -143$ which has been measured in this investigation at 300 K a spin polarisation of 38% is found. At 100 K and 10 K microwave power saturation was unavoidable even at 60 dB attenuation for the dark measurements (T_1 increases the as sample is cooled), thus the intensity under illumination

could not be directly compared to that from the dark spectra at equivalent temperature. However, from knowledge of η^{dark} at 300 K the intensity under optical illumination at a temperature T can be compared to the intensity in the dark at 300 K to calculate p_0, since:

$$\mathscr{I}_T^{\text{light}} = \frac{\eta_T^{\text{dark}}}{\eta_{300\,K}^{dark}} \mathscr{I}_{300\,K}^{\text{dark}} \tag{8-6}$$

Values of 62% and 65% were determined from the measurements conducted at 100 K and 10 K, respectively, for the NV^- resonance lines arising from the transitions $M_S = -1 \rightarrow 0$ for the site parallel to **B** (applied along ⟨111⟩). The assumption that $p_{-1}^{\text{light}} = p_1^{\text{light}}$ means identical spin polarisation results would be expected from intensity measurements of the $M_S = 0 \rightarrow 1$ resonance line (line 1 in figure 8-5); values of p_0^{light} only changed by 1–2% when using the $M_S = 0 \rightarrow 1$ resonance line, suggesting that this assumption is reasonable.

The lower spin polarisation determined in this investigation compared to those determined by Harrison *et al.* could be explained due to the lower intensity of the light source used in this investigation. Harrison *et al.* utilised a 600 nm output from a Coherent ring-dye laser and it is stated that the laser power used was such that the magnitude of the EPR signal did not diminish with an order of magnitude decrease in laser power [13]. Hence it is reasonable to assume conditions have been optimised to obtain the highest possible spin polarisation. Saturation, however, would lead to a systematic over-estimation of the degree of spin polarisation. Hence the redetermined values, obtained using the new assumptions discussed above should still be treated with caution.

In this study, with the highest possible intensity from this lamp, achieved by placing the lamp as close as possible to the light-guide, an enhancement factor $\mathscr{I}^{\text{light}}/\mathscr{I}^{\text{dark}} = -240$ was achieved at 300 K. This only translates into an increase in p_0^{light} to 42%. Figure 8-7 illustrates the enhancement factor as a function of lamp power with this experimental setup. Even at the maximum at a lamp power of ~ 200 W it is apparent that the enhancement factor is still rising, albeit slowly. It important to consider that with the lamp used the power density at the sample is modest and in this investigation an order of magnitude decrease in the lamp power results in spin polarisation being lost, in contrast to the measurements of Harrison *et al.* obtained with a laser source [13].

Measurements made by Tucker on a comparable experimental setup (with a 100 W Hg lamp) found that, when using the full output of the lamp, the power reaching the sample is ~ 200 mW [22]. Since this is spread over the area of the quartz rod (~ 20 mm^2) the power density is of the order 10 $mW\,mm^{-2}$. Several orders of magnitude higher power densities are likely to be achievable with a laser setup and over such a range the intensity of the NV^- resonance line, as shown in figure 8-7, may rise considerably.

8.4.2 Identification of the $^4A_2$ excited state of NV^0

In §8.3 the presence of additional resonance lines, under conditions of optical illumination, was discussed. The orientation dependence of these lines is mapped out in figure 8-9. The large splitting of the outermost resonance lines observed with $\mathbf{B} \parallel \langle 111 \rangle$ implies that a zero-field splitting is primarily responsible for the orientation dependence of these lines, therefore implying a system with $S \geq 1$.

With $\mathbf{B} \parallel \langle 110 \rangle$ six pairs of resonance lines were observed. With this orientation of the applied magnetic field for an $S = \frac{3}{2}$ state of a trigonal defect the g and D interactions (assumed axially symmetric about the trigonal axis) will produce two sets of three lines corresponding to the allowed $\Delta M_S = \pm 1$ EPR transitions. A hyperfine coupling (also assumed axially symmetric about the trigonal axis) with an $I = \frac{1}{2}$ nucleus would split each of the six lines in two, producing the pattern of six pairs of lines observed. With $\mathbf{B} \parallel \langle 111 \rangle$ only four pairs of lines were observed, however, this can be explained by virtue of an overlap of the central pair with N_s^0.

Following the arguments above, the angular dependence of all the EPR spectra for the new system have been simulated assuming $S = \frac{3}{2}$ and a single $I = \frac{1}{2}$ nuclei, whilst constraining g, D and A to be axially symmetric about $\langle 111 \rangle$. Spin-Hamiltonian parameters for the new defect, determined from room-temperature data, are given in table 8-5.

Since these resonance lines are observed in sample B, which is ^{15}N-doped, it is sensible to initially assign this isotope to the observed hyperfine interaction. With $\mathbf{B} \parallel \langle 110 \rangle$ resonance lines from the $\Delta M_S = 1, \Delta m_I = 1$ transitions could be observed around the lowest field pair (corresponding to a $M_S = -\frac{3}{2} \leftrightarrow -\frac{1}{2}$ transition from sites which lie perpendicular to $\mathbf{B}$), as shown in figure 8-11. It is important

Table 8-5: Spin-Hamiltonian parameters for $^{15}NV^0$. g, D and A have principal axes along $\langle 111 \rangle$.

$g_\parallel$	$g_\perp$	D MHz	$A_\parallel$ MHz	$A_\perp$ MHz	A_s MHz	A_p MHz	η^2
2.0029(2)	2.0035(2)	1685(5)	−35.7(3)	−23.8(3)	−27.8(2)	−4.0(1)	0.062(2)

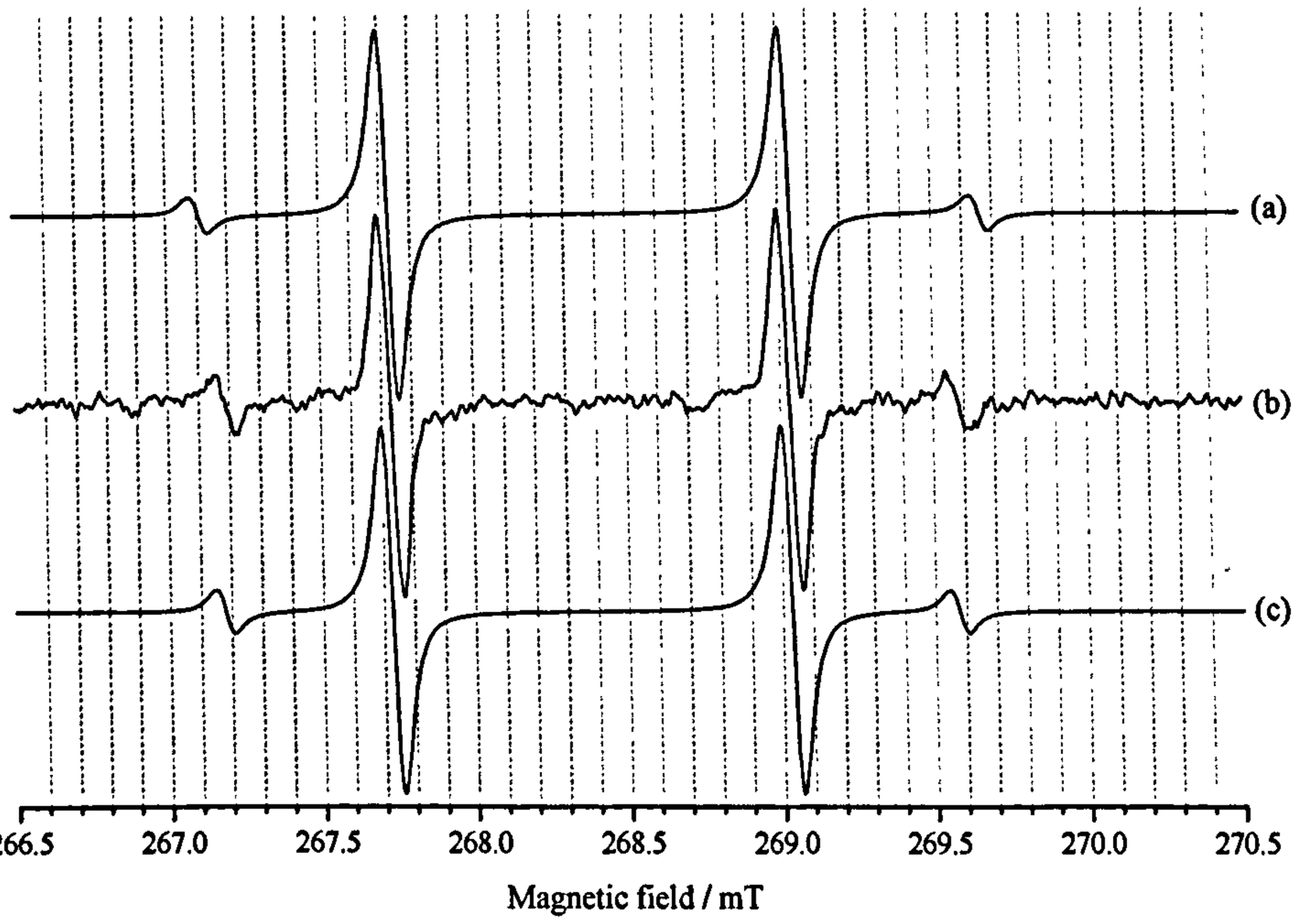

Figure 8-11: Lowest field pair of lines from the $S = \frac{3}{2}$ defect observed with the applied magnetic field along $\langle 111 \rangle$. The weak, outmost lines originate from forbidden electron-nuclear double-spin flips. (a) shows simulated data assuming positive values for $A_\parallel$ and $A_\perp$ (b) is the experimental data and (c) is simulation obtained using negative values for $A_\parallel$ and $A_\perp$. $D > 0$ for both simulations.

to note that replacing ^{15}N with another $I = \frac{1}{2}$ nucleus (e.g. ^1H) does not yield a satisfactory fit, regardless of the sign of A and D. Hence nitrogen has been unambiguously identified as a constituent in this defect.

Examining the magnitudes of the hyperfine components it is noted that $|A_\parallel| > |A_\perp|$. This indicates that there is a small localisation of the unpaired electron probability density on the nitrogen, with the experimental wave-function parameters given in table 8-5 suggesting a localisation of around 6% (see §3.4.3). Since the nuclear g value for ^{15}N is −0.5664, a negative sign is assigned to $A_\parallel$ and $A_\perp$. This has the consequence of setting D as positive, since only with $A_\parallel, A_\perp < 0$ and $D > 0$

can the position and intensity of the forbidden electron-nuclear double-spin flips be reproduced (see figure 8-11).

The EPR spectrum for the new defect has only been observed when the sample is illuminated and, as can be seen from figure 8-5, spectra are spin polarised. Figure 8-6 shows the variation of the room-temperature EPR intensity, and hence spin polarisation of the new $S = \frac{3}{2}$ centre, with the energy of the exciting light. The threshold for observation of the spin-polarised $S = \frac{3}{2}$ system is 2.2(1) eV, with preferential (but not equal) population of the $M_S = \pm\frac{1}{2}$ levels with respect to the $M_S = \pm\frac{3}{2}$ levels. Unlike the ground state of NV^-, the $S = \frac{3}{2}$ system could not be observed without optical excitation, even with extensive signal averaging; upon removal of the illumination the signal disappeared in $\ll 1$ s. The magnitude of spin polarisation did not vary strongly with temperature between 10 K and 300 K.

The apparent requirement of optical excitation for EPR detection of the $S = \frac{3}{2}$ system invites the assertion that this is an excited state of a defect. The close agreement between the threshold energy for spin polarisation and the energy of the ZPL for NV^0 suggests the association of this system with the $^4A_2$ excited state of NV^0, with spin-selective intersystem crossing giving rise to the spin polarisation. In this case it is necessary to explain the lack of observation of the $S = \frac{1}{2}$ ^2E ground state of this defect. Overlapping spectra was dismissed in §8.1, but the dynamic Jahn-Teller distortion of the ^2E ground state [15] could broaden the EPR lines sufficiently to preclude detection (e.g. a ten fold increase in linewidth would reduce detection sensitivity by a factor of 100). Neither problem would apply for the $^4A_2$ excited state, if this were populated by optical excitation. This state would be expected to be relatively low lying (i.e. below the $^2A_1$ excited state), and since it is the only $S = \frac{3}{2}$ state, it is likely that it would have a sufficiently long lifetime for detection by EPR.

The $^4A_2$ state is derived from the configuration $a_{1N}^2 a_{1C}^1 e^2$ (§8.1), hence the unpaired electron probability density is expected to be predominately localised in the carbon dangling orbitals surrounding the vacancy, as is the case for NV^-. A large zero-field splitting arising from exchange coupling (cannot be dipolar in origin since $D > 0$) is therefore expected and observed. The data for the $^4A_2$ excited state of NV^0 indicates that approximately 6% of the unpaired electron

probability density is localised on the nitrogen, which is much larger than that determined for the ground state of NV^-, derived from the configuration $a_{1N}^2 a_{1C}^2 e^2$. The properties of the $^3A_2$ ground state of NV^- are insensitive to the order or energy separation of a_{1C} and a_{1N} levels and the unpaired electron probability density on the nitrogen was found to be negligible. However, for NV^0, if the ordering in energy of the a_{1C} and a_{1N} levels were reversed then the configuration $a_{1C}^2 a_{1N}^1 e^2$ would still produce the $^4A_2$ excited state but now there would be significant unpaired electron probability density on the nitrogen and hence a larger nitrogen hyperfine interaction. This is not likely, but it is probable that there is some mixing of the a_{1N} and a_{1C} one electron levels and this gives rise to the observed non-zero nitrogen hyperfine interaction in the $^4A_2$ state of NV^0.

8.5 Conclusions and further work

New hyperfine parameters for the NV^- centre have been determined, showing that the nitrogen hyperfine interaction has $|A_\perp| > |A_\parallel|$ and, from the positions of the forbidden electron-nuclear double-spin flip transitions, it has been argued that the sign of the ^{14}N hyperfine interaction is negative. The anisotropic component of the nitrogen hyperfine component can be explained in terms of a dipolar interaction between a nitrogen nucleus and the unpaired electron localised on the three carbon atoms. The determined ^{13}C hyperfine parameters (observed with the aid of spin polarisation by optical illumination) support this; 84% of the unpaired electron probability density is localised on the three carbon atoms nearest to the vacancy, with a further 12% on a group of six next-nearest carbon atoms.

The results of optical illumination have also confirmed previous experimental findings that spin polarisation results in preferential population of the $M_S = 0$ spin level [13]. However, in previous work microwave power saturation is likely to have been a problem, hence the previously published magnitudes of spin polarisation for an ensemble of NV^- defects should be treated with caution.

In this investigation microwave power saturation effects have been negated and a maximum spin polarisation of 65% (at 10 K) has been observed in the samples examined. Due to the modest power density at the sample with the illumination

used it is likely that higher values could be achieved. A 1000 W Hg-Xe lamp has been set up and further experiments are planned to investigate whether higher spin polarisations can be obtained. Further samples are also to be investigated.

A new $S = \frac{3}{2}$ system involving nitrogen has been detected in a ^{15}N-doped HPHT diamond and there is a considerable body of evidence supporting the assignment of this to the $^4A_2$ excited state of NV^0. The symmetry of the EPR spin-Hamiltonian parameters identifies this as a trigonal defect with a nitrogen atom on the trigonal axis. The production of the defect by irradiation damage and annealing in N_s-doped diamond concurrently with NV^- adds additional support to the assignment.

The threshold for the optical excitation of the $S = \frac{3}{2}$ excited state matches the energy of the ZPL of NV^0, providing further support for assignment to the $^4A_2$ state. This state is expected to be low lying, with a sufficiently long lifetime (and spin lattice relaxation time) such that selective intersystem crossing could build up a spin-polarised population under conditions of optical excitation. If only 1% of the NV^0 defects were excited into the $^4A_2$ state, then spin polarisation comparable to that measured for the NV^- would produce the observed EPR intensity, assuming that NV^- and NV^0 are in comparable concentrations, as was indicated by the optical absorption measurements.

It is worth noting that the experimental studies were greatly simplified by using a ^{15}N-doped diamond; the ^{14}N quadrupole interaction would have complicated the spectra. Measurements on similarly prepared ^{14}N-doped samples are planned to determine the quadrupole interaction. ^{13}C hyperfine measurements would also be useful in confirming the localisation of the unpaired electron probability density, but to-date these satellites have been undetectable with a 1.1% natural abundance of ^{13}C.

The lack of detection of the ground state of NV^0 is likely to be due to a the presence of a dynamic Jahn-Teller coupling, revealed in uniaxial stress splitting studies of the ZPL [15]. This invites the suggestion that the interconversion between lower symmetry states results in the broadening of the EPR lines, to the extent that it prevents their detection. If this is the case then application of uniaxial stress should lock the defect into a lower symmetry configuration enabling EPR and optically detected magnetic resonance studies of the ground state.

It should be noted that a donor is not required for the production of NV^0 in contrast to the situation for NV^-, simplifying its production for applications exploiting the spin physics. Hence the detection of the ground state of NV^0 could have important implications for quantum information processing applications.

References

[1] G. Davies and M. F. Hamer, P. Roy. Soc. Lond. A Mat. **348**, 285 (1976).

[2] T. A. Kennedy, J. S. Colton, J. E. Butler, R. C. Linares, and P. J. Doering, Appl. Phys. Lett. **83**, 4190 (2003).

[3] F. T. Charnock and T. A. Kennedy, Phys. Rev. B **64**, 041201 (2001).

[4] A. Beveratos, R. Brouri, T. Gacoin, A. Villing, J. P. Poizat, and P. Grangier, Phys. Rev. Lett. **89**, 187901 (2002).

[5] C. Coulson and M. Kearsley, Proc. Roy. Soc. Lond. A Mat. **241**, 433 (1957).

[6] N. R. S. Reddy, N. B. Manson, and E. R. Krausz, J. Lumin. **38**, 46 (1987).

[7] E. van Oort, N. B. Manson, and M. Glasbeek, J. Phys. C Solid State **21**, 4385 (1988).

[8] D. A. Redman, S. Brown, R. H. Sands, and S. C. Rand, Phys. Rev. Lett. **67**, 3420 (1991).

[9] N. B. Manson, X. F. He, and P. T. H. Fisk, J. Lumin. **53**, 49 (1992).

[10] J. H. N. Loubser and J. A. van Wyk, Diamond Research **11**, 11 (1977).

[11] J. Harrison, M. J. Sellars, and N. B. Manson, J. Lumin. **107**, 245 (2004).

[12] N. B. Manson, J. P. Harrison, and M. J. Sellars, Phys. Rev. B **74**, 104303 (2006).

[13] J. Harrison, M. J. Sellars, and N. B. Manson, Diam. Relat. Mater. **15**, 586 (2006).

[14] F. Jelezko, T. Gaebel, I. Popa, M. Domhan, A. Gruber, and J. Wrachtrup, Phys. Rev. Lett. **93**, 130501 (2004).

[15] G. Davies, J. Phys. C Solid State **12**, 2551 (1979).

[16] D. C. Hunt, D. J. Twitchen, M. E. Newton, J. M. Baker, T. R. Anthony, W. F. Banholzer, and S. S. Vagarali, Phys. Rev. B **61**, 3863 (2000).

[17] C. V. H. Stroemann, F. Tshisikhawe, J. O. Hansen, and R. C. Burns, *Synthesis of diamond* (2006), Patent WO2006061672.

[18] X. F. He, N. B. Manson, and P. T. H. Fisk, Phys. Rev. B **47**, 8816 (1993).

[19] A. Abragam, J. Horowitz, M. H. L. Pryce, and K. W. Morton, Proc. Roy. Soc. Lond. A Mat. **230**, 169 (1955).

[20] J. H. Wood and G. W. Pratt, Phys. Rev. **107**, 995 (1957).

[21] C. Glover, Ph.D. thesis, University of Warwick (2003).

[22] O. D. Tucker, Ph.D. thesis, University of Oxford (1995).

Chapter 9

The negative nitrogen-vacancy-hydrogen defect

9.1 Background and motivation for study

The negatively charged nitrogen-vacancy-hydrogen defect (NVH^-), first identified by Glover *et al.* [1], is routinely detected by EPR in as-grown SC-CVD diamond. Studies have shown [2] that in cases of moderate-high (100–1000 ppb) concentrations of single substitutional nitrogen (N_s) NVH^- may account for as much as 10% of the total nitrogen content. In device grade material the concentration of NVH^- is found to be below EPR detection limits [1, 2], but since it has been shown to be an electron trap it may still influence electronic properties when present in low concentrations.

Hydrogen has been shown to compensate the substitutional boron acceptor [3], therefore a greater understanding of hydrogen-related defects is helpful when considering the use of diamond in electronic applications. Such interest has prompted theoretical work concerning the role of hydrogen in diamond (see for example Goss [4]). From an academic point of view, the NVH^- defect in particular demands further experimental investigation due to recent debate [5] concerning the role of quantum mechanical behaviour of the hydrogen atom in this centre, as covered briefly in §2.2.2.2.

EPR investigations of the NVH^- defect revealed a defect of trigonal (C_{3v}) symmetry [1]. The original model therefore suggested that the hydrogen is bonded to the nitrogen atom, such that the hydrogen and nitrogen atoms, as well as the vacancy, are all contained along a ⟨111⟩ axis, ensuring C_{3v} symmetry. However, subsequent theoretical modelling has suggested that such a defect is unstable and instead it has been proposed that the hydrogen atom bonds directly to one of the

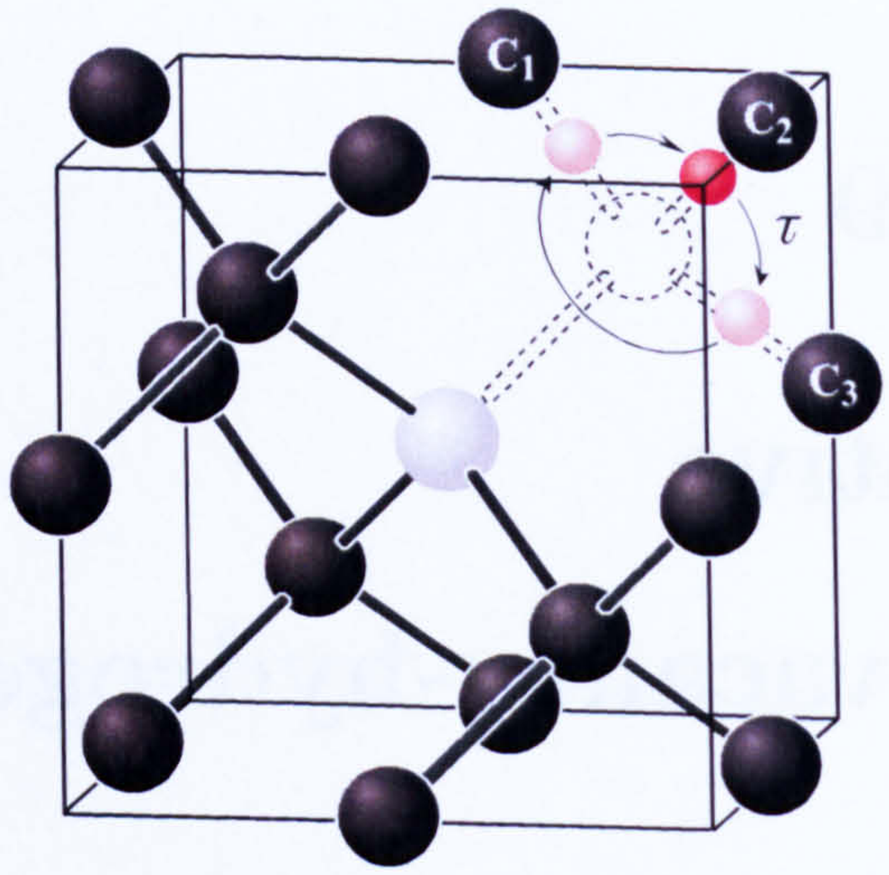

Figure 9-1: The dynamic NVH^- model. In this model the hydrogen atom (smallest shaded sphere) tunnels between the three positions indicated around the vacancy (dashed circle), with the lifetime of each site given by τ. Hence, at a given instant, the defect will have C_{1h} symmetry. In an EPR experiment the hydrogen atom appears to be situated in its time-averaged position along the [111] axis and the defect has apparent C_{3v} symmetry.

three nearest-neighbour carbon atoms around the vacancy [5–7]. In the static case this would yield a defect of C_{1h} symmetry, but tunnelling of the hydrogen between the three possible configurations would yield a time-averaged C_{3v} symmetry (see figure 9-1).

For the theoretical dynamic model to agree with the experimentally observed C_{3v} symmetry the lifetime (τ) of each C_{1h} configuration must be sufficiently short such that an EPR experiment yields the time-averaged position of the hydrogen atom and it has been estimated that for NVH $\tau \sim 10^{-11}$ s [7]. However, to-date no experimental evidence proving or disproving the dynamic model has been published and measurement of τ has been made.

In this chapter further EPR investigations of the NVH^- defect are presented. Measurements have been taken at both X and Q-band at temperatures between 8 and 750 K on SC-CVD samples containing ^{15}N and deuterium (D) in natural abundance as well as samples where the source gases have been enriched with these isotopes. These measurements have allowed the previously published experimentally determined spin-Hamiltonian parameters for this centre [1] to be refined as well as an investigation of the effect of isotopic substitution. The results of these

studies also provide the first experimental indication that the hydrogen atom in the NVH^- defect exhibits dynamic behaviour.

9.2 Experimental details

The data obtained in this chapter has been obtained from three homoepitaxially grown freestanding SC-CVD diamonds grown by Element Six Ltd, which have all been doped with nitrogen. One sample has been grown without isotope enrichment and therefore contains 99.99% ^1H and 99.6% ^{14}N. The other two samples were isotopically enriched; one with ~ 90% enrichment of ^{15}N (i.e. grown with $^{15}N_2$ in the gas phase) and the other was grown with a D_2-enriched source gas (i.e. a D_2:CH_4 mixture), resulting in a sample with ~ 80% enrichment of D. All the samples have been investigated as-grown.

Both X and Q-band spectrometers have been used to investigate NVH^- in these samples. X-band measurements have been obtained on the Bruker EMX system (§4.2) which permitted measurements to be taken at room temperature, low temperature (8 K) and high temperature (up to 750 K) using the experimental setups described in §§4.2.2–4.2.3. For the Q-band spectrometer (§4.3) only room-temperature measurements were made.

9.3 Results

The sample isotopically enriched with 90% ^{15}N was investigated first (as in Glover *et al.* [1]), as the resultant spectrum for NVH^- is considerably simplified; ^{15}N has $I = \frac{1}{2}$ and hence the central $g = 2$ region is free from a large $^{14}N_s^0$ resonance line and the NVH^- spectra does not have the additional complication of the quadrupole (P) interaction.

Room-temperature X and Q-band spectra have been collected for this sample with the applied magnetic field (B) parallel to ⟨100⟩, ⟨111⟩ and ⟨110⟩. The acquired spectra have then been compared to simulated EPR spectra for $^{15}NVH^-$ generated using the spin-Hamiltonian parameters determined by Glover *et al.* [1], which were determined solely from X-band data. Figure 9-2 shows X and Q-band

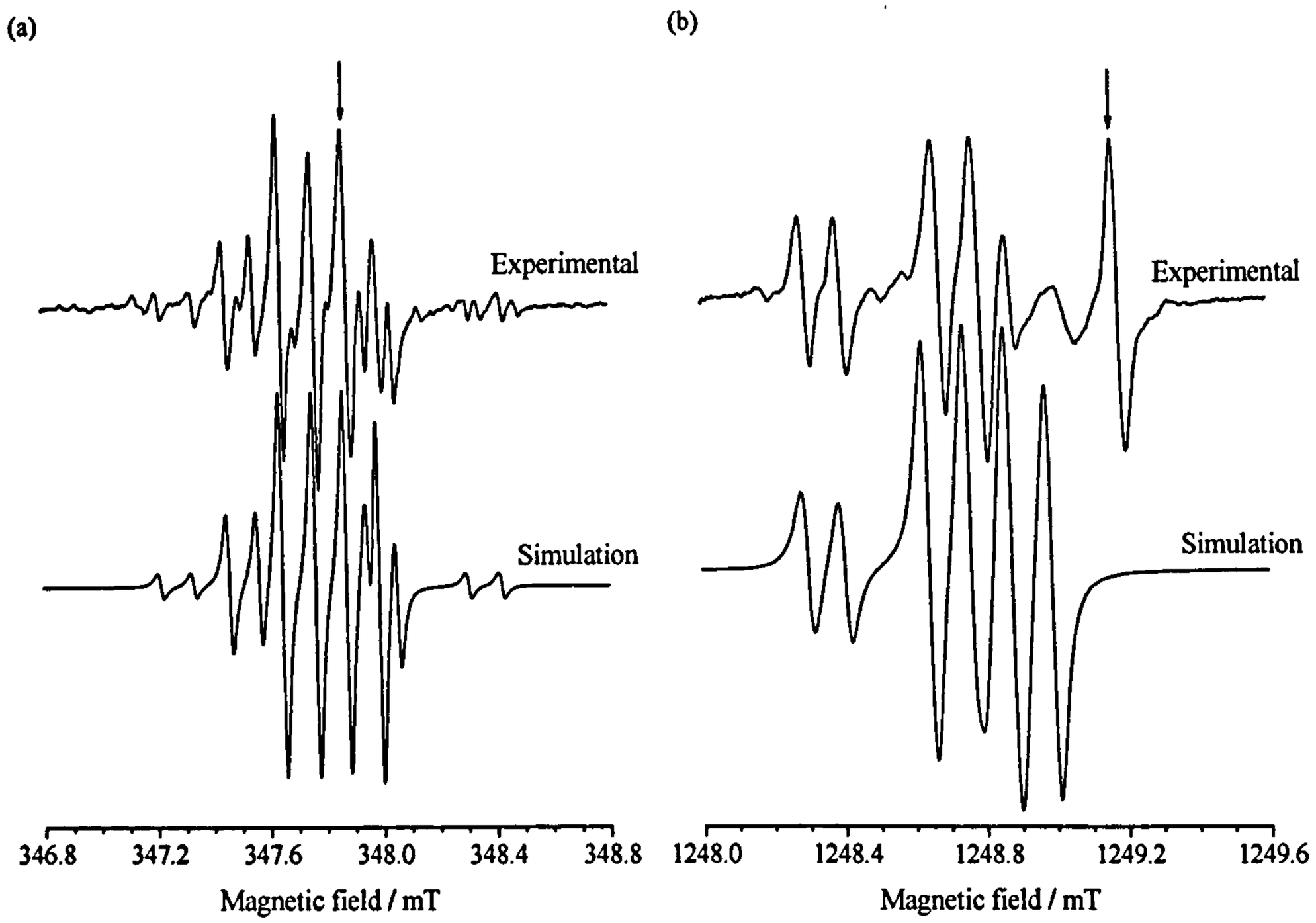

Figure 9-2: Room-temperature $^{15}NVH^-$ spectra obtained with $\mathbf{B} \parallel \langle 111 \rangle$ at X-band (a) and Q-band (b). In both cases the simulated data has been generated using the spin-Hamiltonian parameters determined by Glover *et al.* [1] (see also table 9-1). Resonance lines arising from residual $^{14}N_s^0$ are indicated by arrows.

data acquired from this sample with $\mathbf{B} \parallel \langle 111 \rangle$.

This data reveals that the published parameters do not accurately reproduce the position of the resonance lines as observed at Q-band. Since the positioning of the resonance lines at Q-band using the published parameters were incorrect it was apparent that this data (in combination with X-band data) could be used to refine the spin-Hamiltonian parameters for $^{15}NVH^-$. Table 9-1 shows the optimised parameters.

After determining the spin-Hamiltonian parameters for $^{15}NVH^-$ X and Q-band EPR spectra were acquired from the sample containing natural abundance of ^{15}N. Room-temperature spin-Hamiltonian parameters for $^{14}NVH^-$ could be determined from data collected with **B** parallel to $\langle 100 \rangle$, $\langle 111 \rangle$ and $\langle 110 \rangle$ directions.

The sample containing predominately $^{14}NVH^-$ was also used to investigate the effect of temperature on the EPR spectrum. Figure 9-3 shows X-band data collected with $\mathbf{B} \parallel \langle 111 \rangle$, obtained at 8 K and 750 K. The high-temperature spec-

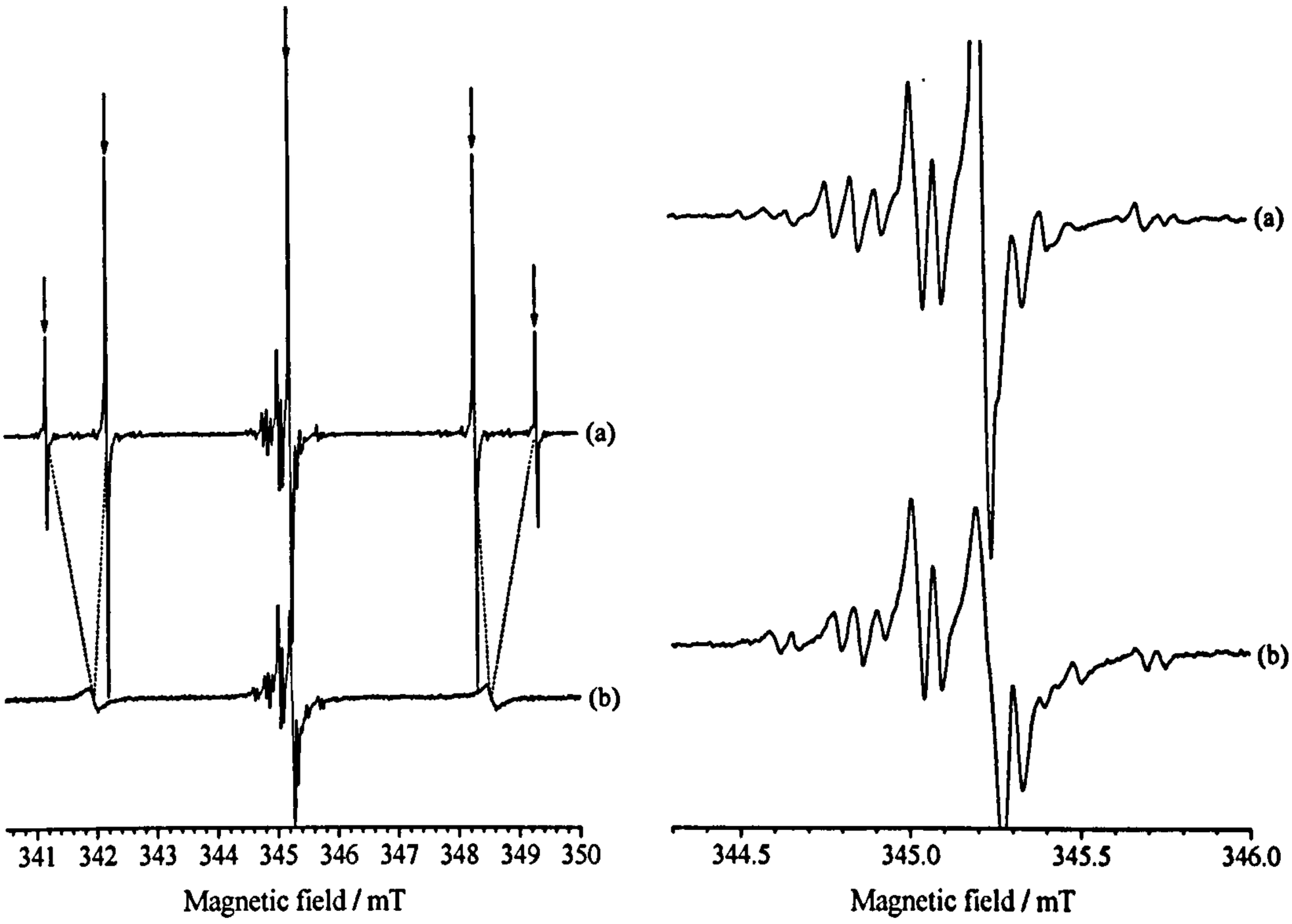

Figure 9-3: Comparison between EPR spectra obtained at X-band with $\mathbf{B} \parallel \langle 111 \rangle$ at a temperature of (a) 8 K and (b) 750 K. Spectra were collected from a sample containing $^{14}N_s^0$ (indicated by arrows) and $^{14}NVH^-$. The sub-figure on the left shows the entire spectrum, indicating that at 750 K motional averaging of the $^{14}N_s^0$ spectrum is apparent. To the right is a magnified view of the $^{14}NVH^-$ resonance lines.

trum shows motional averaging of the N_s^0 spectrum, but no difference in the EPR spectrum from $^{14}NVH^-$ is apparent between these temperatures.

Room-temperature data obtained at X and Q-band for the sample isotopically enriched with ~ 80% D is shown in figure 9-4. These figures show that all the spectra appear to have a broad lineshape underneath resonance lines from NVD^- and N_s^0. As for $^{14}NVH^-$ spectra obtained at low temperatures revealed no differences in the EPR spectra (other than temperature-related microwave power saturation effects).

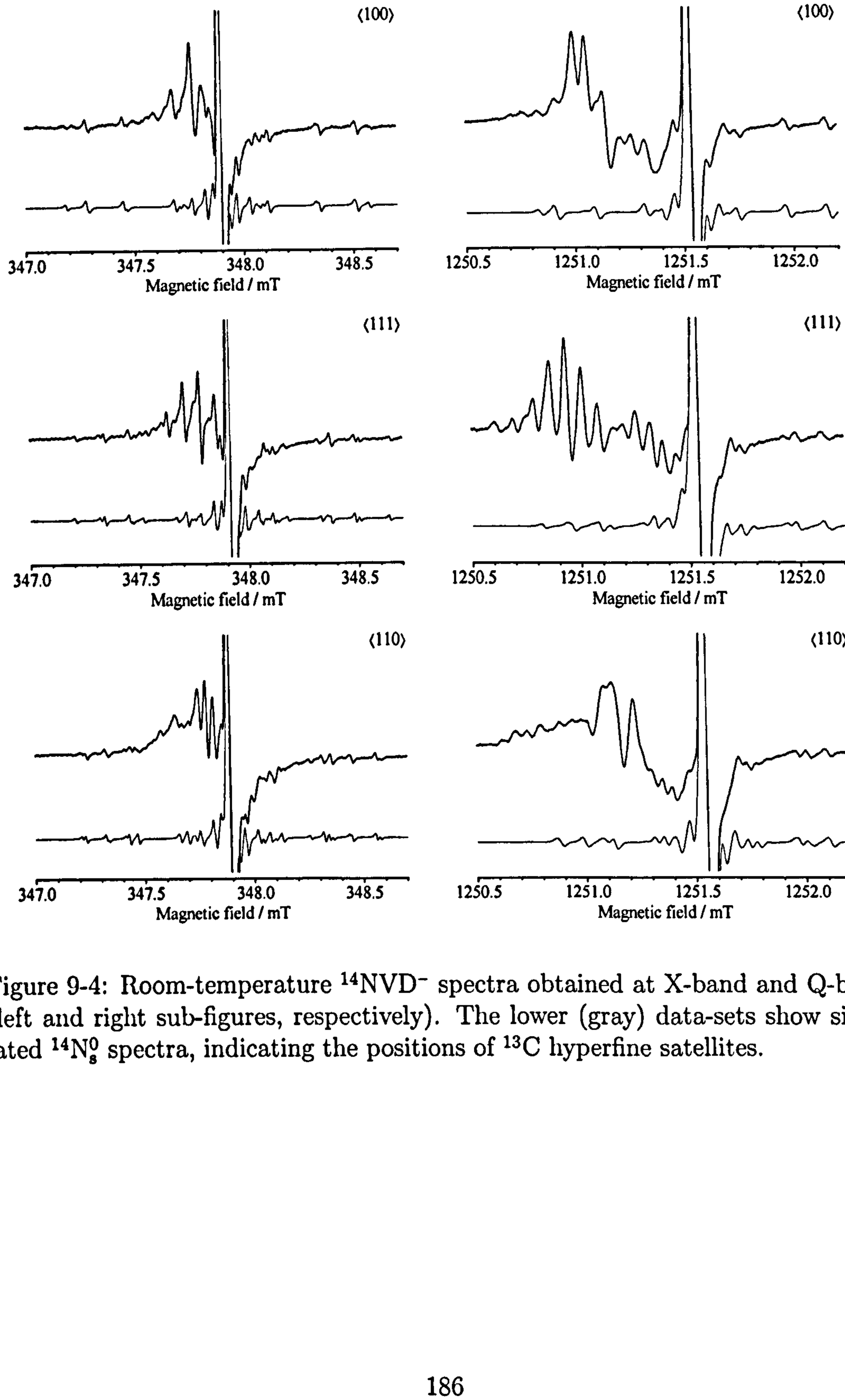

Figure 9-4: Room-temperature $^{14}NVD^{-}$ spectra obtained at X-band and Q-band (left and right sub-figures, respectively). The lower (gray) data-sets show simulated $^{14}N_s^0$ spectra, indicating the positions of ^{13}C hyperfine satellites.

9.4 Discussion

9.4.1 $^{15}NVH^-$ and $^{14}NVH^-$ spin-Hamiltonian parameters

The determined room-temperature spin-Hamiltonian parameters for $^{15}NVH^-$ are shown in table 9-1. These agree with the values determined by Glover *et al.* [1] within error, but the precision of these new values is greatly improved due to the use of both X and Q-band EPR spectra. Figure 9-5 shows the fit obtained to the spectrum obtained with $\mathbf{B} \parallel \langle 100 \rangle$, which is good agreement in terms of the position and relative intensity of the $^{15}NVH^-$ resonance lines. With **B** directed along $\langle 111 \rangle$ and $\langle 110 \rangle$ directions the new parameters result in a improved fit for the positions of the resonance lines, as shown in figures 9-6a and b. However, these spectra also reveal that the linewidths of the $^{15}NVH^-$ resonance lines varies within the spectrum with these orientations of **B**. Hence a simulation where the linewidths are assumed to be constant results in a poor reproduction of the experimental data in terms of the amplitude of the resonance lines. The implications of this differential broadening are discussed in §9.4.2.

It is important to ensure that the optimum spin-Hamiltonian parameters for $^{14}NVH^-$ are determined before attempting to fit the spectra resulting from enrichment of D (§9.4.3). The determined parameters for $^{15}NVH^-$ were used as starting parameters for the fitting of $^{14}NVH^-$, with the hyperfine parameters from ^{14}N rescaled by the ratio of g_N values (see table 3-1). The parameters were then permitted to vary resulting in the values shown in table 9-1. This data again agrees with the previously determined values and hence confirms that the nitrogen hyperfine interaction scales in the expected way. Poor agreement was again observed in terms of the relative amplitudes of the resonance lines.

9.4.2 Evidence for the motional averaging of NVH^-

The apparent differential broadening of resonance lines from NVH^- is an interesting experimental finding which demands further scrutiny. The first possibility which should be considered is microwave power saturation, the degree of which can vary between resonance lines resulting from a given defect. However, in the case of a trigonal defect with the magnetic field directed along $\langle 111 \rangle$ the effect

Table 9-1: Room-temperature spin-Hamiltonian parameters for $^{15}NVH^-$ and $^{14}NVH^-$ determined in this study, compared to those previously determined by Glover *et al.* [1]. Note that Glover *et al.* assumed identical g and ^1H hyperfine parameters for $^{14/15}NVH^-$ and the ^{14}N hyperfine parameters were determined from the ^{15}N values by scaling with the g_N values for $^{14}N/^{15}N$. $g_\parallel$ and $A_\parallel$ are directed along [111] in all cases and hyperfine parameters are expressed in MHz.

Defect	Parameter	Published	This study
$^{15}NVH^-$	$g_\parallel$	2.0034(1)	2.0034(1)
	$g_\perp$	2.0030(1)	2.0029(1)
	$A_\parallel$ (^1H)	±13.69(20)	±13.57(3)
	$A_\perp$ (^1H)	∓9.05(20)	∓8.97(3)
	$A_\parallel$ (^{15}N)	±2.94(10)	±2.87(4)
	$A_\perp$ (^{15}N)	±3.30(10)	±3.36(3)
$^{14}NVH^-$	$g_\parallel$	2.0034(1)	2.0034(1)
	$g_\perp$	2.0030(1)	2.0029(1)
	$A_\parallel$ (^1H)	±13.69(20)	±13.50(4)
	$A_\perp$ (^1H)	∓9.05(20)	∓9.04(3)
	$A_\parallel$ (^{14}N)	∓2.09(10)	∓2.06(2)
	$A_\perp$ (^{14}N)	∓2.36(10)	∓2.36(3)
	P (^{14}N)	∓4.80(10)	∓4.88(3)

of saturation is usually more evident for the resonance lines arising from the site parallel to the magnetic field, due to only one relaxation pathway being permitted ($\Delta M_S = \pm 1$ and $\Delta m_I = 0$), as discussed in §7.4.1 for the (V-Si-V)^0 centre. Figure 9-6a shows that this is not the case for $^{15}NVH^-$; broadened resonance lines only appear from specific resonance lines from the sites which make an angle of 70.5° with respect to the magnetic field. A microwave power sweep added experimental evidence towards discounting microwave power saturation as a cause for the effect. Instead the consequences of dynamics of the NVH^- centre will be considered, to see if tunnelling of the H atom between the three equivalent C_{1h} configurations (figure 9-1) could result in the differential broadening of the NVH^- resonance lines.

To simulate the impact of inter-conversion between the different configurations generalised Bloch equations which take into account the rate of tunnelling ($1/\tau$)

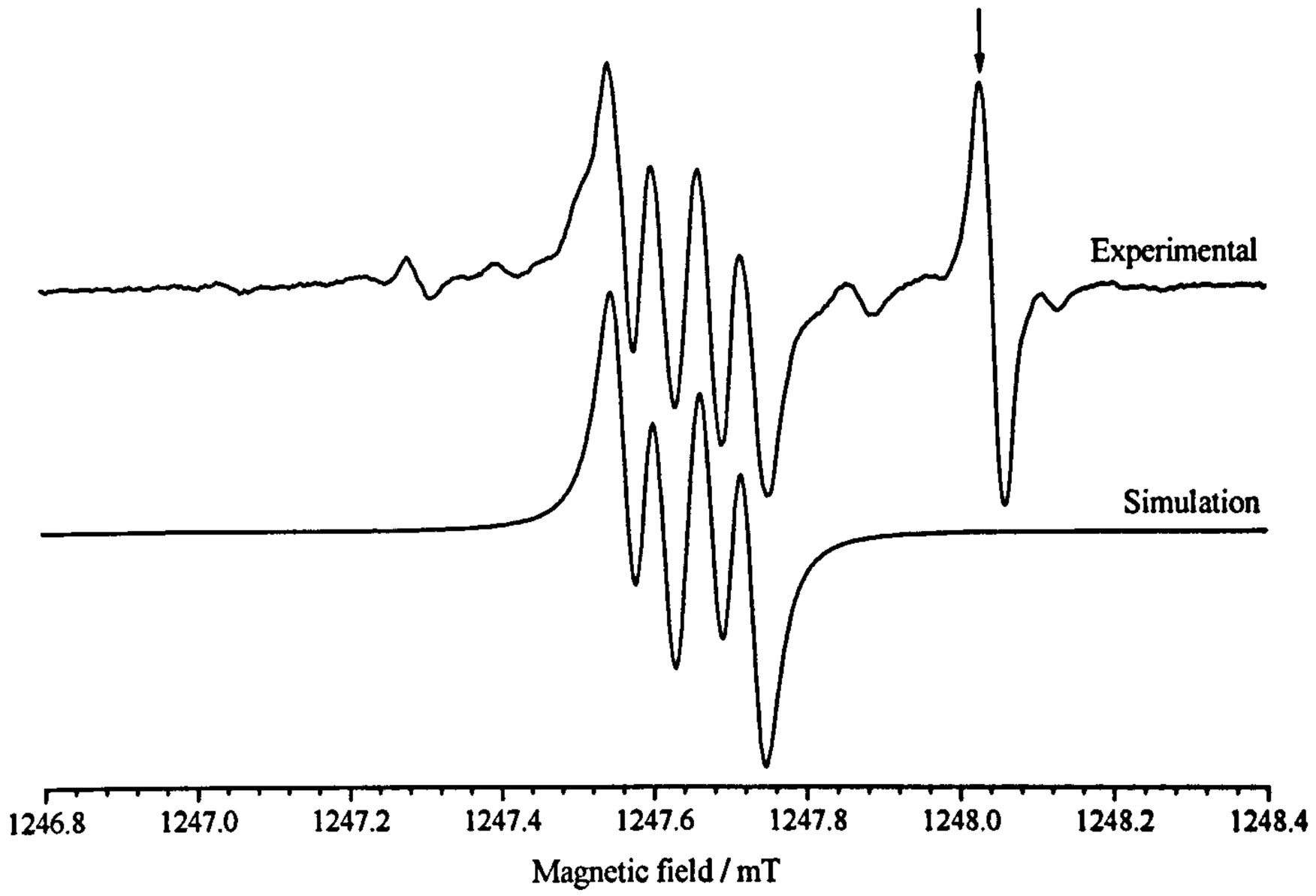

Figure 9-5: Room-temperature $^{15}NVH^-$ spectrum obtained at Q-band with **B** $\parallel$ ⟨100⟩. The simulated data has been produced using the newly determined spin-Hamiltonian parameters (table 9-1). The central resonance line from residual $^{14}N_s^0$ is indicated by the arrow.

need to be used. Here the treatment of Weil *et al.* [8] will be followed. This treatment considers a defect which can consist in two forms (a and b) which result in different EPR spectra and, for the sake of simplicity, the case where each form results in only a single resonance line will be considered first. The probability of each state may be different and hence probabilities f_a and f_b are assigned to the two different configurations. The total complex transverse magnetisation (c.f. the static case in §3.6), G, is then given by [8]:

$$G = \mathrm{i}B_1 M_z^0 \frac{\overline{\gamma} + \tau(f_a\gamma_a\alpha_b + f_b\gamma_b\alpha_a)}{\tau\alpha_a\alpha_b + f_a\alpha_a + f_b\alpha_b}, \tag{9-1}$$

where the term α is defined for each state as follows:

$$\alpha_a = {\tau_{2a}}^{-1} - \mathrm{i}(\omega_{Ba} - \omega) \tag{9-2}$$

$$\alpha_b = {\tau_{2b}}^{-1} - \mathrm{i}(\omega_{Bb} - \omega) \tag{9-3}$$

and the mean gyromagnetic ratio $\overline{\gamma}$ is given by:

$$\overline{\gamma} = f_a\gamma_a + f_b\gamma_b \tag{9-4}$$

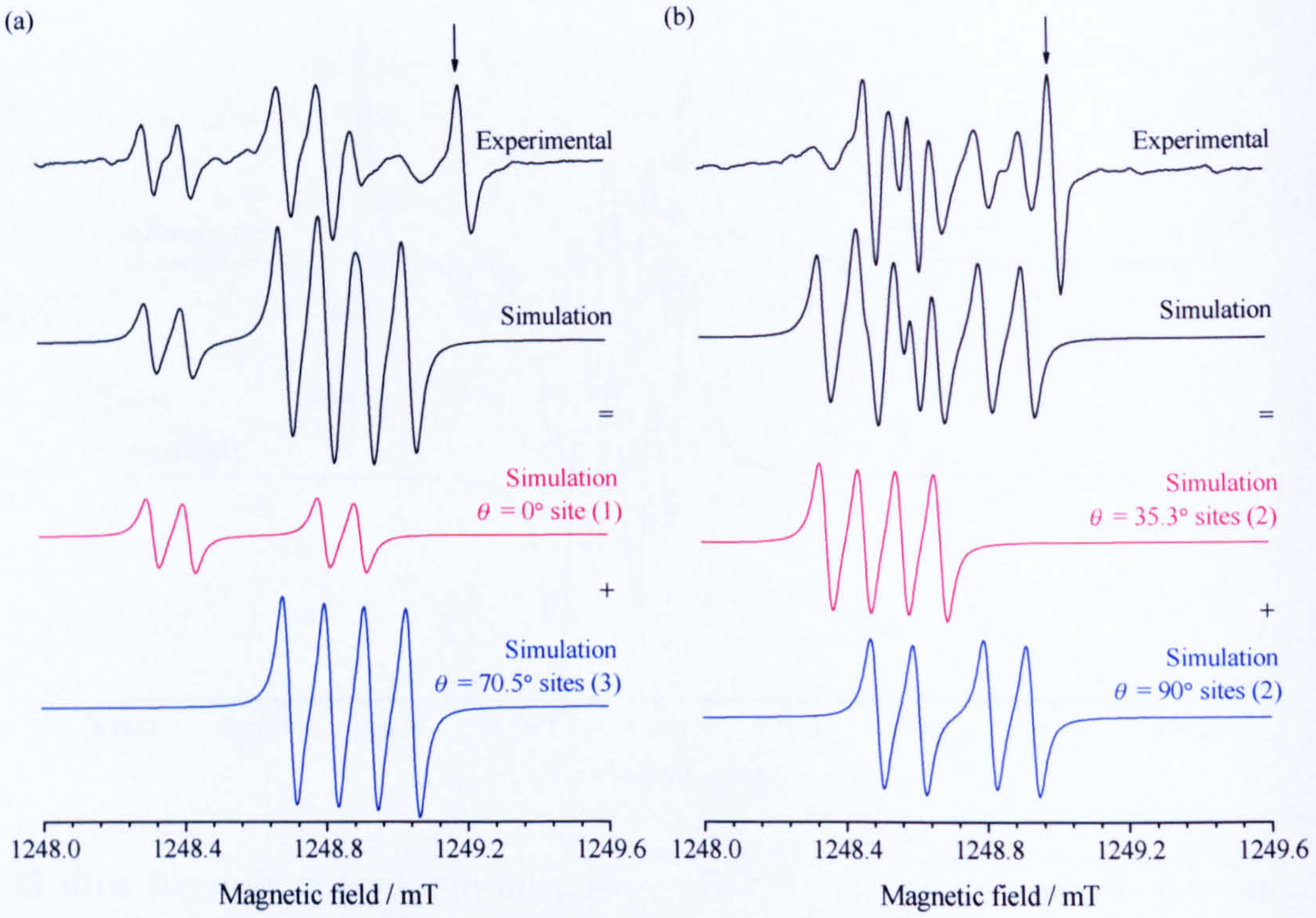

Figure 9-6: Room-temperature $^{15}NVH^-$ spectra obtained at Q-band with **B** parallel to (a) ⟨111⟩ and ⟨110⟩. The simulated data has been produced using the newly determined spin-Hamiltonian parameters (table 9-1). The central resonance line from residual $^{14}N_s^0$ is indicated by the arrow.

The EPR spectrum $Y(B)$ is proportional to the imaginary component of G and hence this generalised equation permits a synthetic EPR spectrum (with Lorentzian lineshapes) to be produced for any given lifetime (τ). An example of the use of this expression is shown in figure 9-7 where the interconversion between two states, where $f_a = 2f_b$, is shown as a function of τ. This figure shows the *slow*, *intermediate* and *fast* regimes (compared to characteristic parameter $|\overline{\gamma}|\Delta B_0$), where first the two resonance lines begin to broaden, followed by coalescence and finally, in the fast limit, the combined resonance lines narrow and approach the linewidths seen in the static case.

Two important parameters will be considered in this model; the lifetime required for coalescence, which is given by:

$$\tau_{\text{coalescence}} = \frac{\sqrt{2}}{|\overline{\gamma}|\Delta B_0} \tag{9-5}$$

and the linewidth (Γ) in the *fast* regime when the resonance lines have coalesced:

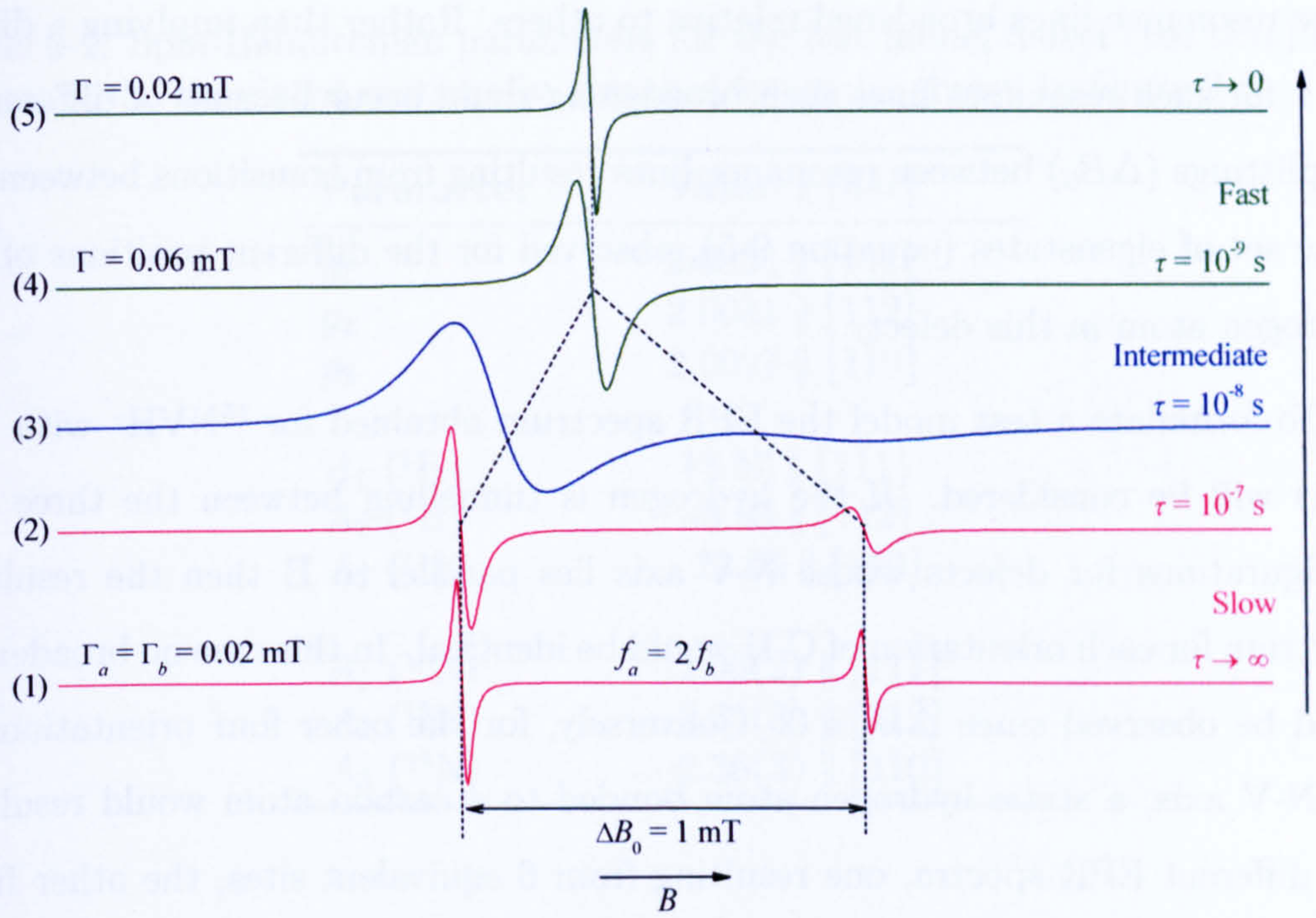

Figure 9-7: Synthetic first-derivative Lorentzian spectra, generated using the imaginary component of equation 9-1, showing the effect of inter-conversion between two defect configurations (a and b) for a given lifetime (τ). In this example the probability of the system being in state a is twice that of state b ($f_a = 2f_b$). In the static configuration (1) the two resonance lines are separated by 1 mT and both have an initial linewidth of 0.02 mT.

$$\Gamma = \Gamma_0 + f_a f_b \tau (\Delta B_0)^2, \tag{9-6}$$

where Γ_0 is the linewidth in the static (unsaturated) case.

To use this treatment for a dynamic NVH^- centre it is necessary to know the *static* spin-Hamiltonian parameters for the C_{1h} symmetry configuration resulting from H atom bonded to one of the C atoms (figure 9-1). These parameters are not known, but the effect of tunnelling of the H atom can be considered using a test model which has lower symmetry. For this the generalised Bloch equation given in equation 9-4 has been implemented in an Excel spreadsheet, allowing dynamics to be explored as a possible explanation for the broadening observed in particular NVH^- resonance lines.

It is apparent that if the NVH defect is dynamic then the EPR spectra corresponds to the *fast* limit case shown in 9-7 since C_{3v} symmetry is observed, but with

some resonance lines broadened relative to others. Rather than implying a different τ for such resonance lines such broadening could occur because of differences in splittings (ΔB_0) between resonance lines resulting from transitions between the same set of eigenstates (equation 9-6), observed for the different positions of the hydrogen atom in this defect.

To formulate a test model the EPR spectrum obtained for $^{15}NVH^-$ with $\mathbf{B} \parallel \langle 111 \rangle$ will be considered. If the hydrogen is tunnelling between the three C_{1h} configurations for defects whose N-V axis lies parallel to $\mathbf{B}$ then the resulting spectrum for each orientation of C-H would be identical. In this case no broadening could be observed since $\Delta B_0 = 0$. Conversely, for the other four orientations of the N-V axis, a static hydrogen atom bonded to a carbon atom would result in two different EPR spectra, one resulting from 6 equivalent sites, the other from 3. Hence experimentally, for this orientation of the applied magnetic field, two configurations would be seen for the sites which make an angle of 70.5° with respect to $\mathbf{B}$, with one configuration twice as likely as the other ($f_a = 2f_b$). This tallies with what is seen experimentally; broadening only occurs for resonance lines resulting from the 9 sites whose N-V axis is *not* parallel to $\mathbf{B}$ (see figure 9-6a).

In the test model the nitrogen hyperfine interaction is left unchanged, since this is close to be isotropic. First the symmetry of the hydrogen hyperfine interaction was lowered. To avoid the resonance lines resulting from sites whose N-V axis lies parallel to the magnetic field changing position $A_\parallel = A_1$ for the hydrogen atom is unchanged in our test model. The lowering of the symmetry was then achieved by setting $A_2 = A_\perp + \delta$ and $A_3 = A_\perp - \delta$ (see table 9-2). This ensures that the resonance lines will coalesce at the experimentally observed position in the intermediate-fast limit.

It is apparent that simply modifying the hyperfine interaction for the hydrogen atom in NVH^- in this way is not sufficient to result in different linewidths, as ΔB_0 is equal for each pair of resonance lines. However, the symmetry of the electronic Zeeman interaction would be lowered for the static C_{1h} NVH^- configuration and hence in the test model g_2 and g_3 have been altered in a similar manner to the hydrogen hyperfine parameters. The spin-Hamiltonian parameters for the test model are given in table 9-2 and the stick spectra obtained using these values are

Table 9-2: Spin-Hamiltonian parameters for the test model defect (see text) used to create the simulated motionally-averaged spectrum shown in figure 9-8.

Parameter	**Value ∥ [*hkl*]**
g_1	2.0034 ∥ [111]
g_2	2.0031 ∥ [11$\bar{2}$]
g_3	2.0027 ∥ [1$\bar{1}$0]
A_1 (^{1}H)	13.57 ∥ [111]
A_2 (^{1}H)	−5.05 ∥ [11$\bar{2}$]
A_3 (^{1}H)	−13.05 ∥ [1$\bar{1}$0]
A_1 (^{15}N)	−2.06(2) ∥ [111]
A_2 (^{15}N)	−2.36(3) ∥ [11$\bar{2}$]
A_3 (^{15}N)	−2.36(3) ∥ [1$\bar{1}$0]

shown in figures 9-8a and b, for X and Q-band frequencies, respectively.

For these parameters $\tau = 2 \times 10^{-8}$ s results in an excellent reproduction of the experimentally observed ^{15}NVH$^-$ spectra for both X and Q-band data sets. It must be emphasised that this set of parameters and value of τ do *not* represent a unique solution for obtaining the degree of differential broadening observed experimentally; as evident from equation 9-6 both τ and ΔB_0 determine Γ in the fast limit and the current experimental data does not permit these parameters to be independently determined.

The parameters used do not correspond to the static C_{1h} configuration, where is likely that both g and A (hydrogen) are shifted away from ⟨111⟩. Despite this the test model proves useful for demonstrating that dynamics of the NVH$^-$ centre are a possible source of the unusual linewidth broadening observed experimentally. Indeed, using the model it is possible to understand why X and Q-band spectra reveal the effect to different extents: The g anisotropy will lead a frequency dependence in the value of ΔB; at Q-band the pairs of resonance lines resulting from the same EPR transitions will be further split and hence the linewidth will be increased (equation 9-6).

Considering the suggested value of $\tau \sim 10^{-11}$ s determined theoretically [7] then ΔB_0 can be estimated from equation 9-6. For this lifetime coalescence of the resonance lines, and hence the experimental observation of C_{3v} symmetry,

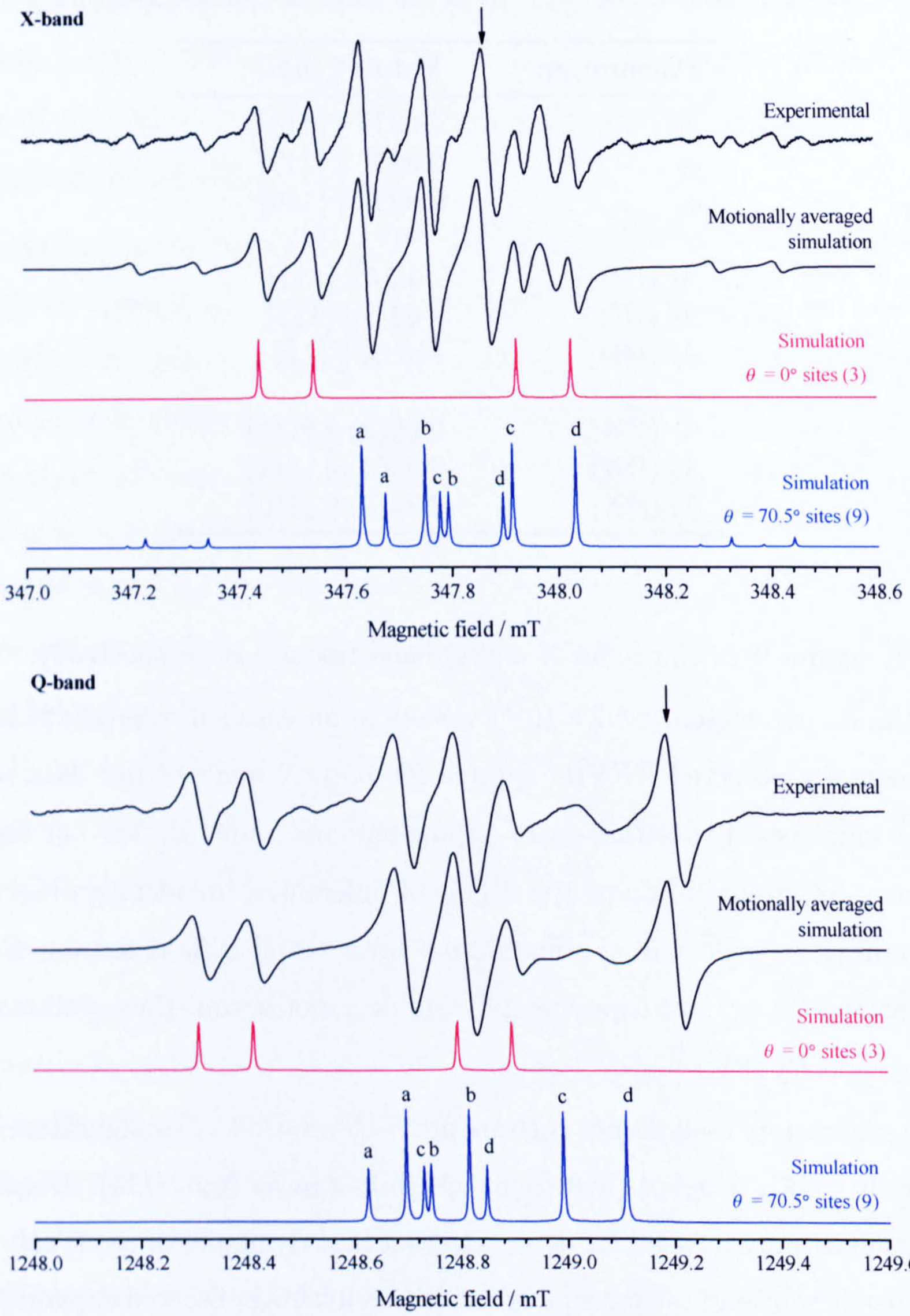

Figure 9-8: Motionally-averaged X and Q-band spectra generated using the test model defect spin-Hamiltonian parameters given in table 9-2 simulated with $\mathbf{B} \parallel \langle 111 \rangle$. Averaging occurs between the pairs of lines labelled (a–d). In this example $\tau = 2 \times 10^{-8}$ s. Experimental data showing the experimental ^{15}NVH$^-$ spectra is included for comparison, with the arrow indicating the position of the central resonance line from residual $^{14}N_s^0$ and single Lorentzian line of appropriate amplitude has been added in the simulation to account for this.

would occur with value of $\Delta B_0 \sim 800\,\mathrm{G}$. This is unreasonably high given the fact that ΔB_0 is determined by the g and A anisotropy in this model. Hence, if the experimental data are indicating dynamic effects, τ is likely to be two orders of magnitude higher.

With tunnelling of the hydrogen hinted at by the new experimental data it is important to consider the experimental spectrum for NVH^- as a function of temperature, as this may affect the value of τ. At low temperatures τ could be lengthened sufficiently to observe the static case, or at high temperatures τ may be decreased such that the broadening effect is suppressed. Unfortunately to-date variable temperature measurements have been only be conducted at X-band and on the sample containing natural abundances of ^{14}N and hence the broadening phenomena is hard to observe. Nevertheless, the data shown in figure 9-3 indicates that between 8 K and 750 K no differences in the NVH^- spectrum can be observed and at low temperatures the symmetry has not been reduced to C_{1h}. This is in agreement with earlier measurements that observed no "freezing-in" of the defect at cryogenic temperatures [1]. Such experimental results suggest that, if tunnelling of the hydrogen atom is occurring, then the lifetime of each C_{1h} symmetry configuration is primarily determined by temperature independent quantum mechanical tunnelling in this temperature range.

9.4.3 The NVD^- centre

With the suggestion of the dynamics of the hydrogen atom being evident from the experimental EPR data an obvious consideration is the effect that the isotopic substitution of ^1H with D has on the spectrum. Since D is heavier the tunnelling rate would be expected to be significantly reduced (τ increased) and the system may approach the intermediate-slow limit (figure 9-7).

Initial spin-Hamiltonian parameters for $^{14}NVD^-$ have been estimated using the new parameters for $^{14}NVH^-$ and scaling the ^1H hyperfine interaction by the ratio of g_N values for $D/^1H$. Simulations using these parameters compared to X and Q-band data with $\mathbf{B} \parallel \langle 111 \rangle$ are shown in figures 9-9a and b. Here the magnitude of P for the D atom has been assumed to be zero.

The pattern of resonance lines observed with $\mathbf{B} \parallel \langle 111 \rangle$ (particularly at X-

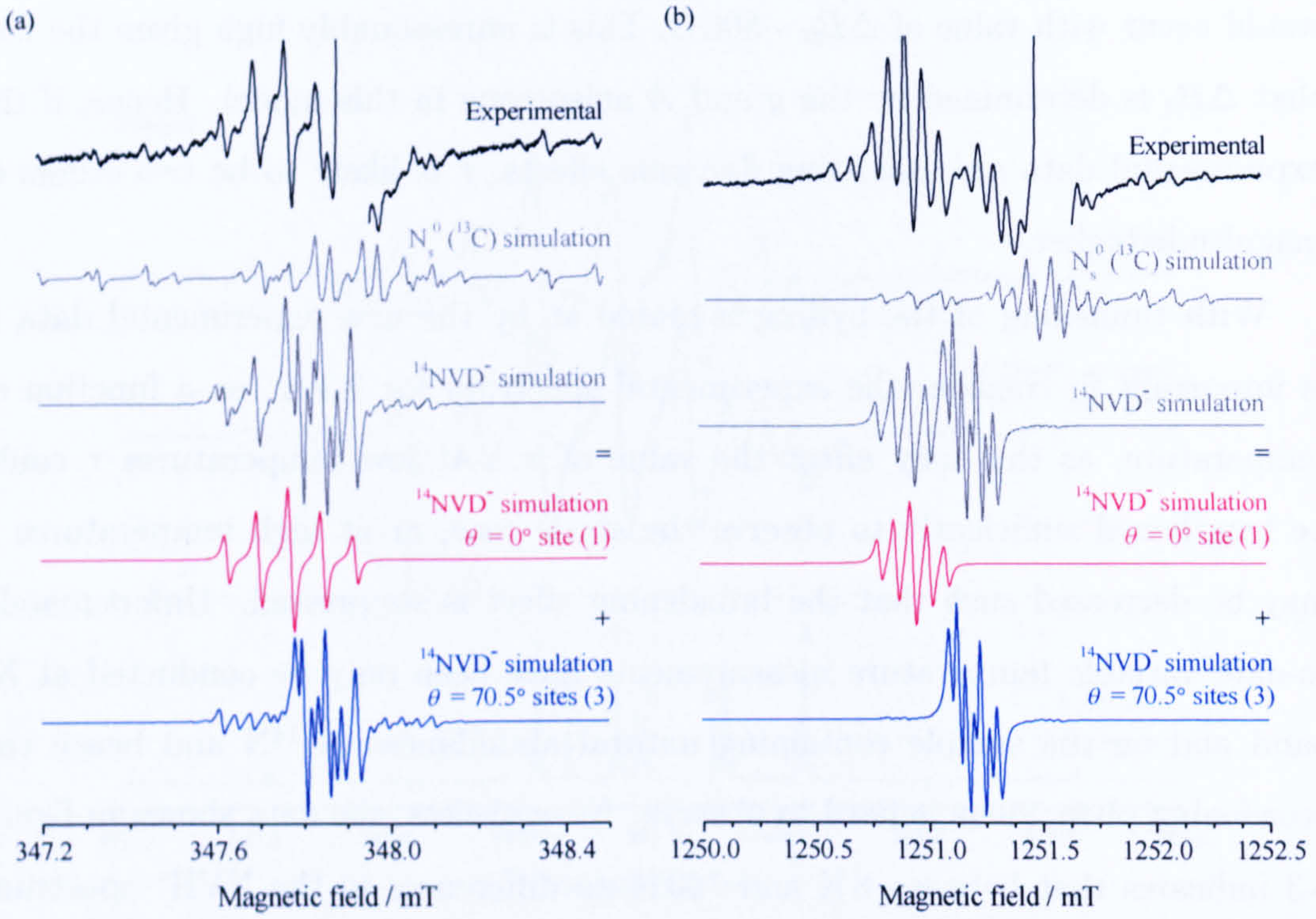

Figure 9-9: Room-temperature ^{14}NVD$^-$ spectra obtained at X-band (a) and Q-band (b), with $\mathbf{B} \parallel \langle 111 \rangle$. The simulated data for ^{14}NVD$^-$ has been produced using the determined spin-Hamiltonian parameters for ^{14}NVH$^-$ (table 9-1) and scaling the ^{1}H hyperfine parameters by the ratio of g_N for D/^{1}H. Note that the central $^{14}N_s^0$ resonance line has been cropped to avoid cluttering the figures.

band) is reminiscent of a spectrum which would result from an unpaired electron interacting with two nuclei with similar hyperfine interaction, with the resultant resonance lines displaying a ratio of intensities 1:2:3:2:1. This is partly a consequence of the reduction in magnitude of the hyperfine interaction for the hydrogen atom; after rescaling by the g_N values $A_\parallel = 2.07(1)$ MHz for the D atom, which is close to the value of $A_\parallel$ for ^{14}N (table 9-2). However, it is apparent that the spectra is dominated by the resonance lines from the sites with their N-V axis parallel to **B**; resonance lines arising from other sites appear absent or dramatically reduced in amplitude. Preferential alignment of the NVD$^-$ centre has been investigated as a cause for this effect, but all $\langle 111 \rangle$ orientations of **B** resulted in the same pattern of resonance lines. It was also noted that the experimental data obtained for different orientations of **B** (shown in figure 9-4) appears to show a broad underlying structure. In combination these two observations invite the sug-

gestion that certain resonance lines are being broadened sufficiently to preclude their detection. Since for B ∥ ⟨111⟩ the resonance lines from sites with their N-V axis parallel to the magnetic field are unaffected this experimental observation is also compatible with the suggestion that ^{1}H/D is tunnelling between different C_{1h} configurations. For NVD^- the broadening of the resonance lines is more severe due to the increase in τ. As for NVH^- no change in the X-band EPR spectra was observed at cryogenic temperature.

9.5 Conclusions and further work

Multi-frequency EPR measurements on SC-CVD diamonds containing NVH^- have revealed a transition dependent line-broadening effect, which varies with the microwave frequency. This provides the first experimental evidence for the dynamic model of the NVH^- centre, where the hydrogen atom tunnels between C_{1h} symmetry configurations resulting from the hydrogen atom being bonded to one of the three nearest-neighbour carbon atoms surrounding the vacancy.

It is evident that further experimental work is required before conclusive evidence is obtained. Critical to the success of correctly modelling the effect of motional averaging in the NVH^- centre is knowledge of the spin-Hamiltonian parameters for the C_{1h} symmetry defect, resulting from the hydrogen atom bonded to one of the carbon atoms. Once these parameters are known the dynamic treatment discussed can be used to experimentally determine the tunnelling frequency required in order to obtain agreement with the experimentally observed broadening of certain NVH^- resonance lines. A simple test model has demonstrated that such dynamics could result in the pattern of broadening observed experimentally, but the rate of tunnelling would need to be ~ 2 orders of magnitude lower than the theoretically determined value.

Since low temperatures have been shown to be insufficient to lock the NVH^- centre into a lower symmetry configuration the application of uniaxial stress is likely to be the key to observing C_{1h} symmetry experimentally in EPR. Theoretical estimations of the spin-Hamiltonian parameters in the static C_{1h} case would also permit the dynamic model to be tested against the experimental observations.

References

[1] C. Glover, M. E. Newton, P. Martineau, D. J. Twitchen, and J. M. Baker, Phys. Rev. Lett. **90**, 185507 (2003).

[2] R. J. Cruddace, Ph.D. thesis, University of Warwick (2007).

[3] J. Chevallier, A. Lusson, D. Ballutaud, B. Theys, F. Jomard, A. Deneuville, M. Bernard, E. Gheeraert, and E. Bustarret, Diam. Relat. Mater. **10**, 399 (2001).

[4] J. P. Goss, J. Phys. Condens. Mat. **15**, R551 (2003).

[5] M. J. Shaw, P. R. Briddon, J. P. Goss, M. J. Rayson, A. Kerridge, A. H. Harker, and A. M. Stoneham, Phys. Rev. Lett. **95**, 105502 (2005).

[6] J. P. Goss, P. R. Briddon, R. Jones, and S. Sque, J. Phys. Condens. Mat. **15**, S2903 (2003).

[7] A. Kerridge, A. H. Harker, and A. M. Stoneham, J. Phys. Condens. Mat. **16**, 8743 (2004).

[8] J. A. Weil, J. R. Bolton, and J. E. Wertz, *Electron Paramagnetic Resonance* (Wiley-Interscience, New York, 1994).

Chapter 10

Summary and further work

10.1 Introduction

In this thesis EPR has been employed for the study of point defects in synthetic single-crystal diamond. The results chapters presented demonstrate the capabilities of EPR. For example, the ability to probe the structure and constituents of paramagnetic defects was used extensively in chapter 6, for the identification of silicon-related defects, whilst the capability to resolve dynamic processes around a paramagnetic centre has allowed experimental evidence for the quantum mechanical tunnelling of hydrogen in the nitrogen-vacancy-hydrogen centre to be obtained (chapter 9). Additionally, EPR combined with optical excitation was employed in chapter 8 for the investigation of samples containing nitrogen-vacancy centres, which allowed optically excited states of the neutral and negative charge states of this defect to be probed. The importance of these investigations, along with the key conclusions, are summarised in §§10.3–10.5.

EPR is also a quantitative technique. The work presented in chapter 5, which introduced a new method for the fitting of EPR spectra, is discussed in the following section.

10.2 Improved fitting methods for EPR

Critical to the success of the determination of paramagnetic centre concentrations by EPR is the ability to accurately and reproducibly determine the integrated intensity of resonance lines arising from the defect of interest.

The developed EPR spectrum fitter, discussed in chapter 5, utilises a generalised resonance lineshape and accounts for the effects of magnetic field modulation. This results in a simulated spectrum which more closely reflects that of the

experimental data, compared to that produced using Lorentzian or Gaussian lineshapes. A more accurate integrated intensity is therefore obtained and the use of a systematic fitting method means the reproducibility of quantitative measurements is increased; EPR measurements over a period of one year suggest an standard error of 5% for the concentration of an individual sample. The improvement in the simulation of EPR lineshapes was also demonstrated to permit small/broad overlapping resonance lines to be more readily resolved from large background signals.

In the future alternative optimisation routines for the least-squares fitting are likely to be implemented, as the performance of the current Nelder-Mead routine [1] in cases of more than two overlapping spectra is poor and the global minimum is often not found. It is planned to integrate the simulation package EPR-NMR with the fitting software.

If the concentration of paramagnetic defects is sufficiently high then the lineshape and linewidth depend on concentration. Hence in heterogeneous samples the simulated lineshape may not satisfactorily reproduce the experimental spectrum. It is possible to check if the concentration determined from lineshape analysis [2] matches that from the integrated intensity of the simulation (as would be the case for a homogeneous sample). However, concentration determination in heterogeneous samples are problematic.

10.3 Silicon-related defects in diamond

Silicon is a common impurity in CVD diamond, often accidently incorporated due to the etching of silicon-containing materials present in the reactor [3, 4]. Its influence on the growth is not understood, but recent doping studies suggested that the controlled incorporation of low levels of silicon may be beneficial, with a dramatic effect on the optical properties of the diamond deposited, especially when nitrogen is present in the growth environment [5]. The silicon-related centre which gives rise to a ZPL at 1.68 eV has also been demonstrated as a stable single photon source, which may be employed in quantum information processing applications [6]. However, the structure of this centre has yet to be determined conclusively

by experiment.

Chapter 6 presented results which allowed the identification of the structure of two silicon-related centres in diamond for the first time. Two previously observed EPR spectra, KUL1 and KUL3 [7, 8], were investigated. KUL1 was shown to originate from a neutral silicon split-vacancy defect, $(V\text{-}Si\text{-}V)^0$, whilst KUL3 was identified as $(V\text{-}Si\text{-}V)^0$ decorated by a hydrogen atom between the silicon atom and a nearest-neighbour carbon atom, denoted $(V\text{-}Si\text{-}V{:}H)^0$. The $(V\text{-}Si\text{-}V)^-$ defect is thought to be responsible for the ZPL at 1.68 eV [9] and this charge state would also be expected to be paramagnetic ($S = \frac{1}{2}$), but no spectra were observed that could be assigned to this defect. It is proposed that a dynamic Jahn-Teller coupling in the ground state may be responsible for the absence of a detectable spectrum; averaging between different configurations (depending on the rate of inter-conversion) could cause significant broadening of the resonance lines to the extent that it prevents their detection.

Further investigations of $(V\text{-}Si\text{-}V)^0$ were presented in chapter 7, where it was shown that this defect is preferentially aligned with respect to the growth direction in samples grown on {110} substrates. This finding is significant, as it not only implies that the defect is grown in (primarily at least) as a unit, but it also demonstrates that the incorporation of silicon affects the subsequent growth. The degree of preferential alignment is also suggested to be related to the degree of the surface roughening, revealing how the study of defects in the bulk can provide information about processes occurring at the surface during growth.

10.4 The nitrogen-vacancy centre in diamond

The negatively charged nitrogen-vacancy centre (NV^-) has attracted attention within the diamond and quantum information processing communities, due to its use in single photon sources [10] and the potential for it to be employed in solid state quantum computation [11].

Chapter 8 presents a number of results that are important in this context. The hyperfine parameters, which can be used to estimate the unpaired electron probability density at nuclei with non-zero spin, have been redetermined for $^{14}NV^-$ and

$^{15}NV^-$ centres, whilst two sets of ^{13}C hyperfine satellites were resolved. It was demonstrated that the sign of the ^{14}N hyperfine interaction is negative, contrary to the conclusion of previous investigations [12]. The determined ^{13}C hyperfine parameters suggest that ~ 84% of the unpaired electron probability density is located on the three carbon atoms nearest the vacancy, with a further ~ 12% on a group of six equivalent carbon atoms. These were assigned to next-nearest neighbours, although recent theoretical work has suggested the possibility of resolvable hyperfine interactions existing for ^{13}C atoms located up to 7 Å from the vacancy [13]. Hence this assignment is likely to be reinvestigated.

The degree of spin polarisation of the $M_S = 0$ spin state of the ground state of NV^- under optical illumination was examined and it was shown that a simple experimental setup involving a 200 W Hg-Xe lamp and low-pass filters permitted the threshold energy for spin polarisation to be determined. A value of ~ 1.9 eV was obtained, close to that expected, as the energy of the ZPL for NV^- is 1.945 eV.

This result was important as it demonstrated that, using this experimental setup, the energy required for spin polarisation could be employed to correlate EPR spectra with defects which give rise to a ZPL. Hence, when a previously unobserved spin polarised $S = \frac{3}{2}$ defect was observed under conditions of optical illumination in a HPHT sample which had been irradiated and annealed to create NV centres, the energy threshold for spin polarisation was measured. This was shown to be ~ 2.1 eV, close to the position of the ZPL for NV^0 (2.156 eV). The defect had trigonal symmetry and the involvement of nitrogen was demonstrated. These findings represented a considerable body of evidence supporting the assignment of this spectra to the $^4A_2$ excited state of NV^0. As for $(V\text{-}Si\text{-}V)^-$ it is suggested that a dynamic Jahn-Teller coupling [14] is responsible for the apparent absence of EPR lines from the ground state of NV^0.

10.5 The negative nitrogen-vacancy-hydrogen defect

The topic of the final results chapter was the further investigation of the negatively charged nitrogen-vacancy-hydrogen defect (NVH^-). Experimental EPR

measurements [15] reveal a defect of trigonal symmetry, which invites the suggestion that the hydrogen atom is bonded to the nitrogen atom. However, theoretical modelling suggests that such a model is unstable and it was proposed that the hydrogen atom bonds to one of the three nearest-neighbour carbon atoms around the vacancy [16].

In addition to determining more accurate spin-Hamiltonian parameters for this defect the results in chapter 9 revealed a transition dependent line-broadening effect, which varies with the microwave frequency but is temperature independent in the range 8–750 K. A dynamic averaging of the position of the hydrogen atom in this defect, as suggested by Goss *et al.* [16], was shown to provide a plausible explanation for this observation.

To correctly model a dynamic NVH^- centre it is necessary to know the spin-Hamiltonian parameters for the C_{1h} symmetry configuration resulting from the hydrogen atom being bonded to one of the carbon atoms. These parameters are currently not known, but the effect of tunnelling of the hydrogen atom was considered using a test model of lower symmetry. The use of suitable spin-Hamiltonian parameters would permit the tunnelling rate of the hydrogen atom in this defect to be found experimentally. This work is to be completed in the near future.

10.6 Next steps

In the investigations presented in this thesis two defects, regularly observed in PL and optical absorption, whose paramagnetic ground states remain elusive in EPR measurements, have been mentioned: NV^0 and $(V\text{-}Si\text{-}V)^-$. Both these centres have potential applications in quantum information processing and hence the detection of the ground states could have important implications. This is particularly true in the case of the NV^0 defect; a donor is not required for the production of NV^0 in contrast to the situation for NV^-, which may simplify its production. Hence the detection of the ground state of NV^0 and $(V\text{-}Si\text{-}V)^-$ are important future targets.

The suggestion that a dynamic Jahn-Teller coupling is responsible for the inability to detect EPR signals from these defects suggests that the application of uniaxial stress whilst conducting EPR measurements could be beneficial, as this

would lock the defects into a lower symmetry configuration. Additionally such a method could allow the static C_{1h} spin-Hamiltonian parameters for the NVH^- to be determined, as discussed in the previous section. The experimental equipment to make such studies possible is currently being development (EPSRC Grant Reference: EP/C00891X/1) and it is apparent that its use could provide the answers to many of the questions that remain from this work.

References

[1] J. A. Nelder and R. Mead, The Computer Journal **7**, 308 (1965).

[2] J. A. van Wyk, E. C. Reynhardt, G. L. High, and I. Kiflawi, J. Phys. D Appl. Phys. **30**, 1790 (1997).

[3] C. D. Clark and C. B. Dickerson, Surf. Coat. Tech. **47**, 336 (1991).

[4] P. Joeris, I. Schmidt, and C. Benndorf, Diam. Relat. Mater. **5**, 603 (1996).

[5] S. D. Williams, D. J. Twitchen, P. M. Martineau, G. A. Scarsbrook, and I. Friel (2007), UK Patent Application: GB 2428690 A.

[6] C. L. Wang, C. Kurtsiefer, H. Weinfurter, and B. Burchard, J. Phys. B At. Mol. Opt. **39**, 37 (2006).

[7] K. Iakoubovskii and A. Stesmans, Phys. Status Solidi A **186**, 199 (2001).

[8] K. Iakoubovskii, A. Stesmans, K. Suzuki, J. Kuwabara, and A. Sawabe, Diam. Relat. Mater. **12**, 511 (2003).

[9] J. P. Goss, R. Jones, S. J. Breuer, P. R. Briddon, and S. Oberg, Phys. Rev. Lett. **77**, 3041 (1996).

[10] A. Beveratos, R. Brouri, T. Gacoin, A. Villing, J. P. Poizat, and P. Grangier, Phys. Rev. Lett. **89**, 187901 (2002).

[11] F. T. Charnock and T. A. Kennedy, Phys. Rev. B **64**, 041201 (2001).

[12] X. F. He, N. B. Manson, and P. T. H. Fisk, Phys. Rev. B **47**, 8816 (1993).

[13] A. Gali, M. Fyta, and E. Kaxiras, Phys. Rev. B **77**, 155206 (2008).

[14] G. Davies, J. Phys. C Solid State **12**, 2551 (1979).

[15] C. Glover, M. E. Newton, P. Martineau, D. J. Twitchen, and J. M. Baker, Phys. Rev. Lett. **90**, 185507 (2003).

[16] J. P. Goss, P. R. Briddon, R. Jones, and S. Sque, J. Phys. Condens. Mat. **15**, S2903 (2003).